HIGH FREQUENCY CURRENTS AND HETERODYNE MIXING IN SUPERCONDUCTING TUNNEL JUNCTIONS

A Dissertation

Presented to the Faculty of the Graduate School

of

Yale University

in Candidacy for the Degree of

Doctor of Philosophy

by

Anthony Hodge Worsham II

May, 1992

ABSTRACT

HIGH FREQUENCY CURRENTS AND HETERODYNE MIXING
IN SUPERCONDUCTING TUNNEL JUNCTIONS

Anthony Hodge Worsham II

Yale University

1992

Both $Nb/AlO_x/Nb$ and $Ta/Ta_2O_5/PbBi$ tunnel junctions have been produced for studying the interaction of applied radiation with a Superconductor-Insulator-Superconductor (SIS) tunnel junction. The junctions were of sufficient quality and size [0.5 - 4 $(\mu m)^2$] to study strong quantum mixing effects at 80-110 GHz. The Ta junctions showed the closest approach to the quantum noise limit yet reported, 0.61 ± 0.32 quanta, compared to the quantum limit of 0.5 quanta. The Nb devices were used in a broad-band receiver with no mechanical tuning elements. This receiver has among the lowest noise temperatures (T_R = 41 K at 80 GHz) reported at this time, particularly among receivers with no mechanical tuning elements.

A slotted-line technique and the Nb devices were used to measure the admittance of the tunnel junction at 87.1 GHz. The admittance is composed of the quantum conductance and quantum susceptance. This work reports the first direct observation of the singularity in the quantum susceptance, which is related to the singularity in the reactive quasiparticle currents.

ACKNOWLEDGEMENTS

I have been extremely lucky in that I have had four mentors during my stay at Yale. I consider these four people to be responsible for all of my good accomplishments. I absolve them all for my failings. With their help, teaching, and encouragement, I was able to learn and enjoy the time that I spent pursuing my small part of frontier pushing. In chronological order: Prof. Dan Prober, who taught me excitement, physical understanding, and interdependence; Elie Track, who taught me perseverance, irreverence, philosophy, and reality; Guang-Ji Cui, who taught me hard work and caution; and Dag Winkler, who taught me detail, methodology, honesty, and perspective. I am constantly amazed by the breath of knowledge and the range of interests that these persons possess.

In addition to these four, I have benefited from numerous discussions with Thomas Cunningham, Paul Dresselhaus, Mark Feldman, Steven Klepper, Paul McEuen, Oded Millo, Kevin Smith, and especially George Ugras.

The professional and exceptional help given by Gene Madia, Bob Wisnieff, Han Dang, and Glen Dean, will always be appreciated. Without the help of our collaborators Neal Erickson and Paul Goldsmith at the University of Massachusetts, much of what is presented here would not be possible. This is also true of our collaborators, Carl Mears, Qing Hu, and Paul Richards at the University of California, Berkeley, who have showed that knowledge and precision are a very fruitful combination of traits to possess. I wish to thank Carl Mears for our numerous conversations from which I benefitted immeasurably. The collaborative efforts of Joon-He Kang, John Przybysz, and especially Michael Rooks are also greatly appreciated.

I wish to thank Jim Harper of IBM who loaned the ion gun used in the Ta work, and Dickie Downing, whose excellent machining allowed the Yale receiver work to happen. I also wish to thank Tony Kerr of NRAO for modifying the IF switch used in our

mixer experiments. I also benefitted from some analysis programs sent to me by Anders Skalare.

I wish to thank the members of my thesis committee, Prof. Robert Wheeler, Prof. Victor Henrich, and Prof. T.P. Ma. A special thanks is offered to my "outside reader," Dr. S.-K. Pan.

Beyond science, I wish to thank those people who have given me encouragement and friendship throughout my stay here: Charlie Collins, Sherwin Collins, Jim Dolot, Taite, and the Kahns. I wish to particularly thank Loretta Smith, whose care, concern, and love have been a constant help and source of support throughout.

Finally, I wish to thank my sisters Carla and Mariam, my mother Wilma, and my late father William for their love, support, and confidence.

TABLE OF CONTENTS

Page

ACKNOWLEDGEMENTS ii

LIST OF SYMBOLS AND ABBREVIATIONS ix

LIST OF FIGURES xiii

LIST OF TABLES xiv

I INTRODUCTION 1

1.1 Motivation 1

1.2 The Response of the Tunnel Junction to a Single Frequency 2

1.3 The Response of the Tunnel Junction to Multiple Frequencies 2

1.4 A Novel Device 3

II TUNNELING, A THEORETICAL OVERVIEW 4

2.1 Tunneling in SIS Junctions 4

2.1.1 Tunneling 5

2.1.2 Density of States in a Superconductor 6

2.2 Effect of Radiation 7

2.2.1 Werthamer's Equation 7

2.2.2 Single Integral Representations 10

2.2.3 The Dissipative Currents 11

2.2.4 The Reactive Currents 16

2.2.5 The Kramers-Kronig Relations 16

2.2.6 Response to a Sinusoidal Signal 18

2.2.7 Photon Assisted Tunneling and Direct Detection 20

2.2.8 Quantum Sloshing 22

2.2.9 Current at the Applied Frequency 22

III SIS MIXERS, A THEORETICAL OVERVIEW 25

3.1 The Heterodyne Device 25

3.2 Classical Mixer Theory 27

3.3 Quantum Mixer Theory 31

3.3.1 Determination of $Y_{mm'}$ 33

3.3.2 Gain and Output Impedance 35

3.4 Noise 36

3.4.1 Shot Noise 36

3.4.2 Thermal Noise 39

3.4.3 Quantum Noise 39

IV SIS DEVICES 42

4.1 Devices Required for Mixing 42

4.1.1 Current Density 42

4.1.2 Resistance and Device Size 44

4.1.3 Leakage Currents, Ruggedness, and Operation Temperature 45

4.2 Nb/AlO$_x$/Nb Trilayers 45

4.2.1 Substrates 48

4.2.2 Deposition of the Al Underlayer 49

4.2.3 Deposition of the Trilayer 50

4.2.4 Defining the Junction Area 52

4.2.5 Wiring, Contact, and Ground Plane Layers 54

4.2.6 Wafer Cutting 56

4.3 The Junctions 57

4.4 Critical Examination of the Device Process 57

4.5 Ta Devices 62

V RECEIVER DESIGN AND MIXING RESULTS 66

5.1 Receiver Design 66

5.1.1 The Local Oscillator and Dewar 68

5.1.2 The Signal Path 70

5.1.3 The Device 72

5.1.4 Scale Modeling and Embedding Admittance 75

5.1.5 The IF System 76

5.1.6 DC Biasing and Heat Sinking 78

5.2 Measurement 79

5.2.1 Selecting Devices 80

5.2.2 Sample Mounting 80

5.2.3 Cooling the Dewar 83

5.2.4 Finding the Optimum LO Power and DC Bias 83

5.2.5 Measurement of Receiver Noise Temperature and Gain 85

5.2.6 Measurement of the IF Noise Temperature 85

5.2.7 Determination of the IF Mismatch 87

5.3 Experimental Results 87

5.3.1 Corrections to the Simple Mixer Noise Formula 89

5.3.2 DSB vs. SSB 95

5.3.3 Measured Receiver Noise Temperatures 97

5.3.4 Mixer Noise Temperatures 101

5.3.5 Mixer Gain 101

5.4 Theoretical Modeling 103

5.4.1 Arrays vs. Single Junctions 105

5.4.2 Finding the Embedding Admittance 105

5.4.3 Theoretical fits to the pumped I-V 108

5.4.4 Calculated Embedding Admittances 114

5.4.5 Modeling of Mixer Noise and Gain 116

5.5 Quantum Limited Noise at Berkeley 121

5.5.1 The Experiment 121

5.5.2 The Modeling and Results 121

VI QUANTUM CONDUCTANCE AND SUSCEPTANCE 127

6.1 Theory of Quantum Conductance and Susceptance 127

6.1.1 Quantum Conductance 129

6.1.2 Quantum Susceptance 131

6.1.3 Effect of the Quantum Admittance on the DC Pumped I-V curve 133

6.2 Review of Previous Work 137

6.3 Experimental Set-Up 138

6.4 Measurement of the Standing Wave 139

6.4.1 Measurement of Power vs. Bias Voltage 139

6.4.2 The Standing Wave 139

6.4.3 Fits to the Standing Wave Equation 149

6.5 Transmission Line Matching Review 150

6.6 Results and Analysis 151

6.6.1 Equivalent Circuit 151

6.6.2 Γ for the Four Junction Array 153

6.6.3 Theoretical Predictions 160

6.6.4 The Measured Quantum Admittance vs. DC Voltage 164

6.7 Discussion of Discrepancies 168

6.7.1 Passive Terms and Noise Rounding 168

6.7.2 Quantum Discrepancies 173

6.8 Two Junction Array Results 174

VII TUNING IN SIS MIXERS 181

7.1 Mechanical and Passive Tuning 181

7.2 Josephson Tuning 182

7.2.1 Chip Design 183

7.2.2 Testing Results 186

7.3 Quantum Tuning 187

7.3.1 The Model 187

7.3.2 The Variable Embedding Admittance 189

7.3.3 The Effects of the Quantum Admittance 191

VIII CONCLUSIONS 197

APPENDIX A - Nb/AlO$_x$/Nb Trilayer Tunnel Junction Fabrication Process 198

APPENDIX B - Ta/Ta$_2$O$_5$/PbBi Tunnel Junction Fabrication Process 203

APPENDIX C - The Programming Sequence to Analyze Standing Wave Data 207

REFERENCES 209

LIST OF SYMBOLS AND ABBREVIATIONS

α	Argument of the Bessel function $J_n(\alpha)$, α is usually $= eV_\omega/\hbar\omega$
α	Loss between the mixer and hot/cold load
B	Bandwidth in Hertz
BCS	Bardeen-Cooper-Schrieffer
B_Q	The quantum susceptance
c_k	Bloch states
Δ	Superconducting energy gap
ΔV	The voltage width of the current rise at the gap of the SIS tunnel junction
DSB	Double side band
f(E)	Fermi distribution function
FET	Field effect transistor
G	Conductance
G	Gain
γ	Attenuation factor
Γ	The total reflection coefficient ($= \rho e^{i\theta}$)
G_Q	The quantum conductance
H	Hamiltonian
$\hbar$	Planck's constant/2π ($= 1.0546 \times 10^{-34}$ Joules-seconds)
$H_{mm'}$	H matrix element for calculating the mixer noise
I_c	Junction critical current
IF	Intermediate frequency
I_J	Josephson current
I_{J1}	The Josephson sine current
I_{J2}	The Josephson cosine current

I_{LO}	Magnitude of the LO current source
I_o	The dc current
I_{qp1}	The reactive quasiparticle current
I_{qp2}	The dissipative quasiparticle current
I-V	Current (I) vs. Voltage (V)
J_c	Junction current density
J_n	n^{th} order Bessel function of the first kind
j_p	Pair response function
j_{qp}	Quasiparticle response function
KK	Kramers-Kronig
λ_c	The waveguide cut-off wavelength
λ_g	The wavelength in the waveguide
$\lambda_{mm'}$	Normalized small signal impedance matrix element
L_J	Josephson inductance
LO	Local oscillator
$N_n(0)$	Density of States at the Fermi level for a normal metal
ω	Radial frequency (= 2π x frequency)
ω_J	Josephson frequency (= $2eV/\hbar$)
ω_m	Frequency m of the mixer $\omega_m + m\omega_{LO}$ $(m = 0, \pm 1, \pm 2, ...)$
P_{IF}	Power at the intermediate frequency
P_{inc}	Incident power
P_s	Power at the signal frequency
ϕ	Macroscopic phase across the tunnel junction
R_n	Normal state tunnel junction resistance
ρ	Reflection coefficient
ρ_m	Reflection coefficient at the mixer output
rf	Radio frequency, always greater than 75 GHz in this work

S_B	Spectral density of the bath noise
S_I	Responsivity
S_{IF}	Spectral density of the IF noise
SIS	Superconductor-Insulator-Superconductor
S_{LO}	Spectral density of the noise from room temperature leakage
S_m	Spectral density of the mixer noise
SSB	Single side band
T_B	Bath temperature (usually = 4.4 K) or bath noise temperature
θ	Phase, usually of the standing wave
θ_R	Constant phase offset
T_{IF}	IF noise temperature
T_{LO}	Noise temperature from room temperature leakage
T_c	Superconducting critical temperature or transition temperature
T_{kq}	Tunneling matrix element
T_m	Mixer noise temperature
T_R	Receiver noise temperature
V_g	The gap voltage
V_o	The dc bias voltage
VSWR	Voltage standing wave ratio
V_ω	Amplitude of the voltage at the frequency ω (usually the LO)
WR	Rectangular waveguide
$W(\omega)$	Fourier terms of the applied *rf* voltage
X_p	The impedance due to the passive on-chip circuitry
Y_{emb}	Embedding admittance
Y_I	Admittance at the image frequency
YIG	Yttrium-Iron-Garnet
Y_{LO}	Admittance at the local oscillator frequency

Y_m	Admittance seen by the mixer at the frequency ω_m
$Y_{mm'}$	Element of the Y matrix for mixer conversion
Y_S	Admittance at the signal frequency
Z_{IF}	Output impedance of the mixer
Z_L	Load impedance
$Z_{mm'}$	Matrix element of the augmented Z matrix
Z_o	Waveguiding impedance

LIST OF FIGURES

Figure		Page
2-1	Superconducting density of states and excitation spectra.	8
2-2	The four tunneling currents in an SIS tunnel junction.	12
2-3	Tunneling mechanisms.	14
2-4	The semiconductor model.	15
2-5	Photon assisted tunneling steps.	21
3-1	Block diagram of a heterodyne receiver.	26
3-2	Frequency spectra of the mixer.	26
3-3	Schematic representation of a non-linear diode mixer.	29
4-1	Schematic side view of the Nb/AlO$_x$/Nb device fabrication.	46
4-2	Top view of the Nb/AlO$_x$/Nb junction area.	55
4-3	I-V traces of Nb/AlO$_x$/Nb tunnel junctions.	58
4-4	Schematic side view of the Ta/Ta$_2$O$_5$/PbBi device fabrication.	63
5-1	Side view of the ridge coupling.	71
5-2	The SIS heterodyne device and equivalent circuit.	73
5-3	Receiver schematic.	77
5-4	Schematic of the chip mounting.	81
5-5	Current and IF power vs. voltage characteristics of device B.	84
5-6	IF output power vs. input blackbody temperature of device E at 80 GHz.	86
5-7	The output power vs. the input power at the circulator for device E at 80 GHz.	88
5-8	Unpumped and pumped I-V's for device E.	90
5-9	Unpumped and pumped I-V's for device I.	91
5-10	The noise equivalent circuit for the receiver.	93
5-11	The pumped I-V traces of device E at the USB and LSB.	96
5-12	DSB Receiver noise temperature for selected devices.	98

5-13 DSB receiver noise temperatures for reported devices in the 100 GHz band. 99

5-14 DSB Mixer noise temperatures. 102

5-15 DSB Mixer gains. 104

5-16 Equivalent circuit for modeling. 106

5-17 A comparison of the experimental and theoretical pumped I-V fit. 106

5-18 Unpumped and pumped I-V curves of a $Ta/Ta_2O_5/PbBi$ tunnel junction. 110

5-19 Unpumped, pumped and theoretical pumped I-V curves of device E. 111

5-20 I-V characteristic showing the proximity effect. 113

5-21 Calculated embedding admittances of devices E and I. 115

5-22 Experimental and calculated mixer noises for devices E and I. 117

5-23 Experimental and calculated coupled gains for devices E and I. 119

5-24 Quantum limited mixer noise of a $Ta/Ta_2O_5/PbBi$ tunnel junction. 123

5-25 Available gain vs. frequency of a $Ta/Ta_2O_5/PbBi$ tunnel junction. 124

5-26 Mixer noise and gain vs. pump power of $Ta/Ta_2O_5/PbBi$ tunnel junction. 125

6-1 Geometric construction of the low-power G_Q. 130

6-2 Geometric construction of the low-power B_Q. 132

6-3 Circuit used in calculating effects of G_Q and B_Q on pumped I-V shape. 134

6-4 I-V traces of a theoretical BCS junction with various embedding. 134

6-5 Results of Berkeley experiment which measured B_Q and G_Q. 136

6-6 Schematic of the standing wave measurement apparatus. 140

6-7 Schematic of the waveguide section between the device and the YIG source. 141

6-8 Power vs. dc voltage data taken to determine the standing waves. 146

6-9 Standing waves. 148

6-10 Equivalent circuits used in the analysis. 152

6-11 Unpumped and pumped I-V traces of device J. 154

6-12 Reflection coefficient and phase of device J for the low-power input. 156

6-13 Reflection coefficient and phase of device J for the medium-power input. 158

6-14 Reflection coefficient and phase of device J for the high-power input. 159

6-15 Theoretical G_Q and B_Q of device J for the high-power input. 161

6-16 Theoretically expected load admittance of device J for the low-power input. 163

6-17 Experimental and theoretical G_Q and B_Q of device J for the low input power. 165

6-18 Experimental and theoretical G_Q and B_Q of dev. J for the medium input power. 166

6-19 Experimental and theoretical G_Q and B_Q of device J for the high input power. 167

6-20 Effect of capacitance uncertainty on the experimentally deduced G_Q and B_Q. 170

6-21 Effect of waveguiding impedance on the experimentally deduced G_Q and B_Q. 172

6-22 Unpumped and pumped I-V traces of device K. 175

6-23 Reflection coefficient and phase of device K at the low input power. 176

6-24 G_Q and B_Q for device K with low input power. 178

6-25 Reflection coefficient and phase of device K at the high input power. 179

6-26 G_Q and B_Q for device K with high input power. 180

7-1 Top view and equivalent circuit of Josephson and quantum tuning device. 184

7-2 DC and Kramers-Kronig currents of modeled device. 188

7-3 Admittance of the quantum tuning junctions. 190

7-4 Effect of the quantum admittance on the mixer pumped I-V curve. 192

7-5 Gain of the quantum tuned device. 193

7-6 Gain and noise of device with fixed embedding admittance. 195

LIST OF TABLES

Table		Page
2-1	Properties of the four tunneling currents in an SIS tunnel junction.	24
3-1	Mixer noise contributions.	41
4-1	Properties of selected Nb/AlO_x/Nb devices.	59
4-2	Properties of selected Nb/AlO_x/Nb devices worldwide.	60
5-1	Mixer noise and gain characteristics of selected Nb/AlO_x/Nb devices.	120

I INTRODUCTION

1.1 Motivation

Since Josephson (1962) first predicted an ac supercurrent flowing across a tunnel junction in response to an applied dc voltage, much interest has been given to the effects of dc voltage and applied radiation on the tunnel junction. Most of this attention has focused on the pair currents, where many applications exist, including Superconducting QUantum Interference Devices (SQUIDs), oscillators, and voltage standards. Tucker's quantum mixer theory [Tucker, 1979] opened the door to understanding the interaction of applied radiation to the quasiparticles flowing in the junction, leading to the application of heterodyne mixing. The vast majority of this thesis will focus on the interaction of quasiparticles with applied radiation. The applied radiation discussed will be in the frequency range of 80-120 GHz. These frequencies are high enough so that the response of even moderately good tunnel junctions is in the quantum regime, yet these frequencies are low enough to be accessible using waveguide systems. Waveguide systems are inherently better understood and characterized than more open, quasi-optical systems. Given these benefits, this frequency range (W-band) is an excellent range in which to explore the currents flowing in the tunnel junction, the fundamental quantum limits of heterodyne mixing, and the engineering/physics involved in detecting this radiation.

The *rf*-induced currents are important since they are a basic prediction of the quantum tunneling theory [Josephson, 1962; Werthamer, 1966; Harris, 1974,1975]. In addition, dissipative and reactive currents exist in other systems, including resonant tunneling diodes [Liu, 1991]. The technique for measuring the dissipative and reactive currents discussed in this thesis could be extended to these other systems.

Heterodyne mixing is of interest since superconductor-insulator-superconductor (SIS) mixers are the most sensitive detectors of radiation from ~30 to 300 GHz [Tucker and Feldman, 1985; Blundell and Winkler, 1991]. The use of these devices in radioastronomy

has created a desire for sensitivity and ease of use. The quantum theory of mixing [Tucker, 1979] has proven to be a powerful tool with which to analyze the results of the interaction of radiation with the device. In addition, it is a useful tool in designing future radiation detectors. Some of the work presented here verifies one of major predictions of Tucker's theory, quantum limited noise in SIS mixers. Much of the work presents results for a "useful" receiver which offers broad bandwidth operation and requires no mechanical tuning over the frequency range 80-110 GHz.

Some of the ideas learned by studying the high frequency currents and mixing in SIS tunnel junctions lead to a novel application which combines aspects from both mixing and the single frequency response. A novel device, which may have applications in future high frequency receivers, is modeled in this work.

1.2 The Response of the Tunnel Junction to a Single Frequency

Chapter II discusses the underlying physics which govern the interaction of the SIS tunnel junction with applied radiation. This interaction leads to dissipative and reactive currents in both the pair and quasiparticle currents. Chapter VI reports a set of experiments which measure the dissipative and reactive quasiparticle currents. These are the first reported experiments to directly measure these fundamental tunneling currents over the full dc voltage bias and input power range. The standing wave technique used to measure the quasiparticle currents is a unique way in which to probe the high frequency impedance of the SIS tunnel junction.

1.3 The Response of the Tunnel Junction to Multiple Frequencies

Chapter III gives the theoretical background of mixing two frequencies in an SIS tunnel junction. Chapter V describes two separate "multiple frequency" experiments. One involved a collaboration with Carl Mears, Qing Hu, and Paul Richards at the University of California, Berkeley. This work showed the lowest reported noise in SIS mixers, relative

to the quantum limit. The experimental results have been extensively modeled and show good agreement with the quantum mixer theory predictions. My part of this collaboration was the fabrication of the devices. The quality of these devices was important in achieving the quantum limited noise. Many of the fabrication issues of these devices are discussed in Chapter IV.

The second "multiple frequency" experiment is using a receiver designed and built at Yale by Dag Winkler, with help from Nuray Ugras. The SIS devices for this mixer receiver were fabricated by me at the Westinghouse Science and Technology Center in collaboration with researchers there. The receiver has proven to be an excellent prototype of a "useful" receiver, where "useful" refers to its 4.4 K operation temperature, broad bandwidth, and lack of mechanical tuning elements. The mixing results for the devices used here have also been modeled using the quantum mixer theory.

1.4 A Novel Device

Chapter VII presents some modeling calculations using a novel device to electrically tune an SIS mixer. The dc voltage bias dependence of the high frequency impedance of the SIS tunnel junction is exploited as a variable on-chip impedance element. This device combines many of the ideas found in the single frequency and multiple frequency work. Only modeling calculations are presented, although they rely on the measured dc I-V trace of a device. Devices similar to the one described here have been fabricated, but are as yet experimentally untested.

II TUNNELING, A THEORETICAL OVERVIEW

This chapter provides the theoretical framework necessary in order to understand the results on the observation of the effects of the high frequency currents in superconducting tunnel junctions. The chapter is divided into two sections.

1.) Theory of tunneling
2.) Tunneling in the presence of radiation

The section on the theory of tunneling will review the relevant Hamiltonian and present the tunneling current in the absence of applied radiation. The discussion will lead to the second section, which describes the tunneling currents in response to applied radiation.

2.1 Tunneling in SIS Junctions

The theory of tunneling in superconductors is covered in many excellent reviews [Wolf, 1985; Tinkham, 1975; Duke, 1969; Rickhazen, 1969]. Only the essential ideas will be presented here. Since the discovery of tunneling between superconductors by Giaever (1960), tunnel junctions have been studied extensively. Superconductor-Insulator-Superconductor (SIS) tunnel junctions exhibit both quasiparticle and pair tunneling [Josephson, 1962; for a review see Barone and Paterno, 1982]. SQUIDs (Superconducting QUantum Interference Device) have utilized the pair tunneling and been demonstrated as ultra-sensitive voltmeters and magnetometers [Van Duzer and Turner, 1981]. Other interesting applications of SIS tunnel junctions are oscillators [Jain et al., 1984] and voltage standards [Hamilton et al., 1987]. We are primarily interested in this thesis in the tunneling of quasiparticles across the tunnel barrier. These quasiparticle are the elementary excitations from the superconducting ground state [Bardeen, Cooper, and Schreifer, 1957] and lead to a non-linear current voltage trace.

2.1.1 Tunneling

All of the tunneling results have their roots in perturbation theory using a tunneling Hamiltonian. There is a non-zero probability of charge transfer between the two metal electrodes separated by a thin insulator. Bardeen (1961) first considered the tunnel junction to be two many body systems which are weakly coupled through the tunnel barrier. Subsequent work constructed the Hamiltonian which described the tunneling across the barrier [Cohen, Falicov, and Phillips, 1962]. The additional term which describes the tunneling is

$$H_T = \sum_{kq\sigma} [T_{kq}\, c_k^{\dagger} c_q + T_{kq}^{*}\, c_q^{\dagger} c_k] = H_T^{+} + H_T^{-} \qquad 2\text{-}1$$

where T is the tunneling matrix element and the one-electron operator c_k and c_q represent Bloch states on the left and right hand sides of the junction respectively. The total tunneling Hamiltonian for the system is

$$H = H_R + H_L + eV(t)N_L + H_T \qquad 2\text{-}2$$

where H_R and H_L are the full Hamiltonians describing the left and right electrodes, and $eV(t)$ is a time dependent potential applied to the number operator for the left electrode, N_L. The tunneling matrix elements found in H_T are considered to be sufficiently small so that the flow of current is treated to the lowest order in the coupling. The dc current is obtained using Green's functions and linear response theory [Ambegaokar and Baratoff, 1963; Werthamer, 1966; Rogovin and Scalapino, 1974]. The main result, in useable form is

$$I_{dc}(V) = \frac{2\pi e}{\hbar} |T|^2 \int_{-\infty}^{\infty} dE\, N_1(E)\, N_2(E-eV)\, [1 - f(E - eV)] \qquad 2\text{-}3$$

where N_1, N_2 are the density of states of the excitations on the left and right side electrodes, $f(E) = [\exp(E/kT) - 1]^{-1}$ is the Fermi distribution function, and T is the tunneling matrix element (which has units of energy). For the normal metal tunnel junction,

$$I_{dc}(V)_{\text{normal metal electrodes}} = V/R_n \qquad 2\text{-}4$$

$$\text{where } R_n = \frac{\hbar}{2\pi e^2\, N_1(0)\, N_2(0)\, |T|^2} \qquad 2\text{-}5$$

which is a valid equation for a resistor when the density of states on both sides of the tunnel junction are constant, equal to their values at the Fermi level. For SIS tunnel junctions, the solution to eq. 2-3 requires knowledge of the superconducting density of states.

2.1.2 Density of States in a Superconductor

According to the BCS theory, the superconductor is a condensate of electron pairs [Bardeen, Cooper, and Schrieffer, 1957]. These pairs are coupled by the exchange of a virtual phonon which causes an attractive electron-electron interaction which is stronger than the Coulomb repulsion between the two electrons. The pairs, called Cooper pairs, are of equal and opposite spin and wavevector ($k\uparrow$, $-k\downarrow$) and exist below a temperature T_c. A review of the BCS results can be found in Tinkham (1975) and Rickhazen (1969). The calculated result for the density of quasiparticle states in the superconductor is

$$N_s(E) = N_n(0)\frac{|E|}{(E^2 - \Delta^2)^{1/2}} \qquad \text{for } |E| \geq \Delta$$

$$= 0 \qquad \text{for } |E| < \Delta \qquad 2\text{-}6$$

$N_n(E)$ is the normal metal density of states. The superconducting density of states and excitation spectra are shown in Fig. 2-1a, along with the normal metal results. Using this density of states, the dc tunneling current of the BCS quasiparticles can be calculated from eq. 2-3. The results are summarized in section 2.2.2.

2.2 Effect of Radiation

2.2.1 Werthamer's Equation

Werthamer (1966) gives an expression for the current flowing in a tunnel junction in the presence of an arbitrary applied voltage. In this approach, the quasiparticle density of states, the temperature, and the tunneling probability are hidden in the response functions, j_{qp} and j_p. Werthamer's result for the total tunneling current of the SIS junction in response to an applied radiation V(t) is

$$I(t) = \mathrm{Im} \int_{-\infty}^{\infty} d\omega\, d\omega' \Big\{ W(\omega)W^*(\omega')\, e^{-i(\omega-\omega')t}\, j_{qp}(\omega' + \frac{\omega_J}{2})$$

$$+ W(\omega)W(\omega')e^{-i(\omega+\omega')t+i\phi}\, j_p(\omega + \frac{\omega_J}{2}) \Big\} \qquad 2\text{-}7$$

where the applied dc voltage is found in $2eV_o/\hbar = \omega_J$, and the applied *rf* voltage is found in

$$\int_{-\infty}^{\infty} d\omega W(\omega)\, e^{-i\omega t} = \exp(-i\frac{e}{\hbar} \int^{t} dt' \{V(t') - V_o\}) \qquad 2\text{-}8$$

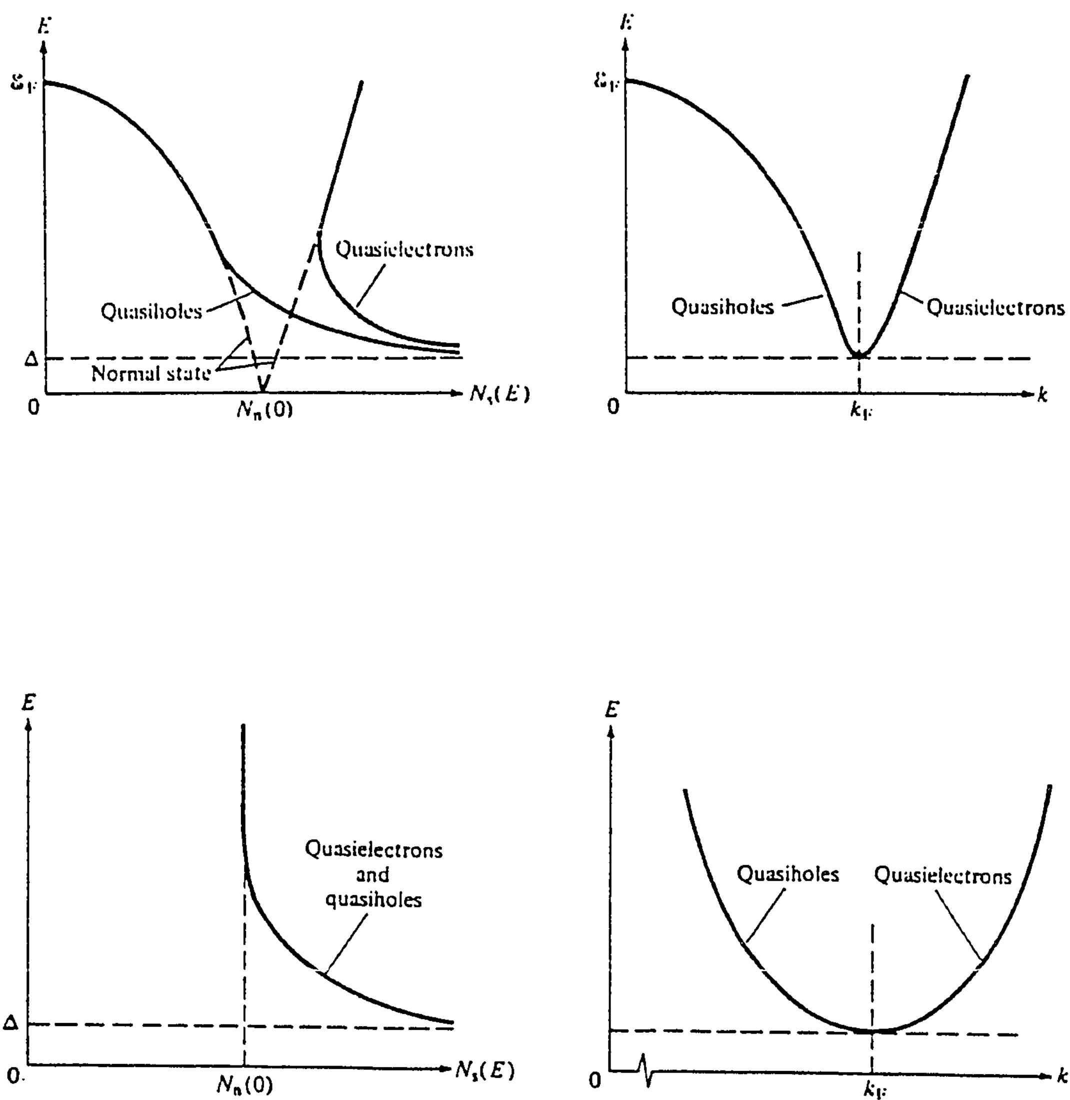

Fig. 2-1 a) and b) The density of states and excitation spectra for a superconductor. c) and d) The density of states and excitation spectra expanded aroud the k_F. (From Van Duzer and Turner, 1981).

The Fourier components $W(\omega)$ are the result of the time dependent applied *rf* voltage $V(t')$. The quasiparticle and pair response functions are j_{qp} and j_p, respectively. The double integral results from the effect of the applied *rf* voltage on both sides of the tunnel junction. The phase, ϕ, contains the well known Josephson oscillations, $\phi = \phi_o - \omega_J t$. This form of the tunneling current is especially useful since it contains the tunneling current contributions of both pairs and quasiparticles. Although this expression is complete, i.e., it contains all of the information necessary to compute the current in the tunnel junction, it is difficult to solve analytically since the response functions contain information regarding the pair and quasiparticle density of states, the temperature, and the gap parameter. Analytic solutions exist in the dc case, $V(t) = V_o$. Setting $W(\omega) = W(\omega')$ $= \delta(0)$ and $\omega = \omega' = 0$, eq. 2-7 reduces to:

$$I(t) = \mathrm{Im}\left\{j_{qp}\left(\frac{\omega_J}{2}\right)\right\} + \mathrm{Im}\left\{j_p\left(\frac{\omega_J}{2}\right)\right\}\cos\phi + \mathrm{Re}\left\{j_p\left(\frac{\omega_J}{2}\right)\right\}\sin\phi \qquad \text{2-9}$$

This expression, first derived by Josephson (1962) shows that for a dc voltage bias and in the absence of applied radiation, the tunneling current can be described as being composed of three parts. The first term on the right is simply the imaginary part of the quasiparticle response function. It represents all of the quasiparticle tunneling across the tunnel barrier for an applied voltage $V_o = \hbar\omega_J/2e$. In addition, since the remaining two terms oscillate at the Josephson frequency ω_J for non-zero voltages, the quasiparticle current is the only time averaged dc contribution to the tunneling current for finite V_o in the voltage bias case. The two remaining current terms on the right of eq. 2-9 are called the Josephson cosine and Josephson sine currents for obvious reasons.

One sees immediately from eq. 2-9 that in the absence of applied radiation, the tunneling current contains no contribution due to the real part of the quasiparticle response function. This term is only seen in the tunneling current for finite frequency applied

radiation. For this reason, along with the fact that the pair currents were predicted and demonstrated to be useful for a variety of applications [for a review see Barone and Paterno, 1981; and K.K. Likharev, 1979], the effect of the real part of the quasiparticle response function was largely ignored. Now, with the advances in high frequency measurement techniques, the effects due to the real part of response function can be measured. This measurement is a major part of this thesis. With this motivation, the tunneling current flowing in an SIS tunnel junction can be understood as containing *four* terms, which are historically called I_{qp1}, I_{qp2}, I_{J1}, and I_{J2} where the subscripts 1 and 2 refer to the real and imaginary parts of the response functions respectively.

2.2.2 Single Integral Representations

In the absence of applied radiation, solutions exist for all four elementary tunneling currents. As seen in eq. 2-9, the current contribution due to I_{qp1} is zero for constant applied voltage. This does not preclude us from giving its functional form. Just as I_{J1} and I_{J2} are modulated by the phase ϕ, I_{qp1} can be thought of as being modulated by the phase $Im\{\exp[-i(\omega - \omega')t]\} = 0$ at dc. These single integral representations are given by Larkin and Ovchinnikov (1967) and Harris (1974,1975)

$$I_{qp1}(V) = \frac{1}{2eR_n} \int_{-\infty}^{\infty} \left\{ \frac{(E - eV)\, \theta(\Delta_1 - |E - eV|)\, \theta(|E| - \Delta_2)}{[\Delta_1^2 - (E - eV)^2]^{1/2}\, (E^2 - \Delta_2^2)^{1/2}} \right.$$

$$\left. + \frac{(E + eV)\, \theta(|E| - \Delta_1)\, \theta(\Delta_2 - |E - eV|)}{(E^2 - \Delta_1^2)^{1/2}\, [\Delta_2^2 - (E + eV)^2]^{1/2}} \right\} \times E[1 - 2f(|E|)]\, dE \qquad \text{2-10}$$

$$I_{J1}(V) = \frac{-\Delta_1 \Delta_2}{2eR_n} \int_{-\infty}^{\infty} \left\{ \frac{\theta(\Delta_1 - |E - eV|)\, \theta(|E| - \Delta_2)}{[\Delta_1^2 - (E - eV)^2]^{1/2} (E^2 - \Delta_2^2)^{1/2}} \right.$$

$$+ \frac{\theta(|E| - \Delta_1)\, \theta(\Delta_2 - |E + eV|)}{(E^2 - \Delta_1^2)^{1/2}\, [\Delta_2^2 - (E + eV)^2]^{1/2}} \Bigg\} \times [1 - 2f(|E|)]\, dE \qquad 2\text{-}11$$

$$I_{qp2}(V) = \frac{1}{eR_n} \int_{-\infty}^{\infty} dE \frac{|E|\, \theta(|E| - \Delta_1)}{(E^2 - \Delta_1^2)^{1/2}} \frac{|E + eV|\, \theta(|E + eV| - \Delta_2)}{[(E + eV)^2 - \Delta_2^2]^{1/2}}$$

$$\times [f(E) - f(E + eV)] \qquad 2\text{-}12$$

$$I_{J2}(V) = \frac{-\Delta_1 \Delta_2}{eR_n} \int_{-\infty}^{\infty} dE \frac{(\text{sgn } E)\, \theta(|E| - \Delta_1)}{(E^2 - \Delta_1^2)^{1/2}} \frac{[\text{sgn } (E + eV)]\, \theta(|E + eV| - \Delta_2)}{[(E + eV)^2 - \Delta_2^2]^{1/2}}$$

$$\times [f(E + eV) - f(E)] \qquad 2\text{-}13$$

where

sgn E =	+1 for E > 0	θ(E) =	0 for E < 0
	-1 for E < 0		1 for E > 0

$f(E) = [\,1 + \exp(E/k_BT)]^{-1}$; Δ_1, Δ_2 are the energy gaps of the two superconductors, and R_n is the normal state resistance of the junction. The tunneling probability determines R_n. The equations are grouped in this way to show that the similarities in the functional form are *not* between the two terms which are from the same response function. Instead, we see that the two terms, I_{J1} and I_{qp1}, are similar and the two terms, I_{J2} and I_{qp2}, are similar. Both I_{J1} and I_{qp1} are odd functions of V. I_{J2} and I_{qp2} are even functions of V. The four currents are shown in figure 2-2.

2.2.3 The Dissipative Currents

The dissipative quasiparticle current is well known [Giaever, 1960; Fisher and Giaever, 1961]. Essentially, the sharp step in the dc I-V characteristic with no applied rf voltage comes from the fact that at $V = \Delta_1 + \Delta_2$, there is enough energy to break a pair and

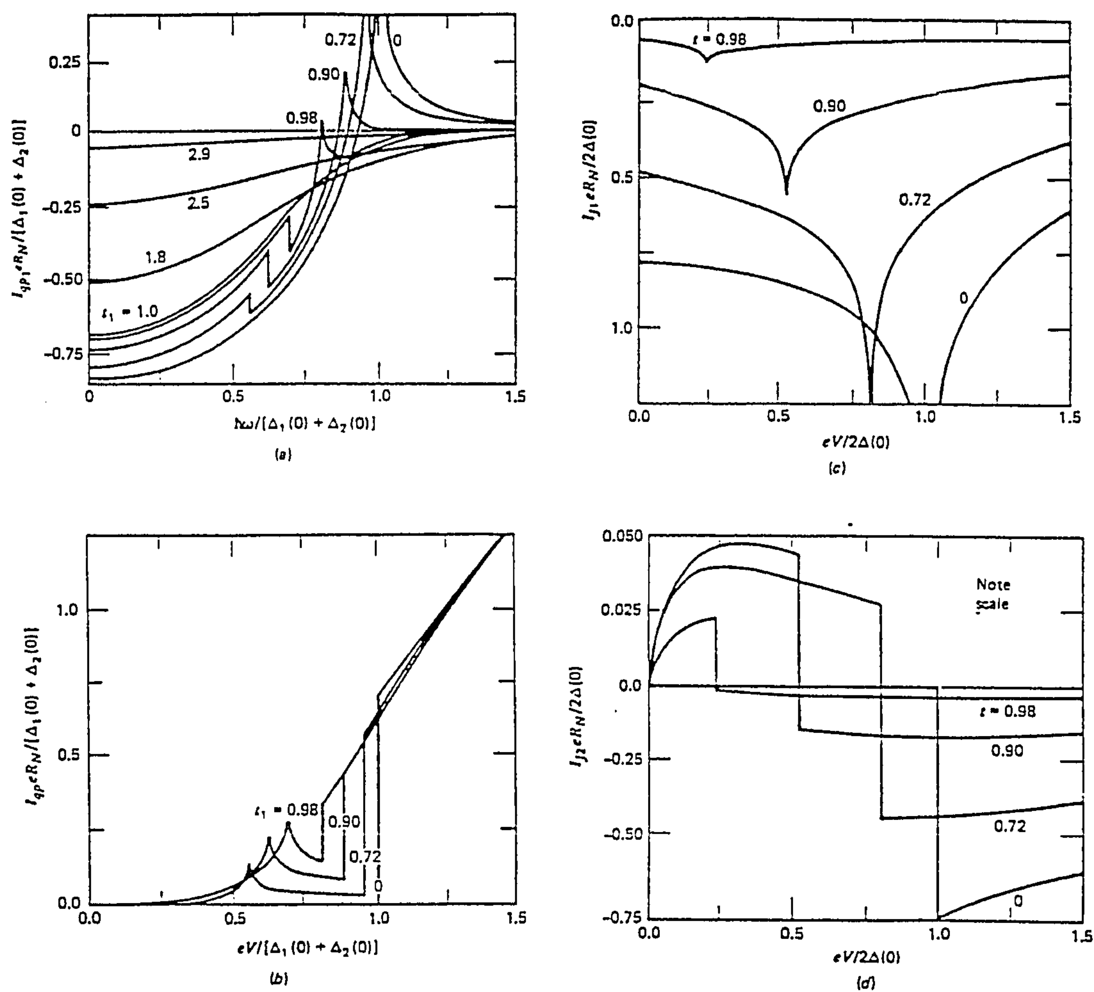

Fig. 2-2 The tunneling currents in an SIS tunnel junction at temperature $t = T/T_C$. a) The reactive quasiparticle current. b) The dissapative quasiparticle current. c) The Josephson sine current. d) The Josephson cosine current. a) and b) are shown for tunnel junctions with unequal gap superconductors. (From Harris, 1974,1975).

have the resulting quasiparticles tunnel across the barrier. A model for the possible processes is given in Fig. 2-3 ($\Delta_1 + \Delta_2 = 2\Delta$). It is the extreme non-linearity of this current-voltage characteristic that led many researchers to explore the use of the SIS tunnel junction as a heterodyne device [Dolan et al., 1979; Richards et al., 1979; Rudner and Claeson, 1979]. Well above the gap voltage, the current approaches that expected for a classical resistor. At these large bias voltages, the quasiparticle density of states approaches the normal metal density of states, as can be seen in eq. 2-6.

The quasiparticle tunneling can be represented very well using the "semiconductor model" of Fig. 2-4. The superconducting electrode density of states, given by eq. 2-6, has no allowed states with energies less than Δ. The effect in the semiconductor model is to push the normal metal filled and available states at energies less than Δ to the gap edge. The result is singularities at both the valence and conduction band edges. Tunneling across a barrier can only occur between filled states on one side of the tunnel barrier and empty states on the other side of the barrier. The magnitude of the tunneling current is proportional to these filled and empty density of states. In this model, the applied dc energy, eV, is seen as the energy difference between the Fermi energies of the two superconducting electrodes. The semiconductor model is expanded to include finite temperature quasiparticle excitations by exciting quasiparticles to the conduction band. The density of the excited quasiparticles is governed by Fermi statistics.

The cosine term, I_{J2} is much more elusive. Josephson (1962) called it the phase dependent part of the quasiparticle current. In light of this, it is not surprising that the cosine current is zero below the sum gap voltage at zero temperature. At these voltages, quasiparticles cannot be created with energy less than 2Δ for $T = 0$. Many groups have measured the Josephson cosine current over a limited bias voltage range (see for example Halse and Taunton, 1976; Vincent and Deaver, 1974; Falco et al., 1973). The Josephson cosine current is ignored in the work presented in this thesis.

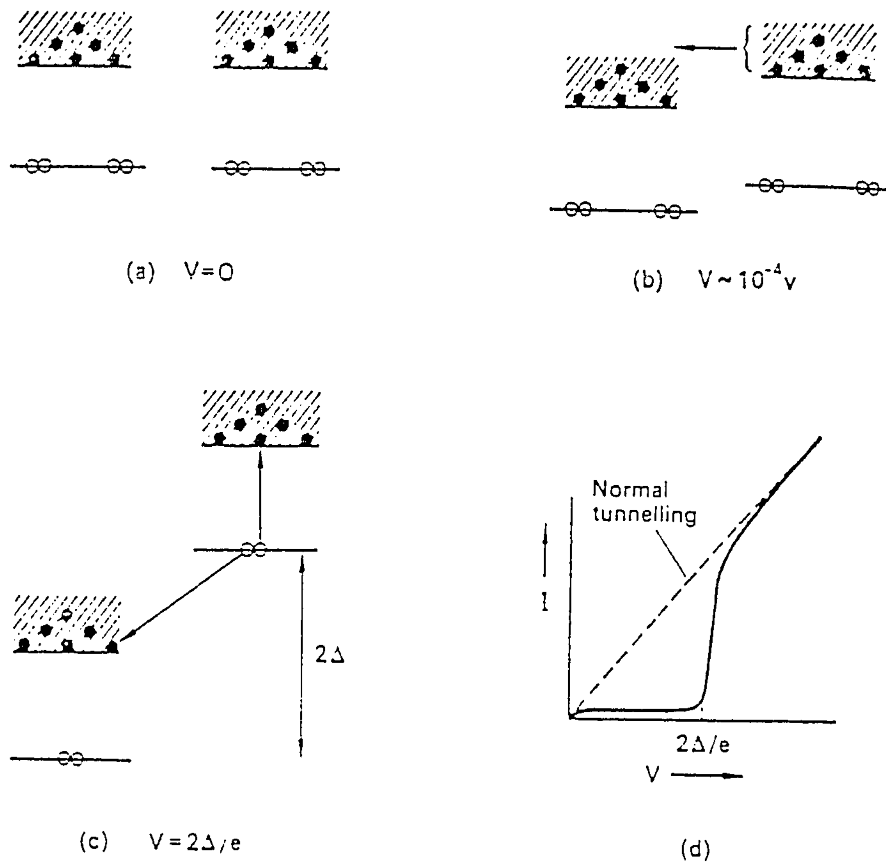

Fig. 2-3 Tunneling mechanisms. a) b), and c) energy levels. The open pairs of circles denote Cooper pairs, the filled circles denote quasiparticles. d) I-V trace. (From Rose-Innes and Rhoderick, 1978).

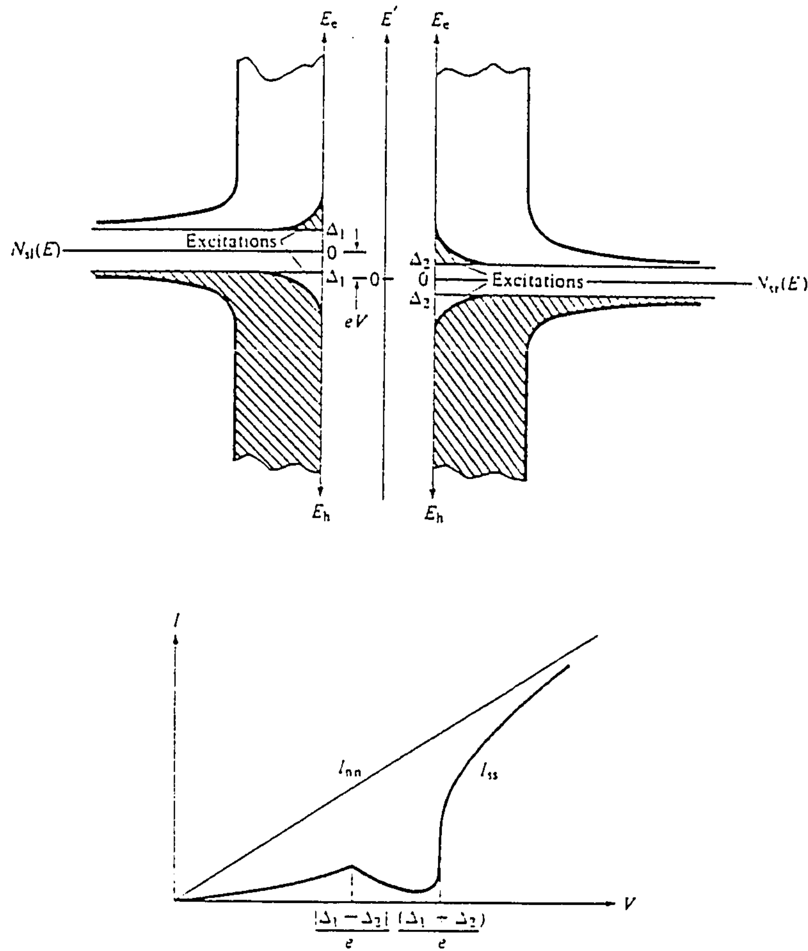

Fig. 2-4 The semiconductor model. a) The semiconductor model showing thermally excited quasiparticles above the superconducting energy gaps, Δ_1 and Δ_2. b) The resulting I-V trace at finite temperatures. Josephson currents are not addressed in this model. (From Van Duzer and Turner, 1981).

2.2.4 The Reactive Currents

From Fig. 2-2, one immediately sees that, in fact, the functional forms of the two currents I_{qp1} and I_{J1} have similarities; both have a logarithmic singularity at the sum-gap ($eV/2\Delta = 1$). The singularity in the Josephson sine term, I_{J1}, is called the Riedel singularity after the first person to recognize the divergence of $Re(j_p)$ in eq. 2-11 at $eV=2\Delta$ (Riedel, 1964). The singularity in I_{qp1}, to my knowledge, is unnamed.

By definition, reactive currents are those which flow out of phase with the applied voltage. In the case of an applied voltage which is purely dc, reactive currents are defined as those that are non-dissipative. The finite value of I_{J1} at zero voltage is called the dc Josephson current. Since there is current flowing with no voltage drop, it is clear that this current must be non-dissipative (at least for $V_0 = 0$). At finite voltages, I_{J1} exists and is still reactive; it is modulated by ω_J, as seen earlier in equation 2-9.

What of the quasiparticle current, I_{qp1}? Since it does not appear in the dc current, it is not obvious whether it is reactive. In a simple circuit model, the passive elements which are reactive are the inductance L and the capacitance C. At zero voltage, the Josephson sine current behaves like the current passing through an ideal inductor of impedance $i\omega L = 0$ at dc, since $\omega = 0$. For the ideal inductor, one gets dc current without a dc voltage drop. The reactive quasiparticle current can be thought of as being capacitive at dc. The capacitance is clearly reactive, but its impedance is $1/i\omega C = \infty$ at dc.

2.2.5 The Kramers-Kronig Relations

Wilkens (1969) was the first to point out explicitly that I_{J1} and I_{J2} were Kramers-Kronig transforms of each other. That is:

$$I_{J2}(V') = P\frac{1}{\pi}\int_{-\infty}^{\infty}\frac{I_{J1}(V)}{V - V'}dV \qquad I_{J1}(V') = P\frac{1}{\pi}\int_{-\infty}^{\infty}\frac{I_{J2}(V)}{V - V'}dV \tag{2-14}$$

where P indicates the Cauchy principle value. The Kramers-Kronig relationships, first used to explain the relationship between the optical conduction and absorption (the real and imaginary parts of the index of refraction), imply that in a linear causal system, the dissipative term and the reactive term are related. As seen in Fig. 2-2, the logarithmic singularity in I_{J1} (the Riedel peak in Fig. 2-2c) is seen at the same bias voltage as the sharp step in I_{J2} (Fig. 2-2d). From the form of the Kramers-Kronig transform, it can be seen that a sharp step will give a logarithmic singularity upon integration. It is perhaps striking that the these two currents are Kramers-Kronig transforms of each other. One of the conditions for Kramers-Kronig relations, a linear response, seems to be violated in the extremely non-linear tunnel junction system. The dilemma is solved by the realization that the total tunneling currents are not the Kramers-Kronig transforms of each other, just the real and imaginary parts of the response functions.

The real and imaginary parts of the quasiparticle response functions are also Kramers-Kronig transforms. Again, Fig. 2-2 shows that the sharp rise in the tunneling current in the dissipative quasiparticle current at the sum gap corresponds to the logarithmic singularity in the reactive quasiparticle currents. For a very special case, the *total* tunneling currents are related by Kramers-Kronig transforms. This is the case of a pure sinusoidal applied voltage $V(t) = V_\omega \cos\omega t$ which is small, $eV_\omega << \hbar\omega$, Harris (1975) has shown that in this case, I_{qp1} and I_{qp2} are Kramers-Kronig transforms. This is a case in which we will be interested. The Kramers-Kronig transforms can be thought of as a powerful tool which allows one to determine the in-phase response given the out-of-phase response and vice-versa.

2.2.6 Response to a Sinusoidal Signal

From the phase factor of eq. 2-8, the response of the junction to a sinusoidal potential in the time domain can be calculated. In response to the applied signal $V(t) = V_0 + V_\omega \cos\omega t$, the phase factor becomes

$$\int_{-\infty}^{\infty} d\omega W(\omega)\, e^{-i\omega t} = \exp\left(-i\frac{e}{\hbar}\int^{t} dt'[V(t') - V_0]\right) = \exp\left\{-i\,\frac{eV_\omega}{\hbar\omega}\sin\omega t\right\}$$

$$= \sum_{n=-\infty}^{\infty} J_n\left(\frac{eV_\omega}{\hbar\omega}\right)\exp(-in\omega t) \qquad 2\text{-}15$$

where the relationship $\exp(\pm iz\sin\phi) = \sum_{-\infty}^{\infty} J_n(z)\exp(\pm in\phi)$ is used and J_n is the nth order Bessel function [Gradshteyn and Ryzhik, 1965]. Therefore, the Fourier transform coefficient to be used in eq. 2-7 is

$$W(\omega') = \int_{n=-\infty}^{\infty} J_n(\alpha)\,\delta(\omega' - n\omega) \qquad 2\text{-}16$$

where $\alpha = \frac{eV_\omega}{\hbar\omega}$. Using 2-16, and ignoring the Josephson contribution to the total current, eq. 2-7 becomes

$$I(t) = \mathrm{Im}\int_{-\infty}^{\infty} d\omega\, d\omega' W(\omega) W^*(\omega') e^{-i(\omega-\omega')t}\, j_{qp}(\omega' + \frac{\omega_J}{2})$$

$$= \mathrm{Im} \sum_{n\,m=-\infty}^{\infty} J_n(\alpha) J_{n+m}(\alpha) e^{im\omega t}\, j_{qp}(n\omega + \frac{\omega_J}{2})$$

$$= a_o + \sum_{m=1}^{\infty} [2a_m \cos m\omega t + 2b_m \sin m\omega t] \qquad 2\text{-}17$$

where the strengths of the current components at the various frequencies are given by

$$a_o = \sum_{n=-\infty}^{\infty} J_n^2(\alpha)\, \mathrm{Im}[\, j_{qp}(n\omega + \frac{\omega_J}{2})] \qquad 2\text{-}18$$

$$2a_m = \sum_{n=-\infty}^{\infty} J_n(\alpha)\, [J_{n+m}(\alpha) + J_{n-m}(\alpha)]\, \mathrm{Im}[\, j_{qp}(n\omega + \frac{\omega_J}{2})] \qquad 2\text{-}19$$

$$2b_m = \sum_{n=-\infty}^{\infty} J_n(\alpha)\, [J_{n+m}(\alpha) - J_{n-m}(\alpha)]\, \mathrm{Re}[\, j_{qp}(n\omega + \frac{\omega_J}{2})] \qquad 2\text{-}20$$

The advantage of keeping the response functions in the equations instead of substituting the BCS predictions is that tunnel junctions are rarely adequately described by BCS theory. From eq. 2-9, it is apparent that only $\mathrm{Im}[j_{qp}(\omega_J/2)]$ contributes to the time averaged tunneling current at non-zero bias voltages for a dc applied voltage. Therefore, a measurement of the dc I-V trace of the tunnel junction is sufficient to determine the real part of the quasiparticle response function in the voltage bias case. Quantitatively

$$\mathrm{Im}[j_{qp}(n\omega + \omega_J/2)] = I_{dc}(V_o + n\hbar\omega/e) \qquad 2\text{-}21$$

which implies

$$\mathrm{Re}[j_{qp}(n\omega + \omega_J/2)] = I_{KK}(V_o + n\hbar\omega/e) \qquad 2\text{-}22$$

where I_{KK} is the Kramers-Kronig transform of I_{dc}.

2.2.7 Photon Assisted Tunneling and Direct Detection

The term a_0 in 2-18 is simply that given by Tien and Gordon (1963) to describe the photon assisted tunneling steps first observed by Dayem and Martin (1962). The dc current is given by

$$a_0 = I_0 = \sum_{n=-\infty}^{\infty} J_n^2(\alpha)\, I_{dc}(V_0 + n\hbar\omega/e) \qquad \text{2-23}$$

The photon assisted tunneling steps are the dc manifestation of applying radiation to the SIS tunnel junction. Fig. 2-5 shows the photon assisted tunneling steps. The dc quasiparticle curve which results from the applied radiation is sometimes called the "pumped I-V." The photon assisted tunneling steps arise because the input energy, $\hbar\omega$, gives the quasiparticle enough energy to tunnel across the barrier into an available state. This allows for dc current at voltages less than the gap voltage. Because the incident photons are quantized in energy, steps appear in the dc I-V curve corresponding to the absorption or emission of an integral number of photons. The theory assumes that the tunnel junction is driven by a potential of the form $V(t) = V_\omega \cos\omega t$. This implies that there are no higher harmonic voltages affecting the shape of the dc I-V trace. Although the basic equation governing the interaction of radiation with the tunnel junction (eq. 2-7) allows for *arbitrary* incident waveforms, the solutions are usually intractable. In all of the work presented here (and most elsewhere), the assumption of a pure sinusoidal *rf* input frequency is used.

From eq. 2-23, it can be seen that a change in the amplitude of the incident radiation will change the dc current I_0. Thus, the tunnel junction can be used as a direct detector. The direct detector uses the non-linearity of the junction to rectify the incoming *rf* signal.

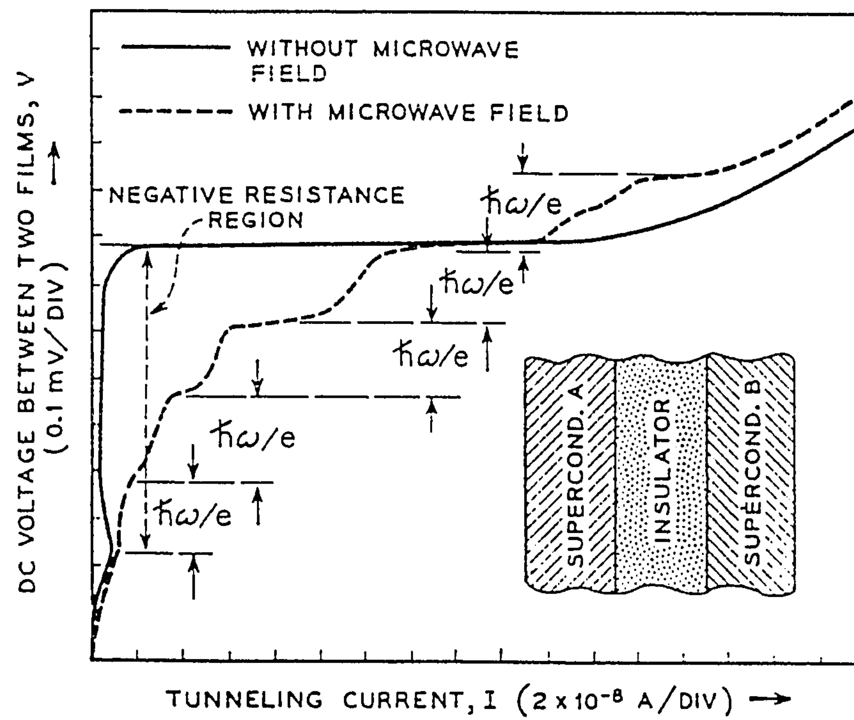

Fig. 2-5 Photon assisted tunneling. The incident radiation is at freqency $\omega/2\pi$ with energy $\hbar\omega/e = 0.16$ mV. (From Tien and Gordon, 1963).

The responsivity is given by the change in the dc current for a given incident *rf* power by [Tucker and Feldman, 1985]

$$S_I = \frac{\Delta I_{dc}}{P_{inc}} = \frac{e}{\hbar\omega}\left[\frac{I_{dc}(V_o + \hbar\omega/e) + I_{dc}(V_o - \hbar\omega/e) - 2I_{dc}(V_o)}{I_{dc}(V_o + \hbar\omega/e) - I_{dc}(V_o - \hbar\omega/e)}\right]$$

which in the classical limit becomes $S_I = (d^2I/dV^2)/2(dI/dV)$. The quantum limit is $S_I = e/\hbar\omega$ for very sharp devices on the scale of the photon width. The SIS tunnel junction has been used as a direct detector with responsivity within a factor of 2 of the quantum limit [Richards et al., 1980]. The photon assisted tunneling steps and the direct detector studies were, prior to this thesis, the major realization and utilization of the interaction of a single frequency with the quasiparticle currents.

2.2.8 Quantum Sloshing

The tunneling across the barrier must conserve energy, ie., $E_L + \hbar\omega = E_R$ for tunneling from left to right with single photon absorption. In general, there are many virtual tunneling possibilities, including those which don't obey conservation of energy. In these processes, the quasiparticle makes a virtual transition across the tunnel junction and then tunnels back. This has been called "quantum sloshing" [Tucker, 1979]. The quasiparticles slosh between states which are not coupled by an integral number of photons. This process conserves the number of quasiparticles, but adds a phase factor to the tunneling impedance. A measurement of this phase factor and the amplitude of the reactive quasiparticle current is discussed in chapter VI.

2.2.9 Current at the Applied Frequency

Using equations 2-19 and 2-20, we can relate the expected amplitudes of the various current components to the measured I-V trace in the absence of applied radiation.

As evident in equation 2-17, the quasiparticle tunneling currents are flowing at harmonics of the input *rf* frequency, $m\omega$. At the input frequency ω, the tunneling current is (recall $V(t) = V_o + V_\omega \cos\omega t$)

$$I_\omega(V_\omega,t) = 2a_1 \cos \omega t + 2b_1 \sin \omega t \qquad \text{2-24}$$

$$2a_1 = \sum_{n=-\infty}^{\infty} J_n(\alpha)\,[J_{n+1}(\alpha) + J_{n-1}(\alpha)]\, I_{dc}(V_o + n\hbar\omega/e) \qquad \text{2-25}$$

$$2b_1 = \sum_{n=-\infty}^{\infty} J_n(\alpha)\,[J_{n+1}(\alpha) - J_{n-1}(\alpha)]\, I_{KK}(V_o + n\hbar\omega/e) \qquad \text{2-26}$$

Here, the quasiparticle response functions have been replaced with the measured dc I-V trace and its Kramers-Kronig transform. In order to predict the current flowing in the tunnel junction at a frequency ω, one needs to measure the dc I-V curve, calculate its Kramers-Kronig transform, and determine $V_\omega(V_o)$. The determination of $V_\omega(V_o)$ is discussed in section 5.4.2. The remarkable aspect of these equations is that the measurement of the dc I-V characteristic is nearly sufficient to predict the real and imaginary currents flowing in response to an applied *rf* voltage!

At this point, it is wise to review the features of the currents in the tunnel junction. Table 2-1 shows the origin and significance of the four current terms. As seen in this chapter, the reactive quasiparticle current is not seen at all in a dc measurement. Chapter 6 of this thesis describes an experiment which measures the real and imaginary contributions of the quasiparticle currents. Since the voltage and input power dependences of the quasiparticle currents are fundamental predictions of the theory of tunneling between superconductors, the work presented in this thesis further verifies these theories.

Table 2-1. Summary of the important features of the four tunneling currents in a voltage biased SIS junction.

Current	I_{qp1}	I_{qp2}	I_{J1}	I_{J2}
Common name	Reactive quasiparticle	Dissipative quasiparticle	Josephson sine	Josephson cosine
Origin	Real part of quasiparticle response function	Imaginary part of quasiparticle response function	Real part of pair response function	Imaginary part of pair response function
Phase	Reactive	Dissipative	Reactive	Dissipative
Polarity	Even	Odd	Even	Odd
Major feature	Logarithmic singularity at sum gap	Step singularity at sum gap	Logarithmic singularity at sum gap	Step singularity at sum gap
DC observable without applied *rf*	None	Resistive dc I-V characteristic	Current at zero voltage	None
DC observable with applied *rf*	Shape of photon asssted tunneling steps (Section 6.1.3)		Shape of Shapiro steps (Section 6.1.3)	
Physical explanation	quantum sloshing	quasiparticle tunneling	pair tunneling	quasiparticle-pair interference

III SIS MIXERS, A THEORETICAL OVERVIEW

3.1 The Heterodyne Device

The theory and application of SIS mixers is a mature subject, as evidenced by the number of recent review papers covering the subject [Blundell and Winkler, 1991; Winkler, Ivanov, and Claeson, 1991; Richards and Hu, 1989]. This chapter will concentrate on the theoretical aspects of mixing, while the experimental aspects will be covered in Chapter V. Before beginning the analysis of mixer theory, it will be helpful to review the basic operation of mixing and the basic nomenclature.

The usual mixer is shown in Fig. 3-1. The mixer has two inputs and one output. One of the inputs is at a high power and it is called the local oscillator (LO). It is supplied by the user as a reference source and is monochromatic. The other input is the signal. It is typically an unknown. The two input signals "mix" together, forming a number of peaks in the frequency spectrum as shown in Fig. 3-2. The major terms which are produced by the mixing are the sum frequency, the difference frequency, the image frequency, and the second harmonics of the LO and the signal. The sum frequency is $f_{LO} + f_s$. The difference frequency, $f_s - f_{LO}$, is called the intermediate frequency, f_{IF}, and is typically orders of magnitude smaller in frequency than the LO or the signal. The image frequency, f_i, come from $f_{LO} - f_{IF}$ and $2f_{LO} - f_s$. The second harmonic terms are at frequencies $2f_{LO}$ and $2f_s$.

In most work, the terms which are at a higher frequency than the signal and LO are neglected. Typically, these currents are shunted by capacitance in the system and therefore do not play a part in the mixing results. This leaves the mixer with 4 frequencies. Since in general it is easier to amplify and detect smaller frequencies, the mixer is used as a frequency to frequency transducer. It takes the signal frequency and converts it to the intermediate frequency through the interaction with the local oscillator and the device.

Mixers are characterized by their coupled gain, G_c, and their noise, T_M. The

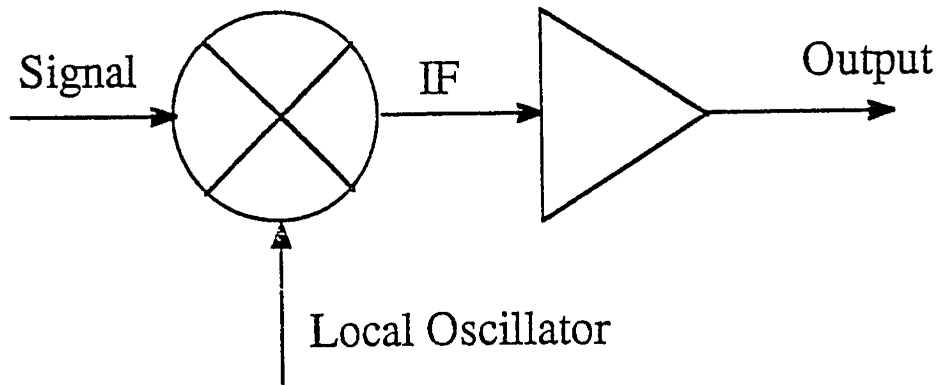

Fig. 3-1 The usual picture of the mixer. The local oscillator is large amplitude; the signal and IF are small.

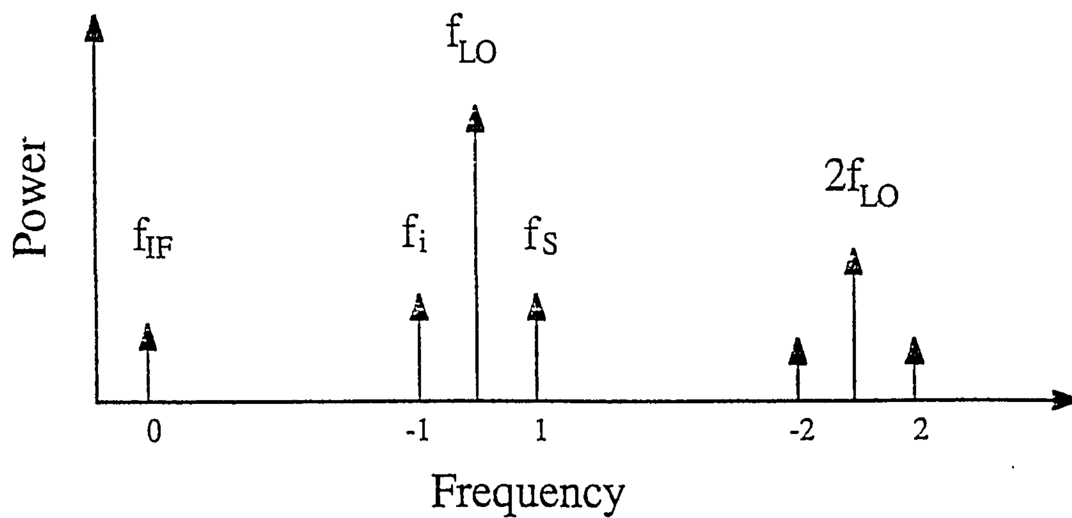

Fig. 3-2 The main frequencies produced by mixing. The number below the frequency axis refer to the index value m used in the calculations.

coupled gain is simply the ratio of the power coupled out at the IF to the power available at the signal frequency, P_s.

$$G_C = \frac{P_{IF}}{P_s} \qquad 3\text{-}1$$

Some theoretical predictions are formulated in terms of the available gain. The available gain is the ratio of the available power at the IF (assuming a matched load) to the available power at the signal. It can be expressed as

$$G_A = \frac{P_{IF}}{P_A} \frac{1}{(1 - |\rho|^2)} \qquad 3\text{-}2$$

where ρ is the amplitude of the reflection coefficient at the mixer output. A perfect match implies an output reflection ρ = 0. In this case the coupled and available gain are the same. The reflection coefficient is determined by the match between the output impedance of the device, Z_{IF}, and the input impedance of the amplifier which follows the mixer, Z_L. The reflection coefficient can then be defined by

$$\frac{1}{(1 - |\rho|^2)} = \frac{|Z_{IF} + Z_L|}{4 R_L R_{IF}} \qquad 3\text{-}3$$

The conventions Z = R + iX and Y = G + iB are used throughout this work. From eq. 3-3, it is seen that a match occurs when the imaginary parts of the Z_{IF} and Z_L resonate each other, $X_{IF} = -X_L$, and the real parts are equal, $R_{IF} = R_L$.

3.2 Classical Mixer Theory

The classical mixer theory [Torrey and Whitmer, 1948] begins with the determination of the small signal matrix elements. The ultimate goal of the theory is to

predict the gain (loss) and the noise expected for a device with a particular I-V characteristic. The voltage and current across the junction can be expressed as a sum of contributions from frequencies $\omega_m = m\omega + \omega_o$, where $\omega = \omega_{LO}$ and $\omega_o = \omega_{IF}$

$$v_{sig}(t) = \mathrm{Re} \sum_{m=-\infty}^{\infty} v_m \, e^{i\omega_m t} \qquad 3\text{-}4$$

$$i_{sig}(t) = \mathrm{Re} \sum_{m=-\infty}^{\infty} i_m \, e^{i\omega_m t} \qquad 3\text{-}5$$

For small signal levels compared to the LO, the currents are related to the applied voltages through matrix elements given by:

$$i_m = \sum_{m'} Y_{mm'} \, v_{m'} \qquad 3\text{-}6$$

The matrix $Y_{mm'}$ is called the small signal admittance matrix. At this point, one places current generators I_m with output admittances Y_m at each port of the mixer (Fig. 3-3), and determines the total response at each frequency. The total current is given by

$$I_m = i_m + Y_m v_m = \sum_{m'} [Y_{mm'} + Y_m \delta_{m,m'}] \, v_{m'} \qquad 3\text{-}7$$

As seen in Fig. 3-3, the current at port m is composed of the current generated through interaction with the nonlinear element and the current flowing through the output admittance. Eq. 3-7 can be inverted to give the voltage at port m

$$v_m = \sum_{m'} Z_{mm'} \, I_{m'} \qquad 3\text{-}8$$

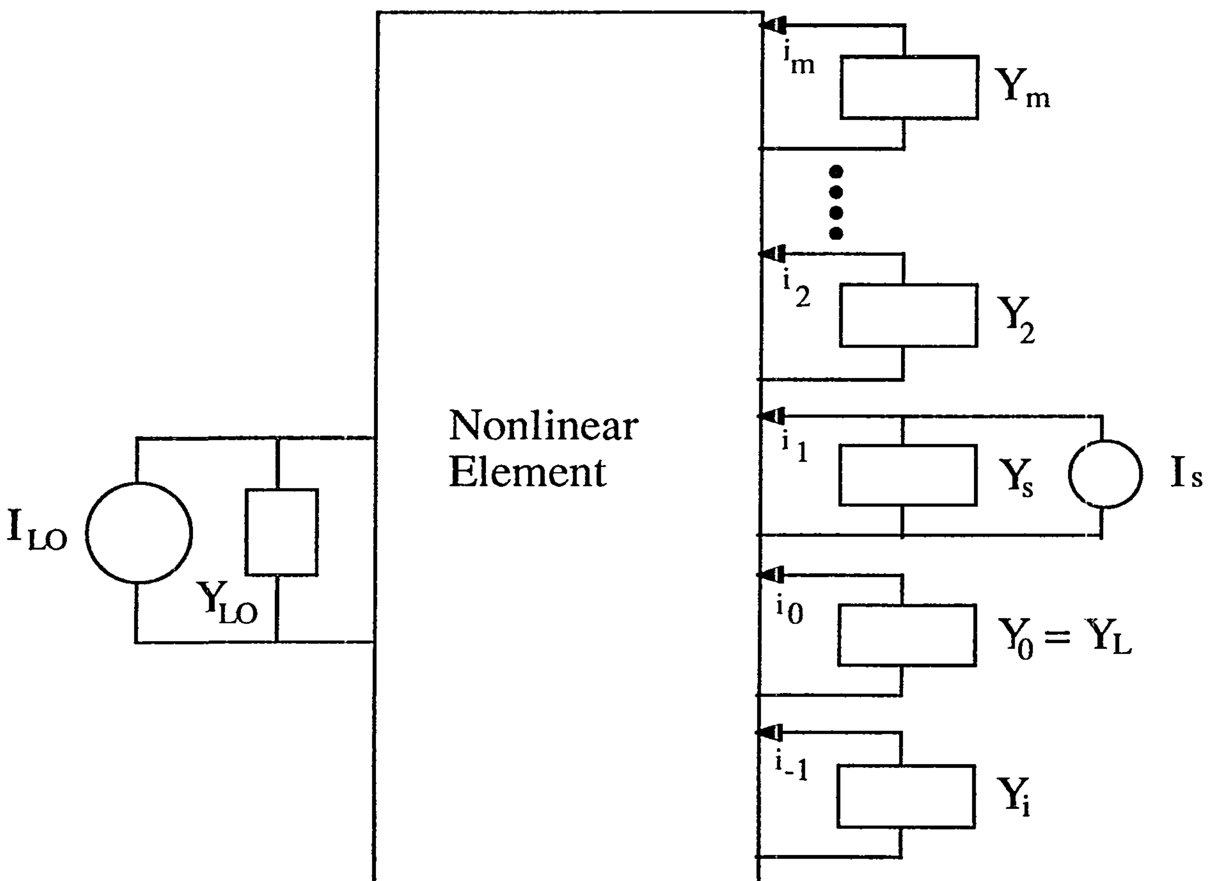

Fig. 3-3 The "black box" picture of the mixer. At each port (i_m), there is an output admittance Y_m. The two input signals are at the LO and signal frequencies.

where $Z_{mm'}$ is the inverted augmented Y matrix given in matrix notation as

$$\| Z_{mm'} \| = \| Y_{mm'} + Y_m \delta_{m,m'} \| \qquad 3\text{-}9$$

An important parameter to determine is the gain. This is the ratio of the power at port m=0 (the IF or load) to the power at port m=1 (the signal). The impedance element that relates the voltage at port m = 0 to the current at port m =1 is Z_{01}. The power at the load is given by

$$P_{IF} = \frac{1}{2} G_L |v_o|^2 = \frac{1}{2} G_L | Z_{01} |^2 | I_s |^2 \qquad 3\text{-}10$$

while the available power at the the signal frequency is given by

$$P_s = \frac{1}{8} \frac{| I_s |^2}{G_s} \qquad 3\text{-}11$$

Thus the coupled gain of the system is given by

$$G_C = \frac{P_{IF}}{P_s} = 4 G_s G_L | Z_{01} |^2 \qquad 3\text{-}12$$

For a classical mixer, the matrix elements of eq. 3-6 can be determined from the instantaneous response of the dc I-V curve to applied radiation. In the presence of an applied radiation $V_o + V_\omega \cos\omega t$, the classical conductance is determined by the time dependent modulation of the dc I-V curve which gives

$$G(t) = \frac{d}{dV_o} I_{dc}(V_o + V_\omega \cos\omega t) = \sum_m G(m\omega) e^{im\omega t} \qquad 3\text{-}13$$

where $G(m\omega)$ is a Fourier transform coefficient of $G(t)$. These values of the conductance coefficients yield the value of the small signal admittance matrix elements

$$Y_{mm'} = G([m-m']\omega) \qquad 3\text{-}14$$

where the Fourier coefficients of the conductance are given by

$$G(m\omega) = \frac{1}{2\pi} \int_{-\pi/\omega}^{\pi/\omega} G(t)\, e^{-im\omega t}\, dt \qquad 3\text{-}15$$

Given the small signal admittance matrix parameters, according to eqs. 3-9 and 3-12, the gain can be solved if one knows the proper conductance to put at the output of each frequency source. This is not trivial. Typically, the solution is made tractable by using only three ports, $m = -1,0,1$. The gain expression in terms of the small signal matrix parameter values is given in the next section since the quantum mixer theory will also include reactive terms which can be set to zero to recover the proper gain equation for the classical case.

3.3 Quantum Mixer Theory

The quantum mixer theory, [Tucker, 1979] describes the mixing results in an SIS tunnel junction. The word "quantum" appears because the tunnel junction does not behave classically in response to an applied *rf* frequency, as we have seen in Chapter 2. The major predictions of the quantum theory are 1) the possibilities of gain [Tucker, 1980] which has been observed by a number of groups [Kerr et al., 1981; McGrath et al., 1981; D'Addario, 1984; Räisänen et al., 1987], 2) quantum limited noise [Tucker, 1979] also observed by a number of groups [McGrath et al., 1988; Pan et al., 1989; Mears et al., 1990], and 3) negative dynamic resistance, first observed by Smith et al. (1981) and Kerr et al. (1981).

These predictions, particularly the low noise and possibility of gain, led to the advances in SIS mixer receivers.

In order to differentiate between cases where the classical theory is sufficient, and where the quantum theory is necessary, it is necessary to see at what point the tunnel junction stops behaving classically. This is most easily seen in the nature of the photon assisted tunneling steps described in Section 2.2.7. The Tien-Gordan equation, once again, is

$$I_0(V_0, V_\omega) = \sum_{n=-\infty}^{\infty} J_n^2(\alpha)\, I_{dc}(V_0 + n\hbar\omega/e) \qquad 3\text{-}16$$

The low-amplitude classical limit is at low frequencies, where $eV_\omega << \hbar\omega$ and $\hbar\omega <<$ $e\Delta V$, where ΔV is the voltage width of the non-linearity. Here, the Bessel function amplitudes can be expanded for small argument. In this limit, the Taylor series expansion of the current in terms of the applied voltage V_ω to second order gives

$$I_0 = I_0(V_0,0) + \frac{V_\omega^2}{2}\, \frac{I_0(V_0 + \hbar\omega/e) + I_0(V_0 - \hbar\omega/e) - 2I_0(V_0)}{2(\hbar\omega/e)^2}$$

$$\approx I_0(V_0,0) + \frac{V_\omega^2}{2}\, \left.\frac{d^2 I_0}{dV_\omega^2}\right|_{V_\omega = 0} \qquad 3\text{-}17$$

In this limit, the classical result contains the second derivative of the dc I-V curve with respect to the applied *rf* amplitude. Clearly, the shapes of the photon assisted tunneling steps shown in Fig. 2-5 are not described well by this expression. The classical limit will only apply when the energy of of the incident photon is small compared to the strength of the non-linearity of the device, $\hbar\omega/e < \Delta V$, where ΔV is the voltage width of the current rise in the device.

3.3.1 Determination of $Y_{mm'}$

The quantum mixer theory starts with an expression that we are already familiar with from Chapter II. The quasiparticle current in an SIS tunnel junction in the presence of a sinusoidal applied voltage is

$$I(t) = \mathrm{Im} \int_{-\infty}^{\infty} d\omega\, d\omega' W(\omega) W^*(\omega') e^{-i(\omega-\omega')t}\, j_{qp}(\omega' + \frac{\omega_J}{2}) \qquad 3\text{-}18$$

Instead of looking at the response of the tunnel junction to a single frequency as we did in Chapter 2, Tucker (1979) considers the response of the tunnel junction to a combination of two frequencies, namely $V(t) = v_{LO}(t) + v_{sig}(t)$. The calculations are too complicated to reproduce here, but using Werthamer's expression, and keeping the linear terms in v_m and i_m, the small signal admittance matrix parameters become

$$Y_{mm'} = \frac{-ie}{2\hbar\omega_m} \sum_{nn'=-\infty}^{\infty} W_\omega(n\omega)\, W_\omega(n'\omega)\, \delta_{m-m',n'-n}$$

$$\times \left\{ \left[j_{qp}(n\omega + \frac{\omega_J}{2}) - j_{qp}(n\omega - \omega_{m'} + \frac{\omega_J}{2}) \right] - \left[j_{qp}^*(n'\omega + \omega_{m'} + \frac{\omega_J}{2}) - j_{qp}(n'\omega + \frac{\omega_J}{2}) \right] \right\}$$

3-20

These matrix elements are difficult to compute since the Fourier factors W_{LO} are given for an arbitrary applied voltage (eq. 2-8). Luckily, the case of a sinusoidal input will lead to Bessel function amplitudes of the Fourier factors, as we have seen before. For an applied voltage of the form $V_{applied}(t) = V_0 + V_\omega \cos\omega t + v_{sig}(t)$, where $v_{sig}(t)$ is small compared to V_ω (in order for the response to be linear),

$$G_{mm'} = \frac{e}{2\hbar\omega_m} \sum_{nn'=-\infty}^{\infty} J_n(\alpha)\, J_{n'}(\alpha)\, \delta_{m-m',n'-n}$$

$$\times \left\{ I_{dc}(V_0 + n'\hbar\omega/e + \hbar\omega_{m'}/e) - I_{dc}(V_0 + n'\hbar\omega/e) \right.$$

$$\left. + I_{dc}(V_0 + n\hbar\omega/e) - I_{dc}(V_0 + n\hbar\omega/e + \hbar\omega_{m'}/e) \right\} \qquad 3\text{-}21$$

$$B_{mm'} = \frac{e}{2\hbar\omega_m} \sum_{nn'=-\infty}^{\infty} J_n(\alpha)\, J_{n'}(\alpha)\, \delta_{m-m',n'-n}$$

$$\times \left\{ I_{KK}(V_0 + n'\hbar\omega/e + \hbar\omega_{m'}/e) - I_{KK}(V_0 + n'\hbar\omega/e) \right.$$

$$\left. + I_{KK}(V_0 + n\hbar\omega/e) - I_{KK}(V_0 + n\hbar\omega/e + \hbar\omega_{m'}/e) \right\} \qquad 3\text{-}22$$

With these matrix elements, and knowledge of the output admittance at the various frequencies, the mixer gain can be calculated using eq. 3-12. In the limit of small IF frequency ($\omega_{IF} << \omega_{LO}$), along with the assumption that higher harmonics of the LO and the signal are shorted by the junction capacitance, Tucker and Feldman (1985) have shown that the matrix elements can be simplified to

$$G_{00} = \sum_{n=-\infty}^{\infty} J_n^2(\alpha) \frac{d}{dV_0} I_{dc}(V_0 + n\hbar\omega/e)$$

$$G_{10} = G_{-10} = \frac{1}{2} \sum_{n=-\infty}^{\infty} J_n(\alpha)[J_{n-1}(\alpha) + J_{n+1}(\alpha)]\ \frac{d}{dV_0} I_{dc}(V_0 + n\hbar\omega/e)$$

$$G_{01} = G_{0-1} = \frac{e}{\hbar\omega} \sum_{n=-\infty}^{\infty} J_n(\alpha)[J_{n-1}(\alpha) - J_{n+1}(\alpha)]\ I_{dc}(V_0 + n\hbar\omega/e)$$

$$G_{11} = G_{-1-1} = \frac{e}{2\hbar\omega} \sum_{n=-\infty}^{\infty} J_n(\alpha)[J_{n-1}^2(\alpha) - J_{n+1}^2(\alpha)]\, I_{dc}(V_o + n\hbar\omega/e)$$

$$G_{1-1} = G_{-11} = \frac{e}{2\hbar\omega} \sum_{n=-\infty}^{\infty} J_n(\alpha)[J_{n-2}(\alpha) - J_{n+2}(\alpha)]\, I_{dc}(V_o + n\hbar\omega/e)$$

$$B_{00}, B_{01}, B_{0-1} = 0$$

$$B_{10} = B_{-10} = \frac{1}{2} \sum_{n=-\infty}^{\infty} J_n(\alpha)[J_{n-1}(\alpha) - J_{n+1}(\alpha)]\, \frac{d}{dV_o} I_{KK}(V_o + n\hbar\omega/e)$$

$$B_{11} = B_{-1-1} = \frac{e}{2\hbar\omega} \sum_{n=-\infty}^{\infty} [J_{n-1}^2(\alpha) + J_{n+1}^2(\alpha) - 2J_n(\alpha)]\, I_{KK}(V_o + n\hbar\omega/e)$$

$$B_{1-1} = B_{-11} = \frac{e}{2\hbar\omega} \sum_{n=-\infty}^{\infty} [J_{n-2}(\alpha)J_n(\alpha) - 2J_{n+1}(\alpha)J_{n-1}(\alpha) + J_n(\alpha)J_{n+2}(\alpha)]\, I_{KK}(V_o + n\hbar\omega/e)$$

3-23

These 18 terms correspond to the real and imaginary parts of the nine matrix elements relating the current at port m to the voltage at port m' where m,m' = -1,0,1.

3.3.2 Gain and Output Impedance

By inverting the augmented small signal matrix of eq. 3-9 and using eq. 3-12, the gain can be expressed as

$$G_C = G_o\ \eta\ g_s \frac{(\xi + g_s)^2 + (\gamma - b_s)}{[(\xi + g_s)(1 + g_s) + (b_s^2 - \gamma^2)]} \frac{4g_L}{(g_L^o + g_L)^2 + b_L^2}$$

where $G_o = \frac{G_{01}}{2G_{10}}$, $\eta = \frac{2G_{01}G_{10}}{G_{00}(G_{11} + G_{1-1})}$, $\xi = \frac{G_{11} - G_{1-1}}{G_{11} + G_{1-1}}$, $\gamma = \frac{B_{1-1}}{G_{11} + G_{1-1}}$

$$\beta = \frac{B_{10}}{G_{10}}, \quad g_s = \frac{G_s}{G_{11} + G_{1-1}}, \quad b_s = \frac{B_{11} + B_s}{G_{11} + G_{1-1}}, \quad g_L = \frac{G_L}{G_{00}}, \quad b_L = \frac{B_L}{G_{00}} \qquad 3\text{-}24$$

These expression are given by Tucker and Feldman (1985) and modified to include the susceptive term in the load admittance, B_L (Winkler, 1987). The mixer output conductance is real and is given by

$$G_L{}^o = 1 - \eta \frac{(\xi + g_s) + \beta(b_s - \gamma)}{(\xi + g_s)(1 + g_s) + (b_s^2 - \gamma^2)} \qquad 3\text{-}25$$

The equations were given to show the relative complexity of calculating the theoretically predicted gain. To summarize, the input parameters are $I_{dc}(V_o)$, $I_{KK}(V_o)$, $\omega_{LO} = \omega$, ω_{IF} or ω_s, $V_\omega(V_o)$, Y_s and Y_L. The expressions in eq. 3-23 are only true for case of a double sideband mixer, one whose image frequency admittance is given by $Y_i = Y_s^*$. When the mixer is not double sideband, the full matrix elements, as expressed in eqs. 3-21 and 3-22, must be used. The classical result for the gain is given by using the matrix elements of eq. 3-14 and disregarding the reactive terms in eq. 3-24.

3.4 Noise

The determination of the noise is done in a similar way as the determination of the gain. The sources of noise in the SIS mixer are the (1) shot noise due to the LO current tunneling through the tunnel junction, (2) thermal noise generated at each sideband termination and (3) the noise from the quantum fluctuations of the input radiation fields.

3.4.1 Shot Noise

The quantum mixer theory [Tucker, 1979] predicts the shot noise contributions due to the noise of the mixing element. The model assumes a noise generator in parallel with a

noiseless mixer. The noise current at the output of the mixer is related to the small signal H matrix

$$<[I_o]^2> = B \sum_{mm'} \lambda_{0m}\lambda_{0m'}^{*} H_{mm'} \qquad 3\text{-}26$$

where the parameter λ_{0m} is the normalized small signal impedance matrix element given by

$$\lambda_{0m} = Z_{0m}/Z_{00} \qquad 3\text{-}27$$

and the H matrix, as yet undefined, will be different for the classical and quantum cases. In the quantum case, the H matrix is determined by the temperature, the unpumped I-V curve, and the Bessel function amplitudes of the applied potential by

$$H_{mm'} = e \sum_{nn'} J_n(\alpha)J_{n'}(\alpha)\, \delta_{m-m'}\delta_{n-n'}$$

$$\text{x } \{\coth [\beta(eV_o + n'\hbar\omega_{m'})/2]\, I_{dc}(V_o + n'\hbar\omega/e + \hbar\omega_{m'}/e)$$

$$+ \coth[\beta(eV_o + n\hbar\omega - \hbar\omega_{m'})/2]\, I_{dc}(V_o + n\hbar\omega/e + \hbar\omega_{m'}/e)\} \qquad 3\text{-}28$$

where $\beta = 1/kT$. The equivalent SSB current source, I_s which corresponds to the noise current of eq. 3.26 is given by

$$<[I_o]^2> = \frac{1}{2} |\lambda_{01}|^2 <[I_s]^2>^2 \qquad 3\text{-}29$$

An similar expression exists for the image frequency noise source. The noise temperature at the signal (= $P_{shot\ sig}/kB$, where $P_{shot\ sig}$ is the noise power at the signal and B is the bandwidth) and the image frequency due to the shot noise are then given by

$$T_{shot\ sig} = \frac{1}{4kG_s|\lambda_{01}|^2} \sum_{mm'} \lambda_{0m}\lambda_{0m'}^* H_{mm'} \qquad 3\text{-}30$$

$$T_{shot\ im} = \frac{1}{4kG_i|\lambda_{0-1}|^2} \sum_{mm'} \lambda_{0m}\lambda_{0m'}^* H_{mm'} \qquad 3\text{-}31$$

In the limit for which m=m'=0, and the applied *rf* voltage is small, $V_\omega << 1$, the quasiparticle noise at a bias voltage V_o is given by [Rogovin and Scalapino, 1974]

$$<[I_o]^2> = eB\ \{\coth[\beta(eV_o + \hbar\omega)/2]I_{dc}(V_o + \hbar\omega/e) + \coth[\beta(eV_o - \hbar\omega)/2]I_{dc}(V_o - \hbar\omega/e)\} \qquad 3\text{-}32$$

For large bias voltages, $eV_0 >> \hbar\omega$ and $eV_0 >> kT$, the usual shot noise formula is recovered

$$<[I_o]^2> = 2eBI_{dc}(V_o) \qquad 3\text{-}33$$

These shot noise results show that the shot noise will be dependent upon the unpumped I-V curve through the H matrix. In order to limit the shot noise contribution to the mixer noise, it is desirable to have low leakage current junctions, since the shot noise of eq. 3-28 depends upon the amplitude of I_{dc}.

3.4.2 Thermal Noise

The thermal noise contribution is from the terminations at the various sidebands and it simply reflects the fact that these terminations are at the finite bath temperature T_B and therefore radiate. The thermal noise current contribution at port m is given by

$$<[i_m]^2> = \frac{4\hbar\omega_m B}{[\exp(\hbar\omega_m/kT_B) - 1] \times R_m} \qquad 3\text{-}34$$

where R_m is the resistive termination at port m. The contributions at port m are down-converted and show up as noise at the IF output as a current noise generator of amplitude

$$<[i_0]^2>_{thermal} = |\lambda_{0m}|^2 \frac{4\hbar\omega_m B}{[\exp(\hbar\omega_m/kT_B) - 1] \times R_m} \qquad 3\text{-}35$$

where $m \neq -1,0,1$.

3.4.3 Quantum Noise

The quantum noise is discussed by a number of authors [Wengler and Woody, 1987; Devyatov et al., 1986; Tucker and Feldman, 1985; Feldman, 1987a; and Caves, 1982]. The work by Caves is the most general. In this work, he shows that any high gain linear amplifier which is phase preserving must add a noise referred to the input of at least

$$P_{min} \geq |1-(1/G)|\, \hbar\omega B/2 \qquad 3\text{-}36$$

where G is the photon number gain and B is the bandwidth of the amplifier. The photon number gain of the SIS mixer is usually enormous since the output frequency is usually a few orders of magnitude smaller than the input frequency. For G>>1, the minimum added

noise to the shot and termination noise is given by $\hbar\omega/2$ per unit bandwidth. This limit, $\hbar\omega/2$ is used by Mears et al. (1990,1991a) and their results are presented in terms of this quantum of power. With the addition of zero point fluctuations in the signal, $P = \hbar\omega B/2 \coth\{\hbar\omega/2kT\}$, the quantum limit for the entire amplifier becomes $\hbar\omega B$. Work by McGrath et al. (1988) has instead used the Planck blackbody spectrum to relate the quantum limited power to a temperature.

For a DSB mixer, the quantum noise contribution of the mixer can approach zero [Tucker, 1979, Feldman,1987a; Wengler and Woody, 1986]. Caves' principle is not violated for the double sideband mixer since zero point fluctuations (found by quantizing the radiation fields) in the image and signal frequencies add $\hbar\omega B/2$ each to the total noise. In the single sideband case, an additional $\hbar\omega B/2$ of noise is present on the incoming signal. In work by Zorin (1985) the zero point fluctuations are added as a current generator, as in sections 3.4.1 and 3.4.2. In order to include the zero point fluctuations, the H matrix of eq. 3-28 can be modified [Wengler and Woody, 1986]

$$H'_{1,1} = H_{1,1} + 2G_s\hbar\omega_s$$

$$H'_{-1,-1} = H_{-1,-1} + 2G_i\hbar\omega_i$$

Using all of this formulation, the quantum limit to the noise in both the SSB and DSB case (including the noise at the terminations and zero point fluctuations of the input signal) is given by $\hbar\omega B$ at zero temperature. For the analysis of our mixer results, we have included the zero point fluctuations.

Table 3-1. Summary of the dependence of the noise contributions in the DSB and SSB mixer.

	SSB	DSB
Shot and Thermal Noise Depedence	T, I_{dc}, I_{KK}, ω, V_ω, sideband terminations	
Quantum Noise	$\hbar\omega B/2$	0
Vacuum Fluctuations	$\hbar\omega B/2$ (signal)	$\hbar\omega B$ (signal and image)

With an understanding of the theoretical background presented above, one can analyze the experimental results of a "real" receiver, as is done is chapter 5. Also, one can use the theoretical predictions as a guide for the design of future receivers. The fundamental prediction of quantum limited noise is also explored in chapter 5. These results are modeled using the formalism and equations presented above.

IV SIS DEVICES

4.1 Devices Required for Mixing

For the application of SIS mixing, the junction requirements are strict. The devices need to have small area and low leakage, in addition to other requirements. This section reviews the necessary properties.

4.1.1 Current Density

Of fundamental importance in SIS mixers is the $\omega R_n C$ product, where R_n is the normal state resistance of the tunnel junction. $R_n \sim 1/[J_c(d)\ A]$, where $J_c(d)$ is the junction current density, d is the barrier thickness, and A is the junction area. The capacitance is $C = C'(d)\ A$, where $C'(d)$ is the specific capacitance of the insulator. J_c is exponentially dependent upon the barrier thickness, $J_c(d) \sim e^{-d/d_o}$, with d_o a constant. The specific capacitance has a much weaker dependence on barrier thickness, $C'(d) \sim 1/d$, thus the $\omega R_n C$ product is nearly independent of the barrier thickness (and area) for all reasonable current densities

$$\omega R_n C = \frac{\pi^2 f C' \sqrt{\Delta_1 \Delta_2}}{e J_c} \qquad 4\text{-}1$$

Typical best mixer performance have been seen with $\omega R_n C \approx 3\text{-}4$ at 100 GHz [Tucker and Feldman, 1985]. It is believed that for a lower $\omega R_n C$ product, the junction fails to shunt the higher harmonic frequencies adequately, which leads to degraded mixer performance. Higher $\omega R_n C$ products lead to a degraded bandwidth and limited tuning range. An extension of the $\omega R_n C \approx 3\text{-}4$ rule to higher frequencies requires that the current density should increase accordingly, $J_c \sim f$. We discuss a more complicated scaling in the next section.

Recently, Kerr and Pan (1990) and Blundell and Winkler (1991) have shown that the current density requirements are even more severe as the operation frequency is increased. These works claim that the important parameter is not $\omega R_n C$ but instead $\omega R_{in} C$, where R_{in} is the device resistance at the *signal* frequency. The *rf* coupling is determined by the match between the R_{in} and R_ω, where R_ω is the source impedance at the signal frequency. The work of Kerr and Pan used a real I-V trace. The work by Blundell and Winkler used the low IF approximation [Tucker and Feldman, 1985] to the full quantum mixer theory and an idealized dc I-V trace of the tunnel junction described by

$$I_{dc}(V_o) = 0 \qquad V_o < V_g \qquad \text{4-2}$$
$$= V_o/R_n \qquad V_o > V_g$$

R_{in} is given by the $1/G_{11}$ where G_{11} is given in eq. 3-23. In the low LO power limit ($\alpha <<$ 1), their results are

$$\omega R_n C = \frac{400}{f(\text{GHz})} \qquad \text{(Kerr and Pan)}$$

$$\omega R_n C = \frac{(2+\gamma)}{4\gamma} \qquad \text{(Blundell and Winkler)} \qquad \text{4-3}$$

where γ is the signal frequency normalized to the gap frequency, $\gamma = f/f_g$. For $Nb/AlO_x/Nb$ tunnel junction where $f_g \approx 700$ GHz, both results give $\omega R_n C = 3\text{-}4$ at f = 100 GHz. In fact, although these expressions look dissimilar, their frequency dependence is nearly the same above 100 GHz. The approximation of low input LO power causes the Blundell and Winkler expression to be optimistic, since the magnitude of G_{11} decreases (and hence R_{in}

increases) for increasing LO power. As a general rule, they show that $\omega R_n C \sim 1/f$, therefore the current density J_c must scale approximately as f^2.

4.1.2 Resistance and Device Size

The requirements on R_n of the device are somewhat fuzzy. Usually, R_n is ~ 50 Ω, which is the typical impedance of embedding circuitry. The *rf* admittance is given by $G_{11} \approx (2 + \gamma)/4\gamma R_n$ which gives $G_{11} \approx 3.8/R_n$ for Nb devices at 100 GHz. [Blundell and Winkler, 1991]. The requirement on R_{in} ($\approx 1/G_{11}$) on the *rf* side can be seen as requiring that the signal is well matched to the junction. In addition, the IF impedance of the tunnel junction is governed by the dynamic resistance at the bias point of operation of the tunnel junction. The input impedance of the IF amplifier is usually 50 Ω. Often, since a typical output impedance of the mixer is >> 50 Ω, a transformer is used at the IF which matches the high output impedance of the tunnel junction to the 50 Ω input of the amplifier. This transformer can often limit bandwidth, which is a problem for practical receivers. In the absence of the transformer, the design selection of R_n is usually a compromise between providing a high enough impedance at the signal and a low enough impedance at the IF, both to achieve good coupling. The compromise is usually reached, or believed to be reached, with $R_n = 50\ \Omega$.

Given $R_n \sim 50\ \Omega$, the device size is set by the the requirements on $\omega R_n C$. Using the expression by Kerr and Pan (1990) in eq. 4-3, the size should scale as

$$A = \frac{1.3}{f^2 C'} \qquad 4\text{-}4$$

with f in THz, C' in fF/(μm)^2 (= 45 for Nb/AlO$_x$/Nb junctions), and A in (μm)^2.

4.1.3 Leakage Currents, Ruggedness, Operation Temperature

Low noise operation requires low currents below the gap voltage. The currents below the gap voltage contribute to the mixer noise as shot noise (section 3.4.1). Minimizing these leakage currents is a materials and fabrication challenge. $Ta/Ta_2O_5/PbBi$ junctions [Face et al., 1986, 1987] and $Nb/AlO_x/Nb$ junctions [Lichtenberger et al., 1991] have proven to be good materials choices. The fabrication of low leakage junctions requires that the barrier be good, without excess leakage due to a non-uniform barrier, suboxides, and normal metal inclusions [Face et al., 1987].

In addition to these intrinsic properties, it is desirable that the SIS device be rugged so that electrical shock and thermal cycling do not degrade its properties. Clearly, a useful receiver requires that the device can withstand multiple cooling and the occasional electrical jolt.

4.2 $Nb/AlO_x/Nb$ Trilayers

A near ideal choice in meeting requirements of section 4.1 is the $Nb/AlO_x/Nb$ tunnel junction [Gurvitch et al., 1983]. The mixer receiver built at Yale used $Nb/AlO_x/Nb$ tunnel junctions exclusively. All of the Nb devices used in the Yale receiver were fabricated by me at the Westinghouse Science and Technology Center, Pittsburgh, PA with the collaborative help of J.X. Przybysz and J.H. Kang. The fabrication procedure and quality of these devices are discussed in the following sections. The fabrication procedure used to produce the Yale mixer receiver devices is shown in Fig. 4-1 and will be referred to in coming sections. The entire procedure is given in Appendix A.

Many other groups use $Nb/AlO_x/Nb$ tunnel junctions since this type of tunnel junction has proven to be very high quality in terms of its leakage current [Lichtenberger et al., 1991; Kirk et al., 1991]. These junctions have also been made small, to areas of 0.3 $(\mu m)^2$ [Huq et al., 1991]. In addition, $Nb/AlO_x/Nb$ tunnel junctions show no aging in ambient storage over a period of 450 days [Morohashi and Hasuo, 1987]. These junctions,

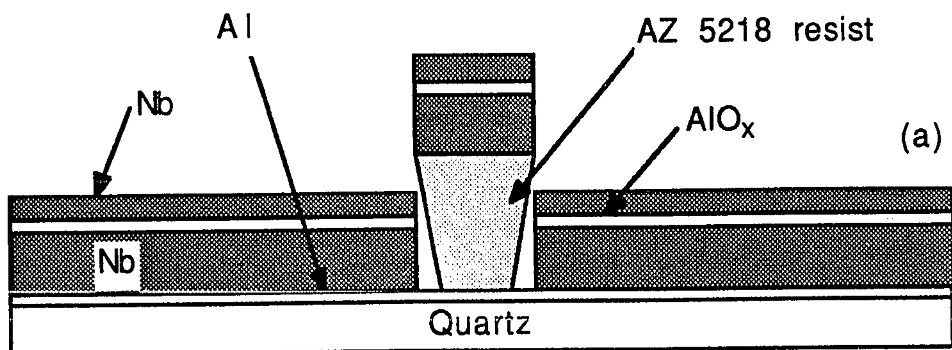

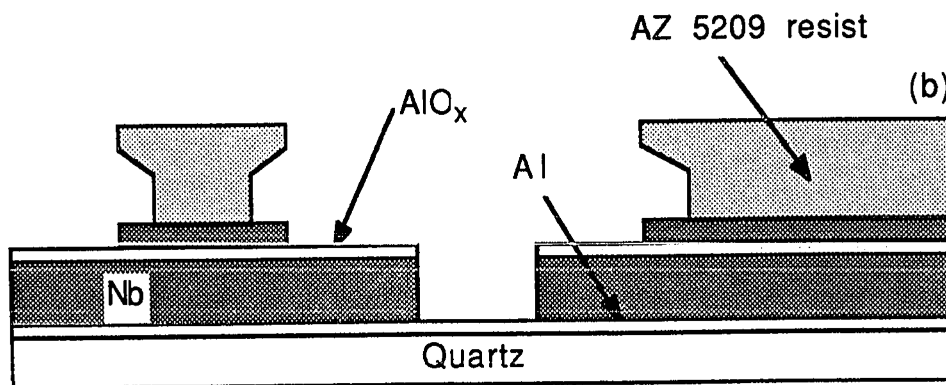

Fig. 4-1 A side view schematic of the fabrication of the Nb/AlO_x/Nb trilayer tunnel junctions. The layer thicknesses are given in the text.

(c)

Insulator deposition and lift-off

(d)

Wiring

Fig. 4-1 cont.

commonly called Nb trilayers, are the standard for many applications including analog to digital converters [Kang et al., 1991], and digital logic circuits [Hasuo and Imamura, 1989]. Since so many applications require robust, reproducible tunnel junctions, the Nb trilayer junction and its fabrication have been well studied [for a review of the device structures and junction characteristics of $Nb/AlO_x/Nb$ tunnel junctions made by a number of groups studying receivers, see Blundell and Winkler, 1991].

4.2.1 Substrates

The devices fabricated for the mixer receiver at Yale were made on 2 mil (51 μm) thick fused or crystal quartz.[1] The substrate thickness and material were chosen based on the scale modeling work done by Winkler et al. (1989). The scale modeling used a 28.4 x replica of the mixer receiver to determine the rf coupling and chip design. According to the scale modeling, substrates thicker than 2 mils give radiative losses, although the losses in 3 mil substrates may be tolerable. The low dielectric constant of quartz ($\varepsilon = 3.8$) reduces the waveguide loading [Goldsmith, 1982]. The quartz wafer size was 1" x 1". This allowed for 102 devices of size 1 mm x 4 mm, as well as some test structures, to be fabricated on a single chip. These substrates were fragile; special handling and processing procedures were necessary in order to fabricate the devices. The edges of the substrates were particularly susceptable to breaking; test structures on future thin quartz wafers should be made in the center of the wafer in order to maximize their yield. In order to decrease breakage losses, the quartz substrates were mounted onto thick (0.56 mm) 2" diameter Si substrates using silicone based vacuum grease.[2] A similar technique, using vacuum grease mounting is described by Danchi et al. (1989). After cleaning the quartz and silicon wafers (See appendix A for cleaning procedures), the vacuum grease was spread in the center 1" by 1" section of the silicon wafer. The quartz substrate was then placed on this grease. After

---

[1]Valpey-Fischer, Hopkinton, MA
[2]Dow Corning Corp., Midland, MI

baking the wafers for 5 minutes at 110° C (this helps smooth the grease), a contact maskaligner was used to press the quartz and Si wafers together by slowing bringing them into contact with a mask. A maskaligner is a nearly ideal choice for this procedure since it is designed to make a flat contact with the mounted substrate. In addition, one could look through the optics of the aligner and see when the contact had caused the grease to become smooth and the bubbles to exit from underneath the quartz wafer. Unfortunately, this practice was not ideal since some grease oozed out from within the Si/quartz sandwich and adhered to the mask. When this happened, the mask and wafer sandwich were separated slowly, in order not lift the wafer sandwich from the vacuum chuck. This took about 5 minutes. Afterward, both the mask and the wafer sandwich were cleaned with a degreaser, such as trichloroethane (TCA). The wafer sandwich could not be soaked in the degreaser, since this would dissolve the contact that had just been made. Instead, it was cleaned by spin cleaning. This was very simply done by placing the Si/quartz sandwich (Si side down!) on the vacuum chuck of a spinner and squirting the top surface with TCA while the device was spun at ~ 4000 rpm. In this way, the solvent did not get between the quartz and the silicon wafers. The devices remained mounted in this way until they were separated in order to deposit the back side metal on the quartz (section 4.4).

4.2.2 Deposition of the Al Underlayer

The sputtering system used to deposit the Al and Nb layers was developed by Westinghouse and the Kurt J. Lesker Company and uses a water-cooled copper block on which the substrate is mounted and heat sunk. The system is designed for the use of 2" silicon wafers. The quartz/Si sandwich was therefore ideal for this system and alleviated the problems involved in processing a 1" square quartz substrate substrate in a system designed for 2" diameter round substrates.

After the wafer mounting procedure, the Si/quartz sandwich was loaded to the Lesker sputtering system. The system is load locked with a base pressure of 1-3 x 10^{-9} Torr. A 100 Å Al film was rf magnetron sputtered onto the substrate at a rate of 25 Å/min.

4.2.3 Deposition of the Trilayer

The Nb trilayer devices used in the Yale receiver were made using the same sputter deposition parameters given in Kang et al. (1991). The differences between the devices described here and those of Kang et al. are the substrate, the device size, the junction current density, and the fabrication procedure.

Chang et al. (1987) have pointed out the importance of cooling the substrate while depositing the films that make up the trilayer. The work by Kang et al. (1991) uses Si substrates. These substrates are heat sunk to the copper block in the Lesker system by mechanical pressure. This heat sinking is adequate to produce high quality films and devices.

Another benefit of the low temperature of the substrate during deposition is that it allows one to pattern films using liftoff. For liftoff, the initial trilayer patterning was done using image reversal photoresist, AZ 5218E.[3] The developed pattern was the area of trilayer deposition. Since we used quartz substrates, the Al underlayer was necessary to obtain the small features in the trilayer pattern. Attempts to pattern the trilayer photoresist liftoff stencil on the bare quartz wafer resulted in a diffuse and blurred resist stencil due to the backside reflections from the Si wafer underneath the quartz substrate. The 2 μm features in this mask level (Fig. 4-2) were washed out. With the Al underlayer, the liftoff stencil could be patterned. All of the masks used in the fabrication of the Nb/AlO_x/Nb devices described in this thesis were made by M.J. Rooks at the National Nanofabrication Facility. All of the patterning was done using a contact printer.

---

[3]Hoechst Celenese, Somerville, NJ

After patterning the photoresist lift-off stencil, the trilayer was deposited (Fig. 4-1a) in the Lesker system. First the Nb base electrode was dc magnetron sputtered at an Ar pressure of 7.1 mTorr to a thickness of 2500 Å at a rate of 1600 Å/min. The rate and Ar pressure are found to produce a Nb film with slightly compressive stress [Kang et al., 1991]. This stress is found to be small (~-10 μm). The residual resistance ratio of the films is normally 8-9, with T_c of 9.2 K.

After the Nb base layer deposition, 100 Å of Al was *rf* magnetron sputtered at a rate of 25 Å/sec. This Al was then oxidized in the load lock chamber to produce the tunnel barrier. At ambient temperature, the oxidation time and pressure of the oxygen during the Al_2O_3 growth determine the current density of the junction. The dependence of the current density on the oxygen pressure is given by Kang et al. (1991) and is in agreement with previous work by Huggins et al. (1985) and Morohashi et al. (1987). The J_c of the Yale junctions was 3000 or 5000 A/cm^2 using an oxidation pressure of 50 and 20 mTorr respectively for a time of 30 minutes. From eq. 4-1, with C' = 45 fF/(μm)^2 for the Al_2O_3 in the trilayer junction [Lichtenberger, et al., 1989; Han et al., 1989], $\Delta_1 = \Delta_2 = 1.4$ mV, f = 100 GHz, this gives $\omega R_n C$ products of 2 and 1.24 for J_c = 3000 and 5000 A/cm^2 respectively. These values are both less than the recommended value of 3-4, which may allow significant higher harmonic currents to flow in the junction in response to an applied radiation. This is discussed in Chapters 5.

The counter electrode Nb was then deposited using the same sputter source and deposition parameters as the base electrode Nb. The counter-electrode thickness was 800 Å. The deposition of the counter electrode completed the trilayer. The patterning of the trilayer was completed by soaking the wafer sandwich in acetone to liftoff the unwanted parts of the trilayer. This process took ~5 minutes, not long enough to affect the vacuum grease adhesion of the two wafers.

4.2.4 Defining the Junction Area

With the R_nC product being set by J_c and R_n set to ~ 50 Ω, the area of the device should be given by eq. 4-4, $A \approx 2\ (\mu m)^2$. Device of 0.5, 2, and 4 $(\mu m)^2$ were fabricated. These small area devices needed to be patterned using a self-aligned approach, since insulating them using another mask layer would require aligning contact holes smaller than the junction size to the junctions. This would be very difficult.

Many techniques exist for defining the junction in a self-aligned way. Many were tried. The simplest process tried was a Selective Niobium Anodization Process (SNAP), described by Kang et al. (1991) and first reported by Kroger et al. (1981). In this method, the junction area is protected with photoresist or SiO_2. The top electrode is then anodized, producing Nb_2O_5, which insulates and defines the tunneling area. Unfortunately, it was not possible to produce junctions of a size smaller than 5 $(\mu m)^2$ since the anodization led to stresses at the edges of the junction due to the factor of 2.5 difference in thickness of Nb_2O_5 and Nb [Imamura and Hasuo, 1989].

In order to fabricate the small area junctions, a modified Selective Niobium Insulation Process (SNIP) was developed. This process is a variation on those given by Shoji et al. (1983) and Morohashi et al. (1985). The SNIP process uses SiO_2 rather than Nb_2O_5 to insulate the junction. The dielectric constant of SiO_2, $\varepsilon = 3.8$, is smaller than that of Nb_2O_5, $\varepsilon = 28$, thus giving a smaller capacitance for equivalent thicknesses.

The modified SNIP process is rather straightforward. The junction area was defined by patterning resist on the trilayer, as shown in Fig. 4-1b. The resist was AZ5209 used in the positive mode with a chlorobenzene soak to give it an undercut liftoff profile [Hatzakis et al., 1980]. The counterelectrode was then reactive ion etched in a Semigroup 1000 etcher, in a plasma of CCl_2F_2 with 8% Ar and 8% O_2. The argon and oxygen help prevent the formation of polymers [Przybysz et al., 1989; Flamm, 1989]. The Al_2O_3 tunnel barrier served as an etch stop for this etching. The underlayer of Al also protected the quartz substrate from being etched, as can be seen in Fig. 4-1b.

While still in the reactive ion etcher, the photoresist dot protecting the device area was "shrunk" in a 300 mTorr plasma of O_2. This procedure ensured that the resist stencil was smaller so that edge coverage of the junction area would be possible in the subsequent deposition of an insulator. In addition, and probably more importantly, the O_2 plasma served to insulate the edges of the exposed Nb counter-electrode. Lower pressure O_2 plasmas were found to attack the top of the photoresist preferentially.

After the dot shrinkage, the Al underlayer was chemically etched. The etch was stopped at Nb and SiO_2. The etch of the Al underlayer was necessary in order to electrically isolate the devices on the chip from each other, and also in order not to short across the tunnel barrier. The thin Al underlayer remained only under the trilayer, and was thus always electrically shunted by the trilayer. To complete the isolation of the junction, 1500 Å of SiO_2 was sputter deposited in an MRC sputtering system. The photoresist dot was then lifted off in acetone, opening a hole in the SiO_2 through which the junction could be contacted, as shown in Fig. 4-1c. It was important to heat sink the wafer sandwich well with vacuum grease to the sputter platform during the deposition of the SiO_2 in order to achieve liftoff of the photoresist dot.

Before describing the completion of the device, an apology is in order. Some of the devices measured, such as a devices J and K described in Chapter VI, had leakage currents far in excess of what is found by Kang et al. (1991) using the same trilayer deposition and oxidation parameters described here. At this time, it is believed that the excess leakage current found in some devices was due to an inadequate passivation of the Al of the tunnel barrier. This Al was etched at the same time that the Al underlayer was etched (this can be seen in the transition from Fig. 4-1b to 4-1c). This etching was done *after* the dot shrinking and Nb passivating O_2 plasma oxidation. Instead of the sequence described above, one should instead follow the sequence 1) reactive ion etch the top Nb, 2) wet etch the Al underlayer (and Al/Al_2O_3 of the tunnel barrier), 3) O_2 plasma shrink and passivation. The O_2 plasma would then passivate the exposed Al edge around the tunnel junction and should

give better quality junctions. This procedure was not followed for the devices described in this thesis.

4.2.5 Wiring, Contact, and Ground Plane Layers

The device consisted now of a patterned trilayer and a defined junction. The junction was contacted with a wiring layer. The wiring layer was Nb and was defined by AZ 5218 image reversal photoresist used in the image-reversed mode. After loading the device in the Lesker sputter deposition system, the exposed Nb was ion beam etched to clean away the native oxide which had formed. After ion beam cleaning, the wiring Nb layer was deposited using the Nb deposition parameters described above for the base and counter electrode. The thickness of the wiring layer was 2000 Å. The wiring layer was patterned by photoresist liftoff. Figure 4-2 shows a top view of the device area. In addition to the wiring layer, the horizontal bar toward the bottom of the figure was deposited. This bar completed an inductor, which is described in Chapter V. Ideally, this bar and the wiring should have been on the same mask level. They were not in the same mask layer because it was not known what length the inductor should be made. By having the inductor bar on a separate mask, the inductor length could be defined once one knew what length was appropriate. This was not done in this work since no devices have been fabricated since the initial mixer experiments. In the future, once the effect of the tuning inductor is well characterized, this mask set could be used to fabricate devices which have the correct tuning inductance.

In order to make contact to the device with the experimental apparatus, Au contact pads were deposited. These were deposited well away from the junction area. The Au contact pads were patterned by liftoff. An ion beam cleaning of the contact area was done prior to the deposition of the contact pads. Since Au does not adhere well to Nb, a thin (100 Å) Ti layer was deposited on the Nb before the 500 Å Au pad was deposited. Once again,

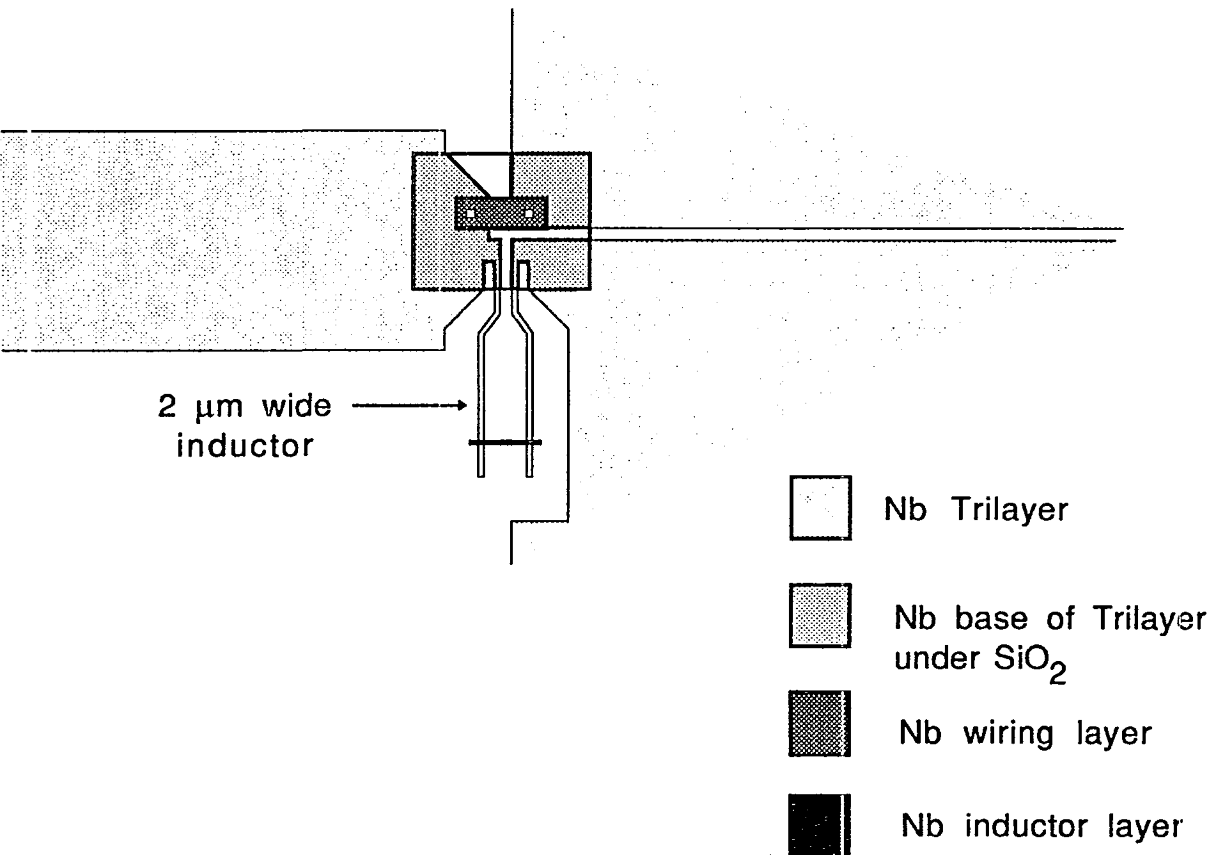

Fig. 4-2 A expanded view of the junction area.

good heat sinking with vacuum grease was important in this fabrication step in order to achieve liftoff of the Ti/Au.

Once the front side of the wafer was completed, it was necessary to deposit the ground plane metal on the back side of the quartz wafer. This required separating the quartz wafer from the host Si wafer. This was done by soaking the wafer sandwich overnight (~ 8 hours) in TCA. Once unstuck, the fragile quartz wafer was remounted on another Si wafer using the method described in section 4.2.1. The original Si wafer was discarded since it had been covered with an assortment of metals and insulators. In practice, the backside of the quartz wafer could not be cleaned well. Perhaps with the use of high vacuum grease, which is completely soluble in TCA, this problem could be overcome.

The backside metal consisted of a superconducting ground plane of 3000 Å of Nb, and 500 Å of Au to make contact between the backside of the wafer and the mixer block during the experiment. Once again, 100 Å of Ti was used between the Nb and Au layers in order to promote adhesion. Since the Nb, Ti, and Au were deposited in-situ in the MRC sputtering system, no ion beam cleaning of the Nb was necessary for the backside metallization.

4.2.6 Wafer Cutting

One of the difficulties of working with fragile samples was that they often broke at the last moment, during the wafer cutting. In order to minimize these losses, the quartz wafers were mounted device side up onto 2" Si wafers with Krazy glue.[4] The quartz wafer was pressed flat to the Si host wafer by placing ~ 6 U.S. quarters on top of it during the Krazy glue drying. The wafer was then spin coated with photoresist to protect its surface during the cutting. The mixer receiver devices were cut at Thermo Carbon, Inc. in Castelberry, FL and Hypres, Inc. in Elmsford, NY. Some of the earlier devices were cut

[4]Krazy Glue Inc., Itasca, IL

by hand using a diamond scribe. Once cut, the individual devices were unglued from the Si host wafer by soaking the wafer in acetone.

4.3 The Junctions

A number of the tested devices are tabulated in Table 4-1. A parameter which describes the device but is not tabulated is the voltage width of the rise of the current at the gap voltage, ΔV. This width is important in determining whether the device will operate in the quantum regime as discussed in section 3.3. For all of the devices presented in table 4-1, $\Delta V < 200\ \mu V$/junction. Since the photon width at 100 GHz is 414 μV, these devices are within the quantum regime. Fig. 4.3 shows the dc I-V trace of three devices with $J_c = 5000$ A/cm^2. The leakage current does not appear to depend upon the number of junctions in the array. Notice the the proximity effect structure (just above the current rise) becomes more complicated as the number of junctions in series increases.

Most comparisons of devices between groups are based on the current density, size, and quality factor. The quality factor, V_m, is usually defined for Nb trilayer devices as $V_m = I_c R_{sg}$ where R_{sg} is the subgap resistance of the junction or array at a voltage n x 2 mV where n is the number of junctions in the array. In cases where the critical current I_c is depressed (due to trapped flux for example), the definition $I_c = 0.7\ I_g$ is used, where I_g is the current rise at the gap voltage. The results for our junctions compare favorably with others reported in this size range, < 1 $(\mu m)^2$, as can be seen in Table 4-2. The main distinction between these devices and the other presented in the table is the fact that these devices were fabricated on 2 mil thick quartz. The successful use of such thin quartz, from start to finish in the process, represented a real accomplishment.

4.4 Critical Examination of the Device Process

The preceding sections of this chapter described a process which worked and produced reasonable quality small trilayer devices. This process represents an evolution

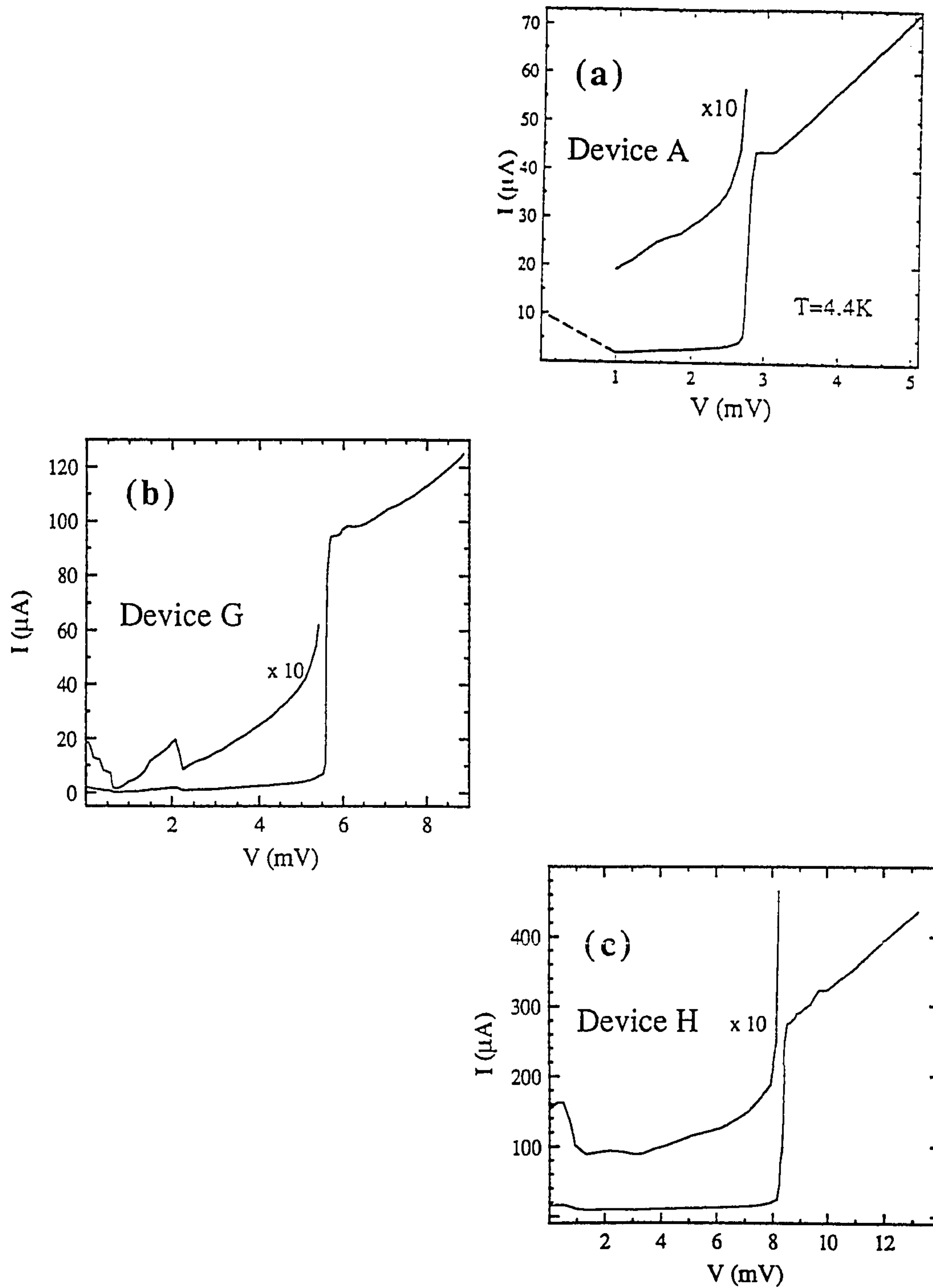

Fig. 4-3 DC I-V traces of Nb/AlO$_x$/Nb trilayer tunnel junctions from the same wafer. J_c = 5000 A/cm^2 for all junctions. a) Single junction. b) Two junction array. c) Three junction array.

Table 4-1. Parameters of several devices. The oxidation conditions to give the quoted J_c were determined from measurements of large area devices on Si substrates. The expected R_n was calculated from the tabulated J_c and expected device area. In all devices, $\Delta V < 200\ \mu V$/junction.

Device	Wafer - Chip Designation	Nominal Area of Individual Junction $(\mu m)^2$	Number of Junctions	Expected J_c (A/cm^2)	$R_n(\Omega)$	Expected R_n from Mask Area (Ω)	Effective Area $(\mu m)^2$	V_m/Junction (mV)
A	3-C2	0.5	1	5000	71	80	0.56	22
B	4-E15	0.5	2	3000	431	260	0.30	48
C	4-B13	0.5	2	3000	125	260	1.04	22
D	1-A4	0.5	3	3000	448	390	0.43	29
E	1-B5	0.5	4	3000	619	520	0.42	50
F	3-A9	2	2	5000	61	40	1.31	28
G	3-A10	2	2	5000	71	40	1.13	41
H	3-A6	4	3	5000	30	30	4.00	28
I	1-A11	4	4	3000	124	65	2.09	18
J	X1-D6	4	4	5000	39	40	4.10	13
K	X1-D3	0.5	2	5000	99	160	0.81	13

Table 4-2 Figures of merit for several $Nb/AlO_x/Nb$ tunnel junctions. Our work is in bold face. The roll-off frequencies (f_{R_nC}) were calculated using a specific capacitance of 45 fF/(μm)^2. The frequency $f_{\delta V_g}$ is the minimum operation frequency to be in the quantum regime based on the voltage width of the current rise at the gap voltage. The maximum operation frequency is given by $f_{4\Delta}$. Modified from Blundell and Winkler (1991).

Material	Geometry	J_c (kA/cm^2)	V_m (mV)	$f_{\delta V_g}$ (GHz)	$f_{4\Delta}$ (THz)	Area (μm)^2	f_{R_nC} (GHz)	Reference
Nb/Al-ox-Al/Nb	edge	0.01-24			0.97-1.1	0.0022	435	Martinez and Ono (1990)
Nb/Al-ox/Nb	**mesa**	**3** **5**	**40** **34**	**24-48**	**1.3** **1.3**	**0.5** **0.5**	**130** **180**	**Worsham et al. (1991)**
Nb/Al-ox/Nb	mesa	2.7	30	34	1.3	2.2	130	Gundlach (1990)
Nb/Al-ox/Nb/Al-ox/Nb/Al-ox/Nb	SNEP stacked	0.01-0.07			0.97-1.4		20	Blamire et al. (1989)
Nb/Al-ox/Nb	self-aligned	1	20	24-48	1.3	0.45	75	Kirk et al. (1989)
Nb/Al-ox/Nb	mesa	0.85 0.4	87 1000	24 48	1.4 1.3	10 64	70 50	Lichtenberger et al. (1989)
Nb/Al-ox/Nb	mesa	1.5	1500	48	1.3	1.4	75	Lichtenberger et al. (1991)
Nb/Al-ox/Nb	SNAP	6.8	30-35	24	1.4	0.7	210	Imamura and Hasuo (1988)
Nb/Al-ox/Nb	SNAP	1.8 20	70 11	12 12	1.4 1.4	50 12.6	100 370	Morohashi et al. (1986)
Nb/Al-ox/Nb	mesa	0.03-0.2 600	20-58	72	1.4		30	Lumley et al. (1985)
Nb/Al-ox/Nb	SNAP	2	60	48	1.4	0.5	90	Bhushan and Macedo (1991)

from a great number of things which did not work. It is perhaps prudent to describe ways in which this process could be further improved.

As seen in Table 4-1, the device resistance does not match well with that expected from the mask area. This was a problem of the lithography. The definition of the junction area was done using a chlorobenzene soak process. The chlorbenzene hardens the resist to exposure and development [Hatzakis et al., 1980]. The hardening of the resist seemed to be on a size scale which was not negligible when compared to the device size of 1 μm. Thus, although devices could be fabricated, their absolute area was very dependent upon the specific depth to which the resist was hardened by the chlorobenzene.

A better way to define the junction area is to use image-reversal resist. The commercially available resist, AZ5209, which was used in the positive mode to define the junctions described above, should be better when used in the image reversal mode. The reason that this was not done is the work already described was that the junction definition mask was designed for use with a positive resist. With the use of the negative of the junction definition mask, one could make image reversed photoresist vias of a size on the order of the resist thickness (0.9 μm for AZ 5209). The image reversal resist gives good undercut profiles and is ideal for liftoff processes [Moritz, 1985; Marriot et al., 1987; Meier et al., 1991].

Other than the irreproducible device size and the large leakage currents seen in some devices, the main problem with this process was the fragile wafers. Even with the mounting procedure described in section 4.2.1, the breakage losses were substantial. These losses occured most often during the mounting and dismounting of the quartz substrate from the Si host wafer. There was no easy solution to this problem since mounting the device required handling. One solution would be to fabricate the devices on reasonably thick quartz (~ 10 mils) and have the quartz ground to a thickness of 2 mils. At this point, one would still have to deposit the ground plane metal, and dice the wafer.

4.5 Ta Devices

The results for the Ta mixer devices are presented in section 5.5. These devices were used to study the quantum limited noise in SIS mixers. Because the leakage current causes shot noise, the quality of these devices, in terms of the leakage current, was much higher than that of the Nb trilayer devices described above. The native oxide of Ta, Ta_2O_5, is known to form a high quality tunnel barrier [Spencer and Rowell, 1981].

A schematic of the device process is given in Fig. 4.4 while the entire process is given in Appendix B. This was not a trilayer process. Much of the process was developed and is reported by Cui et al. (1987). These junctions were made using a window geometry [Huang et al., 1980].

The first step was an evaporation of 3000 Å of Ge onto the 5.8 mil fused quartz substrate. The Ge was necessary to eliminate charging effects from the ion beam cleaning in later processing. The base-electrode consisted of 100 Å of Nb followed by 3000 Å of Ta. These were sputter deposited using a Kaufman-type ion source [Kaufman, 1982]. The Nb is necessary to nucleate the bcc phase of Ta [Face et al., 1983]. The base layer was patterned using a chlorobenzene soak lift-off process (Fig. 4.4a and b). The device area was defined using projection lithography [Feuer and Prober, 1981] and another chlorobenzene soak liftoff process. As shown in Fig. 4.4c and d, the resist protected the junction area during a deposition of 2000 Å of SiO. The device area was ~ $1(\mu m)^2$. The junction area was ion beam cleaned with a mixture of 50% O_2, 50 % Xe and then pure Xe. The O_2-Xe mixture is believed to clean the junction area of organics, while the pure Xe cleans the area of oxides which have formed [Cui et al., 1987]. The barrier was then formed by a dc glow discharge in pure O_2. After the barrier oxide growth, the 3000 Å counter-electrode $Pb_{0.9}Bi_{0.1}$ and 150 Å of In were deposited (Fig. 4-4e). The device was completed by liftoff of these metals (Fig. 4-4f). The In is found to inhibit junction aging effects [Raider]. The dc I-V trace of the device most studied in this work is shown in Fig. 5-18.

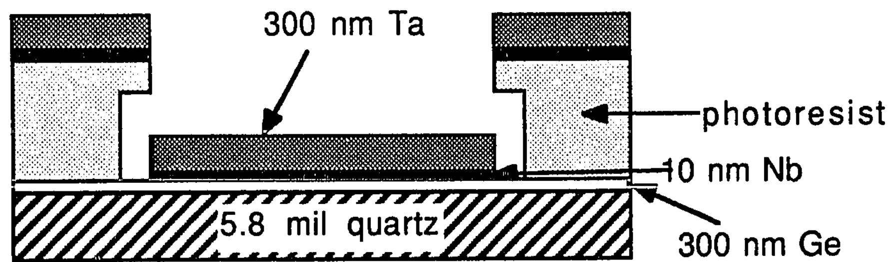

(a) Base electrode definition and deposition

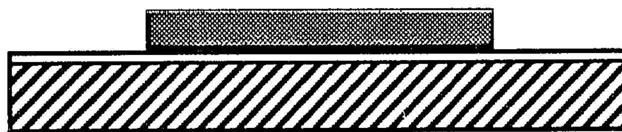

(b) Liftoff

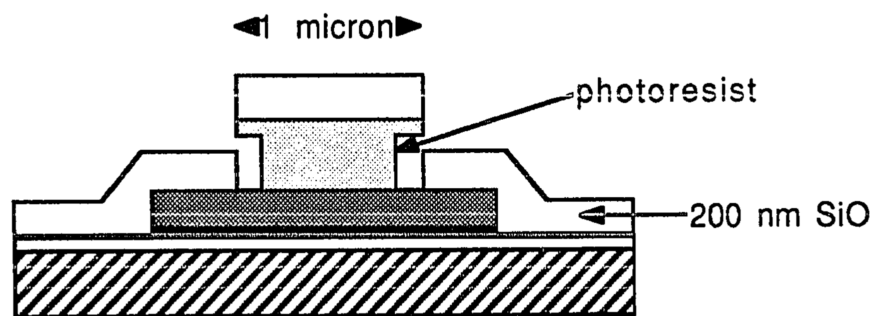

(c) Junction area definition
SiO evaporation

Fig. 4-4 A side view schematic of the $Ta/Ta_2O_5/PbBi$ tunnel junction fabrication.

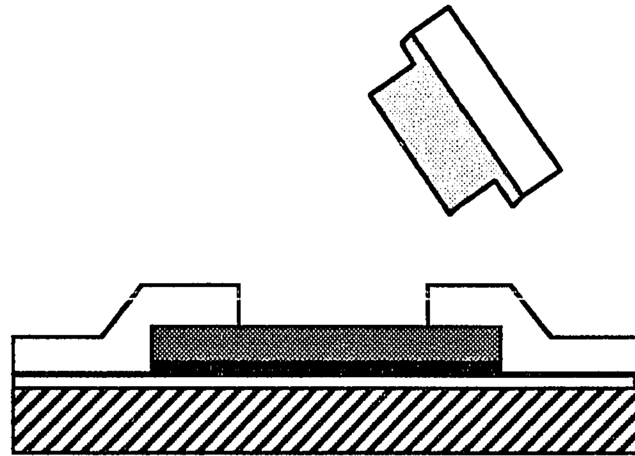

(d) liftoff

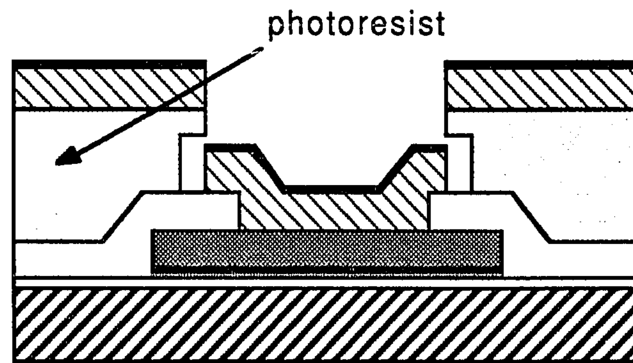

(e) Counter electrode definition
Junction area cleaning
Tunnel barrier growth
PbBi/In deposition

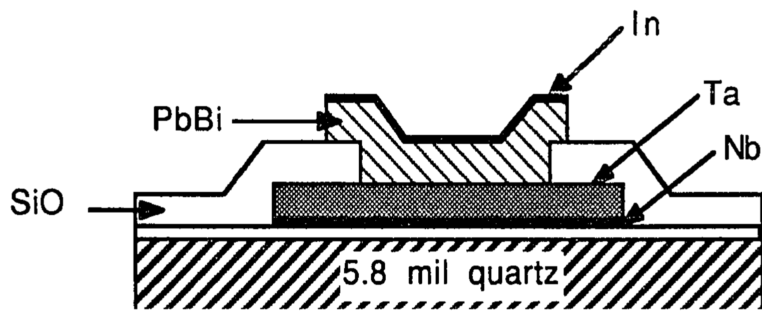

(f) liftoff

Fig. 4-4 cont.

This chapter has shown some of the strict requirements on SIS junctions necessary for good mixer receivers. Some of these requirements led to a novel fabrication process of Nb/AlO_x/Nb devices on 2 mil thick quartz substrates. These devices were used in a mixer receiver described in the next chapter. Nb/AlO_x/Nb devices were also used in a set of experiments which directly measure the quantum conductance and quantum susceptance, discussed in chapter 6. The quantum limited noise experiments discussed in the next chapter necessecitated the high quality Ta/Ta_2O_5/PbBi devices described in this this chapter.

V RECEIVER DESIGN AND MIXING RESULTS

The majority of this chapter describes the receiver design, mixer results, and theoretical modeling of the SIS mixer receiver at Yale. Since the goals and achievements of this work and the work in which I collaborated with Berkeley were so much different, the Berkeley results are presented separately in section 5.5.

5.1 Receiver Design

The receiver built at Yale, primarily by D. Winkler and N.G. Ugras, was designed to be flexible in terms of its physics while meeting all applications requirements. The physics requirements are simple: the system must be understandable and quantifiable. The applications requirements are also simple: the apparatus must be useful (or the prototype must be easily modified) as a receiver in a radio telescope. The design involved a compromise between these two different criteria. This chapter describes the design of the receiver. Additional details are discussed in Winkler et al. (1989) and Winkler et al. (1991a,b).

Advances in sensitivity of the detector required advances in device and receiver technology. According to Dicke's radiometer formula [Dicke, 1946], for a broadband signal source, the signal to noise ratio of the receiver is given by

$$S/N = \frac{T_S}{T_R} (\Delta f \, \Delta t)^{1/2} \qquad 5\text{-}1$$

where T_S is the equivalent black body temperature of the signal source, T_R is the equivalent blackbody "noise temperature" of the receiver, Δf is the observational bandwidth, and Δt is the integration time. To achieve a certain signal to noise ratio, the observation time is proportional to the square of the receiver noise temperature. The finite amout of available observation time at observation telescopes has helped drive the effort to make quieter

receivers. The first receivers which used SIS mixers are described by Phillips et al. (1981), Olsson et al. (1983) and Woody et al. (1985). Since that time, SIS mixers have replaced cooled Schottky mixers at a number of radio-observatories [Blundell et al., 1983; Pan et al., 1983; Sutton, 1983; Gundlach, et al., 1985; Ellison and Miller, 1987; Blundell et al., 1988; Vowinkel et al., 1989].

In addition to noise requirements, the system must be easy to use. This means operation at a useful temperature, broadband operation, and easy tuning. The temperature requirement limits the useful operating temperature to 4.2K, liquid helium, since the radioastronomer does not in general wish to pump on the liquid helium in order to reach a temperature lower than 4.2K.

The broadband operation requirement limits the coupling mechanisms which can be used to couple the LO and the signal into the heterodyne device; a small operation bandwidth limits the frequency range over which a signal can be observed.

The final major design requirement which is important for applications is the freedom from difficult tuning procedures. Many useful and operational receivers use one or two stub tuners in order to effectively couple in the LO and signal [Pan et al., 1989; Kerr and Pan, 1990; Blondel et al., 1988; Ogawa et al., 1990; for a review see Blundell and Winkler, 1991] . These may cause the operator to have to retune the device at each operational frequency. Ideally, one would like a receiver that has no adjustable tuning elements, demonstrated in work apart from this [Kerr et al., 1990]. The receiver design and implemented at Yale met these three major requirements: its operational temperature was 4.4K, the bandwith of operation was the full waveguide bandwidth (80 - 120 GHz), and it had no adjustable tuning elements.

The receiver also was designed to provide the correct embedding admittance to the tunnel junction. The desired embedding admittance is typically of a higher resistance than the junction normal state resistance, and slightly inductive. The experimentally determined embedding admittances for a few devices in this receiver are given in section 5.4.4. In

addition to the *rf* embedding admittance, the design coupled out the IF frequency effectively. Since the output impedance of the mixer is usually large, i.e. the photon assisted tunneling steps are flat for optimal gain of the receiver, matching this large impedance to the IF amplifier with a lower input impedance of 50 Ω is difficult. In work by other groups, an IF transformer has been used to make an impedance transformation from the large output impedance of the mixer to 50 Ω, but the transformers are typically bulky and reduce the instantaneous bandwidth of the receiver. The Yale receiver used no IF transformer. Ideally, one could use low impedance junctions such that the IF output impedance of the junction would be lower and closer to 50 Ω.

In addition to the radioastronomical applications of the receiver, the design also included the elements necessary to test and apply Tucker's quantum theory of mixing [Tucker, 1979] to our results. As outlined in Chap. 3, the quantum mixer theory is used to predict the gain, noise and the dynamic resistance of the mixer. The gain and noise are governed by the I-V characteristic, input LO power, bias voltage, and embedding admittance seen by the junction at the LO and all relevant harmonics and sideband frequencies. The dewar and electronics included the necessary features to independently measure the I-V characteristic, bias voltage, gain, and noise. The determination of the embedding admittance is described in section 5.4.2.

5.1.1 The Local Oscillator and Dewar

The local oscillator was a frequency tripled[1] YIG-tuned oscillator[2] which was coupled into the WR-10 waveguide. The rectangular waveguide dimensions were 0.1" by 0.05" and it was made of OFHC copper. The operation frequency range of the oscillator was 79.5 to 120 GHz. Following the oscillator was a room temperature waveguide

---

[1]Model MU-10, Millitech Corp, S. Deerfield, MA

[2]Model AVD-26240/W, Avantek Corp., Santa Clara, CA

attenuator which was adjusted to give the proper output power to the LO port of the mixer. The attenuator consisted of a waveguide with a silicon vane inserted through the top face of it. The depth of the vane in the waveguide determined the attenuation. For optimal mixer response, the attenuator was changed with each change in the YIG output frequency, since the optimal value of α and the output power of the YIG changed with frequency. The YIG power was coupled into the dewar through a mylar window.

The dewar was a ten inch Infrared Labs dewar[3] whose special features were the large 5" working space above the cold plate and low temperature modification for use with pumped LHe. The lowest temperature achieved with this dewar was 2.0 K (by pumping on the liquid helium with a mechanical pump) and the longest hold time with all components in place was 14 hours at 4.2K. The dewar contained 4 liters of LHe. The outer nitrogen shield contained 4 liters of liquid nitrogen. Internal to the dewar, the waveguide was heatsunk to a liquid nitrogen shield with braided copper shield and subsequently entered the mixer block.

At the mixer block, the LO input waveguide was directed through a low loss broad-band WR-10 cross-coupler[4] where it was attenuated by ~ 23 dB. The purpose of this attenuation was to reduce any room temperature noise coming down the input waveguide. The attenuator also served to reduce reflections from the tunnel junction which could have caused standing waves along the input waveguide. The LO power levels necessary at the input of the mixer (< 50 nW) could easily be obtained from the YIG oscillator through this attenuator except at the very high end of the oscillator's frequency range (115-120 GHz).

After passing through the cross coupler, the LO signal passed through a four-step Chebychev single ridge transformer [Hopfer, 1955; Collin, 1955; Schneider et al, 1968; Hoefer and Burton, 1982] which provided a broad band waveguide-to-microstrip transition

---

[3]Model HD-3(10)w/workheight and temp. modifications, Infrared Labs, Inc., Tuscon, AZ

[4] Designed and built by Dr. Neal Erickson at Millitech Corp., S. Deerfield, MA

(see Fig. 5-1). The impedance transformation from the waveguide impedance of 346 Ω (at 100 GHz) to the microstrip impedance of 50 Ω was necessary since the typical desired embedding admittance has a real part of the order of 50 Ω. The transformations allow for most of the power to be coupled into the microstrip without reflections at the ridge [Winkler et al., 1989] The voltage standing wave ratio of the ridge was measured in a scale model to 1.5:1 for the scaled frequency range of 65.3-128 GHz.

5.1.2 The Signal Path

The signal frequency, in radio astronomy applications, is typically a line source or a combination of line sources. For the laboratory, a broadband hot/cold load was used [Winkler et al., 1991c], similar to that used previously by other groups [Blaney, 1980; McGrath, 1985]. The hot/cold load consisted of 10 mil thick silicon vane coated with 830 Å of NiCr inserted into a slot on the top of a waveguide. This waveguide was coupled into device through the cross coupler and the ridge transformer. The cross coupler does not attenuate the power from the hot/cold load. The hot/cold load was physically at a distance of 2" from the device.

The output power of the hot/cold load coupled into the waveguide is dependent upon its temperature given by the Planck blackbody formula

$$\frac{P}{B} = \frac{\hbar\omega}{\exp(\hbar\omega/kT) - 1} \qquad 5\text{-}2$$

where B is the bandwidth. A diode thermometer was thermally anchored with Stycast to the NiCr film in order to measure the temperature of the vane. A 100 Ω carbon heater was also connected in this way in order to heat the vane. The reflection from the vane was less than -30 dB.

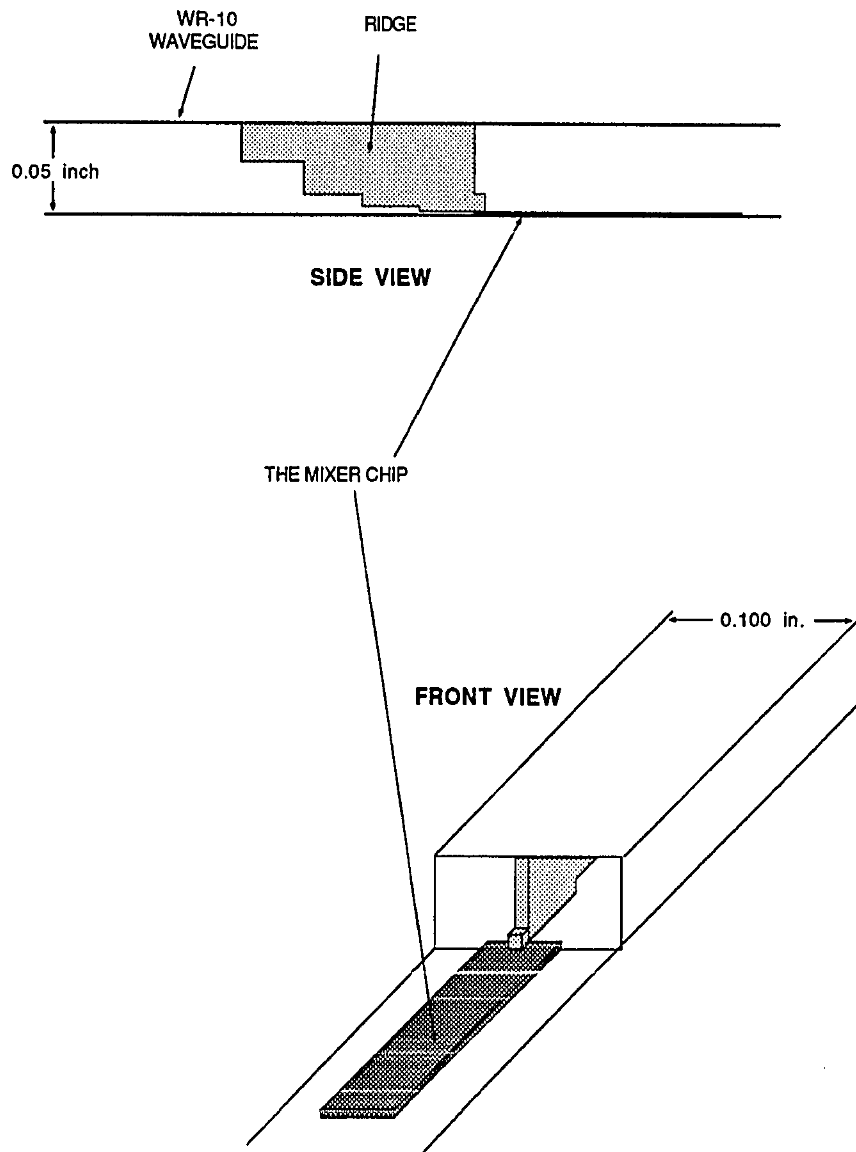

Fig. 5-1 The side view and front view of the ridge to chip coupling (not to exact scale). The chip size is 1mm x 4 mm x 50 μm.

A unique feature of this hot/cold load was that the vane could be removed from the waveguide while at cryogenic temperatures. The vane was mounted on a insulating arm which could be removed or inserted into the waveguide using two solenoids. When the vane was removed, the waveguide was terminated at the bath temperature. The vane itself could be heated to as high as 70 K.

The hot/cold blackbody source is obviously not representative of a line source. A blackbody source is a valid signal source for determining the receiver response as long as the bandwidth is limited and higher harmonic effects are not influencing the receiver results. The blackbody source acts as a continuum of line sources over the bandwidth B. For constructing a "real" receiver for radioastronomical observatories, the hot/cold load could be removed. The signal input port of the mixer block would then be connected to a waveguide which would lead to another window (or horn input) in the dewar through which a signal would be coupled. This has not been done at the time of this writing.

5.1.3 The Device

The previous chapter described the SIS device used in this receiver in detail, but in order to understand the receiver system, the role the device circuitry plays in the *rf* to IF conversion is described here. A drawing of one of the devices studied, a blow-up of the junction area, and the electrical equivalent circuit are shown in Fig. 5-2. The Chebyshev ridge coupled the radiation in the device through a microstripline at point A in (a). The tunnel junction is between points B and C. Since it is desirable to have the input *rf* radiation terminate at the location of the junction itself, the right side of the junction is terminated by a 90° radial stub [Vinding, 1967; Syrett, 1980; Atwater, 1983]. The radial stub acts like an open-circuited quarter wave microstripline. It provides a broadband *rf* ground at a point close to its apex (point C). In addition, the stub is an open circuit for the dc bias of the junction and for the IF signal [Winkler et al., 1989].

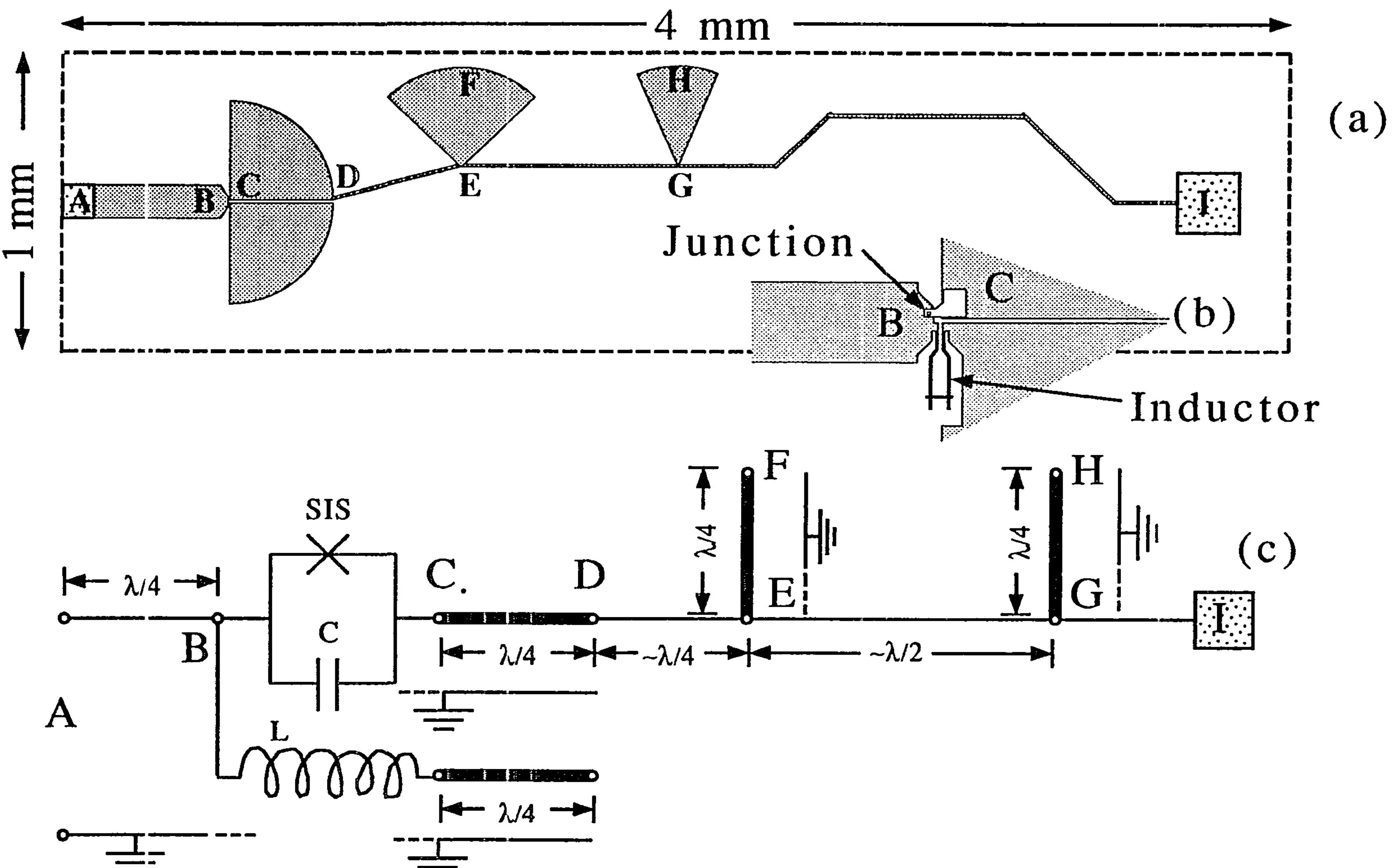

Fig. 5-2 a) Top view of the device. b) Blow-up of the device area. c) The electrical equivalent circuit.

Shown in Fig. 5-2b is an inductor in parallel with the tunnel junction. The purpose of this inductor was to tune out the capacitance of the tunnel junction at the operation frequency; in this case it was designed to resonate the junction capacitance at 100 GHz. The resonance condition is

$$\omega^2 = \frac{1}{LC} \quad \text{5-3}$$

where C is the geometric capacitance of the tunnel junction and L is the inductance of the microstripline inductor. The proper length of the microstripline inductor is given by Termin (1943) where the inductance is in nH, the width w, length l_o, and thickness t are all in mm,

$$L = 0.2\, l_o \{\ln[\, l_o/(w + t)] + 1.193 + 0.2235\, (w + t)/l_o\} \quad \text{5-4}$$

The mixer results are inconclusive regarding whether this was the proper design layout and length. This formula disregards magnetic inductance and the effect of a geometric inductance between the two legs of the inductive loop. Ugras (1991) has determined by modeling the inductor using Touchstone[5] that the geometric inductance effects are substantial (~ 20 % of total inductance) especially where the lines are close together near the junction. Subsequent chip designs will eliminate this problem.

The inductor itself was terminated by a 90° radial stub. By using the 90° radial stubs, the two branches, the junction branch and the inductor branch, were dc isolated from each other. In this design, the inductor branch could be replaced by a Josephson [Wan et al, 1989], soliton [Pagano, et al, 1989] or flux-flow [Nagatsuma et al. 1983] oscillator which could provide an on chip LO without interfering with the dc or IF system.

---

[5]EEsof, Westlake Village, CA

The mixer is a frequency down converter. The two signals which come in through the microstripline (LO and signal) are down converted to the IF. The IF frequency, typically 1.5 GHz left the chip through a low-pass filter. This filter, D-I in Fig. 5-2a, was composed of narrow sections (10 μm lines) and large sections (1/4 wave radial stubs). It is analogous to a standard *rf* choke structure where the thin lines are the inductors and the stubs are capacitors. The circuit way of looking at it is shown in Fig. 5-2b. Since the end of the 90° radial stub is an open circuit, the quarter wavelength line connected to it transforms this open circuit to a short circuit. At this short circuit location, there is another radial stub. The electrical dimensions of this stub reinforce the short circuit. Similarly, the rest of the choke structure is made up of quarter and half wavelength sections. All of this serves to keep the *rf* signal from leaking out this line, while having little effect upon the IF signal.

5.1.4 Scale Modeling and Embedding Admittance

The dimensions of the on-chip circuitry were determined by Winkler et al. (1989) who build a scale model at 28.4 times larger dimensions. The capacitance of the tunnel junction was modeled by a chip capacitor of 1 pF and the inductor was modeled by a wire inductor. The purpose of the scale modeling is to try out ideas and characterize the design of the mixer mount and chip at a frequency for which analysis electronics are available. In addition, the sizes are larger and easier to work with. The scale modeling included the ridge and chip design. The scale model design was to provide an embedding admittance to the junction which was 50 Ω real. Since the mixer design contains no variable tuning elements, it was important that the embedding admittance remain close to this value throughout the frequency band. The results showed that the voltage standing wave ratio (VSWR) was less than 1.8:1 for the scale model chip with the capacitor and inductor over the scaled frequency range 75-110 GHz. The ridge and microstrip together gave a maximum VSWR of less than 2.1:1 for the scaled frequency range 74.6 - 107 GHz.

5.1.5 The IF System

Fig. 5-3 shows a schematic of the entire receiver. The IF systems consisted of all of the post device components. The IF signal was propagated through UT-085 semi-rigid coaxial cable. The IF signal exited the chip at point I in Fig. 5-2a. The chip was contacted to an off chip bias T via a pressed indium contact. The bias T, composed of a chip capacitor of capacitance 62 pF and a wire inductor in parallel, allowed the IF signal to exit through the chip capacitor, while not exiting through the wire inductor. The inductor was used for the dc bias discussed in the next section. Once through the bias T, the IF signal entered an cold IF coaxial switch,[6] specially modified at the National Radio Astronomy Observatory to avoid electrical transients which can destroy the device. The positions on the switch were: a load at the bath temperature, a variable temperature load, a ground, and passthrough. The first three positions were used in calibrating the noise component of the entire IF signal path and will be described in section 5.2.6. For use as a receiver, the switch was in the position shown in Fig. 5-3.

After passing through the IF switch, the IF signal entered a circulator[7] and a directional coupler.[8] The purpose of the circulator was to allow for a test signal to be input to the IF system to measure the IF mismatch of the mixer. The test input signal was at room temperature and entered the circulator through a 20 dB attenuator. If instead of the 20 dB attenuator at the input circulator port we had a 50 Ω termination, the circulator would be an isolator. The circulator also served to minimize the standing wave from the mismatch between the mixer output impedance and the amplifier input impedance. The directional

---

[6]Model M6-413C901S, Dynatech Microwave Technology, Calabasas, CA. Dr. A.R. Kerr of the National Radio Astronomy Observatory was very helpful in modifying this switch.

[7]Model LTE 1241K, Pamtech Inc., Camarillo, CA

[8]Model 16179, Omni Spectra Inc., Merrimack, NH

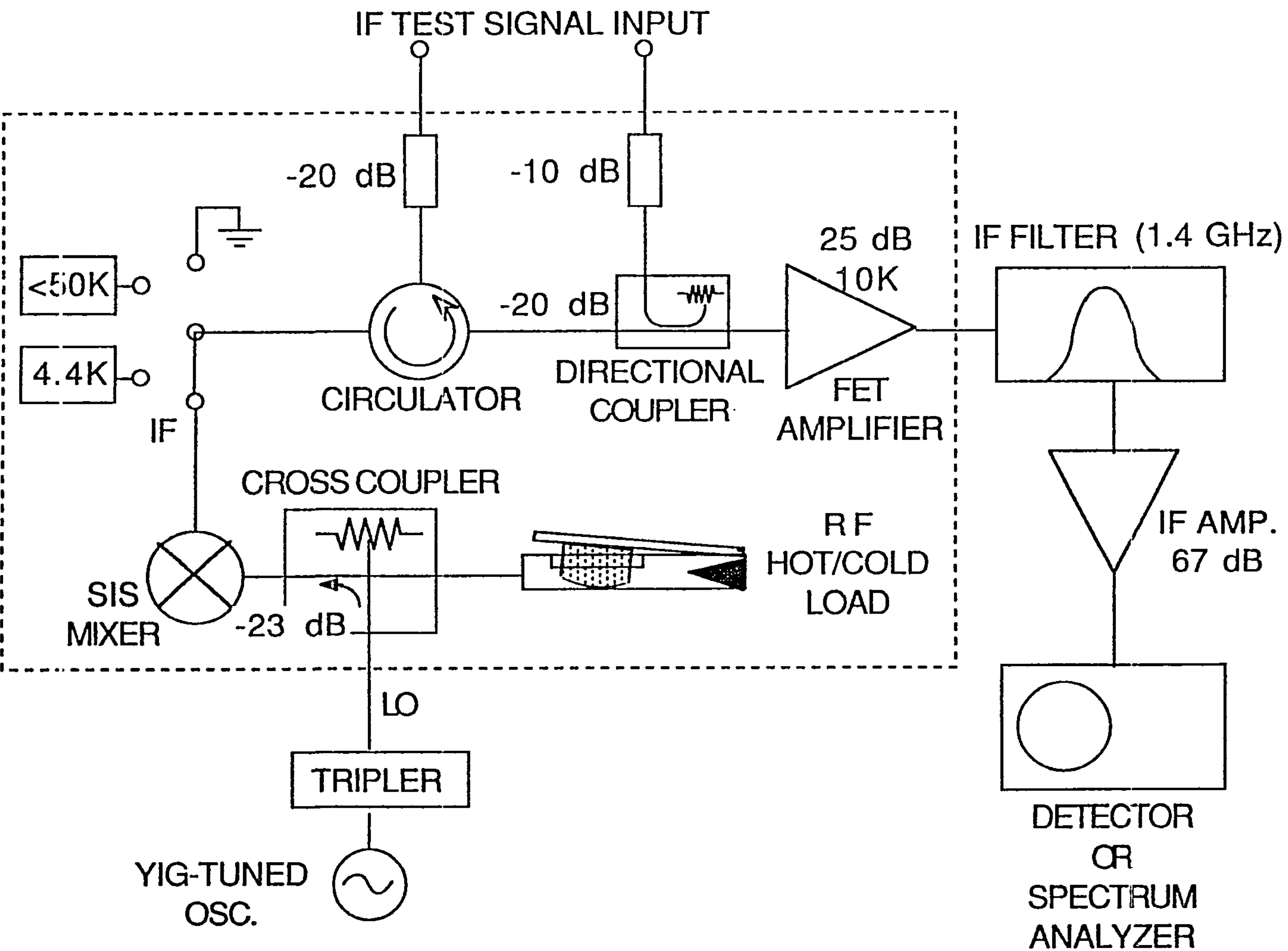

Fig. 5-3 Receiver schematic. The dewar is indicated by the dashed line.

coupler allowed a signal from room temperature to be input to the IF system. This signal was attenuated by 30 dB. Use of this input signal allowed determination of the FET contribution to the receiver gain. Knowledge of the FET gain contribution allows one to determine the contribution to the receiver gain due to the mixer itself. Tests to determine the noise temperature using this method have not yet been performed.

The final cold element through which the IF signal passed was an FET amplifier.[9] The FET amplifier operated at 1.4-1.6 GHz. Once out of the amplifier, the IF signal exited the dewar through a coaxial line. Typically, this signal was filtered at room temperature through a bandpass, amplified by 67 dB using MITEQ amplifiers,[10] and detected with an Anritsu power meter.[11] Additional attenuators were sometimes used in the IF path at room temperature in order to give the proper power level to the amplifiers and the diode detector. The dynamic range of the output signal was limited by the sensitivity of the Anritsu to be greater than 10 μW and limited by the saturation of the MITEQ amplifiers to be less than 200 μW. All of the elements internal to the dewar described in the IF section were well heat sunk to the cold plate, except the IF hot/cold load.

5.1.6 DC Biasing and Heat Sinking

The junction was dc biased between points I and A in Fig. 5-2a. At point A, the ridge connection to the junction served as the dc ground. At point I, the dc bias line was through the inductor in the bias T. The dc biasing wires, as well as all wiring coming into the dewar (thermometers, heaters, solinoid controllers) were heat sunk to the nitrogen shield and the helium cold plate with GE 7031 varnish. The dc bias supply was built and designed by N.G. Ugras. The junction bias could be shorted at room temperature using a

---

[9]Built by Dr. Neal Erickson, Dept. of Physics and Astronomy, University of Mass.

[10]Model AFD3-0102-13-ST, MITEQ, Inc., Hauppauge, NY

[11]Model ML4803A with MA4002B power head, Anritsu Corp., Tokyo, 106 Japan

0-20 kΩ potentiometer, in order to avoid transient pick up which could (and have) shorted (destroyed) junctions while turning on and off equipment.

All components entering the dewar were heat sunk or contained thermal breaks to limit the room temperature leakage to the cold plate. The waveguide LO input contained a 5" section of stainless steel waveguide. The IF semirigid coaxial lines contained stainless steel thermal breaks on the inner conductors. In addition, EMI filters[12] were used on the input wires to reduce noise pickup.

5.2 Measurement

In a typical mixer experiment, the data taken for each frequency determined the pumped I-V (the dc I-V trace in the presence of radiation) and the bias point which give the best receiver noise temperature and gain. The receiver noise temperature is the figure of merit most often compared between groups. The work presented in this chapter uses an internal hot/cold load and is not directly comparable to those receivers which couple the signal from outside the dewar. The external components always add noise. Even a low noise temperature for these components can be as large 25 K (horn-waveguide-window) in the 100 GHz frequency range [Pan et al., 1989]. This contribution is largely unavoidable in radioastronomical receivers since astronomical signals are outside the dewar.

A comparison of mixer noise temperatures between groups is perhaps even more contentious than receiver noise temperatures since it always involves sorting out noise contribution from other elements in the system and eventually determining the contribution from the mixer alone. In addition, the multiple definitions of the mixer noise temperature (or mixer noise power!) makes comparisons more difficult.

---

[12]Erie Products, Inc., Trenton, Ontario, Canada

5.2.1 Selecting Devices

Candidate devices were first tested at room temperature. This was done in a very simple dipstick which used copper-berillium clips to contact the gold pads on the device. The 2-point device resistance was then measured at room temperature. The devices were either seen to be short circuits at room temperature giving a the resistance of $\approx 240\ \Omega$ corresponding to the normal resistance of the niobium leads, open circuits, or neither. The devices which showed neither open nor short characteristics at room temperature have in ALL cases shown tunneling I-V curves at 4.2K when they were screened further using the simple dipstick.

5.2.2 Sample Mounting

An advantage of the mixer block design was the relative ease with which a chip could be mounted. Since the mixer block itself served as the dc ground, there were no independent dc bias lines needed on the ridge side. The connection to the ridge (point A in Fig. 5-2a, see also Fig. 5-1 and 5-4) was made by first unscrewing the top plate of the waveguide; this top plate includes the ridge. This section was placed under the stereo microscope. Indium was gently pressed to the last section of the ridge with a teflon coated wooden Q tip. The edges of the indium which hung over the ridge were cut off at the corners of the ridge. After partially screwing the top plate/ridge section back together with the waveguide, the gold contact pad on the microstripline of the chip is inserted under the ridge section. Placing the chip was relatively easy with the use of dental tools. After placing the chip, the top/plate ridge was screwed in to make contact to the gold pad. The IF output/dc input contact was made by pressing an indium blob on one side to the gold contact pad of the chip and on the other side to the input of the bias T as shown in Fig. 5-4.

The chip design also included a Josephson/quasiparticle set of tuning junctions in many of the chips (Chapter VII discusses the application of these). These junctions were biased through a large gold contact pad at point J in Fig. 5-4. The contact was made with a

(a) SIDE VIEW OF MOUNT

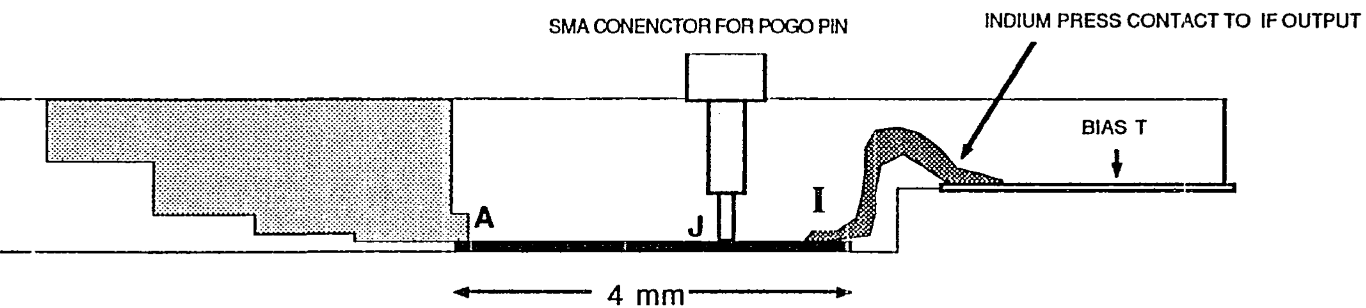

(b) TOP VIEW OF CHIP

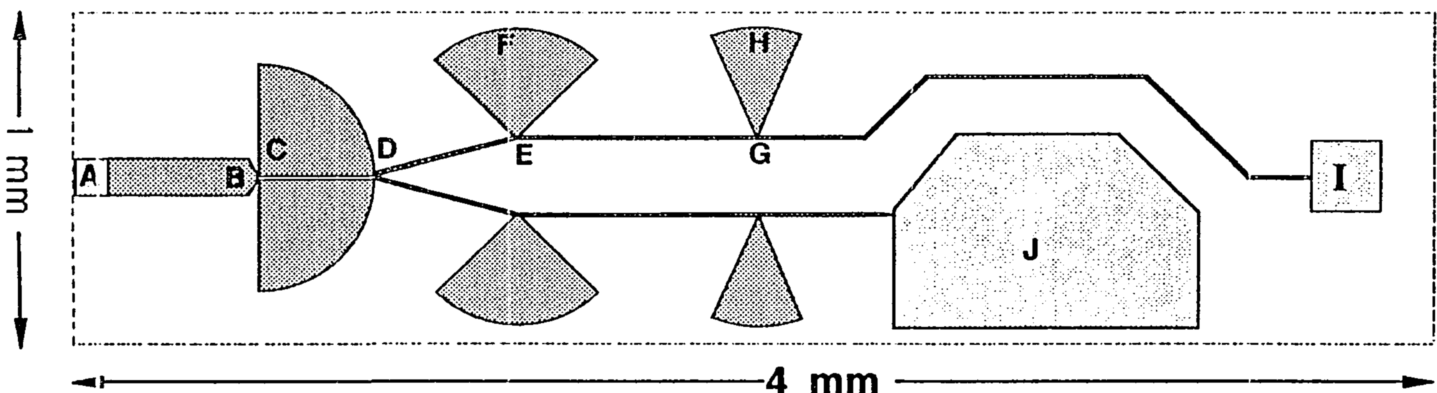

Fig. 5-4 a) Side view of the chip mounting showing the ridge contact at left and the Indium press contact at right. b) The top view of a chip with an electrically tuned inductor.

Pogo pin,[13] inserted in the waveguide shield covering the junction, Fig. 5-4a. Although not all devices had this tuning structure, the pogo pin was part of the mixer block at all times and it pressed the chip flat against the bottom of the mixer mount in which it sat. This eliminated the need to bond the back side metal of the chip (gold) to the bottom of the mixer block. As a test of the reproducibility of the mounting procedure, device E was removed and remounted. The mixing properties of device E were the same for both mountings.

After mounting the chip and replacing the shield containing the Pogo pin, the device resistance was monitored as it and the mixer block were cooled to 77K in liquid nitrogen. This further screening was necessary since the indium press contacts could become undone, particularly on the ridge side where care was taken not to tighten the ridge too much, to avoid breaking the junction or distorting the ridge. The device resistance was measured with a Fluke[14] multimeter on the 1000 Ω manual scale. Surprisingly, no devices were lost by testing them in this simple way. This contacting test at 77 K was roughly 75% reliable in predicting whether the device would remain contacted at 4.2K in the receiver. Of course, those that failed this test were remounted.

Before developing the technique of contacting the ridge using indium, silver paint[15] was used. The silver paint was applied to the gold contacting pad on the microstripline. When it dried, the ridge was secured to make contact. After some initial breakage losses, the indium method was developed since indium is a softer material than dried silver paint. The softness of the indium allowed for good electrical contact to the ridge without excessive tightening. In addition, pressed indium is easily removed.

---

[13]Pylon Company, Inc., Attleboro, MA

[14]John Fluke MFG Co., Inc., Everett, WA

[15]Micro-circuits Company, New Buffalo, MI

5.2.3 Cooling the Dewar

The vacuum space between the outer wall and the nitrogen space and between the nitrogen and helium spaces in the dewar was usually pumped overnight with a diffusion pump ($p \approx 10^{-5}$ Torr) or a mechanical pump ($p \approx 10^{-2}$ Torr). The diffusion pumping allowed for longer hold times in regular operation; typically an additional 1 hour was gained. After overnight pumpdown, the LHe and LN_2 spaces were filled with LN_2. The LN_2 section was kept filled throughout the entire duration of the experiment. The temperature of the cold plate was monitored. When it reached 80 K, the LN_2 was removed from the LHe dewar, and helium was transfered into the LHe dewar. It typically took 8 liters of LHe to both cool the thermal mass connected to the cold plate and fill the 4 liter dewar.

5.2.4 Finding the Optimum LO Power and DC Bias

Since the receiver had no mechanical tuning elements, the optimum LO power (which along with the dc bias voltage constituted all of the tuning elements in this receiver) was reasonably easy to find. At a constant LO frequency, the *rf* hot/cold load was heated and held constant at ≈ 30K and inserted into the signal input waveguide. For a constant frequency, the LO input power was then changed using the room temperature attenuator. For each LO power level, the dc bias was changed and the IF output power was measured with the Anritsu power meter both with the hot/cold load in the waveguide (giving P_{IFH} at temperature T_H) and out of the waveguide (giving P_{IFC} at temperature T_C). The IF output power as a function of the dc bias voltage for the hot and cold load temperatures is shown for device B at 100 GHz in Fig. 5-5. The ratio of the "hot" to the "cold" output power gives the Y factor which relates to the the receiver noise temperature, T_R as

$$Y = \frac{P_{IFH}}{P_{IFC}} = \frac{T_R + T_H}{T_R + T_C} \qquad 5\text{-}5$$

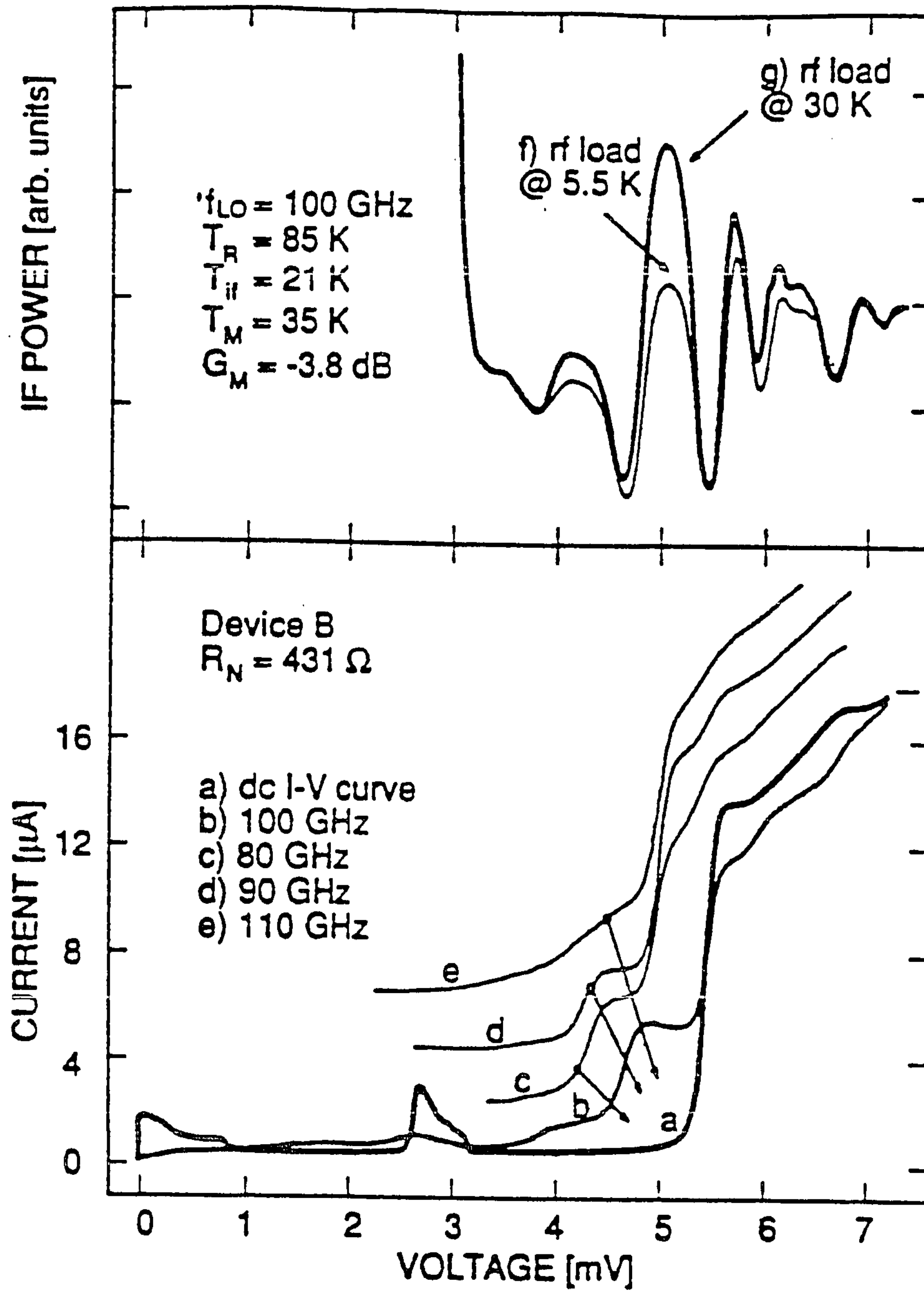

Fig. 5-5 Current and IF power vs. voltage characteristics of device B. Curves c-e have been offset as indicated by arrows.

where T_R is the receiver noise temperature. The dc bias and LO input power which gave the largest Y value were then held constant in order to determine the receiver noise temperature and gain for this frequency.

5.2.5 Measurement of Receiver Noise Temperature and Gain

Since the terminations at the cold temperature and the hot vane temperature were not known to be the same, once the proper input LO power and dc bias voltage were found, the vane was inserted and left in the waveguide. While it was cooling, data were taken which measured the output IF power vs. the vane temperature. A typical data run (Device E at 80 GHz) is shown in Fig. 5-6. The output power is given by

$$P_{out} = Gain\ (P_{in} + P_{noise}) \approx kB\,Gain\ (T_{in} + T_{noise}) \qquad 5\text{-}6$$

with a hot/cold load temperature T_{in}. The intercept point on the temperature axis gives the receiver noise temperature, $T_{noise} = T_R$. The approximation comes from the fact that the power is not linear with the temperature, but instead follows the Planck blackbody law. The receiver gain is determined by the slope of the curve in Fig. 5-6. The slope is approximately kG_RB.

5.2.6 Measurement of the IF Noise Temperature

The IF switch allowed one to determine the noise and gain contribution of everything from the switch onward. This noise is characterized by the IF noise temperature. The main noise contribution in the IF system came from the cold FET amplifier. In this work, a typical IF noise temperature was 12 K. If a HEMT amplifier had been used, the IF noise contribution could have been as low as 2 K. The IF noise temperature and gain measurement were made in a similar way as the receiver noise and gain measurement. A variable IF hot/cold load, [McGrath et al., 1985] was heated and

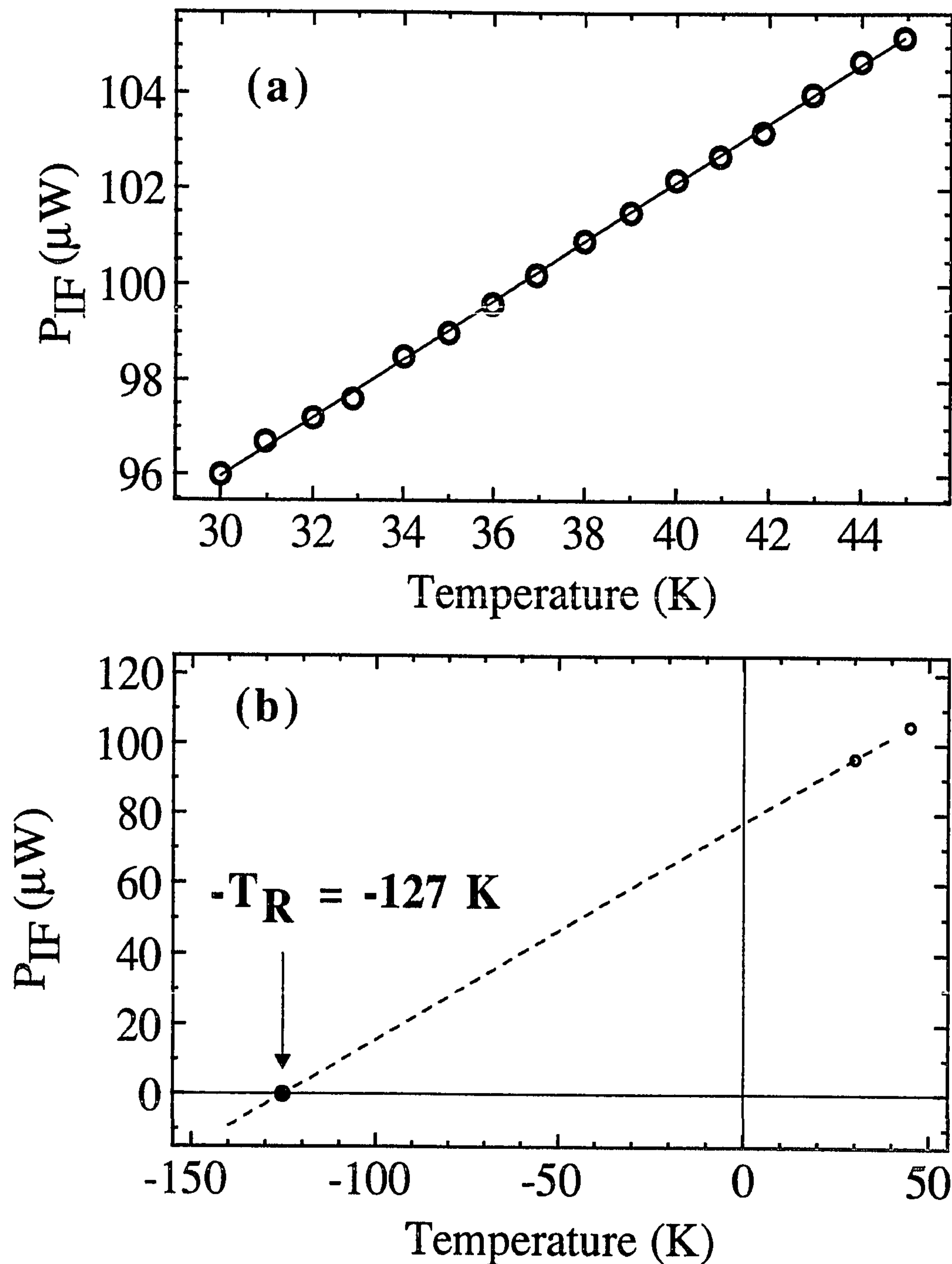

Fig. 5-6 IF output power vs input blackbody temperature of device E at 80 GHz. a) The open circles are the experimental data, the solid line is a linear fit. b) The intersection of the linear fit with the temperature axis gives the noise temperature. Only the highest and lowest temperature experimental data are shown.

cooled while measuring the IF output power. The IF switch was of course switched to the IF hot/cold load. The output power vs. IF hot/cold load temperature gave the IF system gain and the IF system noise, using eq. 5-6 with T_{in} given by the temperature of the IF hot/cold load and T_{noise} the IF noise temperature T_{IF}.

5.2.6 Determination of the IF Mismatch

The IF mismatch was determined by injecting a monochromatic signal at the IF frequency from a crystal oscillator[16] into the circulator port. The output power vs. input power from the reflection from a short circuit and from the mixer were compared in order to determine the IF mismatch. An experimental plot for device E at 80 GHz is shown in Fig. 5-7. The slope of each line is simply $G \rho^2$ where G is the gain of the amplifiers and ρ is the amplitude reflection coefficient. Since the short circuit reflection coefficient is ρ=1, the ratio of the two slopes gives $\rho_m{}^2$. Any attenuation in the coaxial lines simply folds into the gain. The lines in Fig. 5-7 cross each other since extra attenuation was added during the short circuit measurement in order to remain in the dynamic range of the Anritsu power meter. In addition to this measurement, it was determined that the reflections from the IF hot/cold load itself were negligible.

5.3 Experimental Results

The parameter space over which the LO power, frequency, and dc bias point needed to be changed in order to optimize the receiver results was large. Much of the mixer data was taken with the aid of an HP-9153.[17] Since much of the computer assisted data taking equipment was not implemented during the early investigations of the receiver and devices (March, 1990 - June, 1990), the results of devices measured prior to this time are

---

[16]HP8350B with 83525B RF plug in, Hewlett Packard, Palo Alto, CA

[17]Hewlett Packard, Palo Alto, CA

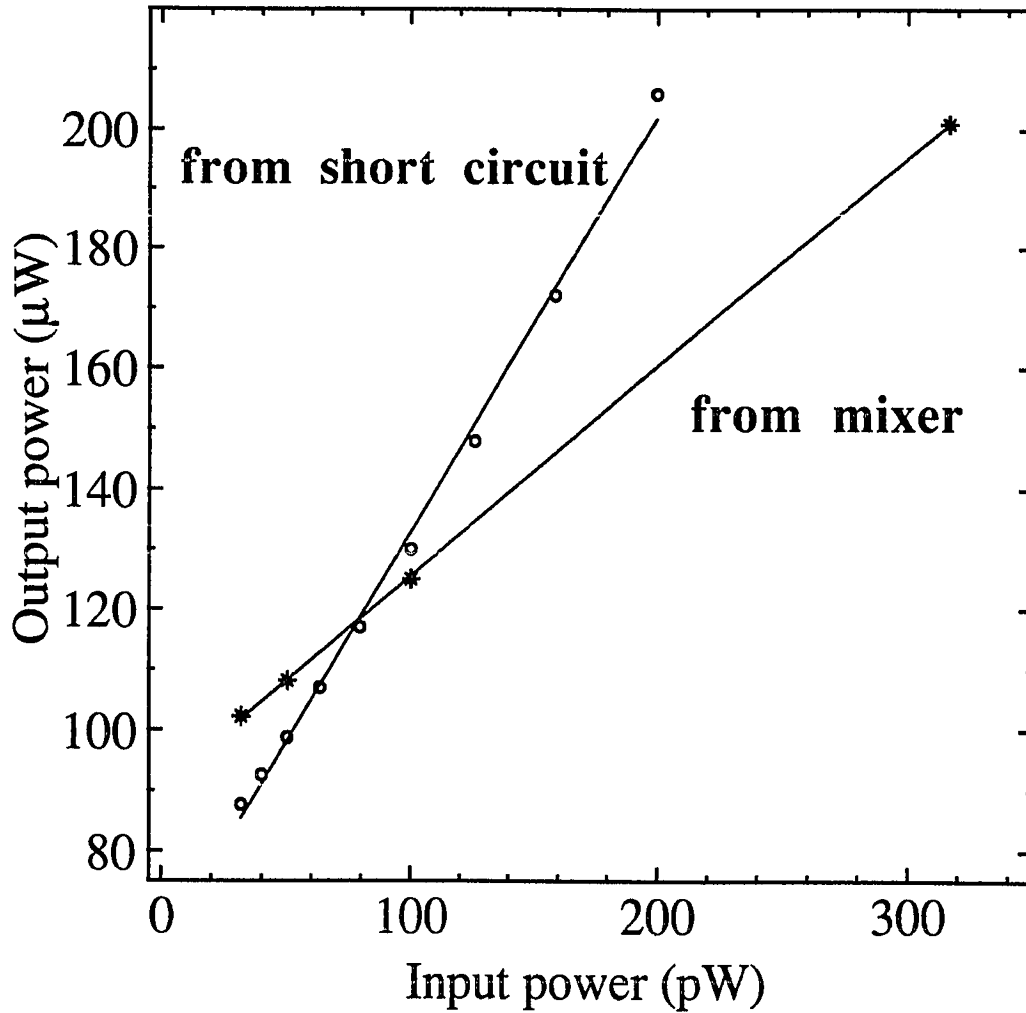

Fig. 5-7 The output power at the IF vs. the input power at the circulator for device E at 80 GHz. The lines are linear fits to the experimental data. The ratio of the slopes of the two lines gives the reflection coefficient, ρ_m^2.

not presented in great detail. The results and analysis presented in this section are largely for two devices, one of which, device I, was a four junction array of 0.5 $(\mu m)^2$ junctions without an on chip tuning inductor, and one of which, device E, was a four junction array of 2 $(\mu m)^2$ devices with an on chip tuning inductor. The unpumped and pumped I-V's for device E are shown in Fig. 5-8. The I-V's for device I are shown in Fig. 5-9. Conclusions regarding the receiver are drawn from the results of these two devices as well as others.

5.3.1 Corrections to the Simple Mixer Noise Formula

By taking into account the contribution from a variety of noise sources, the IF output power in the presence of an input of spectral density S_1 can be expressed as [Mears et al., 1991a]

$$P_{IF} = GB_{IF}\left\{S_{IF} + \rho_m{}^2 S_B + G_m(1 - \rho_m{}^2)\left[S_m + S_{LO} + \alpha S_B + (1-\alpha)S_1\right]\right\} \qquad 5\text{-}7$$

where G is the gain of all of the amplifiers in the system following the mixer, G_m is the *available* gain of the mixer, S_m, S_{LO}, and S_B are the spectral densities of the noise added by the mixer, room temperature noise leaking down the LO waveguide, and the helium bath respectively. α is the power loss between the *rf* hot/cold load and the mixer, and ρ_m is the magnitude of the IF reflection from the mixer due to the admittance mismatch. The equivalent noise circuit is shown in Fig. 5-10. The contribution from the bath noise (S_B) at the signal input is due to the resistive loss in the waveguide between the hot/cold load and the mixer input. All noise temperatures (powers, spectral densities) are referred to the signal input at the mixer, therefore this resistive loss needs to be corrected for when determining the noise temperatures and gains. The bath temperature contribution at the IF

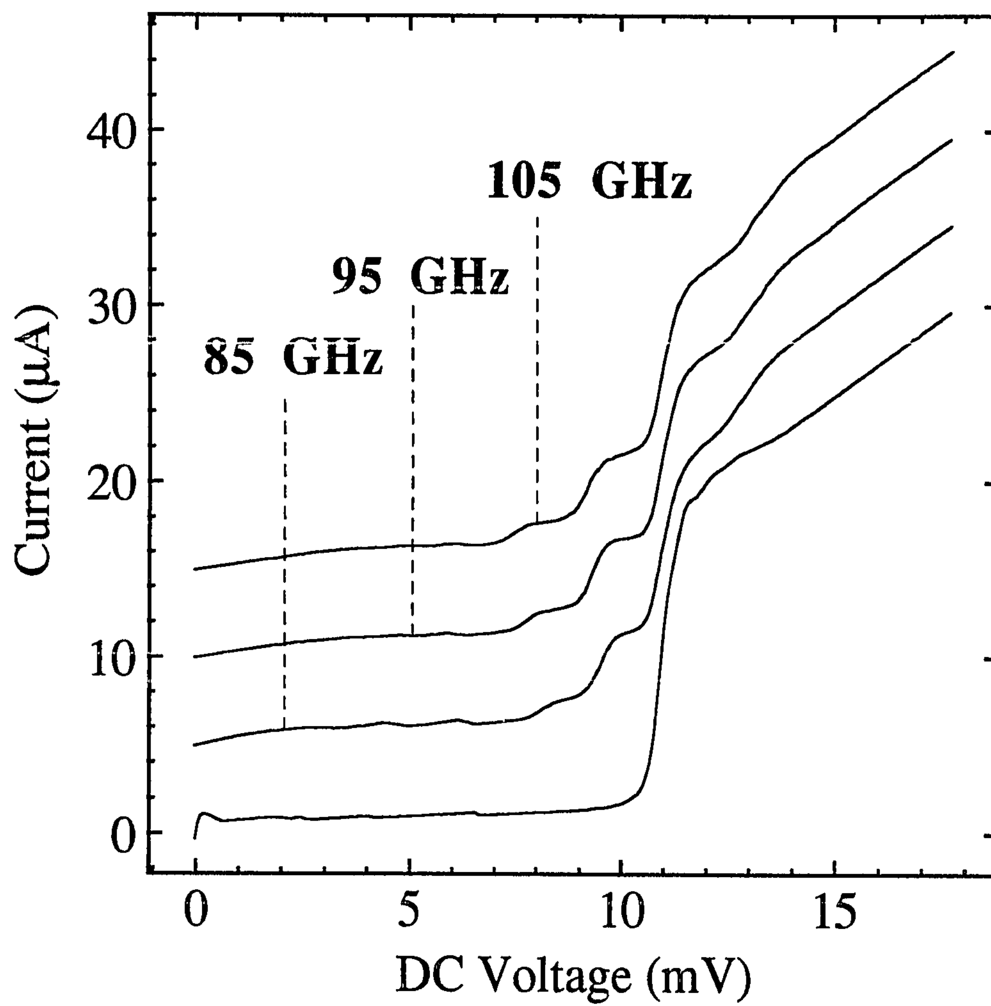

Fig. 5-8 Unpumped and pumped I-V's for device E. The data are offset by 5 μA for clarity.

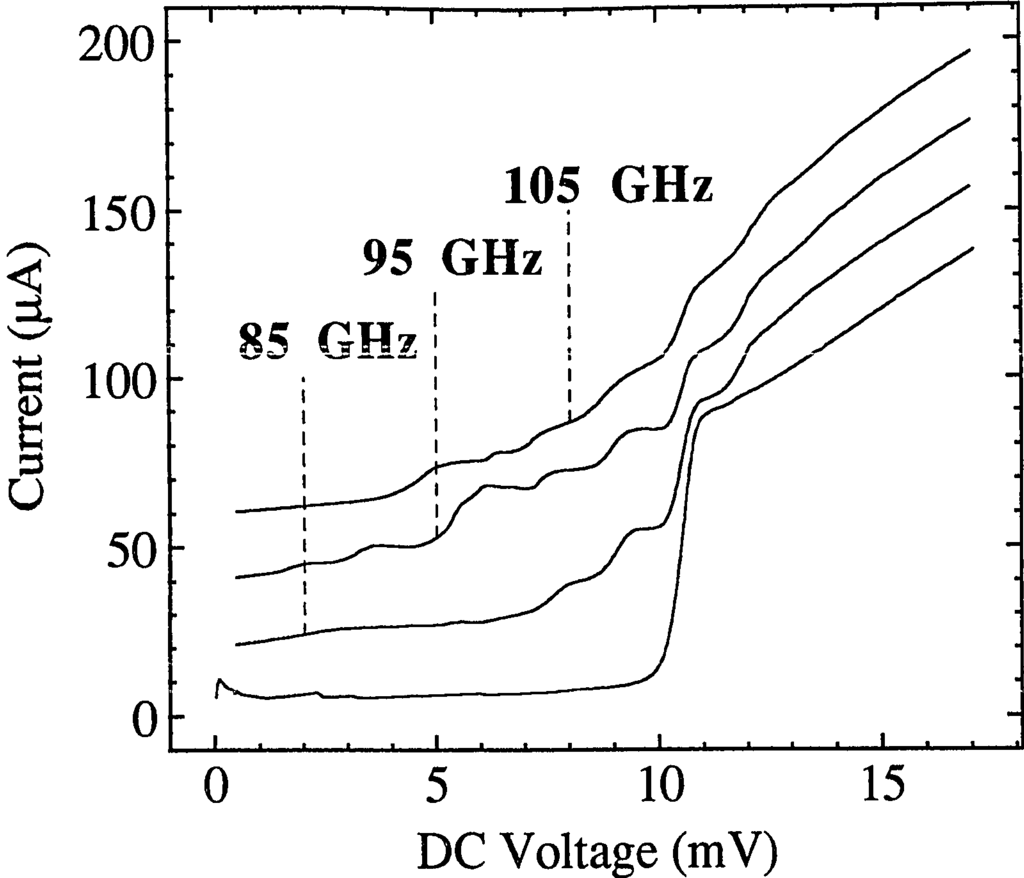

Fig. 5-9 Unpumped and pumped I-V's for device I. The data are offset by 20 μA for clarity.

amplifier input comes from reflection of the cold blackbody radiation of the circulator input port off of the mixer (see Fig. 5.3).

A simple approximation for the receiver noise temperature is sometimes given as

$$T_R = T_m' + \frac{T_{IF}}{G_m^{C'}} \quad 5\text{-}8$$

where the primes are included to indicate that the values in this formula are only approximate. This equation assumes that the added noise terms due to the loss between the hot/cold load and the mixer, the loss term added for room temperature leakage, and the loss added for the bath temperature itself are not important (i.e., $\alpha = 0$, $S_B = S_{LO} = 0$). With these assumptions, and converting the spectral densities to temperature with $S = kT$, eq. 5-7 simplifies to

$$P_{IF} = kGB_{IF} \left[T_{IF} + G_m^{C'} (T_{m'} + T_1) \right] \quad 5\text{-}9$$

where G_m^C is the approximate coupled gain of the mixer. The corrections to the mixer gain and noise obtained using the simple equation can then be expressed as

$$G_m^{C'} = G_m^C (1 - \alpha) \quad 5\text{-}10$$

$$T_m' = \frac{1}{1 - \alpha} \left\{ T_m + T_{LO} + \alpha T_B + \frac{\rho_m^2 T_B}{G_m^C} \right\} \quad 5\text{-}11$$

We see that the coupled gain determined by ignoring loss between the hot/cold load and the mixer signal input is in fact *smaller* that the gain determined by including this loss. The

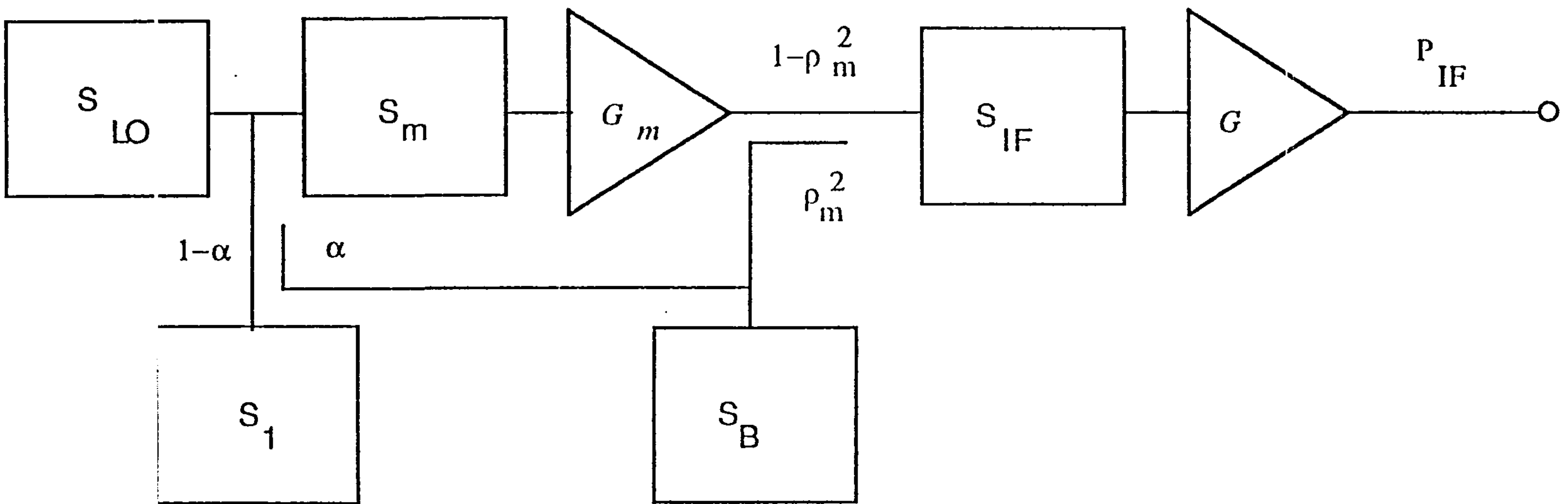

Fig. 5-10 The noise equivalent circuit for the receiver. The noise sources are given as spectral densities, S.

mixer noise determined by using the simple method is *larger* than that determined by adding the correction factors. This is easy to see since α , T_B, T_{LO}, ρ_m, $G_m{}^C > 0$. Since the mixer gain should be maximized and the mixer noise temperature minimized for optimal performance, the simple equations can be seen to be either slightly or significantly pessimistic about the performance of the mixer. In order to compare our results to those predicted by the quantum theory of mixing, we have estimated values for the correction factors. Note that there are no corrections to the receiver noise temperature since it includes all of these effects. The approximate values of the corrections factors in this work are: $\alpha <$ 0.05 (estimate based on attenuation in the waveguide and the length between the hot/cold load and the mixer block), $T_B = 4.4$ K, and $T_{LO} = 1.1 \pm 0.2$ K. The room temperature leakage is minimized by heatsinking the waveguide and coupling the LO through a 23 dB cross coupler. The calculation of the noise temperature leaking down the waveguide follows the derivation by McGrath (1985) and assumes a uniform temperature distribution from 298 K down to 4.4 K along the waveguide. This itself is pessimistic since the approximate lengths of the the waveguide are 6" at room temperature, 7" at $\approx$ LN_2 temperature , and $\approx$ 8" at 4.4 K. The dominant correction to the mixer noise temperature is from the last term in eq. 5-11, which includes the IF mismatch factor and the mixer gain. $\rho_m{}^2$ cannot exceed 1, but the coupled gain can be much less than 1. Mixer IF outputs which are poorly matched to the amplifier can give a large correction to the determined mixer noise temperature, particularly for large loss mixers. The simple equation (5-8) is sometimes used to justify the statement "mixer gain is not an important parameter in determining the overall receiver noise temperature since low noise IF amplifiers are available." This statement is only true for systems where the mixer IF output is well matched to the IF amplifier input, or the operational temperature is small.

The full expression eq. (5-7) for the noise contributions is used in the analysis. Since the community is more comfortable with noise temperatures than with noise powers or noise spectral densities, I have presented all of the results in terms of temperature. In

order to satisfy the requirement that a receiver which is twice as noisy as another has twice the receiver noise temperature, I have used the linear power-temperature relationship throughout. Explicitly, the Planck blackbody formula eqs. (5-2) and (5-7) are used to calculate all results in terms of the spectral density. The results are then presented in temperature using P/B = kT.

5.3.2 DSB vs. SSB

A double side band mixer is one in which the signal and image frequencies are coupled equally. The Yale receiver is double side band since it is a broadband receiver and the coupling does not change significantly for signals which are separated by 3 GHz. The shape of the pumped I-V's are used to determine the embedding admittance at the input frequency. By pumping the junction strongly at the signal frequency and at the image frequency, the shapes can be examined to determine whether the coupling at these two frequencies is the same. Figure 5-11 shows one such determination for device I. For an LO frequency of 90 GHz and a signal frequency of 91.4 GHz, the IF frequency is 1.4 GHz and the image frequency is 88.6 GHz. The shapes of the pumped I-V when strongly pumped at the signal and at the image are similar. The embedding admittance determined for these shapes is at 91.4 GHz: $Y_{S\ emb}$ = (10.02 - i 0.93) mmhos and at 88.6 GHz: $Y_{I\ emb}$ = (11.80 - i 1.18) mmhos. This determination shows that although the embedding admittances are not exactly the same, it is appropriate to use the double side band formula when giving the noise temperature and gain. For a single side band receiver, $Y_{I\ emb}$ is typically very large, giving poor coupling of the image frequency.

The results here for the Yale work are quoted as double side band because the measurement is double side band. To convert to equivalent single side band results, $T_{SSB} = 2T_{DSB}$ and $G_{SSB} = \frac{G_{DSB}}{2}$. The noise temperatures and gains from the sidebands add as

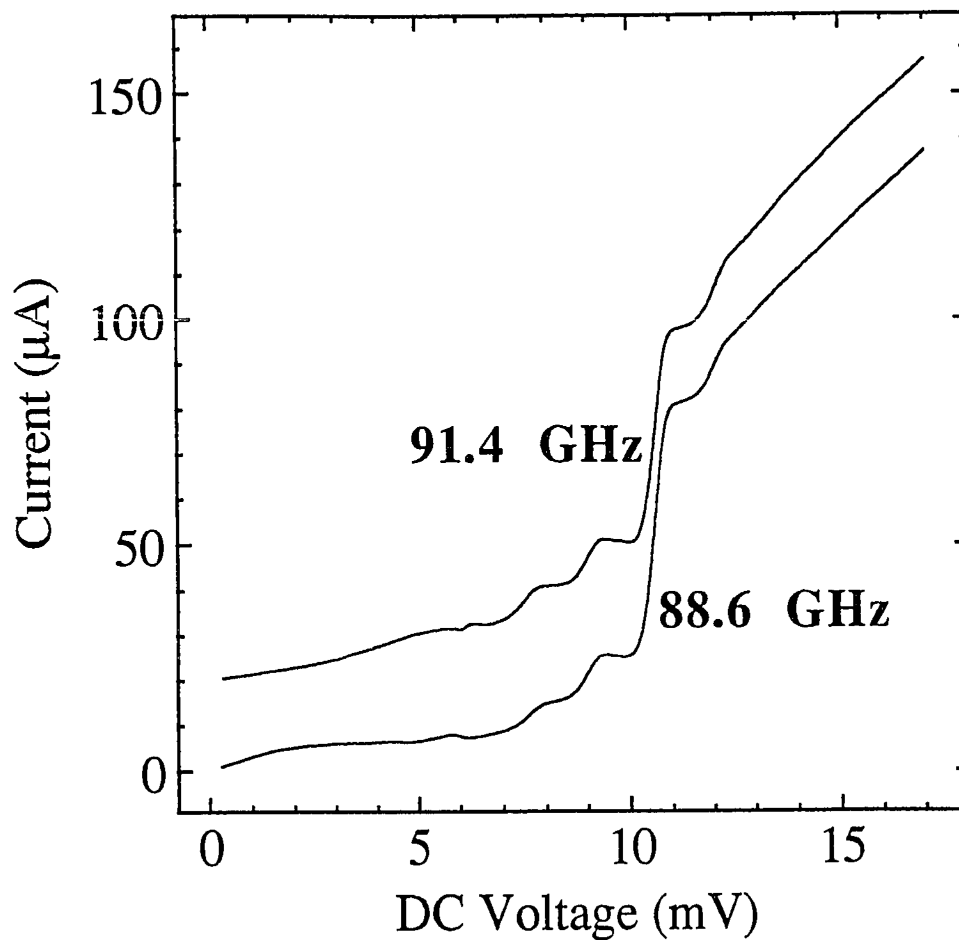

Fig. 5-11 The pumped I-V traces of device E at the upper (USB) and lower (LSB) sidebands of 90 GHz. The determined embedding admittances are (11.80 - i 1.18) mmhos at 88.6 GHz and (10.02 - i 0.93) mmhos at 91.4 GHz. The nearly equivalent shapes of the I-V curves at the LSB and USB indicate that the receiver is DSB. The USB pumped I-V is offset 20 µA. The fitting of the pumped I-V curves to theoretical prediction is discussed in sections 5.4.2 and 5.4.3.

$$\frac{1}{T} = \frac{1}{T_S} + \frac{1}{T_I} \tag{5-12}$$

$$G_S + G_I = G \tag{5-13}$$

5.3.3 Measured Receiver Noise Temperatures

The receiver noise temperatures of five measured devices are shown in Fig. 5-12. The devices were very different from each other. They ranged from a single untuned 0.5 $(\mu m)^2$ device to an array of four $2(\mu m)^2$ devices with inductor tuning. Fig. 5-12 shows that over the frequency range 80-120 GHz, there was a large spread in the receiver noise temperature depending on the device used. The best measured receiver noise temperature was given by device A at 80 GHz; device A also gave the worst measured receiver noise temperature at 100 GHz. Device A was untuned. The results can be intuitively understood only by looking at the various component noises in the system, and the device gains. It should be pointed out that the results shown here for device C are among the best two results reported in this frequency range for a receiver with no adjustable tuning elements. It is also among the best reported worldwide at this time (Fig. 5-13). There is hope for improvement in all of these cases since the IF noise temperature in our system was ~ 12 K. If this can be reduced to 2 K, the receiver noise temperatures will decrease. For example, device I at 90 GHz would see a reduction in the receiver noise temperature from 64 K to 47 K with such an improved IF amplifier.

The receiver results in general showed flat response across the frequency range studied, except for device A. The importance of the achievement of flat response cannot be overstated. Since this was a tunerless mixer receiver, the flat receiver response showed that the *rf* coupling was in fact broadband as designed. If this had not been the case, the

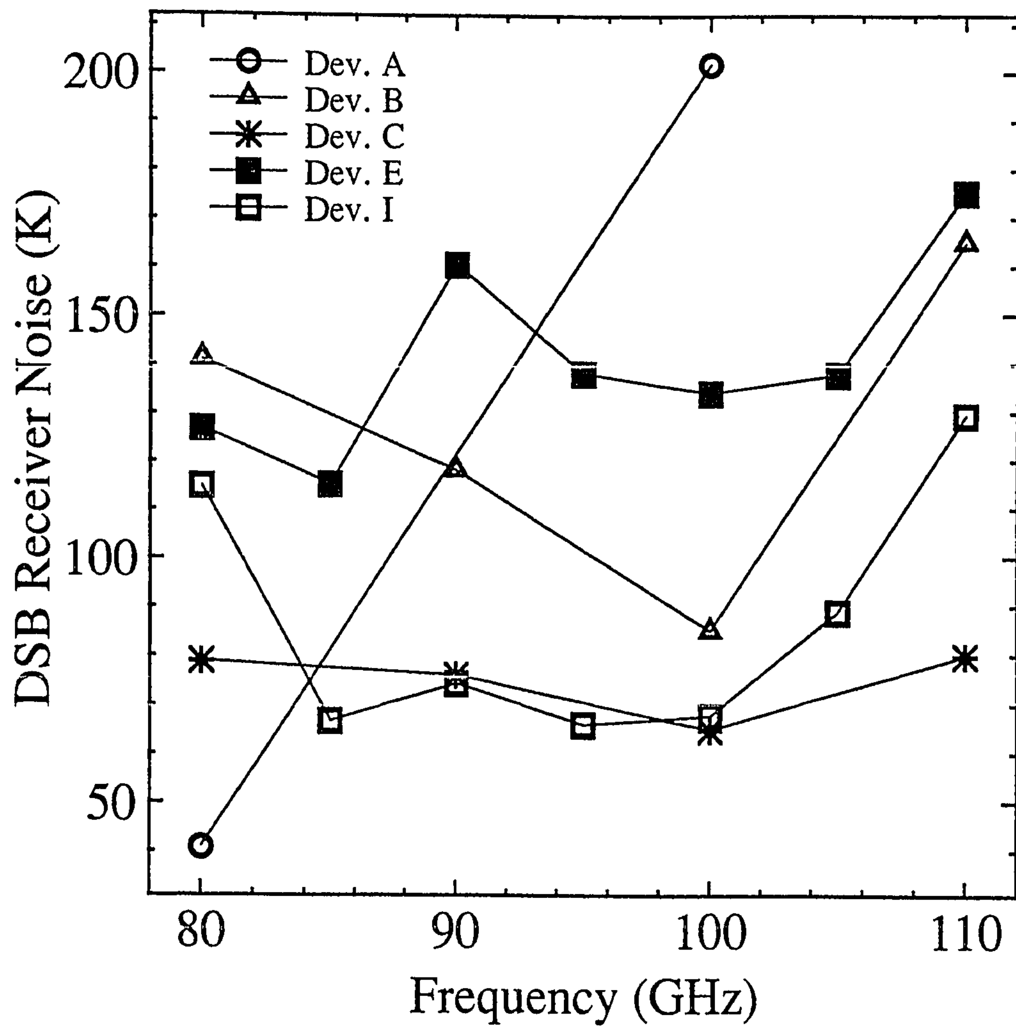

Fig. 5-12 DSB Receiver noise temperature for selected devices.

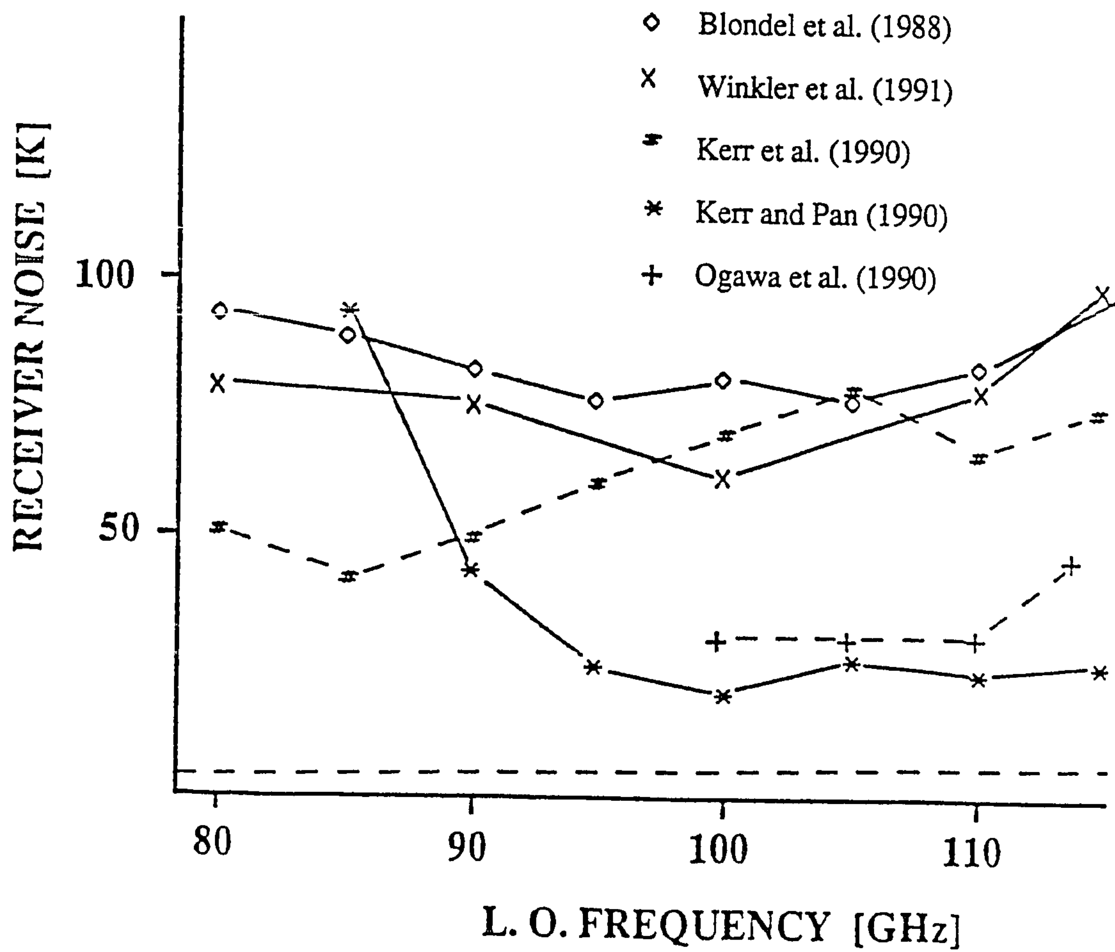

Fig. 5-13 DSB receiver noise temperatures in the 3 mm window. The data for Winkler et al., (1991) is Device C of the previous figure. Of these results, only Winkler et al., (1991) and Kerr et al., (1990) are fixed tuned. From Blundell and Winkler, (1991).

results would be peaked at a certain frequency, and the receiver would be useless as a receiving element for radioastronomy. The flat response allows the radioastronomer to change the frequency of observation without greatly changing the noise characteristics of the receiver.

Device A is a special case. Because there was no inductor tuning to resonate the shunting of the signal by the geometric capacitance, the noise temperature increased dramatically with increased frequency. 80 GHz appears to be close to the optimal frequency for this device. The optimal frequency is determined by the geometric capacitance and the stray capacitances and inductances present in the system. No estimate has been made at this time for the magnitude of the stray effects, but device A showed that in the untuned case, the geometric capacitance dominated as frequency increased. At this time, it is believed that the very good results at 80 GHz were also due to the fact that device A is a single junction and does not suffer from non-uniform junction sizes present in arrays that degrade mixer performance [Feldman].

The other untuned device we measured, device E, confirmed the effect of the geometric capacitance on the degradation of the receiver noise temperatures at high frequencies. This device was a four junction array of 0.5 $(\mu m)^2$ devices. The effective capacitance of the array was 4 times less than that of device A. With the reduced capacitance, the receiver noise temperature generally increased across the band, but not as drastically as that measured for device A. Since the array had a large resistance (619 Ω), the receiver noise temperature suffers from the poor matching at both the *rf* and the IF.

The tuned devices that we measured, B,C and I, showed reasonably flat response across the band. At 110 GHz, above the resonance of the inductor and capacitor, the receiver noise temperature began to increase. Low noise operation at frequencies larger than 110 GHz would probably require shorter inductor lengths which would shift the resonant frequency upward (eq. 5-3).

5.3.4 Mixer Noise Temperatures

As shown in Fig. 5-14a, the measured mixer noise temperature for the untuned devices generally increased with frequency. Fig. 5-14b shows the results of the mixer noise for the inductor tuned devices. In all of the tuned devices, the noise appeared to be a minimum at 100 GHz, near the designed resonance frequency of the inductor and device geometric capacitance. Except for the results of device I at 85 GHz, these curves resemble the parabolic shape one would expect if the mixer noise were strongly correlated to the resonance of the geometric capacitance. The lack of perfect regularity in the shape of the measured noise temperatures vs. frequency is common in receivers (see Fig. 5-13 for examples). In general, this is because of the vast parameter space which must be tested in order to determine the optimum conditions for low receiver noise. In the Yale receiver, the adjustable parameters were the LO power and the dc bias. However, the receiver was broadband so that it should not contain the resonances common in other tuned receivers. The dip in the mixer noise achieved at 85 GHz for device I is not seen as strongly in the receive noise temperature of device I (Fig. 5-12). This point was most likely a fortuitous LO power where the receiver was in fact very close to its best performance. Other data points represent LO powers for which the receiver was near optimum, but not quite.

5.3.5 Mixer Gain

As stated earlier, and seen in eq. 5-7, the mixer gain is an important term in the overall receiver noise temperature. This was particularly true in our case for three reasons: 1) The IF was coupled into a 50 Ω load and used no transformer, thus the coupled gain was in general lower than that which could be achieved with the use of a transformer. 2) The temperature of operation was 4.4 K so the mismatch effect to the coupled gain was important in determining the overall contribution of bath noise from the circulator input port. 3) The IF noise temperature of our FET amplifier was ~ 12 K and the noise contribution from the IF system could be substantial for devices with low gains (eq. 5-7).

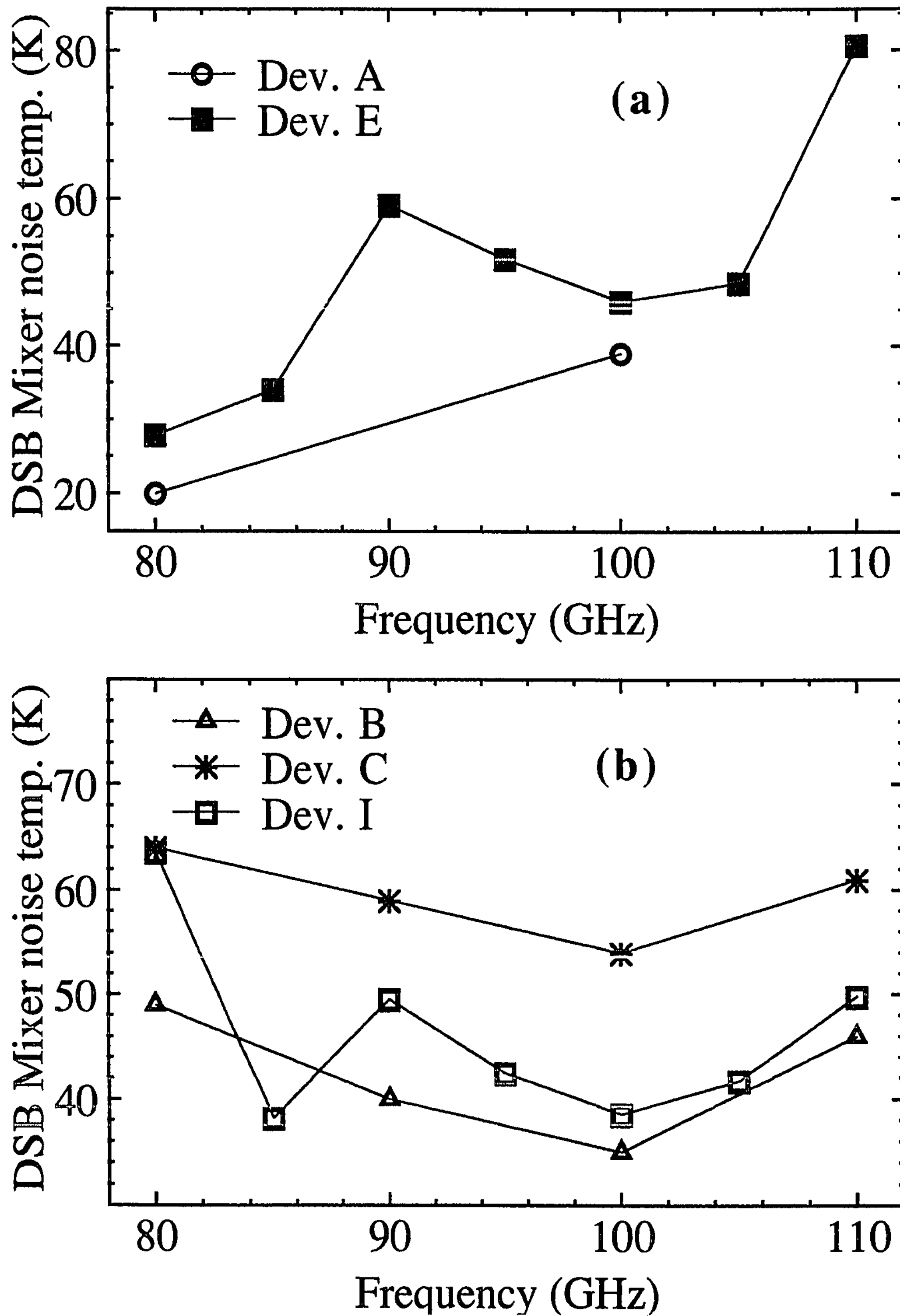

Fig. 5-14 DSB Mixer noise temperatures. a) untuned devices. b) devices with microstripline inductor tuning.

Fig. 5-15a and b show the coupled mixer gain, $G_m{}^C$, measured for the untuned and tuned devices respectively. The untuned devices have, in general, lower measured mixer gains than the tuned devices. This was expected since the tuned devices provided (or were designed to provide) the correct admittance to the *rf* signal over the band, with resonance centered at 95 GHz. $G_m{}^C$ of the tuned devices is a maximum near the designed resonance frequency. Not surprisingly, the gain measured for device A fell sharply as the frequency was increased since the admittance of the geometric capacitance became larger and the device became less well matched as frequency was increased. The other untuned device, E, also showed a falloff of the mixer gain with frequency, but not as drastic as A due to its smaller capacitance.

One of the predictions of the quantum mixer theory, coupled gain, was seen in device C, Fig. 5-15b. The gain was greater than unity across the whole band. The reason that the receiver noise temperatures of device C (Fig. 5-12, see also table 5-1) were not lower in this case was because the IF noise temperature for this receiver measurement was 21 K. Unfortunately, after improving the IF noise temperature, this devices was accidentally destroyed and could not be measured to obtain the expected low receiver noise temperatures. A comparison between device C and device B shows that even though they are nominally the same, the increased resistance of device B caused its IF output to be poorly matched to the 50 Ω IF amplifier input. The coupled gains measured for device B were significantly lower, partly for this reason. The irreproducibility of the fabrication in determining the device area (discussed in Chapter 4) was responsible for the differences in device B and C.

5.4 Theoretical Modeling

We have compared our results to those predicted by the quantum theory of mixing. The theory has been outlined in Chapter 3, and it was used to predict the coupled mixer gain and the mixer noise temperature. In order to speed the rate of data acquisition, the

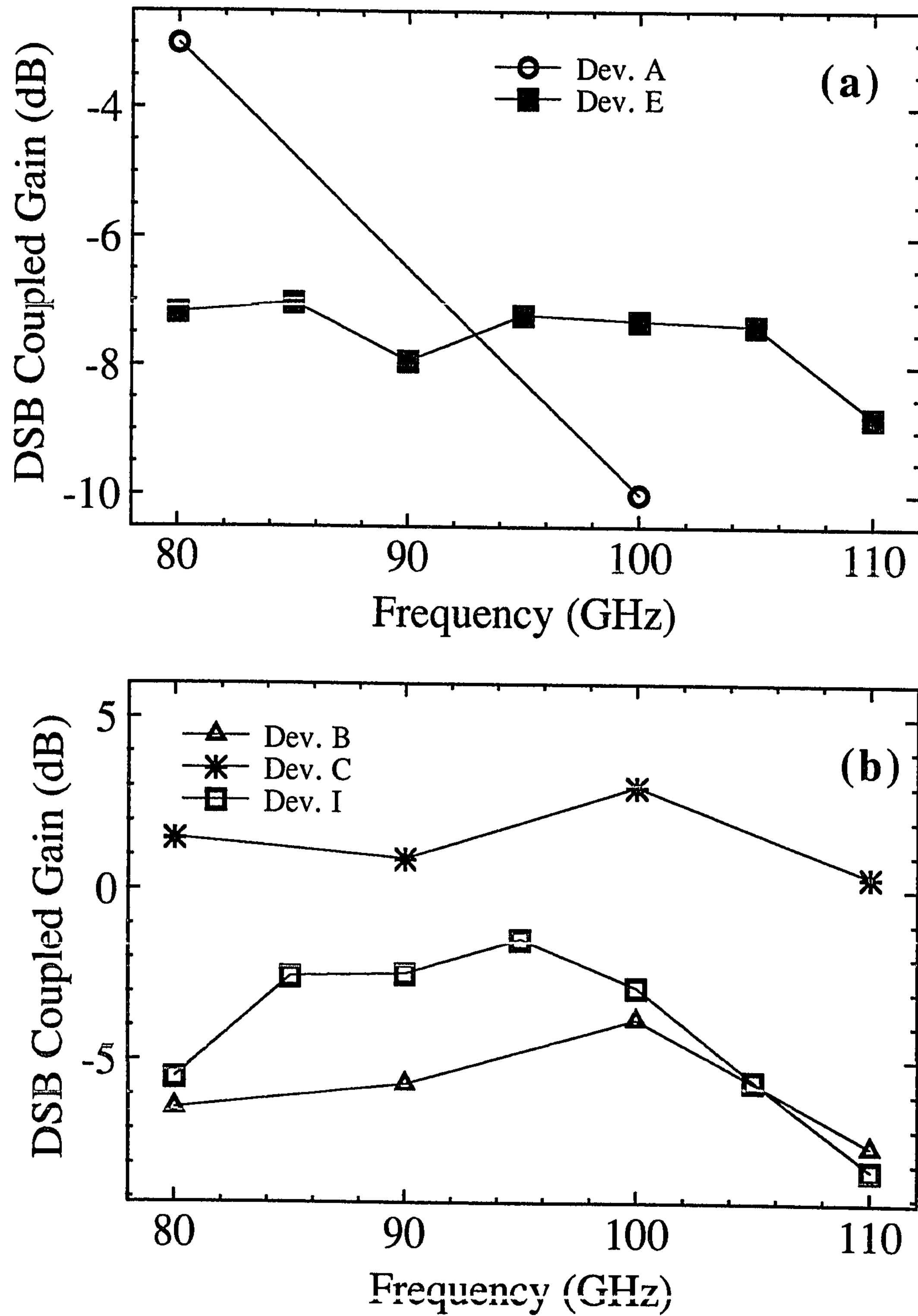

Fig. 5-15 DSB Mixer gains. a) untuned devices. b) devices with microstripline inductor tuning.

experiments were computer controlled. This control was fully implemented in June, 1990. The two mixer devices studied since that time, device E and device I, are therefore better characterized than the others. It is these two devices on which the modelling will focus.

5.4.1 Arrays vs. Single Junctions

Devices E and I were both four junction arrays. All of the theoretical predictions are scaled for use with series arrays by replacing ω with $p\omega$ where p is the number of junctions in the array [Rudner et al., 1981]. By scaling the frequency, all voltages are scaled. A photon width at 100 GHz for a single junction is 414 μV; the photon width at 100 GHz for the array becomes 4 x 414 μV = 1.656 mV. The effect upon the *rf* voltage V_ω is to reduce it by a factor of four from the single junction reduced local oscillator voltage. In practice this reduction is made up for by larger values V_ω required for the array to be pumped correctly for SIS mixing.

5.4.2 Finding the Embedding Admittance

The first step in determining the predictions of the quantum mixer theory is to self-consistently determine the embedding admittance at the LO. The equivalent circuit is shown in Fig. 5-16. It consists of an *rf* current supply driving the junction through a fixed embedding admittance. This embedding admittance is frequency dependent, but it is not dependent upon the magnitude of the drive current or the dc bias voltage of the tunnel junction.

Two ways were used to determine the embedding admittance.

Eyeball Method In this method [Phillips and Dolan, 1982], the pumped I-V is generated using the Tien-Gordon [Tien and Gordon, 1963] expression for the current in the tunnel junction

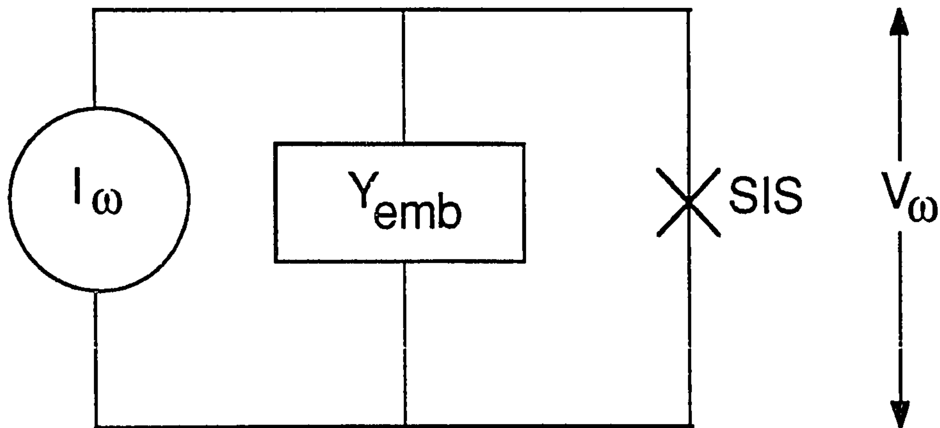

Fig. 5-16 Equivalent circuit for modeling. The device capacitance is included in Y_{emb}.

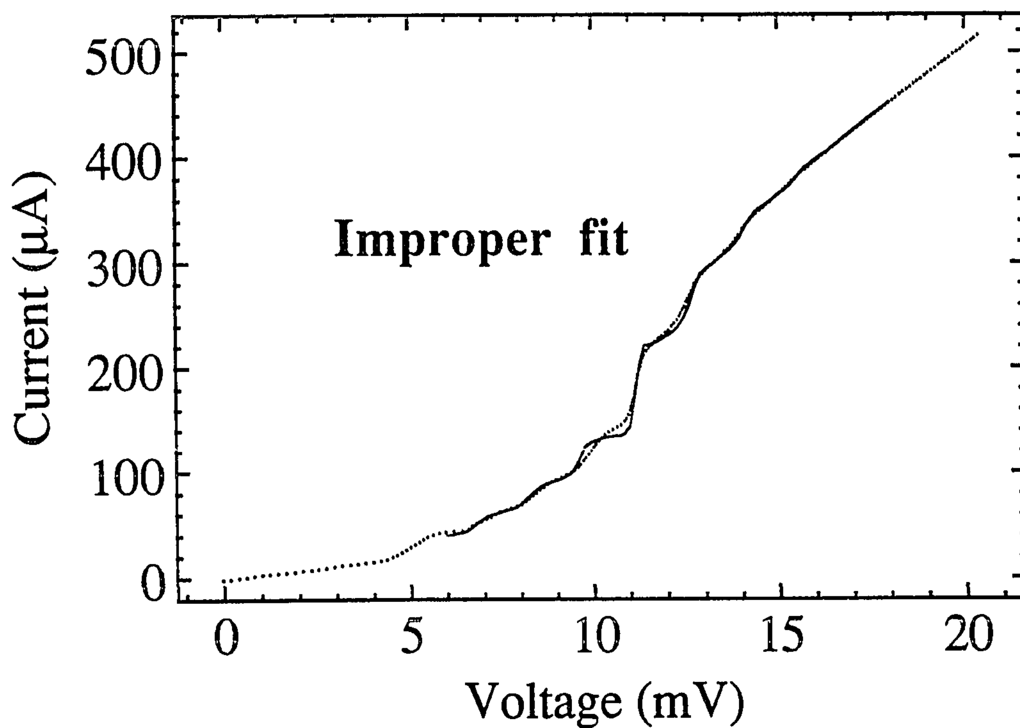

Fig. 5-17 An example of the intrinsic problem with least square fitting in determining the theoretical embedding admittance and pumped I-V. The least square fit is shown as the solid line fit the data points. The example is device E at 95 GHz. The calculated dynamic resistance on the first photon step does not accurately predict the experimentally measured dynamic resistance.

$$I_{dc}(V_o,V_\omega) = \sum_{n=-\infty}^{\infty} J_n(\alpha)\, I_{dc}(V_o + n\hbar\omega/e) \qquad 5\text{-}14$$

for a particular value of the embedding admittance. The current is generally fixed at the middle of the first photon step in order to determine α, and hence the amplitude of the current source of Fig. 5-18. For this method, a number of pumped I-V curves are generated with a variety of embedding admittances and the best fit to the experimental pumped I-V curve gives the embedding admittance at the LO. I have used this method, but only when other methods failed, since it is tedious.

Voltage Match Method The voltage match method was developed by Skalare (1989) and it is an efficient method for self consistently determining the embedding admittance. In this method, the unpumped and pumped I-V curves serve as input. From these, the values of V_ω are solved using eq. 5-14 at each of a number of bias voltages (typically 5-10) which are selected to be on the first, second, and possibly the third photon step below the gap. Once the program has calculated the values of V_ω, it calculates the input admittance of the mixer at ω. For a given embedding admittance Y_{LO}, the program calculates a new value of V_ω. For the k'th bias voltage, the new $V_\omega = V_{\omega k}'$ is given by

$$V_{\omega k}' = \frac{I_{LO}}{Y_{LO} + Y_{\omega k}} \qquad 5\text{-}15$$

The optimum value of the embedding admittance is that which minimizes the value between these pump voltages and the exact pump voltages calculated using the unpumped and pumped I-V curves. The mean square deviation is given by

$$\varepsilon = \sum_k (V_{\omega k} - |V_{\omega k}'|)^2 = \sum_k V_{\omega k}^2 + \sum_k |V_{\omega k}'|^2 - 2\sum_k V_{\omega k}\, |V_{\omega k}'| =$$

$$\sum_k V_{\omega k}^2 + |I_{LO}|^2 \sum_k \frac{1}{|Y_{LO} + Y_{\omega k}|^2} - 2I_{LO} \sum_k \frac{V_{\omega k}}{|Y_{LO} + Y_{\omega k}|} \quad 5\text{-}16$$

The optimum value for I_{LO} is found by differentiating this expression with respect to I_{LO} giving

$$|I_{LO}| = \frac{\sum_k \frac{V_{\omega k}}{|Y_{LO} + Y_{\omega k}|}}{\sum_k \frac{1}{|Y_{LO} + Y_{\omega k}|^2}} \quad 5\text{-}17$$

By substituting this into eq. 5-16, we obtain

$$\varepsilon = \sum_k V_{\omega k}^2 - \frac{\left\{ \sum_k \frac{V_{\omega k}}{|Y_{LO} + Y_{\omega k}|} \right\}^2}{\left\{ \sum_k \frac{1}{|Y_{LO} + Y_{\omega k}|} \right\}^2} \quad 5\text{-}18$$

ε is regarded as a fitting parameter. The determined value of Y_{LO} which minimizes ε is the embedding admittance of the device. This method has proven quite useful in determining the embedding admittance. The major problem with this method is illustrated in Fig. 5-17. Since this method finds the least square error between the actual pumped I-V and the I-V generated by using Y_{emb} and the equivalent circuit, the dynamic resistance of the theoretical best fit and the experimental pumped I-V can be different. Each fit must be examined to determine whether the dynamic resistance is correct. This could, in principle, also be automated, but is not at this time.

5.4.3 Theoretical fits to the pumped I-V

Although the gain and noise calculations are done at a single dc voltage, the results depend upon a great number of dc voltage points separated from the bias point by $np\hbar\omega/e$.

The calculations are much simplified with the use of a single embedding admittance to calculate the value of α at a given bias point using the theoretical model. In principle, V_ω can be solved at each bias point using eq. 5-14. However, none of the results presented here do this. They instead use the pumped I-V to determine the best fit self-consistent embedding admittance and then solve for α using the model of Fig. 5-16. This approach is justified as long as there are no significant harmonic effects [Mears] which effect the shape of the pumped I-V and as long as the junctions in the array are identical to each other [Feldman].

Before turning to the theoretical prediction of mixer gain and noise, we will look at the results of trying to obtain a self consistent embedding admittance which fits the entire I-V curve. Mears et al. (1990, 1991a) have shown that for high quality junctions, the theoretical prediction for the shape of the pumped I-V matches nearly perfectly with the experimental pumped I-V as shown in Fig. 5-18. The junction studied here is nearly ideal. It is a single junction and has no proximity effect knee which is evident in most Nb/AlO$_x$/Nb tunnel junctions. The fits are good over all bias voltages, but they are particularly good below the gap. The frequencies used here are 96.35 GHz (curve b) and 93.65 GHz (curve c). For comparison to these outstanding fits, I show the best fit obtained for the array of Nb/AlO$_x$/Nb devices E shown in Fig. 5-19. The embedding here is 10.10 - i 4.93 mmhos. One sees immediately that the quality of the fit is not nearly as good, particularly above the gap. The lack of excellent fitting of the pumped I-V to a theoretical prediction is due in part to the fact that the areas of the junctions in the array are not equivalent. We have not made an independent measure of the areas, but the measurement of R_n for devices on the same wafer (Chapter 3) indicates that among devices on the same wafer there is a variation in size. It is not surprising then that there is a size difference among junctions within the same array. Essentially, since the individual junctions resistances are not equal, the *rf* voltage does not split evenly between them and the theoretical predictions for a single junction cannot be scaled simply by changing ω into

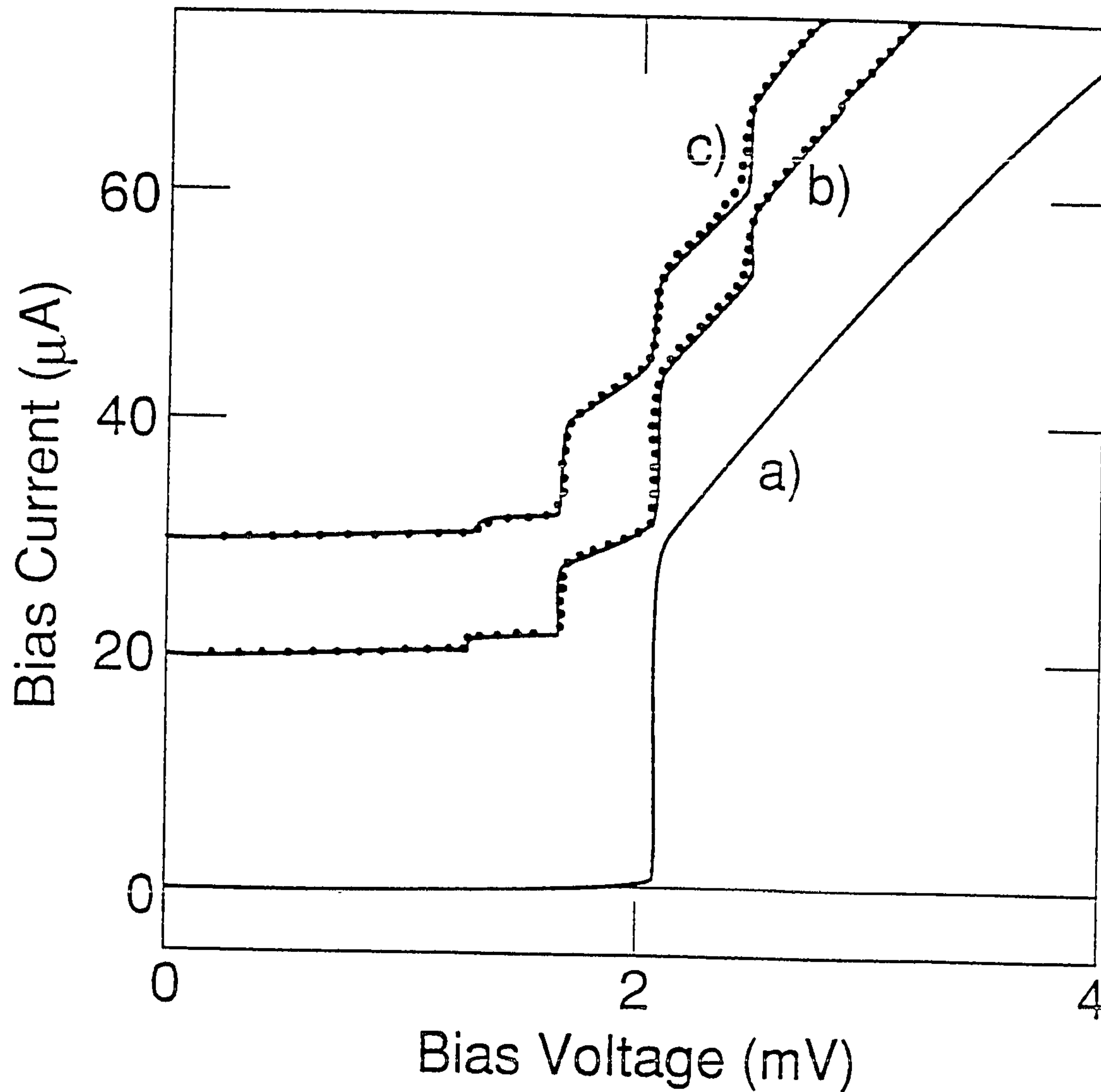

Fig. 5-18 a) unpumped I-V curve of $Ta/Ta_2O_5/PbBi$ tunnel junction at 1.3K. b) Experimental and calculated (solid line) pumped I-V curves at 96.35 GHz. The calculated embedding admittance was Y = 0.14 + i 0.08 mhos. c) Experimental and calculated pumped I-V curves at 93.65 GHz with embedding admittance Y = 0.04 + 0.18 mhos.

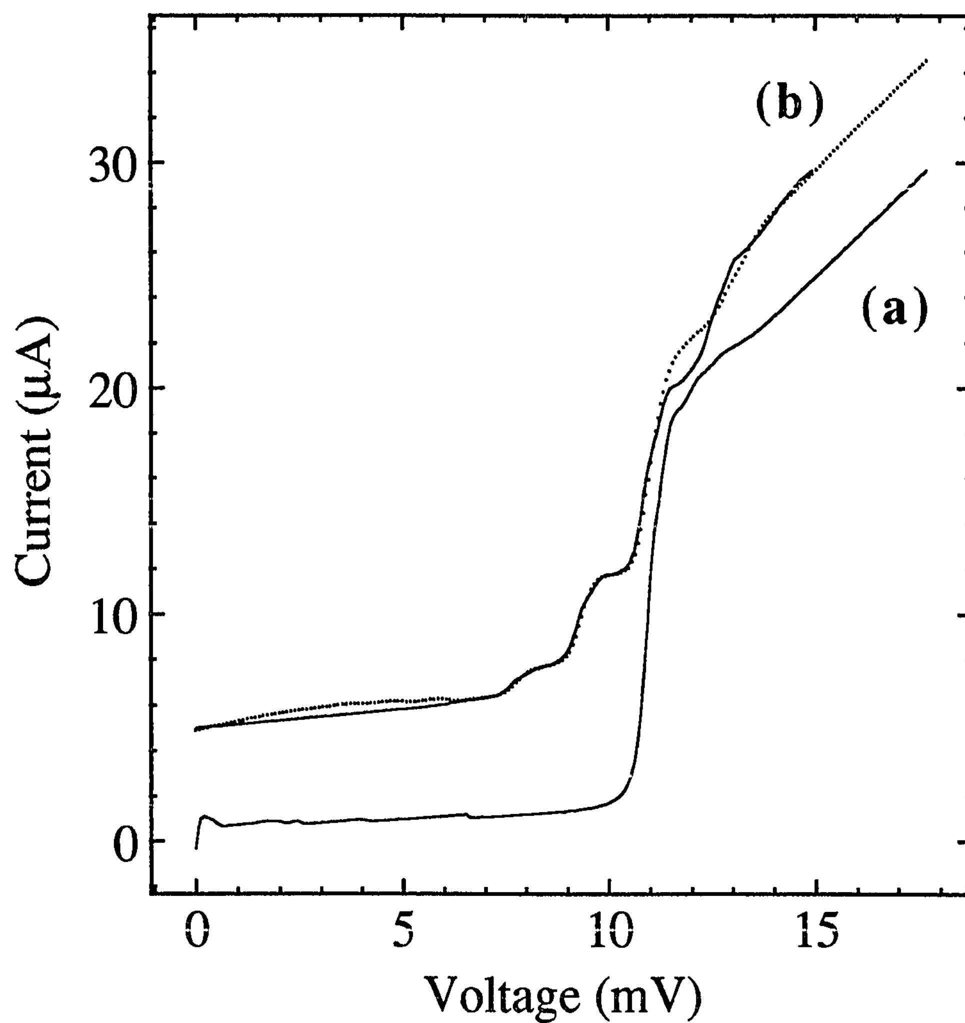

Fig. 5-19 a) Unpumped I-V of device E. b) Experimental and calculated (solid line) pumped I-V at 95 GHz. The calculated embedding admittance was 10.10 -i 4.93 mmhos.

$p\omega$. The non-uniformity of junction sizes within the array certainly has an effect upon the fitting and the theoretical mixing results. To my knowledge, a quantitative theory has not been published regarding the magnitude of this effect, although it is relatively clear that the non-uniform voltage split will degrade the fitting and the mixing results.

Another factor which affects the theoretical predictions is the shape of the unpumped I-V curve itself. The proximity effect knee just above the gap voltage (evident in Figs. 5-5, 5-8, 5-9 and all of the Nb/AlO_x/Nb tunnel junction I-V curves presented in this thesis) is due to the unoxidized Al in the tunnel junction. The shape of the curve, as measured on the chart recorder, does not measure the true shape of this knee. An example of the proximity effect is shown in Fig. 5-20 for a 75 Å Ta overlayer in a Nb/Ta/oxide/PbBi tunnel junction [Ruggiero et al., 1986]. It is believed that due to the shape of the proximity knee and the fact that the normal metal affects the tunneling properties, the mixer results cannot be exactly predicted based on I-V curves of tunnel junctions which contain this effect [Hu et al., 1990b]. The effect of the sharp feature associated with the proximity effect (Fig. 5-20) can be seen in some mixing results, particularly in the work by Ermakov et al. (1991).

In addition to the proximity effect and the non-uniformity of junction areas, an additional effect can occur which can degrade the fitting of the pumped I-V. If there are significant harmonic currents (currents flowing at 2ω) in the tunnel junction, they will have an effect on the measured dc I-V curve that is not explained by the Tien-Gordon expression which assumes these currents to be shunted, i.e., that the junction is rf voltage biased. A simple test of whether the harmonic currents have an effect is to find the best fit embedding admittance as a function of input LO power [Mears]. In the three port model, the amplitude of input power has no effect upon the calculated embedding admittance. If the calculated admittance changes as the power is increased (as more harmonic contributions are present), this is evidence for strong harmonic effects. We have not seen a change in the calculated best fit embedding admittance for a change in the input power, even for small capacitance

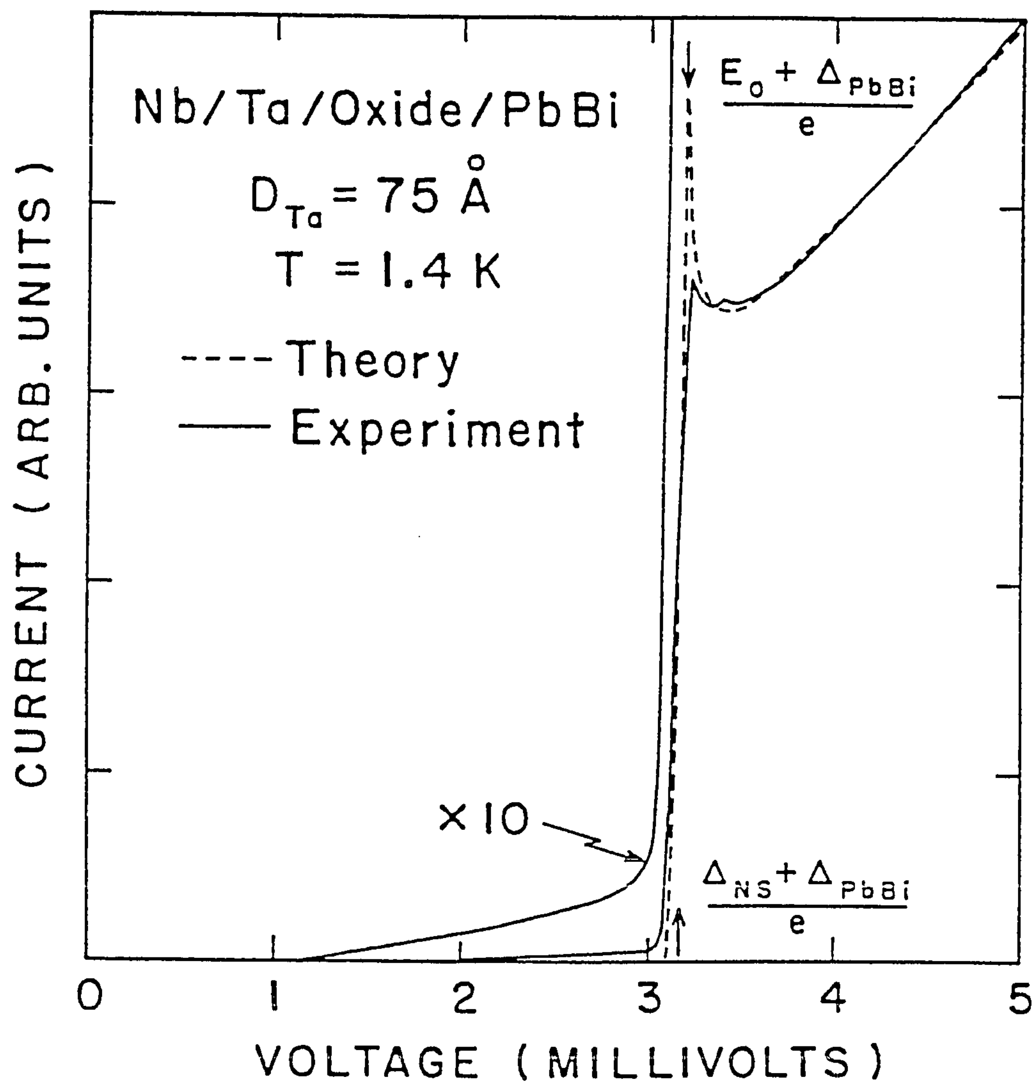

Fig. 5-20 I-V characteristic of a tunnel junction with a base electrode comprised of a 75 Å Ta overlayer on 3000 Å Nb. The proximity effect structure is just above the gap voltage. From Ruggiero et al., (1986).

devices where we expect the harmonic effects to be greatest. From this fact, we conclude that we can ignore harmonic effects.

We have used the theoretical fits with a fixed embedding admittance, in spite of the lack of perfect agreement between the theoretical predictions and the experimentally measured I-V curve. The magnitude of the error involved in doing so is not known at this time.

5.4.4 Embedding Admittance

The embedding admittance is important both in the design of the receiver and in the theoretical prediction of the results. Detailed calculations of the embedding admittance vs. frequency have been carried out using the voltage match method, and are shown for devices E and I in Fig. 5-21. Device E, the open triangles, had no tuning inductor. In spite of this, the calculated embedding admittance remained relatively constant from 80 to 105 GHz. The capacitance of the device is expected to be 4.7 fF, based on R_n and the current density of 3000 A/cm^2 which gives an admittance of i 3.0 mmhos at 100 GHz. This small capacitance may be resonated by the inductance of the wiring connecting the series array of junctions.

The calculated embedding admittance of device I is shown by the filled triangles in Fig. 5-21. The real part of the Y_{emb} became smaller with increasing frequency while the imaginary part became more capacitive. The capacitance of this device is estimated to be 23.5 fF. Fig. 5-21 shows that the embedding admittance becomes more capacitive as the frequency is increased, from a low of -i 11.7 mmhos at 80 GHz to a high of + i 13.0 mmhos at 110 GHz. Using these numbers, the corresponding calculated inductances are 85 and 446 pH respectively. These results are clearly inconsistent with each other, showing that the receiver is not behaving as we expect for this device. It is likely that additional capacitive loss effects were present at higher frequencies, but this has not been confirmed. It is also possible that the frequency dependence of the radial stubs and other

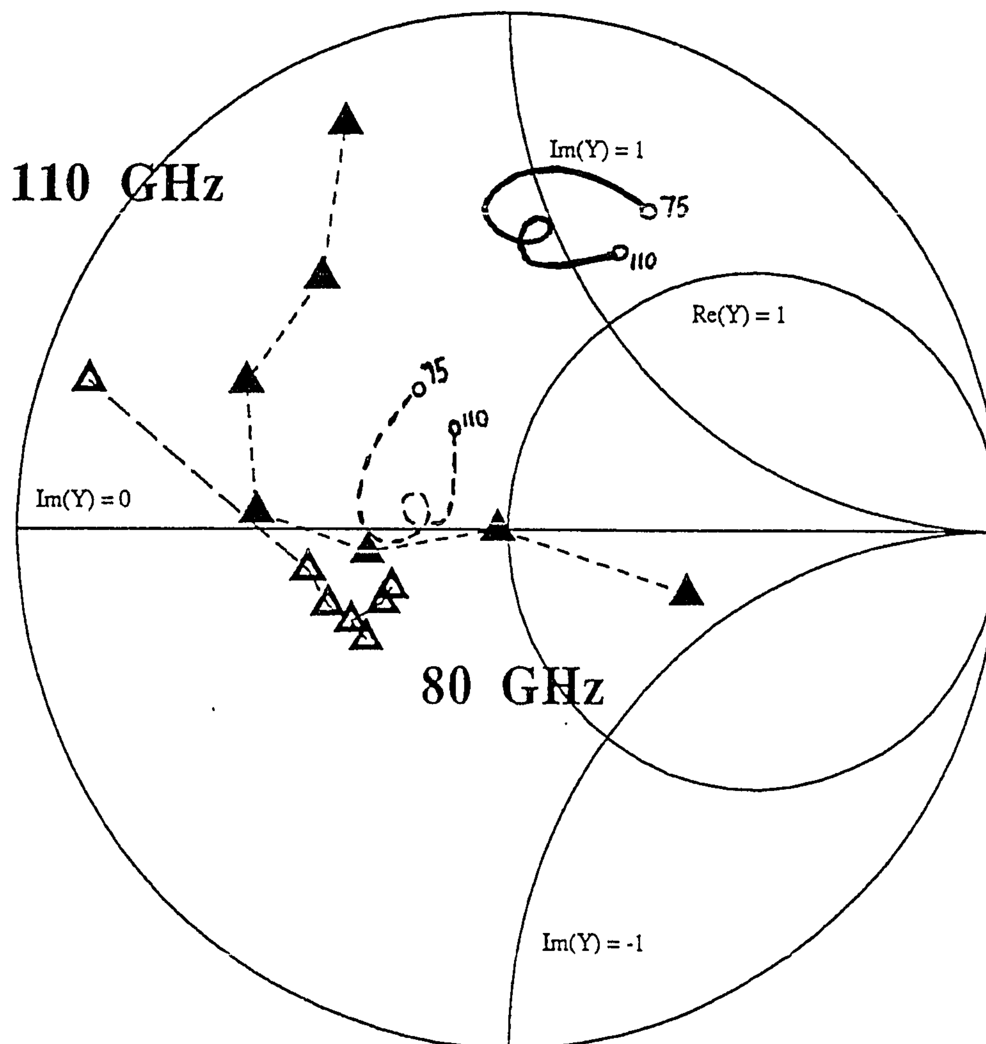

Fig. 5-21 The calculated embedding admittances of devices E (open triangles) and I (filled triangles) vs. LO frequency. The data is from 80-110 GHz in increments of 5 GHz. The small labels refer to the contours of the Smith plot, normalized to Y = 1 in the center. The heavy solid line is the scale model prediction for a single device with area 1 $(\mu m)^2$ and no inductive tuning. The heavy dashed line is the scale model prediction for a 1 $(\mu m)^2$ area device with inductive tuning.

on-chip circuitry are affecting the calculated embedding admittances in this way. More experiments on devices which are nominally the same design are needed before any conclusion can be drawn regarding the embedding admittances and the effect of the tuning inductor.

5.4.5 Modeling of Mixer Noise and Gain

As discussed in Chapter 3.4, the noise is composed of the quantum noise, the shot noise, and the thermal noise. The shot noise and quantum noise contributions are included in the modeling, but the thermal noise contributions at the harmonic sidebands have been neglected. This is valid since the resistive terminations at the harmonics are small. A comparison of the theoretically predicted mixer noise and the experimentally measured mixer noise is shown in Fig. 5-22. The theoretical predictions are more optimistic than expected. A number of problems existed for the devices which could cause the discrepancy in the measured and predicted noise temperatures. Mainly, the devices were nowhere near ideal in terms of the leakage current. The quantum theory predicts the noise due to the elastic tunneling, and it may not adequately predict the noise found in real, leaky devices. It is also possible that the three port model does not accurately predict the noise in our devices, particularly since our $\omega R_n C$ product is much lower (1.2-2) than the optimum found by others for this frequency range [Tucker and Feldman, 1985]. This hypothesis is supported by work by Hicks et al. (1985) and Withington and Kollberg (1989) who find, using a 5-port analysis, that the calculated gain is reduced compared to the 3-port theory for small $\omega R_n C$ product devices. Feldman and Rudner (1983) find experimental evidence that small ($\omega R_n C < 4$) capacitance devices give gains smaller than those predicted by the 3-port theory. Recent work by Tong and Blundell (1990) also shows that in a 5-port analysis. low $\omega R_n C$ products give lower predicted mixer gains. They also find in their analysis that small $\omega R_n C$ devices have a larger range of Y_{LO} which give negative dynamic resistance. It is in these regions in particular that the gain is susceptible to the terminations at the

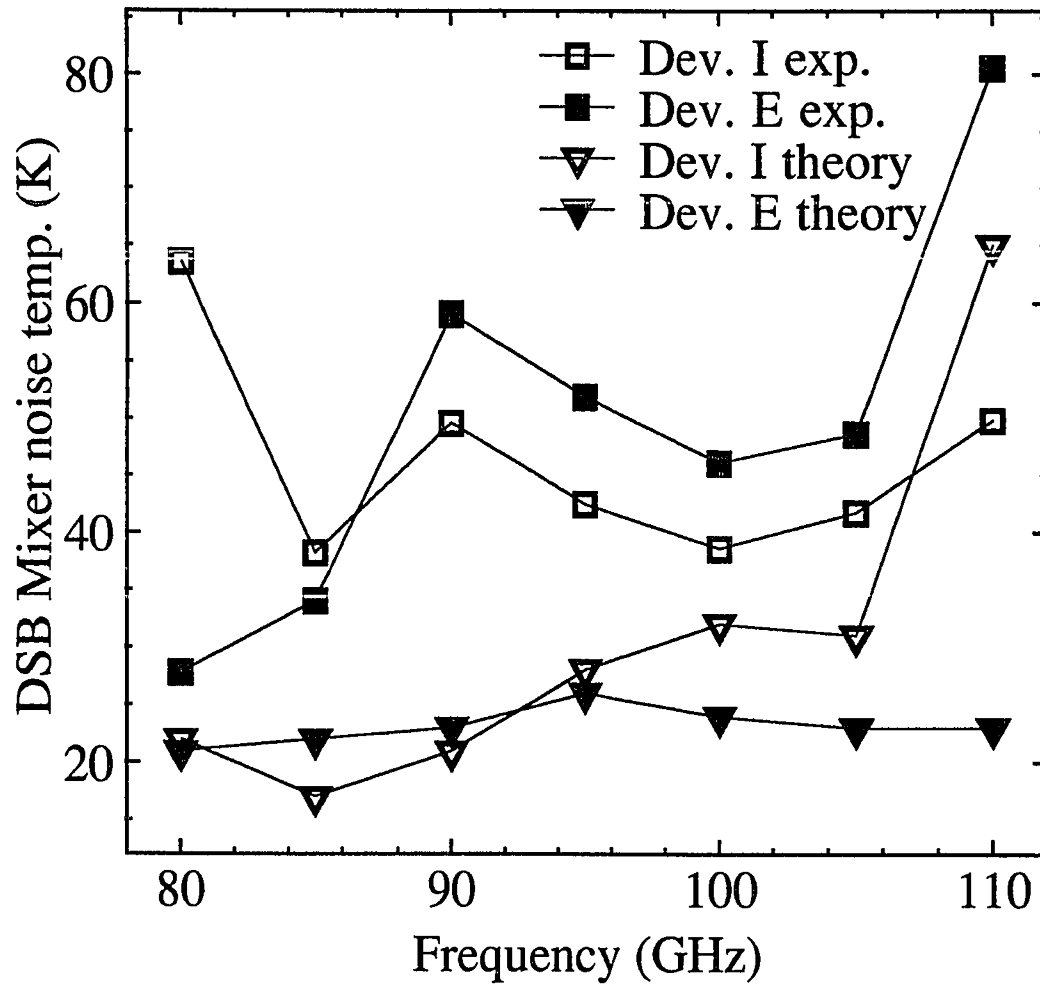

Fig. 5-22 The experimental and calculated mixer noises for devices E and I.

harmonics. These results are consistent with our devices, where $\omega R_n C \leq 2$. It should be noted that the scale modeling of Winkler et al. (1989) did not measure the standing wave ratio of the ridge and device at the second harmonic, although these measurements could be done with our current apparatus.

The non-identicality of the devices in the array should also lead to decreased performance compared to the theoretical predictions. Finally, we have seen evidence for instrumentation noise in the receiver which suppressed the Josephson current and degraded the leakage current. Discrepancies with the theoretical predictions are common, with only the work by Mears et al. (1990,1991a) showing good agreement with the prediction of noise for devices in the strong quantum limit. The work by Feldman et al. (1983) shows good agreement between the measured and predicted gain. A possible solution to the problems associated with non-identical junctions can be found in the work by Ermakov et al. (1991) where the array of junctions are parallel biased at dc and IF. In the parallel biased case, the area of the device is not as important. What becomes important is the value of V_g of each junction. Since this is a materials property, it is more reproducible than the junction area.

A comparison of the measured and theoretical coupled gain is shown in Fig. 5-23. Again, the theoretical predictions overestimate the device performance, although the general trend of the data seems to be the same for the theory and experiment. The theoretical gain was calculated using a load impedance of 50 Ω. The disagreement between theory and experiment may again be explained by the lack of uniform junction size, non-ideal tunneling, and failures in the three port model.

The receiver noise, mixer noise, coupled gain, and other measured quantities of selected devices are presented in Table 5-1.

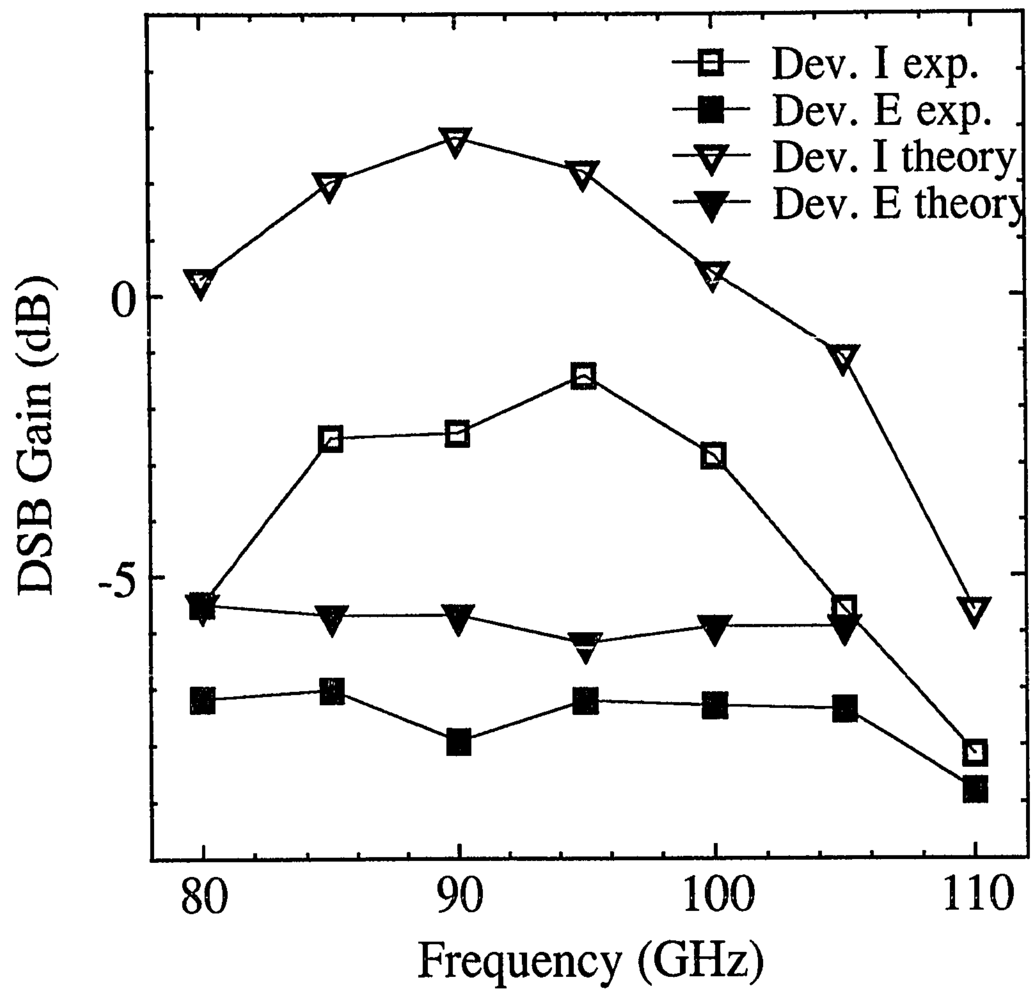

Fig. 5-23 Experimental and calculated coupled gains for devices E and I.

Table 5-1. Summary of the data and results from our measured SIS mixers.

Mixer element	f_{LO} [GHz]	T_R^{DSB} [K]	T_M^{DSB} [K] exp	T_M^{DSB} [K] theor	G_M^{DSB} [dB] exp	G_M^{DSB} [dB] theor
Device A 1 jcn 0.5µm² $R_N = 71\ \Omega$ Untuned	80 100	41 202	20 39		-3.0 -10	
Device B 2 jcns 0.5µm² ea $R_N = 431\ \Omega$ Inductor tuned	80 90 100 110	141 118 85 165	49 40 35 46		-6.4 -5.7 -3.8 -7.5	
Device C 2 jcns 0.5µm² ea $R_N = 125\ \Omega$ Inductor tuned	80 90 100 110 120	79 76 65 80 114	64 59 54 61 75		+1.5 +0.9 +3.0 +0.4 -2.7	
Device E 4 jcns 0.5µm² ea $R_N = 619\ \Omega$ Untuned	80 85 90 95 100 105 110	125 119 158 136 136 136 173	28 34 59 52 46 49 80	21 22 23 26 24 23 -	-7.2 -6.7 -7.9 -7.1 -7.3 -7.3 -8.6	-5.5 -5.7 -5.7 -6.2 -5.9 -5.9 -
Device I 4 jcns each 4µm² $R_N = 124\ \Omega$ Inductor tuned	80 85 90 95 100 105 110	104 65 73 64 66 87 127	62 38 50 42 39 41 49	22 17 21 28 32 31 65	-5.5 -2.5 -2.5 -1.5 -2.9 -5.6 -8.2	+0.3 +2.0 +2.8 +2.2 +0.4 -1.1 -5.6

5.5 Quantum Limited Noise at Berkeley

My contribution to the work done at Berkeley on quantum limited mixing in SIS tunnel junctions was to provide the tunnel junctions. Outstanding junction quality and characteristics were necessary in order to achieve these results. The majority of the work presented in this section is given also in Mears et al. (1990, 1991a). The experimental and theoretical techniques used in this work were similar to that already discussed in this chapter. I will only point out the differences.

5.5.1 The Experiment

Unlike the receiver built at Yale, the Berkeley receiver was single side-band (SSB). The embedding admittances determined at the signal and the image frequencies were very different from each other. These admittances and the tunnel junction I-V curve for an LO of 95 GHz are shown in Fig. 5-18 and caption. Since this work sought to measure quantum limited noise in SIS mixers, it used Ta/Ta_2O_5/PbBi tunnel junctions with extremely low leakage currents in order to limit the shot noise contribution to the mixer noise. The receiver contained a back-short tuning element. In order to find the lowest mixer noise temperature, the tuning element, magnetic field, dc bias, and input *rf* power were optimized. Since the receiver was SSB, the optimization procedure involved injecting a monochromatic signal at either the upper or lower sideband of the LO. The output power at the IF was then maximized.

5.5.2 The Modeling and Results

The theoretical modeling of these devices was essentially the same as for the device presented in section 5.3 with the addition of greater care in determining the magnitude of the noise contributions from components other than the mixer. This was necessary since these devices exhibited mixer noise close to the quantum limit and it was important to calculate the uncertainty in quoting the mixer noise results. In order to calculate the

theoretical predictions, the embedding admittances at both the upper and lower side bands were determined by pumping the device strongly at these frequencies and using the voltage match method (section 5.4.2).

The measured and calculated mixer noise and *available gain* are shown in Figs. 5-24 and 5-25. The mixer noise is given in quanta; the quantum limit is 0.5 quanta for a SSB receiver. This correspond to the added noise from the mixer and does not contain the zero point fluctuations on the incoming signal. The mixer noise was found to be 0.61 ± 0.36 quanta at 93 GHz. This is, to my knowledge, the closest approach to the quantum limit ever demonstrated. The low gain is attributable to the small instantaneous bandwidth of the mixer mount at the *rf* frequency. This caused the receiver operation to be single side band; a favorable embedding admittance was not simultaneously available at both the signal and image frequencies. These results represent the lowest approach to the quantum limit for SIS mixers. It is possible that recent work involving parametric amplifiers [Movshovich et al., 1991] which has shown quantum limited noise at 19 GHz, will evolve to be ultrasensitive detectors in the 100 GHz range.

In addition to measuring the gain and noise vs. frequency, additional experiments were done to determine the gain and noise vs. pump power. The results vs. pump power are shown in Fig. 5-26. The dashed lines are the limits of the theoretical predictions which are consistent with the shape of the dc I-V curve. It should be noted that the experimental results are toward the high end of the theoretically consistent noise temperatures and the low end of the theoretically consistent gains. Thus, even for these nearly ideal devices, the experimentally measured noise and gain begin to deviate in a negative way from the theoretical predictions. It is suggested [Mears et al., 1991a] that the lack of perfect agreement may arise from the fact that the dc I-V curve does not adequately represent the density of states in the tunnel junction and that the very small leakage currents in this device do not arise from elastic tunneling and are therefore incorrectly modeled by the quantum mixer theory. Both of these suggestions are consistent with our results on Nb devices,

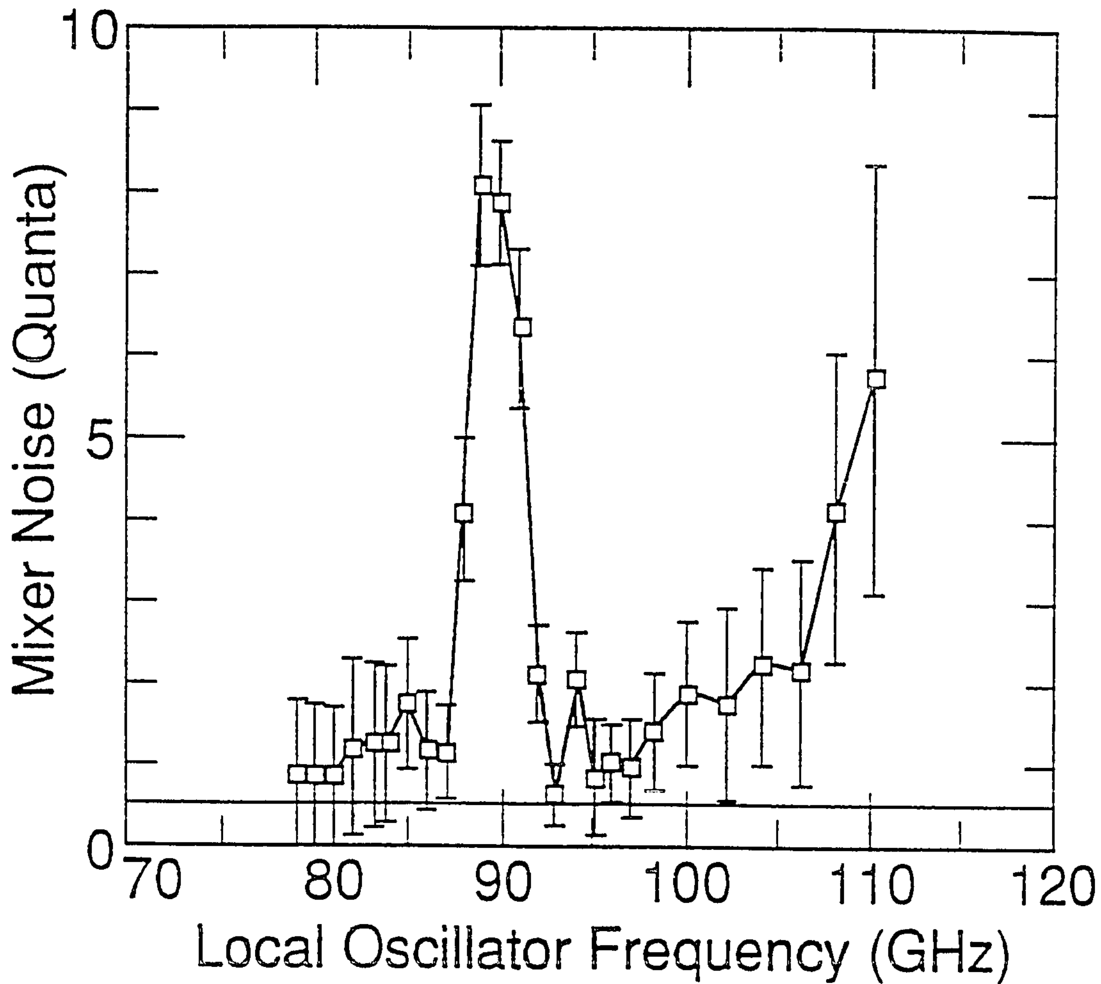

Fig. 5-24 Added mixer noise (in quanta) as a function of LO frequency. The peak in the noise near 90 GHz corresponds to a resonance in the mixer block which makes it impossible to provide favorable embedding admittances. The horizontal line is the quantum limit for a SSB mixer. The best result was 0.61 ± 0.36 quanta at 93 GHz.

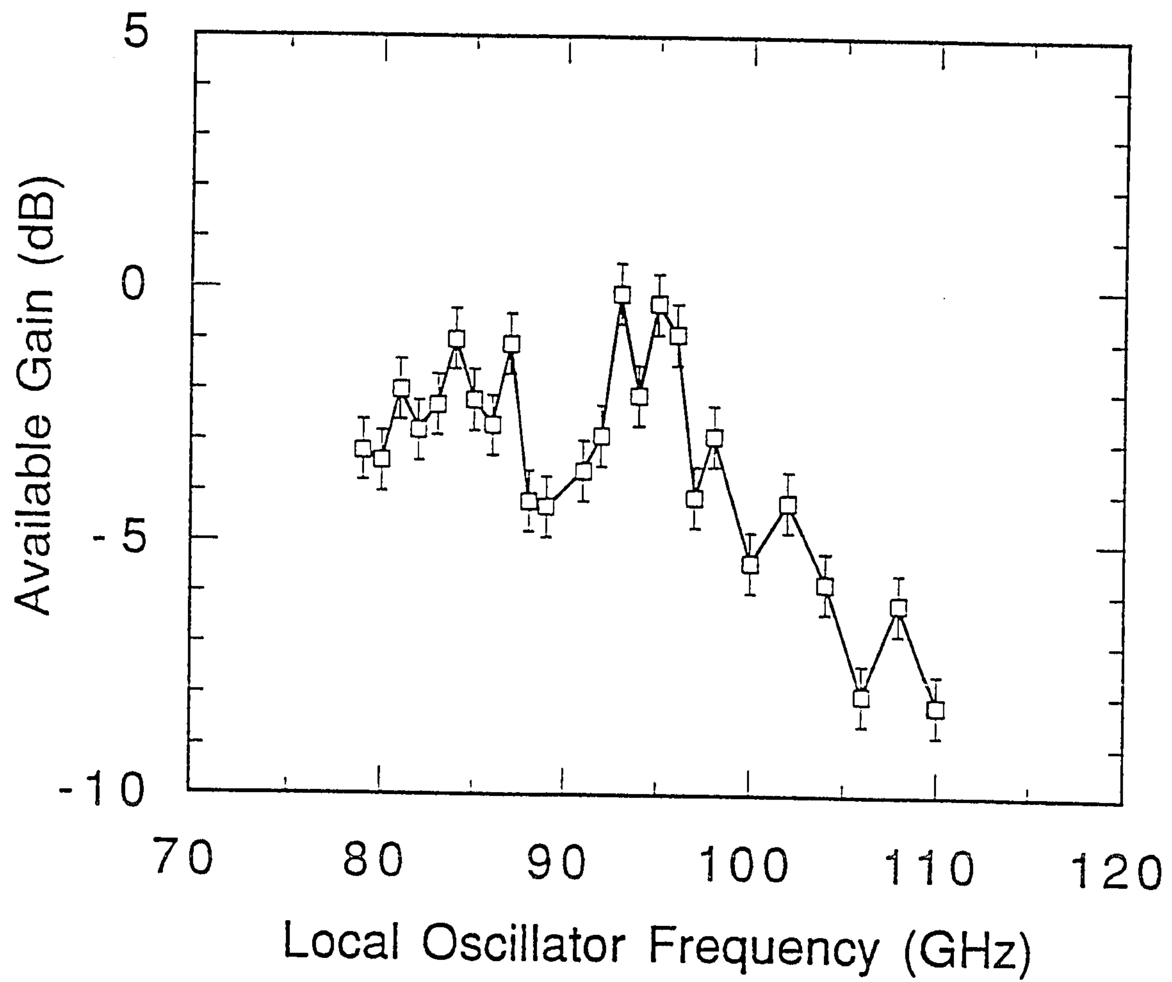

Fig. 5-25 The available gain as a function of LO frequency corresponding to the mixer noises of fig. 5-24.

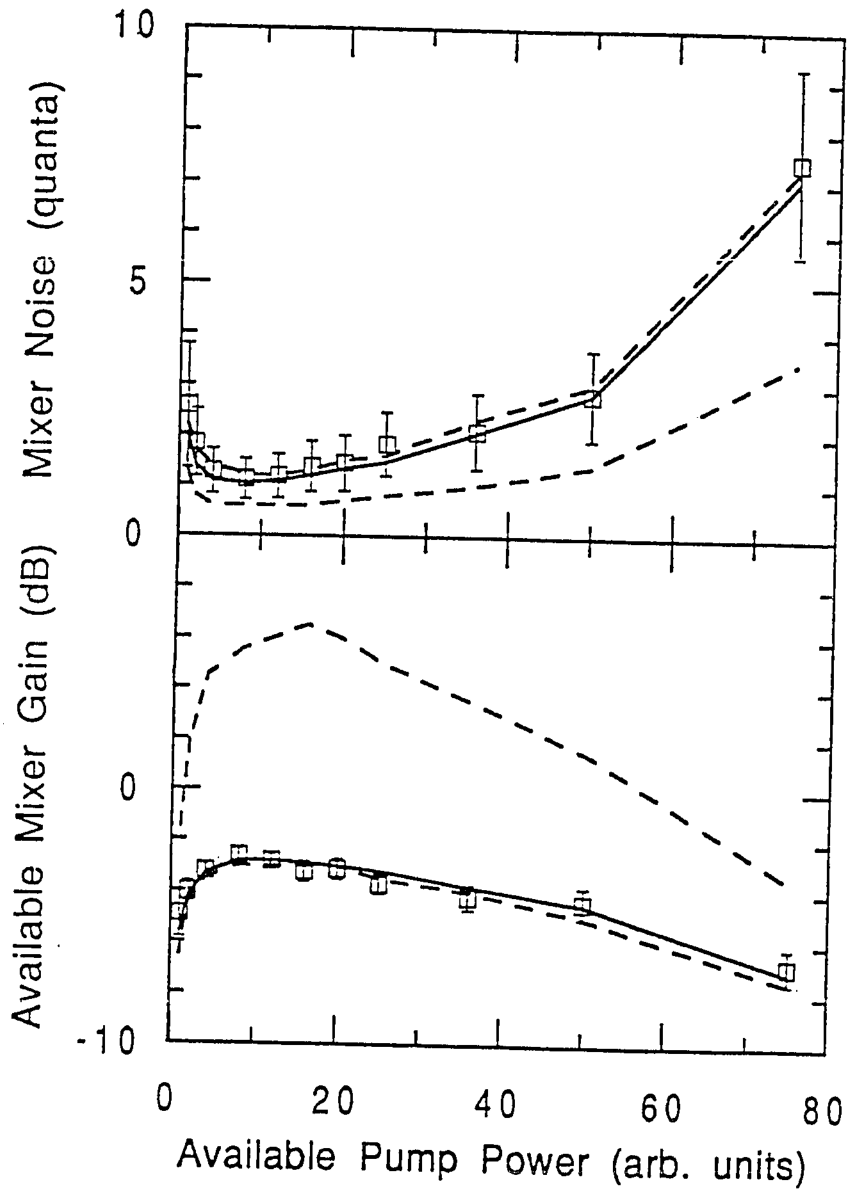

Fig. 5-26 The mixer noise and gain as a function of the available pump power at 95 GHz. There is an optimal pump power for which the gain is high and the noise is low. The dashed lines are the calculated limits of the performance that are consistent with the shape of the pump I-V curves. The solid line is the best fit.

where the leakage currents are considerably greater and the I-V trace contains some clearly non-ideal aspects.

The mixer results presented in this chapter for the $Nb/AlO_x/Nb$ devices are among the best currently reported in the 80-110 GHz frequency range, particularly among receivers with no mechanical tuning elements. This receiver also has no IF transformer. This receiver could be used as a prototype for future high frequency receivers where waveguide may be used ($f \leq 600$ GHz).

The measured mixer noise of the $Ta/Ta_2O_5/PbBi$ devices are the closest reported noise to the quantum limit. These results further verify the the quantum limit of noise in heterodyne receivers, as well as verify an important prediction of the mixer theory.

VI QUANTUM CONDUCTANCE AND SUSCEPTANCE

6.1 Theory of Quantum Conductance and Susceptance

The quantum admittance, which is the sum of the quantum conductance and quantum susceptance, is simply the ratio of the quasiparticle current flowing at ω in the tunnel junction to the voltage applied at ω. The quantum conductance, G_Q, is the real part of this admittance while the quantum susceptance, B_Q, is the imaginary part. The total quasiparticle current flowing at ω is

$$I(t) = G_Q V_\omega \cos\omega t + B_Q V_\omega \sin\omega t \qquad 6\text{-}1$$

The underlying physics has been described in Chapter 2, where the quasiparticle currents are expressed as a function of the amplitude of the applied *rf* voltage (eq. 2-17).

The recent interest in the quantum admittance stems from predictions that the quantum susceptance has a fundamental effect on the shape of the dc pumped I-V curve, [Mears et al., 1989; Hu et al., 1990b] and mixer gain [Mears et al., 1991b]. Until recently, the effects of the susceptance were thought to be subtle and not responsible for the conversion gain seen in SIS mixers [Feldman, 1982]. Many simple models of mixing with SIS tunnel junctions, [Tucker and Feldman, 1985] ignore the reactive currents completely.

In addition to SIS tunnel junctions, other non-linear devices have high frequency reactive currents. Recent work by Liu (1991) predicts the real and imaginary parts of the impedance in resonant tunneling diodes. Resonant tunneling diodes are of interest because of their application as detectors [Sollner et al., 1983], quantum well oscillators [Brown et al., 1989], and transistors [Capasso et al., 1986 and Reed et al., 1989]. The experiment described in this chapter could be extended to measure the high frequency impedance of the resonant tunneling diode.

Feldman and Face (1987) argue that the effect of the quantum susceptance in SIS tunnel junctions is a time delay in the quasiparticle response function. They model this as an additional transmission line length at the input port of the mixer. They further argue that a broad response function, such as that found for a near ideal SIS element, will not be modeled well by this additional time delay. Since most work, including that of Feldman and Face (1987) has dealt with the quantum susceptance at a single constant bias voltage where it is roughly linear in response to the applied signal, an intuitive understanding of the effect of the quantum conductance and susceptance was lacking until recently. This new understanding of the quantum susceptance is found in the bias dependence of the quantum conductance and susceptance.

The dc bias dependence of the quantum admittance is easily found from the high frequency current flowing in the tunnel junction. In this work, the applied voltage is always $V(t) = V_0 + V_\omega \cos\omega t$. Eqs. 2-24 through 2-26 describe the current at ω flowing in response to this applied voltage, thus we can define the quantum conductance, G_Q, and quantum susceptance, B_Q, from the total current as

$$Y_Q = G_Q + iB_Q = I_\omega / V_\omega$$

$$G_Q = \frac{1}{V_\omega} \sum_{n=-\infty}^{\infty} J_n(\alpha) \left[J_{n+1}(\alpha) + J_{n-1}(\alpha)\right] I_{dc}(V_0 + n\hbar\omega/e) \qquad 6\text{-}2$$

$$B_Q = \frac{1}{V_\omega} \sum_{n=-\infty}^{\infty} J_n(\alpha) \left[J_{n+1}(\alpha) - J_{n-1}(\alpha)\right] I_{KK}(V_0 + n\hbar\omega/e) \qquad 6\text{-}3$$

These equations are non-linear since they include terms which correspond to multiple photon processes, $n > 1$. The fact that the voltage amplitude V_ω appears in the general non-linear equation means that in the full expression, G_Q and B_Q depend upon the particular embedding circuitry used. This has been shown in simulations by Mears et al.

(1989). This dependence comes through the bias voltage dependence of V_ω, and is discussed in section 6.1.3.

The Bessel function amplitudes are linear in α for the case of $\alpha = eV_\omega/\hbar\omega << 1$, very small input power, where only single photon processes are possible. In this case, the current is linear in response to the amplitude of the *rf* voltage, and the amplitude of the *rf* voltage drops out of the equations for G_Q and B_Q. By keeping only the lowest order terms in the summation and assuming a very low power input ($\alpha << 1$), G_Q and B_Q become

$$G_Q = \frac{e}{2\hbar\omega}\left[I_{dc}\left(V_o + \frac{\hbar\omega}{e}\right) - I_{dc}\left(V_o - \frac{\hbar\omega}{e}\right)\right] \qquad 6\text{-}4$$

$$B_Q = \frac{e}{2\hbar\omega}\left[I_{KK}\left(V_o + \frac{\hbar\omega}{e}\right) - I_{KK}(V_o) + I_{KK}\left(V_o - \frac{\hbar\omega}{e}\right) - I_{KK}(V_o)\right] \qquad 6\text{-}5$$

where the Bessel functions have been expanded for small argument and only the terms for $n = 0, \pm 1$ have been used. A useful guide for when these low power equation are applicable is when the second order terms in the full expansion are less than 10% of the first order terms. Mathematically, $J_2(\alpha) < 0.1 J_1(\alpha)$, for all α, which for small argument of α gives $\alpha^2/8 < 0.1\alpha/2$ which gives $\alpha < 0.4$. This means that even in the reasonable power range, $\alpha < 0.4$, the linear expressions are a good approximation.

6.1.1 Quantum Conductance

The quantum conductance can be seen in the low-power limit to be the slope of the line connecting the two photon points, $V_o + \hbar\omega/e$ and $V_o - \hbar\omega/e$ as shown in Fig. 6-1a. G_Q in Fig. 6-1b can be seen as having different values in three discrete bias voltage ranges, 1) $V_o < V_g - \hbar\omega/e$; 2) $V_g - \hbar\omega/e < V_o < V_g + \hbar\omega/e$; 3) $V_o > V_g + \hbar\omega/e$.

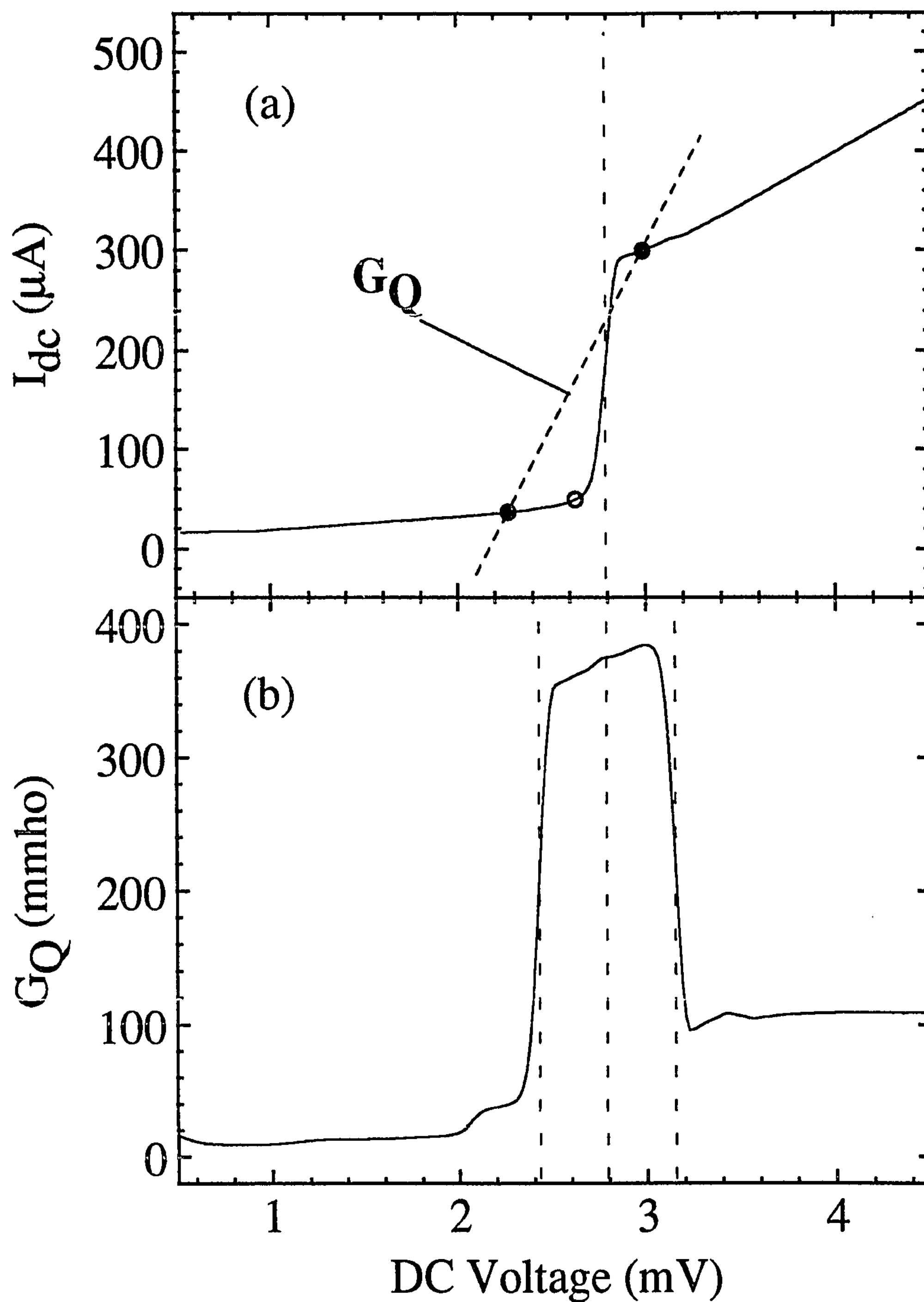

Fig. 6-1 The geometric construction of the low-power G_Q (scaled from device J). The slight features seen at the second photon steps above and below the gap are associated with two photon processes and occur in the plot since the calculation uses the full expression.

In region 1, there is not enough energy supplied by the dc bias voltage for the quasiparticle to absorb a photon and tunnel across the barrier. The quantum conductance is closely approximated by dI/dV, and is small in this region since the tunneling current is small. In region 2, within one photon width of the gap, the quasiparticle can absorb or emit a single photon and tunnel across the barrier. Over this bias voltage range, the conductance is essentially flat; the singularity at the gap voltage in the dc I-V trace is seen at bias voltages one photon width different from the gap voltage. In region 3, for bias voltages above one photon point above the gap, the quasiparticle does not sense the non-linearity at the gap since only single photon emission processes are available. In this region, the quantum conductance is again essentially $dI/dV \approx R_n^{-1}$. The bias voltage dependence of G_Q may have useful application in superconducting devices, where the change in conductance vs. bias voltage could be used as a variable tuned attenuator.

6.1.2 Quantum Susceptance

The quantum susceptance, B_Q, depends upon the Kramers-Kronig transform of the measured dc I-V curve. The KK transform of the I-V curve of Fig. 6-1a is shown in Fig. 6-2a. The low-power quantum susceptance is plotted in Fig. 6-2b. The manner in which the low power susceptance equation is written (eq. 6-5) illustrates the fact that the low-power B_Q is a second finite difference. It is the difference in slopes between the photon emission process and the photon absorption process. This is not surprising since the reactive quasiparticle currents arise from the "quantum sloshing" which is a process by which the quasiparticle tunnels across by absorbing a photon and tunnels back by emitting a photon.

An example of the geometric construction of the low-power quantum susceptance is given in Fig. 6-2a. The singularity in the Kramers-Kronig current is now seen at three points in B_Q vs. dc voltage. At the gap voltage, B_Q is large and negative. The negative

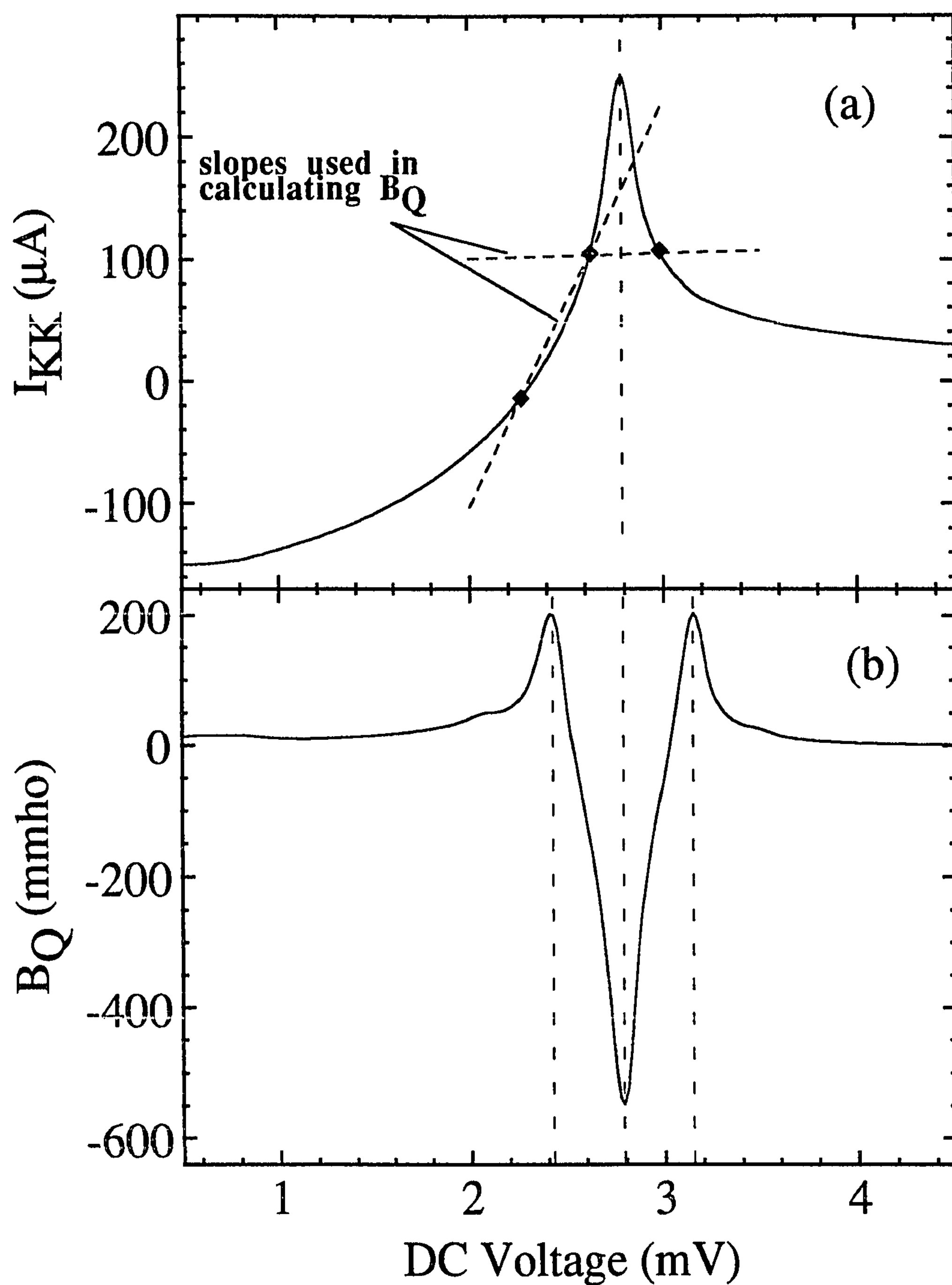

Fig. 6-2 The geometric construction of the low-power B_Q (scaled from device J). The slight features seen at the second photon steps above and below the gap are associated with two photon processes and occur in the plot since the calculation uses the full expression.

susceptance means that it behaves as an inductor at the gap voltage. At one photon point above and below the gap, B_Q has positive (capacitive) peaks.

Hu et al., (1990b) have described the quantum conductance and quantum susceptance as a two level system in which the two levels are on different sides of the tunnel barrier. The susceptance is inductive if the photon absorbed and emitted during the sloshing process is of a lower energy than the incident radiation, $\hbar\omega$. A capacitive susceptance is given when the photon energy is greater than $\hbar\omega$. By integrating over all of the possible processes relating a state on one side of the barrier with a state on the other side of the barrier, one can determine the value of B_Q at a given bias point. One can see this using the semiconductor model of Fig. 2-4. At the gap voltage, $V = (\Delta_1 + \Delta_2)/e$, where the singularities in the densities of states line up across the barrier, there are more available tunneling processes at an energy less than $\hbar\omega$ so that the susceptance is negative at the gap voltage.

6.1.3 Effect of the Quantum Admittance on the dc pumped I-V curve

Mears et al. (1989) show that B_Q has a profound effect upon the shape of the dc pumped I-V curve. In addition, they argue that except for the case of very unusual embedding admittances, negative dynamic resistance is not possible without including B_Q in the analysis. The details of this section follow closely their analysis.

Considering the circuit diagram of Fig. 6-3, the tunnel junction is seen as a real and imaginary admittance in parallel with the embedding admittance. As in the mixer modeling, the embedding admittance contains the geometric capacitance. The shape of the photon assisted tunneling steps is given by Eq. 2-23

$$I_{dc}(V_o) = \sum_{n=-\infty}^{\infty} J_n^2(\alpha)\, I_{dc}(V_o + n\hbar\omega/e) \qquad 6\text{-}6$$

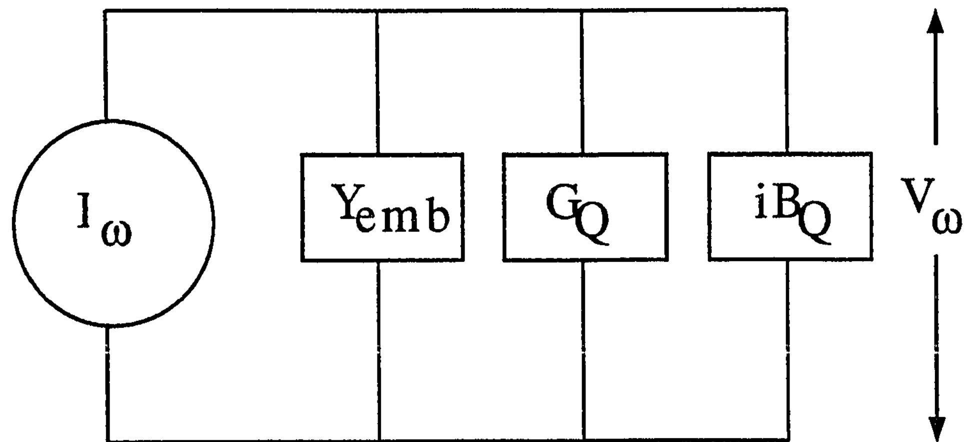

Fig. 6-3 The equivalent circuit used in calculating the effects of G_Q and B_Q on the shape of the dc pumped I-V curve.

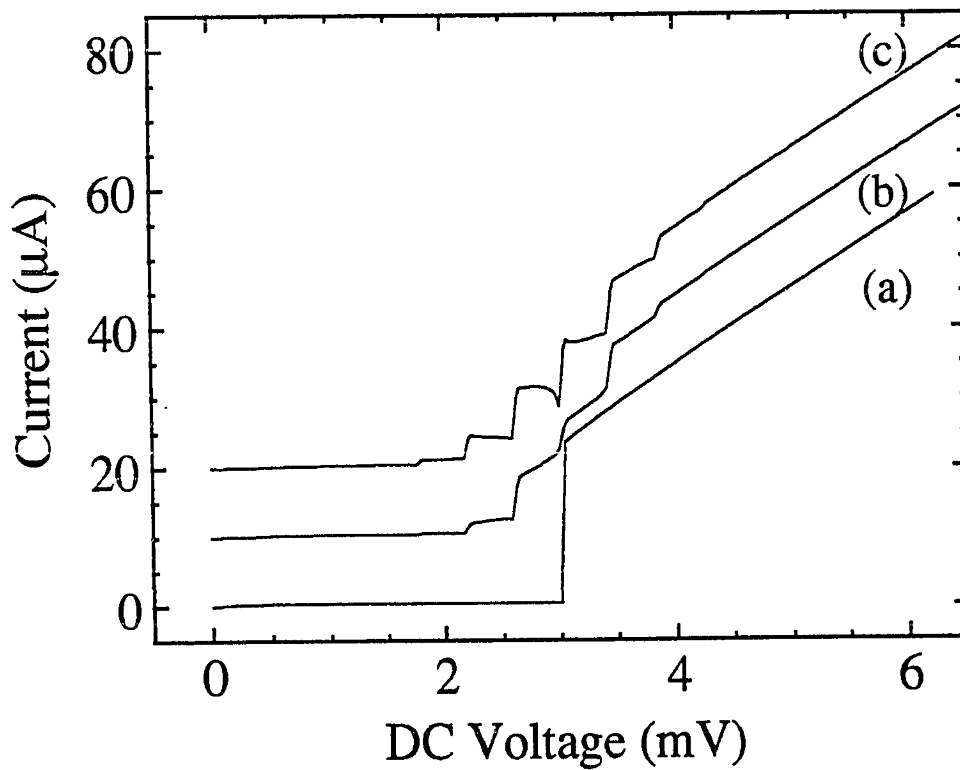

Fig. 6-4 a) The dc I-V trace of a theoretical BCS junction having $\Delta_1 = \Delta_2 = 1.5$ mV. b) The pumped I-V trace with a capacitive embedding admittance given by $Y_{emb} = (20 + j\,50)$ mmhos. c) The pumped I-V trace with an inductive embedding admittance given by $Y_{emb} = (20 - j\,50)$ mmhos. The curves are offset by 10 μA for clarity.

The shape of the pumped I-V is dependent upon I_{dc} and $V_\omega(V_o)$. From the circuit of Fig. 6-3, $V_\omega(V_o)$ will clearly depend upon the relative magnitudes of the three admittance elements. Let us consider two cases. The first case is that of a capacitive embedding admittance, given by $Y_{emb} = (20 + i\,50)$ mmhos. The I-V of the device simulated is shown in Fig. 6-4, and is an ideal BCS junction at 4 K with $\Delta_1 = \Delta_2 = 1.5$ mV and $R_n = 100\ \Omega$. Consider the case of a large pump power such that the first photon step below the gap is clearly visible in the dc I-V trace. At one photon step below the gap voltage, B_Q is capacitive. There is a large mismatch between this capacitance and the capacitive embedding admittance. For this reason, V_ω across the junction is small. As the bias voltage is increased across the first photon step, B_Q begins to resonate the capacitive part of the embedding admittance and V_ω across the junction increases. An increase in V_ω across the photon step causes an increase in the dc tunneling current through eq. 6-6. The photon assisted tunneling curve is shown in Fig. 6-4b.

For the case of an inductive embedding admittance, given by $Y_{emb} = (20 - i50)$ mmhos, the capacitive value of B_Q at the low bias end of the first photon step resonates partially with the inductive part of the embedding admittance. As the dc bias voltage is increased across the first step, B_Q becomes more negative (larger inductive susceptance) and the mismatch between it and the embedding admittance becomes greater. For this reason, V_ω *decreases* as the bias voltage increases. This causes the negative dynamic resistance shown in Fig. 6-4c.

Although it was known that inclusion of the reactive terms in the mixer theory were necessary in order to correctly predict the theoretical results, until recently it was not accepted that the reactive terms had a large effect. Clearly, given this very simple model, the quantum susceptance has greatly affected the shape of the dc pumped I-V curve. Of course, it is the values of quantum admittance *and* the embedding admittance which gave the very different curves of Fig. 6-4. All three elements (G_Q, B_Q and Y_{emb}) are important in determining the shape of the pumped I-V. Since flat photon steps are not possible

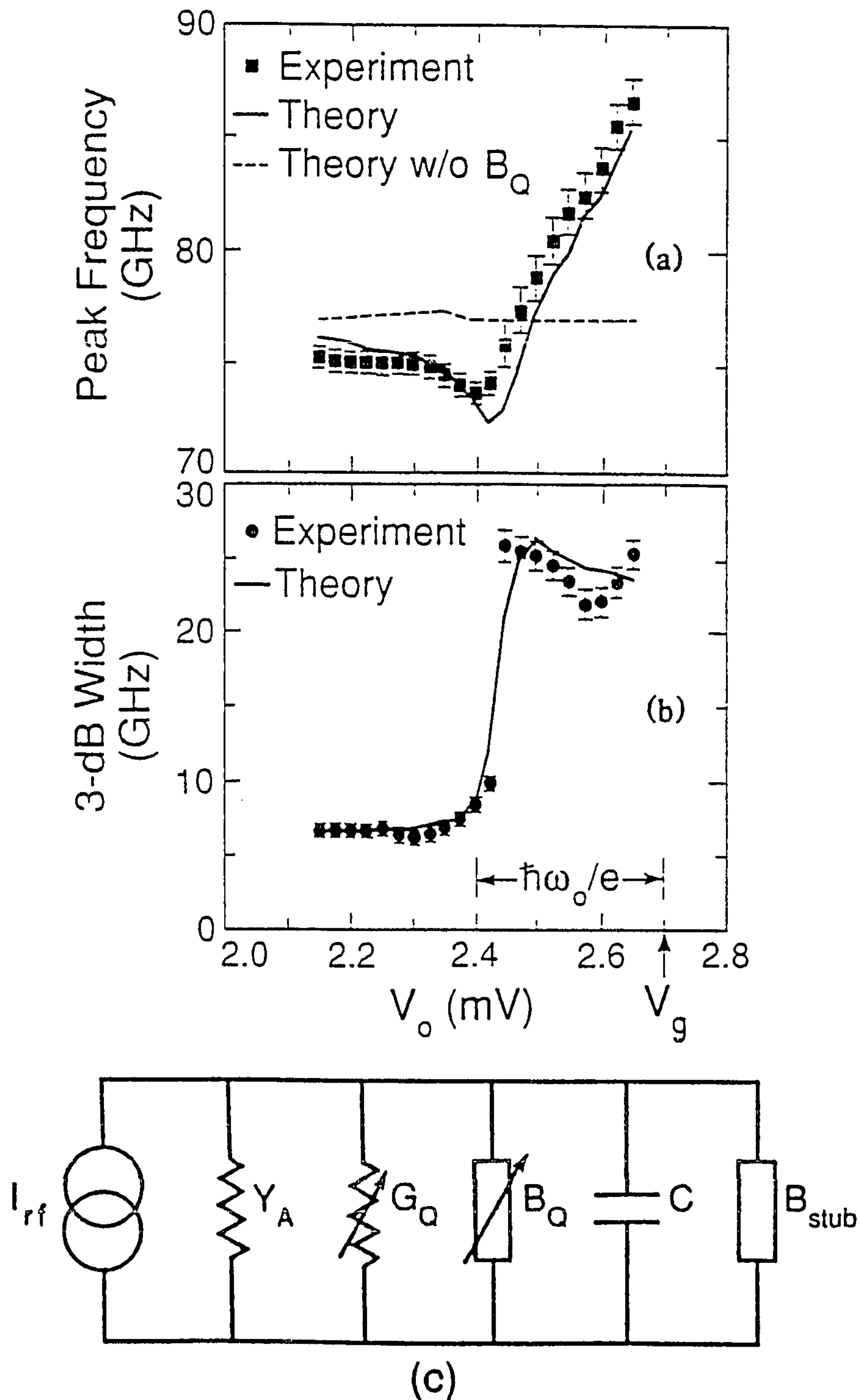

Fig. 6-5 a) and b) The results of Hu et al., (1990a, 1990b) measurement of peak frequency and 3 dB width of the resonance between G_Q, B_Q, and the passive circuit elements shown in c)

without B_Q, it may be said that B_Q is both important and necessary in determining the mixer gain in situations where the input susceptance at the LO and signal are similar.

It should be noted that in addition to affecting the shape of the photon assisted quasiparticle tunneling steps, the dc voltage dependence of V_ω also affects the shape of the ac Josephson effect steps [Shapiro et al., 1964] which are the dc manifestation of the interaction of radiation with the *pair current.* The pair current, in the voltage bias case, is given by [Barone and Paterno, 1982]

$$I_J(t) = \sum_{n=-\infty}^{\infty} \sum_{m=-\infty}^{\infty} J_n(\alpha)\, J_m(\alpha) \{ I_{J1}[eV_o/\hbar + m\omega] \cos\{[(n+m)\omega + 2eV_o/\hbar\,]t + \phi\}$$

$$+ I_{J2}[eV_o/\hbar + m\omega] \sin\{[(n+m)\omega + 2eV_o/\hbar\,]t + \phi\}\} \qquad 6\text{–}7$$

where ϕ is a constant and $\alpha = eV_\omega/\hbar\omega$. The current has a dc component for $V_0 = -(n + 1)\hbar\,\omega/2e$. From this equation, we see that $V_\omega(V_o)$, I_{J1}, and I_{J2} all affect the shape of the dc Josephson trace. With knowledge of the response functions, and by changing the phase ϕ, one could possibly determine the Josephson sine and cosine currents.

6.2 Review of Previous Work

In order to measure directly the effect of G_Q and B_Q (an indirect measurement of G_Q and B_Q can be made by studying the shape of the dc I-V curve, as shown in the previous section), Hu et al. (1990a,b) used a resonant technique. The circuit diagram used in their analysis is shown in Fig. 6-5c. Essentially, by using a Michaelson interferometer, they measured the power coupled into the tunnel junction as a function of the input frequency using the tunnel junction I-V curve as a direct detector (section 2.2.7). This method is only good at low powers where the tunnel junction response is linear to the applied power, hence their measurement is for $\alpha << 1$ and uses eqs. 6-4 and 6-5. When

B_Q is resonant with the geometric capacitance and the on chip tuning inductor, B_{stub}, they see a peak in the power coupled into the tunnel junction. The resonant condition is

$$B_Q + \omega C + B_{Stub} = 0 \qquad 6\text{-}8$$

B_Q is found using eq. 6-8 while G_Q can be derived from the width of this resonance. Their results are shown in Fig. 6-5a and b. The shift in the resonant frequency vs. bias voltage shows that B_Q is becoming more negative as the voltage is increasing. The 3 dB width of the peak measures the match between G_Q and the antenna output admittance, Y_A, which is real. Large peak widths correspond to large conductance in this resonant circuit. Unfortunately, this technique, although showing the existence and effect of the quantum admittance elements, was not able to look at the high power case since the junction response to the input voltage is not linear in this case. This technique was also limited in the range of bias voltage over which G_Q and B_Q could be measured since at bias voltages below two photon steps below the gap, the junction response to radiation is very small. At the gap voltage and above, this method failed due the large mismatch between the output admittance of the antenna and the quantum conductance, as well as the fact that the large currents at these bias voltages cause significant shot noise. The published results did not show G_Q and B_Q calculated from the resonant frequency and 3 dB bandwidth, but instead plotted the experimentally determined and theoretically expected 3 dB bandwidth and resonant frequency.

6.3 Experimental Set-Up

Considerable interest exists in looking for G_Q and B_Q at large input powers and over the complete bias voltage range. In order to do this, we have used a standing wave technique, first suggested by D. Winkler. The experiment uses the fact that the junction admittance may not be matched to the output admittance of the wavegude. This mismatch

caused a standing wave to form along the waveguide. Using standing wave formulae and an equivalent circuit, the standing wave can be analyzed to determine the quantum junction admittance.

The experiment is conceptually very simply. Schematics of the set-up are shown in Figs. 6-6 and 6-7. All of the apparatus internal to the dewar was common to the mixing experiments described in chapter V, with the exception of the 23 dB cross coupler which was removed for these experiments. These will not be discussed here.

A monochromatic signal at the primary frequency was launched down the waveguide from the YIG source. This signal was at 87.1 GHz. At this frequency, we expect strong quantum effects since this corresponds to a voltage of 360 μV, which is greater than the width of the voltage rise of the devices that we studied (~ 150 μV). This signal was coupled through the the ridge transformer into the microstripline on the chip. From the microstripline, the signal traveled to the junction where some of it was absorbed, and some of it was reflected. For this experiment, the 23 dB cross coupler was removed in order to allow the incident and reflected wave to travel freely. The interference between the incoming wave and outgoing reflected wave caused a standing wave to form along the waveguide. This standing wave was measured by coupling a small amount of the power out of the wave and into a slotted line probe[1] [Matthews and Stephenson, 1968] which was inserted into the waveguide at room temperature.

It was important that the slotted line probe did not significantly alter the standing wave pattern. If the probe coupled out too much power (typical standing wave powers were nW), the experimental data were skewed and the probe itself could have caused a standing wave. The proper amount of power coupled into the standing wave probe was found by looking at the dc pumped I-V curve on the chart recorder. When the probe was in too deep (coupling out too much power), it was apparent in the pumped I-V trace as a

---

[1]Model W1818, Hitachi Ltd., Hitachi, Japan

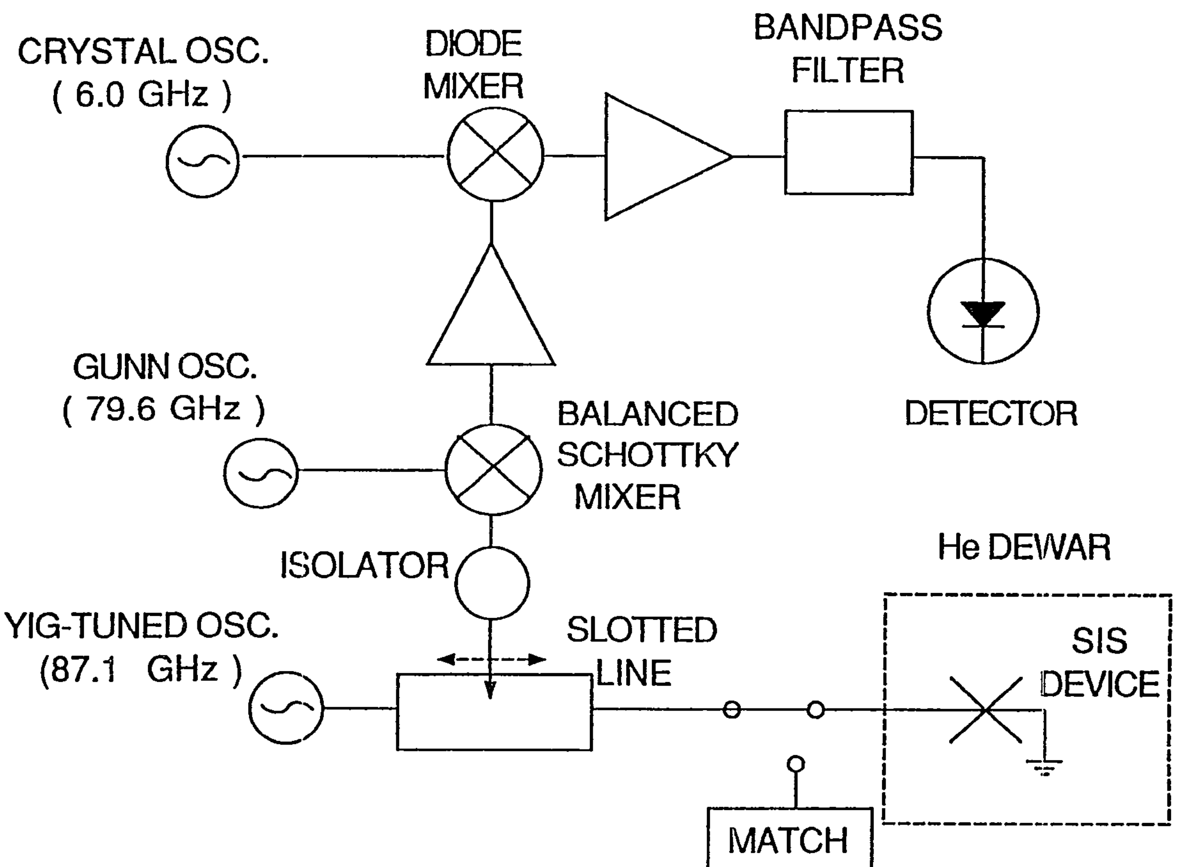

Fig. 6-6 A schematic of the standing wave measurement apparatus.

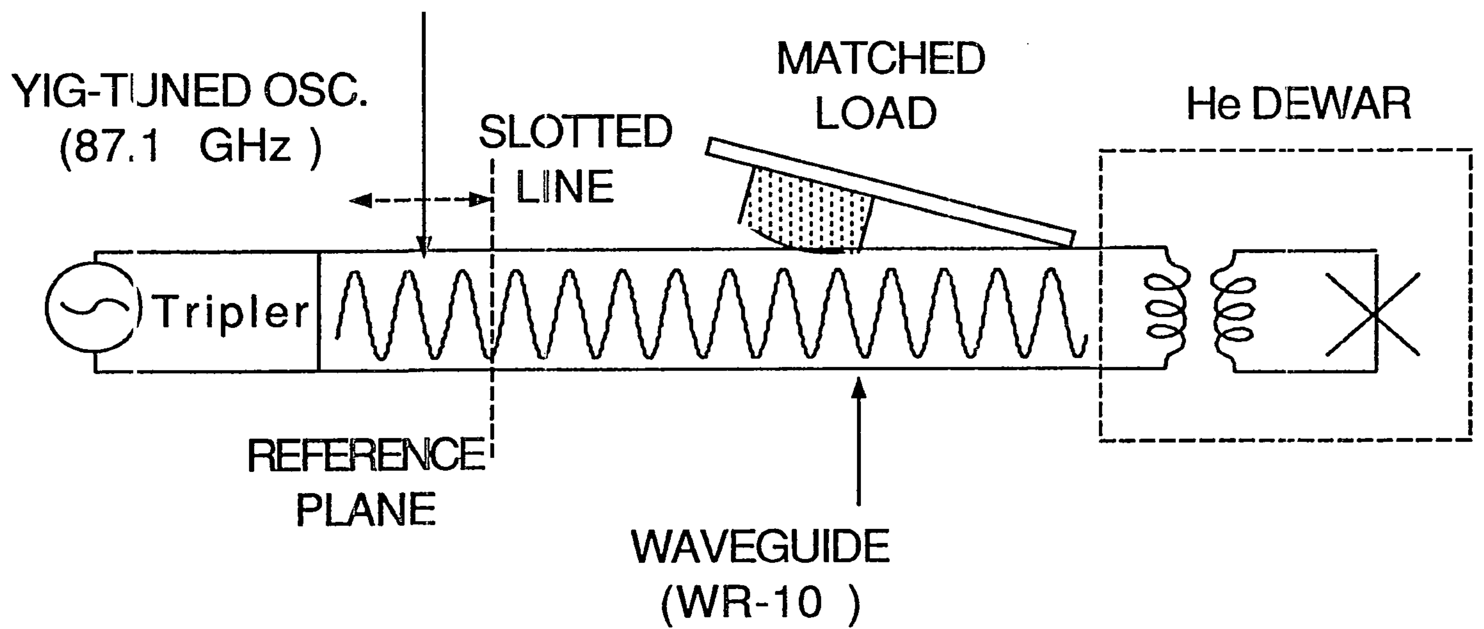

Fig. 6-7 A schematic of the waveguide section between the device and the YIG source. The power standing waves are sinusoidal, as shown. The ridge impedance transformation is shown here as a transformer.

reduction of the current flowing at a given bias point. The trade-off between power coupled out and the effect of the standing wave probe on the results led us to use arrays of junctions where the power levels were higher. The higher power levels used to pump an *array* allowed sufficient power to be coupled out of the standing wave probe without affecting the standing wave pattern or introducing standing waves due to the probe itself.

The power coupled into the standing wave probe (at the primary frequency) was sent through a 10 dB isolator to a room temperature balanced Schottky mixer.[2] The Schottky mixer had a noise temperature $T_M \approx 3000$ K. The Schottky mixer mixed the power coupled from the probe down to ≈ 7.5 GHz with the LO (secondary frequency) provided by a Gunn oscillator at 79.6 GHz. This 7.5 GHz power was amplified with a 4-8 GHz amplifier[3] and mixed in a diode mixer with a 6 GHz reference signal provided by a crystal oscillator.[4] The resultant 1.5 GHz power was amplified by 67 dB using MITEQ amplifiers. The 1.5 GHz signal passes through a 100 MHz bandpass filter centered at 1.5 GHz and is detected with an Anritsu power detector. Since a frequency counter was not available to determine the secondary frequency to within 100 MHz, the crystal oscillator frequency was tuned in order to find the correct frequency which went through the band-pass filter. The frequency was given by $f_{crystal\ osc.} + f_{bandpass} = f_{YIG} - f_{Gunn}$.

The band pass filter was used in order to limit the noise floor power incident at and around the primary signal frequency. This noise, coming primarily from the amplifiers in the circuit, was made to be less than 20% of the standing wave peak power by using the reduced bandwidth filter. The finite bandwidth necessary in order to be able to detect the drifting signal was about 10 MHz. The measured noise power was proportional to the bandwidth.

---

[2]Millitech Corp, S. Deerfield, MA

[3]Model AMT-8033, Avantek Corp., Santa Clara, CA

[4]HP8350B with 83525B RF plug in, Hewlett Packard, Palo Alto, CA

The frequencies used in the experiment were limited by the operational frequency range of the first amplifier. Since the first amplifier (between the Schottky mixer and the diode mixer) operated from 4-8 GHz, the limitation on the tripled YIG and Gunn frequencies was 4 GHz $< | f_{YIG} - f_{Gunn} | <$ 8 GHz. The range of the tripled YIG oscillator was 79.5 to 120 GHz and the range of the Gunn oscillator was 79 - 90 GHz. Given this and using the YIG oscillator as the primary signal source, the measurement could be done at any frequency between 79.5 and 98 GHz.

Attempts were made to use the Gunn oscillator as the primary signal source, with the YIG as the secondary oscillator. Unfortunately, the tripled YIG frequency output is susceptable to mechanical stress. The movement of the slotted line probe caused the secondarly oscillator to move, since the secondary oscillator is rigidly connected to the Schottky mixer, isolator, and slotted line probe (Fig. 6-6). The instability of the YIG could be overcome by retuning the frequency of the crystal oscillator at each new probe position, but this proved time consuming.

Reflections from the vacuum window of the dewar were found to cause standing waves. In order to limit these reflections, a half wave plate made of Rexolite ($\varepsilon = 2.56$) was used as the vacuum window of the dewar. The half wave plate thickness was empirically determined by measuring the transmission of the tripled YIG signal through the plate. The half wave plate passed 87-88 GHz radiation with < 3 % reflection. In order to measure the quantum admittance of the tunnel junction at frequencies different from 87-88 GHz, a new window could be made with a different band pass. No new window has been made at this time.

The main factor of the initial experimental errors was the frequency drift of the YIG oscillator. In addition to being stress sensitive, the YIG output frequency was also temperature sensitive. Initial measurements suffered from this drift. The initial drift, estimated to be ≈ 100 MHz at 90 GHz, constituted ≈ 0.1 % uncertainty in the primary

signal frequency. Given an estimated distance between the junction and the slotted line probe of 50 cm and a 0.1% shift in the frequency (wavelength), the number of wavelengths between the junction and slotted line probe was

$$\frac{50\ \text{cm}}{\lambda_g \pm 0.001\ \lambda_g} \approx \frac{50\ \text{cm}}{\lambda_g}(1 \pm 0.001) \qquad 6\text{-}9$$

Since $\lambda_g \approx 4.7$ mm, a one part in one thousand frequency shift caused an uncertainty in the location of the standing wave maximum of $\approx 0.05\ \lambda_g$. This corresponded to a phase uncertainty of ≈ 30 degrees! For a phase uncertainty of less than 3 degrees (necessary in order to analyze the data), the required experimental frequency must be stable to at least one part in 10,000. The stability was achieved by letting the YIG oscillator stabilize for more than an hour, heat sinking, and vigorous air cooling. The frequency stability was found acceptable when the down shifted power did not drift out of the 100 MHz bandwidth of the bandpass filter, <u>and</u> the data were reproducible during the entire run.

The YIG frequency was found by measuring the dc voltage at which the oscillator was biased and converting this to frequency through the calibration data. The wavelength of the standing wave in the waveguide also gave an independent measurement of the YIG frequency since [Moreno, 1948]

$$\lambda_g = \frac{\lambda}{[\ 1 - (\lambda/\lambda_c)^2\ ]^{1/2}} \qquad 6\text{-}10$$

where λ_g is the wavelength in the waveguide, λ is the wavelength in free space, and λ_c is the cutoff wavelength of the waveguide. The cutoff wavelength is given by twice the rectangular waveguide width; in WR-10, the cutoff wavelength is 5.1 mm. For an 87.1 GHz signal in a WR-10 waveguide, $\lambda_g = 4.70$ mm.

6.4 Measurement of the Standing Waves

6.4.1 Measurement of Power vs. Bias Voltage

In order to speed the experiment, computer control was used. The dc bias voltage was ramped form 0 V to about twice the gap voltage. While taking this bias voltage sweep, the slotted line probe position was kept constant. Each trace of output power vs. bias voltage was taken at a different probe position, 21 in all, covering more than 1/2 wavelength. Two typical power vs. bias traces are shown in Fig. 6-8. The data are for two probe positions separated by $\approx \lambda_g/4$. This separation is equivalent to ~ 180° phase difference. This phase difference is evident in Fig. 6-8. The output power at probe positions x and at x + $\lambda/4$ mirror each other since a maximum at one position corresponds to a minimum at the other. Also evident in the raw data was the fact that this mirroring was not true at low bias voltages. The reason for this was that the trapped flux in the junction changed during the run and reflections due to the *Josephson* currents could not be evaluated.

6.4.2 The Standing Waves

The lateral range of the slotted line probe was 10 mm. Since the wavelength was 4.70 mm, the distance between successive maxima of the standing wave was 2.35 mm; a range of 3 mm was found sufficient to quantify the standing wave. Two such waves are shown in Fig. 6-9.

The standing waves were corrected for the noise floor present in the experiment. The noise came primarily from the amplifiers. It was measured by decoupling the slotted line probe from the waveguide (or equivalently by turning off the *rf* supply). Once either of these was done, the power present at the detector was just due to the noise. The noise had no standing wave and was therefore independent of the probe position. Typically, it was less than 20 % of the peak power of the standing wave.

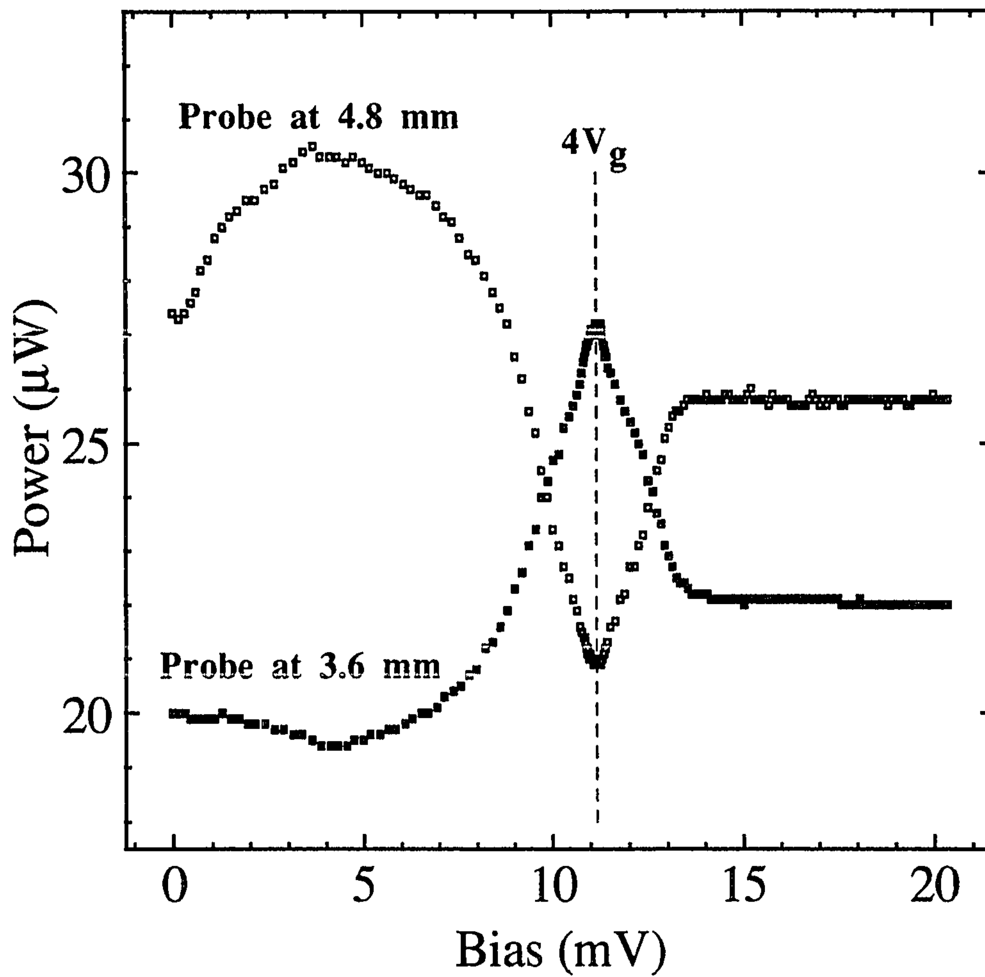

Fig. 6-8 A sample of the power vs. dc voltage data taken to determine the standing waves. The two probe positions shown here are separated by ~ $\lambda_g/4$ so that they are near mirrors of each other.

The measured power of the standing waves was arbitrary in that it depended upon the amplifiers present in the system. In most slotted line experiments, the measured power is normalized to that obtained from a short circuit where the reflection coefficient $\rho = 1$. This was not possible in our experiments since the device was at 4.4 K and in a dewar. It was not only inconvenient to replace it with a short circuit, but since this would involve warming and cooling the dewar, the frequency of the oscillators would be bound to drift significantly in the time it would take (the time would be on the order of a day). Since this was not feasible, we normalized the data to a matched load. The matched load was simply the hot/cold load described in section 5.1.2, but now used at room temperature. The matched load was inserted between the slotted line probe and the dewar. When the vane of the hot/cold load was up, the path was clear and was simply another section of waveguide. When the vane was down, it served as a matched termination at room temperature. The power coupled into the slotted line probe was then measured. For a matched load, $\rho \approx 0$, and we found no probe position dependence to the power. The power measured was simply the sum of the noise and the incident power. The hot/cold load had two advantages over the use of a commercial termination to determine the standing wave normalization. The first advantage is its -30 dB return loss compared to commercial terminations (~-20 dB). The second, and more important advantage, is that the use of the hot/cold load did not require breaking any waveguide connection during the experiment. The breaking of the waveguide connections can lead mechanical stress induced instabilities in the YIG frequency and irreproducible waveguide lengths. The hot/cold load was not designed for this purpose; it was just fortuitous that we had it at our disposal.

For comparison, I have shown a *calculated* short circuit standing wave in Fig. 6-9. In comparison to the data, it is very large. This indicates that the measured reflection coefficients (γ) of the data were small. For the four junction array data, the attenuation factor = $\gamma = 0.27$.

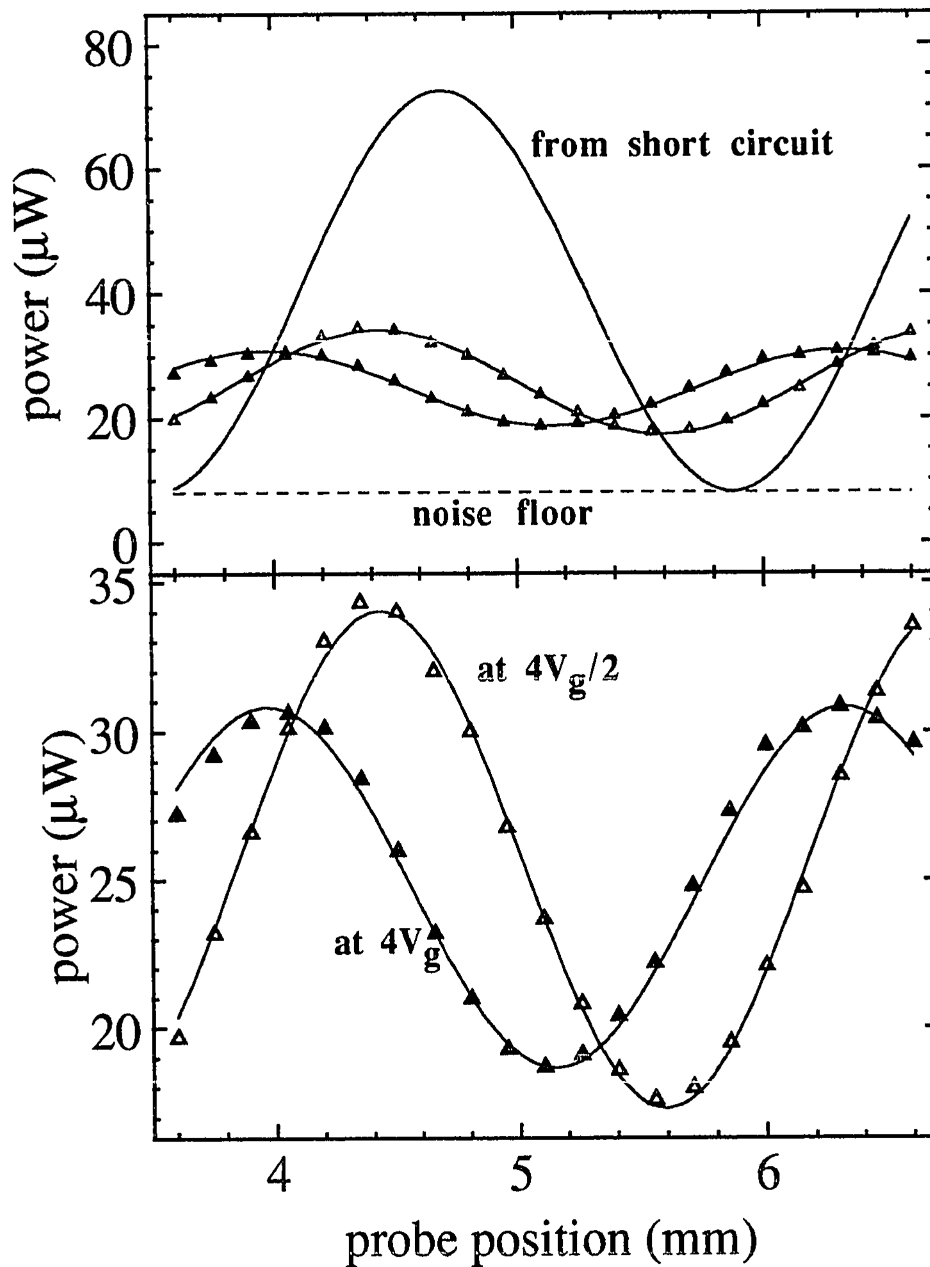

Fig. 6-9 The data is represented by the triangles; the least square fits are the solid lines. a) A wave which would result from the reflection from a short circuit is shown for comparison to two measured standing waves. b) The measured standing waves showing the quality of the least square fit.

Recently, work by Smith et al. (1991) has shown that it is possible to build a standing wave detector on chip, using an SIS junction as a power detector. The work by Smith et al. is designed to measure the match of other on-chip structures, and not to measure the quantum admittance of the tunnel junction. With suitable design, the work by Smith et al. could be extended to an on-chip measurement of the quantum junction properties.

6.4.3 Fits to the Standing Wave Equation

After subtracting the noise background, the experimentally determined standing waves were fit to the standing wave equation. The standing wave equation for *power* P of a standing wave at a distance d from the load is given by the interference between the incoming wave and the outgoing wave [Liboff and Dalman, 1985]

$$\frac{P}{P_{inc}} = [\ 1 + \gamma\rho\ e^{i(4\pi d/\lambda_g\ -\ \theta\ +\ \pi)}\ ]\ [\ 1 + \gamma\rho\ e^{-i(4\pi d/\lambda_g\ -\ \theta\ +\ \pi)}\ ]$$

$$= 1 + (\gamma\rho)^2 + 2\gamma\rho \cos\left[\frac{4\pi d}{\lambda_g} - \theta + \pi\right] \qquad \text{6-11}$$

where P_{inc} is the incident power (after subtraction of the noise background), ρ is the reflection coefficient ($0 \leq \rho \leq 1$), λ_g is the reduced wavelength, $\gamma = \gamma(d)$ is the attenuation factor, and θ is the phase of the standing wave. The factor of π is due to the quarter-wave microstripline. The experiment measured the distance between the slotted line probe and a fixed reference plane within the probe and not the total distance between the slotted line probe and the microstripline. We can express the total distance as a sum of the distance d_1 between the probe and the reference plane (shown in the horizontal axis of Fig. 6-9) and the distance d_2 between the reference plane and the microstripline, $d = d_1 + d_2$. The

relative location of the reference plane is shown in Fig. 6-7. We can then rewrite eq. 6-11 as

$$\frac{P}{P_{inc}} = 1 + (\gamma\rho)^2 + 2\gamma\rho \cos\left[\frac{4\pi(d_1 + d_2)}{\lambda_g} - \theta + \pi\right]$$

$$= 1 + (\gamma\rho)^2 + 2\gamma\rho \cos\left[\frac{4\pi d_1}{\lambda_g} - (\theta - \theta_R)\right] \qquad 6\text{-}12$$

where the unknown distance d_2 has been converted to an unknown phase θ_R given by $4\pi d_2/\lambda_g + \pi = \theta_R$.

The experiment measured the power vs. probe position as in Fig. 6-8 from which the standing waves like those shown in Fig. 6-9 were extracted and fit as also shown in Fig. 6-9. The uncertainty in the dc voltage was ±4 μV. What was finally extracted was $\gamma\rho$ and $\theta - \theta_R$ vs. dc bias voltage.

6.5 Transmission Line Matching Review

Once measured, the standing wave needed to be analyzed to extract the admittance due to the tunnel junction itself. The general equation for the matching of a transmission line to a terminating load is

$$\Gamma = \rho e^{i\theta} = \frac{(Z_L - Z_o)}{(Z_L + Z_o)} \qquad 6\text{-}13$$

where the characteristic admittance of the waveguiding path (waveguide-ridge-microstripline) is given by Z_o and the load impedance is Z_L. According to eq. 6-13, a short circuit, $Z_L = 0$, gives $\rho = 1$, $\theta = \pi$, while an open circuit, $Z_L = \infty$, gives $\rho = 1$, $\theta = 0$. The reflection coefficient, ρ, and phase angle, θ, are usually plotted on a Smith plot. The

Smith plot can be though of as simply a plot of Γ. With the center of the Smith plot at Z_o, and Z_L normalized by Z_o ($Z_L' = Z_L/Z_o$), eq. 6-13 is modified to

$$\Gamma = \rho e^{i\theta} = \frac{(Z_L' - 1)}{(Z_L' + 1)} \qquad 6\text{-}14$$

The distance from the center of the Smith plot gives the reflection coefficient ρ. For any positive and real Z_o, it is easy to show that $0 \leq \rho \leq 1$. The outer perimeter of the Smith plot, $\rho = 1$, contains the open circuit, the short circuit, and all non-resistive loads.

In order to translate these results into admittance, one simply performs the substitution $Y = 1/Z$. This keeps all phases and reflection coefficients the same. However, the location of all loads plotted on the Smith plot expressed as (real, imaginary) are rotated by π since the admittance and impedance Smith plots are rotated by π with respect to each other. In the *admittance* Smith plot, inductive loads, $Im(Z_L) > 0$, will appear in the lower half, while capacitive loads will appear in the upper half.

6.6 Results and Analysis

6.6.1 Equivalent Circuit

One of the major difficulties in determining G_Q and B_Q from the standing waves was determining the equivalent circuit to use in the analysis. The most general circuit is shown in Fig. 6-10a, if all of the reflections are at the tunnel junction. The device is driven by a current source through a characteristic impedance Z_o. In the experiment, the characteristic waveguide impedance (346 Ω) was transformed through a ridge transformer (see section 5.1.1) and microstripline. These transformations are all lumped into Z_o.

The load impedance was composed of contributions from the quantum tunnel junction, its geometric capacitance, stray capacitance, stray inductance, and the on-chip terminating impedance. If all of the elements other than the quantum elements are

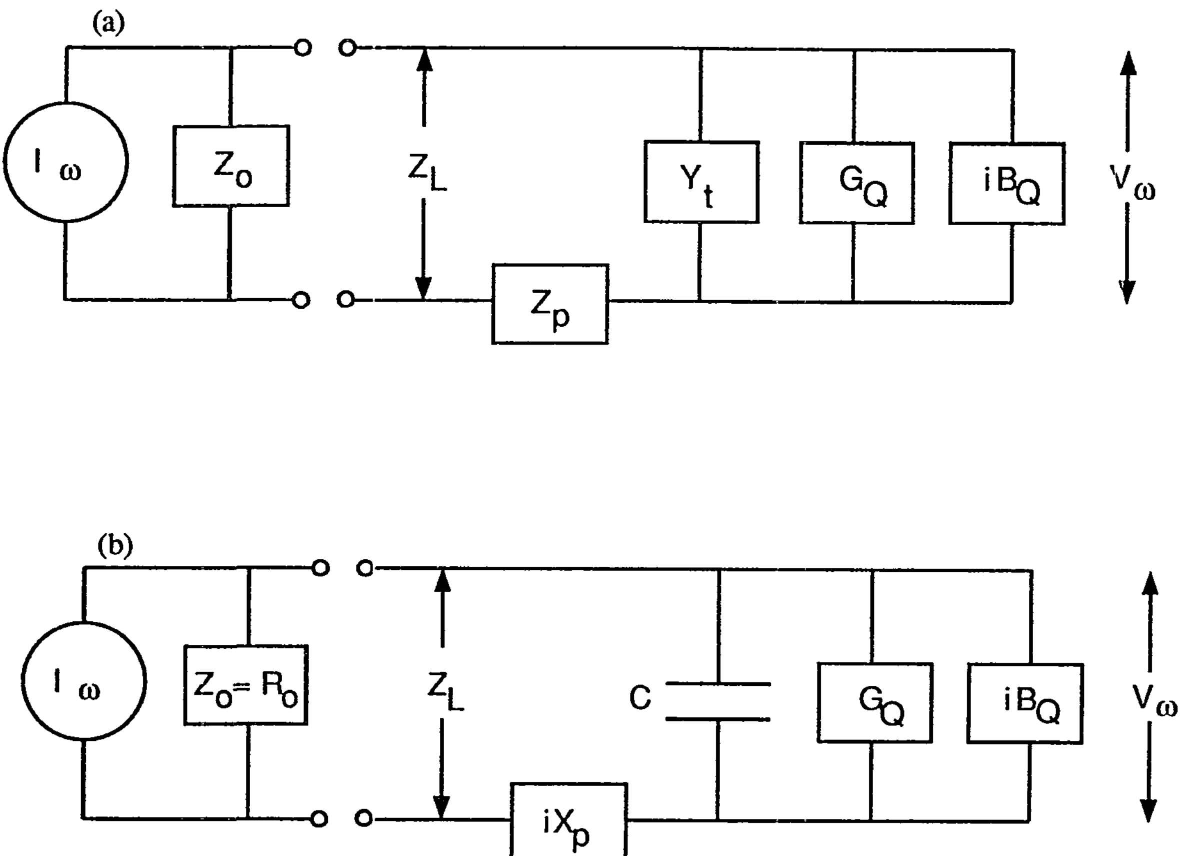

Fig. 6-10 a) The most general equivalent circuit. b) A simplified version of a) which is used in the analysis of the standing wave patterns.

considered as unknowns, the general circuit contains 6 unknowns. These are the real and imaginary parts of the input impedance, passive terminating impedance, and the shunting admittance. In order to make the solutions tractable, the general circuit of Fig. 6-10a has been simplified to that shown in Fig. 6-10b. This circuit ignores all stray impedance values and assumes that the shunting is all through the device capacitance, $i\omega C$, the input impedance is real, R_o, and the terminating impedance is purely reactive, iX_p, and is equal to -i 5 Ω at 87.1 GHz. This terminating impedance, due mostly to the radial stubs, was determined from the scale modeling results [Winkler et al., 1989]. The simplified load impedance is

$$Z_L = iX_p + (G_Q + iB_Q + i\omega C)^{-1} \quad \text{6-15}$$

6.6.2 Γ for the Four Junction Array

The direct measurement of G_Q and B_Q was performed on an array of two junctions and an array of four junctions. Since the four junction array required higher input power levels to pump it, the reflected power levels were greater. Partly because of this, the four junction data are less noisy and fit theoretical predictions more closely. For all of the array analysis, we have assumed that the tunnel junctions were identical to each other and that all of the relevant equations were simply transformed to the correct array equations by changing ω to $p\omega$, where p is the number of junctions in the array.

The unpumped I-V of the four junction array, device J, and the three different pumped I-V curves studied are shown in Fig. 6-11. The three powers which produce the pumped I-V's shown here were chosen to show G_Q and B_Q when 1. only single photon processes are available (curve b), 2. for a typical mixer pumped I-V (curve c), and 3. for a very large input power where the multiple photon processes contribute greatly to the current (curve d).

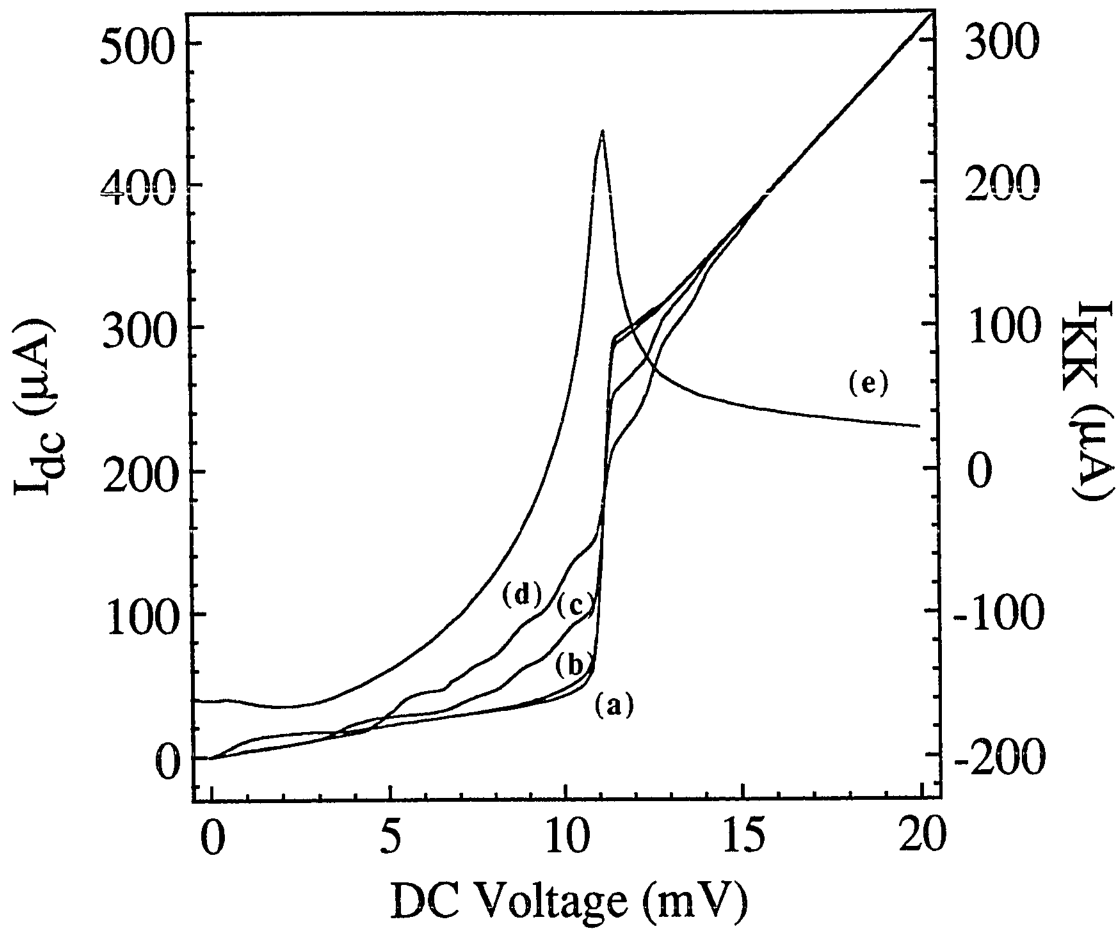

Fig. 6-11 a) The dc I-V trace of the four junction array, device J. b,c,d) The pumped I-V trace using three different power inputs. e) The Kramers-Kronig transform of a).

The measured $\gamma\rho$ and $\theta - \theta_R$ for the low input power are shown in Fig. 6-12. The solid lines are the theoretical predictions; we shall discuss these in section 6.6.3. The dashed lines indicate the limits of the single photon processes. The usual definition of the gap voltage is for a single junction. In the text, I will refer to the array cumulative gap voltage as the array-gap voltage. The photon width in this case is $4\hbar\omega/e$.

The data points were not evenly spaced in voltage. The load line for the biasing was shallow such that it was nearly a dc current bias. This caused many data points to be taken where the current was changing rapidly with voltage, i.e., near the array-gap voltage.

We see in Fig. 6-12 that the reflection coefficient was large at low bias voltages, low at high bias voltages, and had some structure near the array-gap voltage. We can understand this from the equivalent circuit of Fig. 6-10b and eq. 6-15 for the load impedance. Although eqs. 6-14 and 6-15 could be solved explicitly for G_Q and B_Q in terms of ρ and θ, the solutions are algebraically complicated and offer little insight. In fact, solutions to seemingly simple equations like these are what make people appreciate Smith charts. Looking at eq. 6-15, we see that the real and imaginary parts of the load impedance are

$$\mathrm{Re}(Z_L) = \frac{G_Q}{G_Q^2 + (B_Q + \omega C)^2} \qquad 6\text{-}16$$

$$\mathrm{Im}(Z_L) = X_p - \frac{B_Q + \omega C}{G_Q^2 + (B_Q + \omega C)^2} \qquad 6\text{-}17$$

In order for the transmission line to be perfectly terminated, ($\rho = 0$), $\mathrm{Re}(Z_L) = R_o$ and $\mathrm{Im}(Z_L) = 0$. From the form of these equations, we see that near the gap voltage, where we expect B_Q to be large and negative, there can be a resonant condition where B_Q tunes the geometric capacitance, thus reducing the reflection coefficient. This condition is $B_Q + \omega C = 0$. At this point, $\mathrm{Re}(Z_L) = 1/G_Q$, and $\mathrm{Im}(Z_L) = X_p$. Since X_p in our measurements was

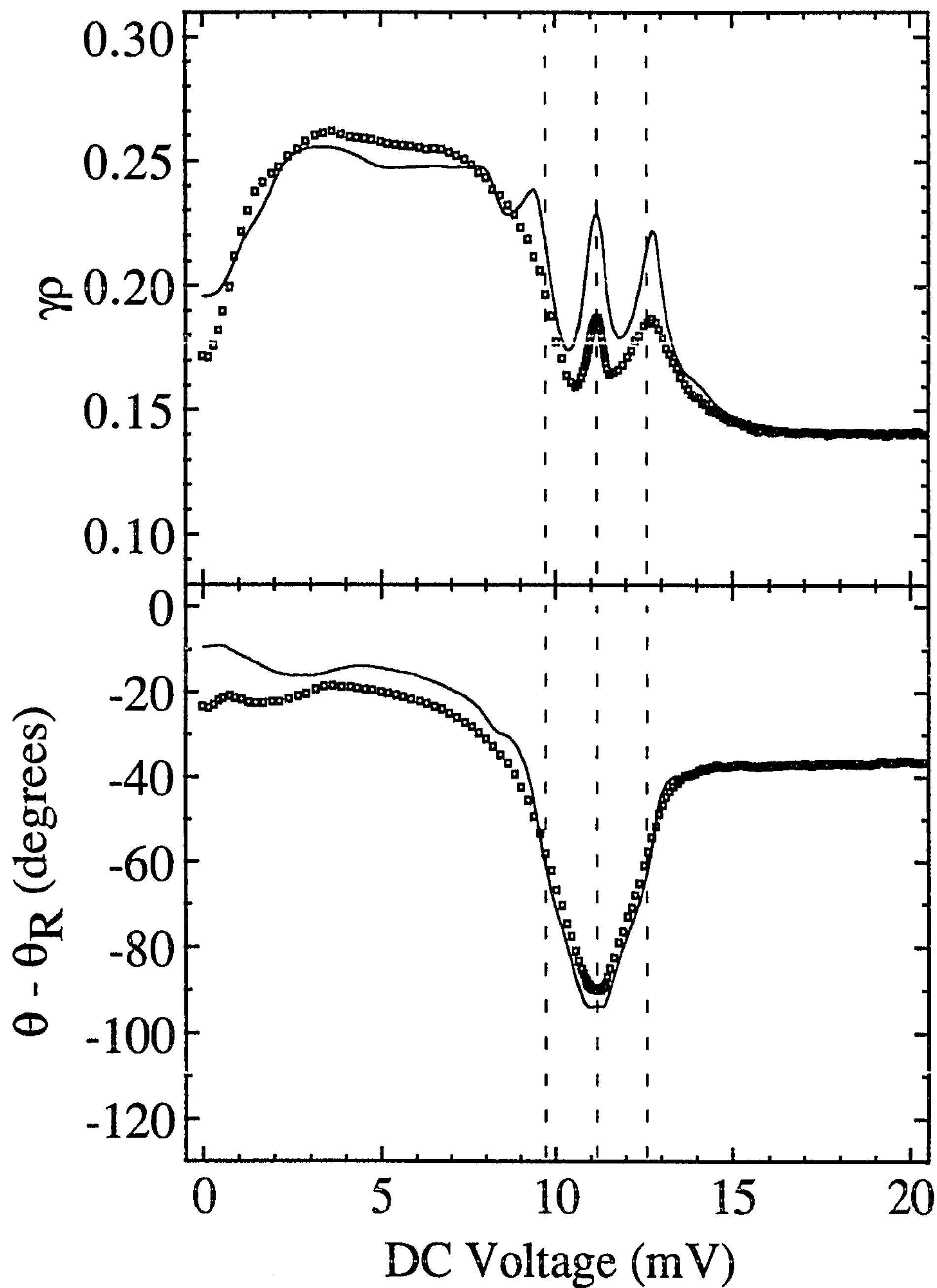

Fig. 6-12 The measured reflection coefficient and phase of device J for the low-power input corresponding to curve b) in Fig. 6-11. The experimental data is the open squares; the expected results from theory are the solid lines. The dashed vertical lines correspond to (from left to right), one photon width below the array-gap, the array-gap, and one photon width above the array-gap voltage.

small (-5 Ω) compared to typical ωC values (+20 Ω) is was not surprising that close to the gap voltage, there were minima in the measured reflection coefficient. The exact dc voltage at which the minima occured was dependent upon all the circuit parameters. As the dc voltage was increased toward the gap voltage from a photon point below, the susceptance became more negative. In doing so, the susceptance passed through a resonance with the geometric capacitance where the reflection coefficient was near minimum. Once past this resonance, the reflection coefficient increased again until the array-gap voltage. A second resonance occured above the gap where the resonance condition was met again. The exact bias location of the resonance can be found by solving for the dc bias voltage for which ρ is a minimum.

The large value of the γρ at low bias voltages (~3-9 mV) came from the fact that the conductance was small at these bias voltages. The load impedance was therefore large, on the order of 500 Ω. This gave a large mismatch between this impedance and the 50 Ω input impedance which caused a large reflection coefficient. The match was much better well above the array-gap voltage ($V_0 > 17$ mV), where $R_L \approx G_n/[G_n^2 + (\omega C)^2] \approx 20\ \Omega$.

Naively, one might expect that the absolute minimum γρ should occur at the dc bias voltage where B_Q resonates the device capacitance. The reason that this is not the case is that G_Q was large within one photon width of the gap, such that the load impedance, even at resonance, is as small as 11 Ω. This gave a large mismatch with the input 50 Ω.

The measured γρ and $\theta - \theta_R$ vs. dc voltage are shown in Fig. 6-13 for the power corresponding to curve c in Fig. 6-11. This power was a typical mixer input LO power. There was more structure in γρ vs. dc voltage than in the low power data. This was due to the multiple photon processes that were now possible at this increased power. We see peaks at a distance of approximately two photon widths from the array-gap. At an even larger input power corresponding to curve d in Fig. 6-11, we see that peaks appearing at three photon widths from the gap (Fig. 6-14).

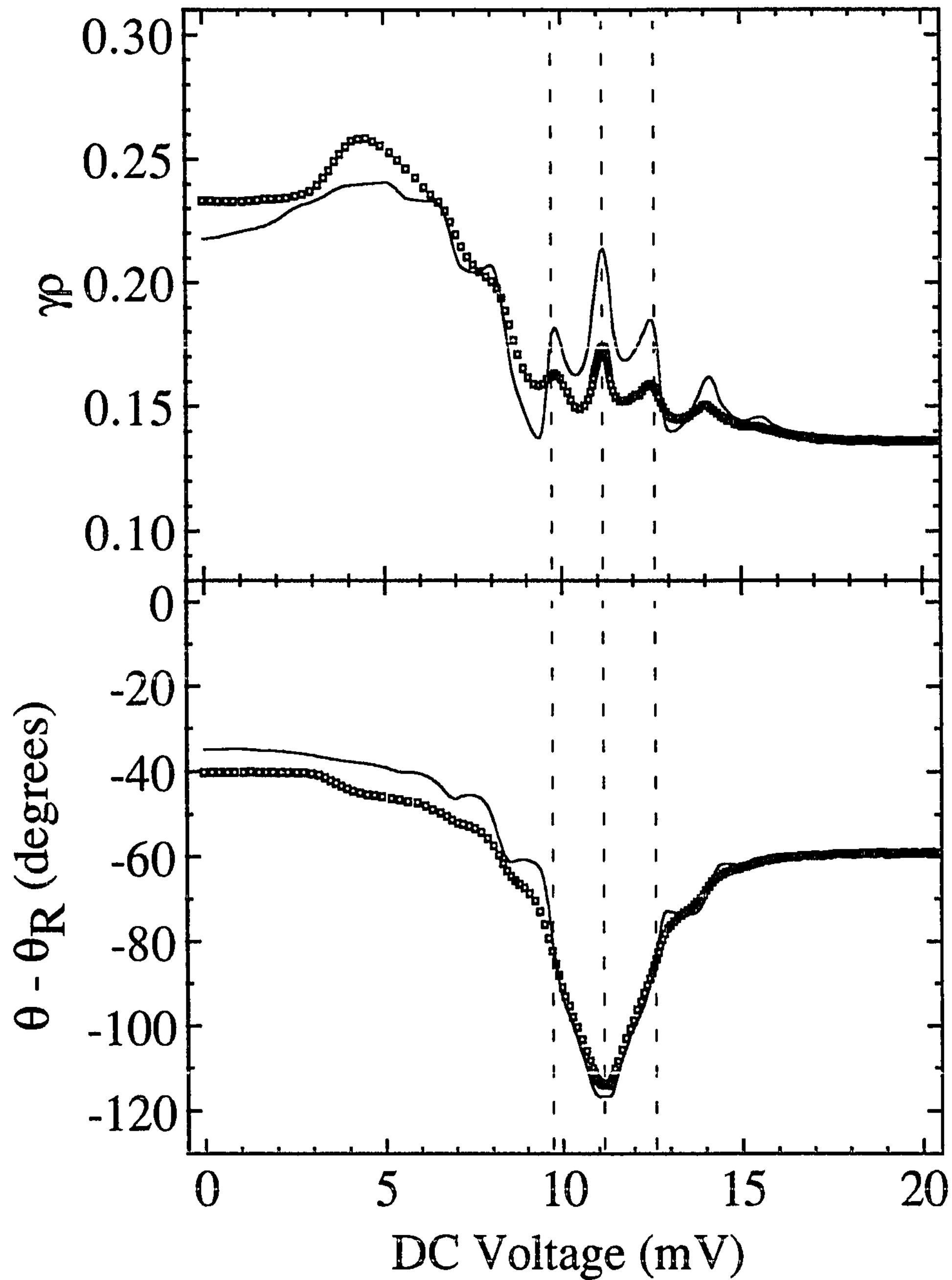

Fig. 6-13 The measured reflection coefficient and phase of device J for the medium-power input corresponding to curve c) in Fig. 6-11. The experimental data is the open squares; the expected results from theory are the solid lines. The dashed vertical lines correspond to (from left to right), one photon width below the array-gap, the array-gap, and one photon width above the array-gap voltage.

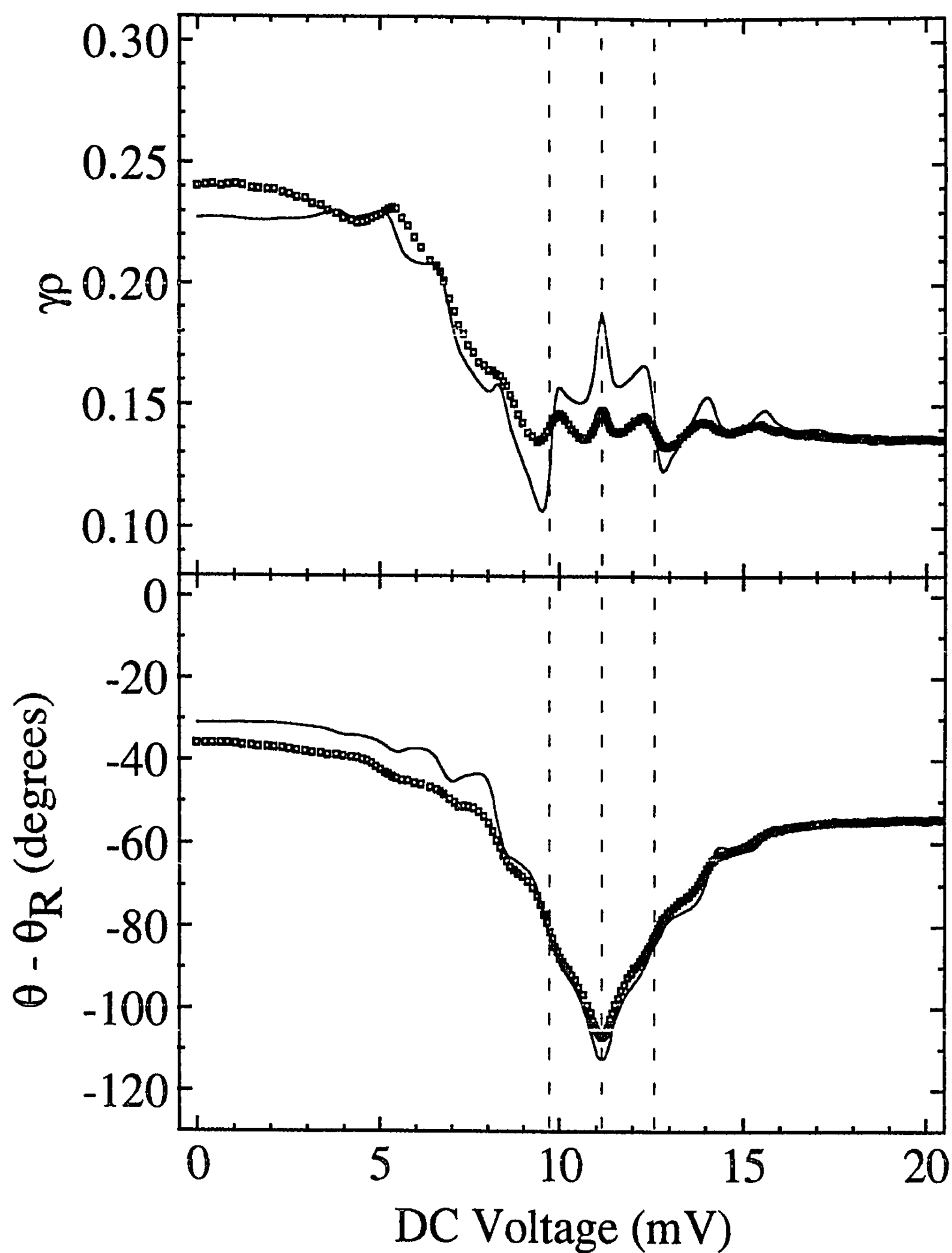

Fig. 6-14 The measured reflection coefficient and phase of device J for the high-power input corresponding to curve d) in Fig. 6-11. The experimental data is the open squares; the expected results from theory are the solid lines. The dashed vertical lines correspond to (from left to right), one photon width below the array-gap, the array-gap, and one photon width above the array-gap voltage.

6.6.3 Theoretical Predictions

In order to understand the results more fully, we need to understand the theoretical predictions. The theoretical predictions are in two parts: 1) G_Q and B_Q, and 2) γp and $(\theta - \theta_R)$. It is simplest to look first at the theoretically expected G_Q and B_Q.

The predictions for G_Q and B_Q are given by eqs. 6-2 and 6-3. The input parameters are the angular frequency, ω, the unpumped I-V curve, the KK of the unpumped I-V curve, and $V_\omega(V_o)$. The first three are trivial. The frequency is known from the oscillator and standing waves, the I-V curve is measured, and the Kramers-Kronig transform is calculated from the I-V curve. The difficulty arises in determining the bias dependence of V_ω. There are three paths to follow. The first is to do as was done for the mixer predictions (section 5.4.2) and self-consistently determine a fixed embedding admittance which gives the measured pumped I-V shape. The second approach is to solve the Tien-Gordon expression (eq. 5-14) at each V_o for V_ω. The third approach is to use the equivalent circuit of Fig. 6 - 10b to determine the embedding admittance and use this to self-consistently solve for $V_\omega(V_o)$. After using one of the methods to solve for $V_\omega(V_o)$, eqs. 6-2 and 6-3 can be solved. The voltage match method [Skalare, 1989] gives Y_{emb} = (16.1 + i 23.2) mmhos and the equivalent circuit gives Y_{emb} = (19.8 + i 24.7) mmhos. These two results are essentially equivalent in that they produce nearly the same theoretical pumped I-V curve. The theoretically calculated G_Q and B_Q for the high pump power case found using the equivalent circuit and the Tien-Gordon equation are shown in Fig. 6-15. We see that there is little difference in the prediction of two methods. The main difference is right at the array-gap voltage where the unpumped and pumped I-V curves cross each other. Near this point, it is difficult to solve the Tien-Gordon expression accurately since the currents are so close to each other. The data points at the array-gap voltage therefore may be spurious. Since the three methods give essentially equivalent results, we have used the easiest, which is the equivalent circuit.

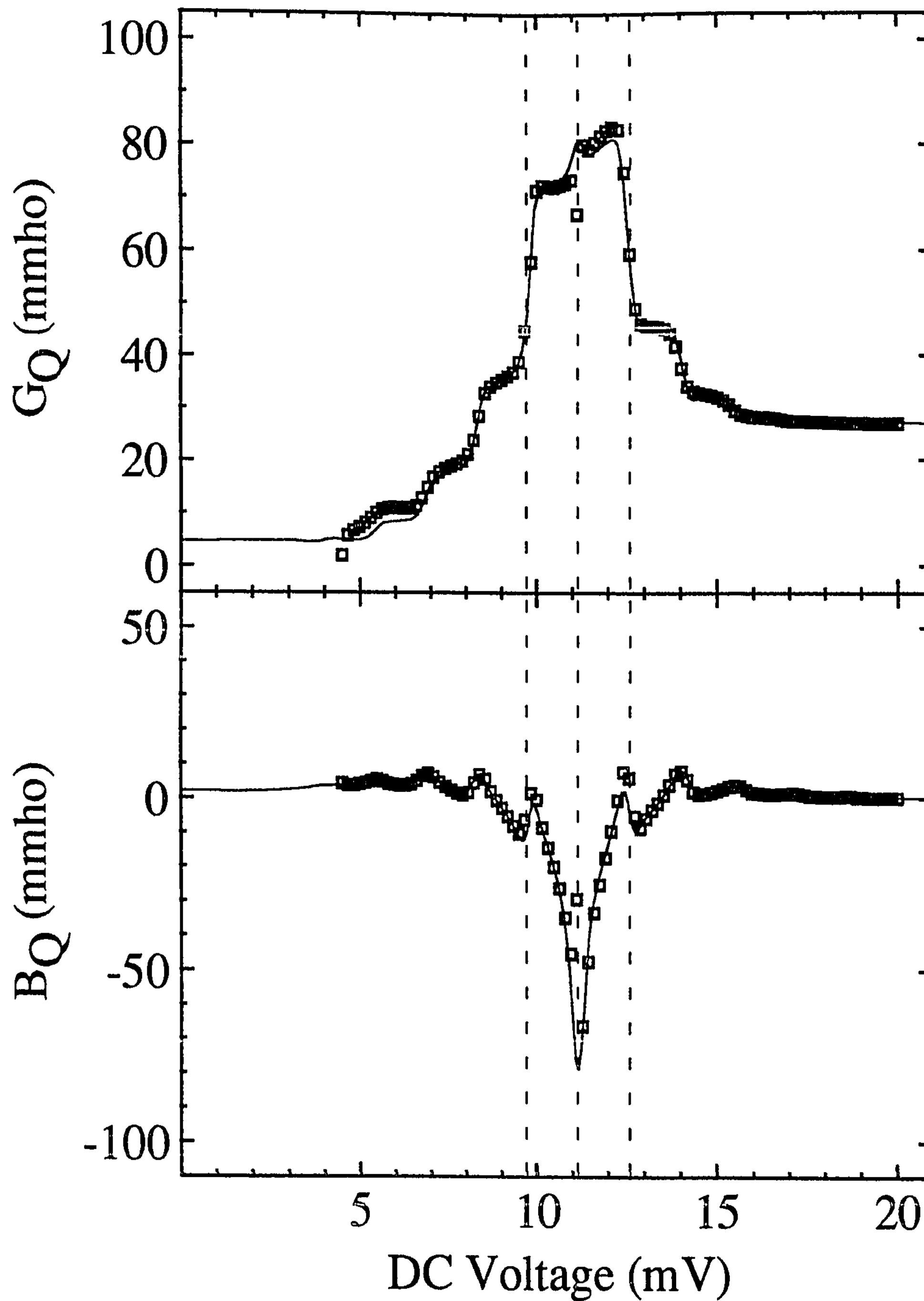

Fig. 6-15 The theoretical G_Q and B_Q of device J for the high-power case using the equivalent circuit (solid lines) and the Tien-Gordon expression (open squares). The results are essentially equivalent. The dashed vertical lines correspond to (from left to right), one photon width below the array-gap, the array-gap, and one photon width above the array-gap voltage.

The second part of the theoretical predictions is to determine what is expected for $\gamma\rho$ and $\theta - \theta_R$ vs. dc voltage. The theoretical predictions for ρ and θ were fairly straightforward. Having solved for G_Q and B_Q as a function of dc voltage, one simply solved eq. 6-15 for the total load impedance and 6-13 for ρ and θ. The low-power theoretical predictions for ρ and θ are shown in Fig. 6-16. We see that the load impedance covers a large portion of the Smith plot. ρ changes from a minimum at 20 mV to a maximum at about 4 mV. The most change is seen near the array-gap, from to 9 to13 mV. Over the entire bias voltage range, the phase changes by 100 degrees.

The attenuation γ and relative phase θ_R were solved for by normalizing the theoretical predictions to the experimental results at high bias voltages. One can see in Fig. 6-16b that above 15 mV the admittance of the load is not changing. G_Q converges to the results of a classical resistor at high bias, G_Q ----> $1/R_n$. B_Q goes to 0. This is easily seen in the constructions of Figs. 6-1 and 6-2. The total load impedance at high bias is then given by

$$Z_{L\ \text{high bias}} = iX_p + (\ 1/R_n + i\omega C\ )^{-1} \tag{6-18}$$

By comparing the theoretically determined ρ and θ at high bias voltage with the experimentally determined $\gamma\rho$ and $\theta - \theta_R$, one determines the attenuation and phase factor. It should be noted that the attenuation is distance dependent and the measured reflection coefficient goes as $\rho\ \exp(-\kappa d)$ where κ is a constant and d is the distance of the measurement from the load. At far distances from the load, the measured $\rho = 0$ since all that is sent down the waveguide will be lost before coming back. In this way, it looks like a perfect match. We did not see distance dependent attenuation in the 10 mm length over which the slotted line probe could be moved. Therefore, the assumption of a constant attenuation over the 3 mm length of these measurements was valid.

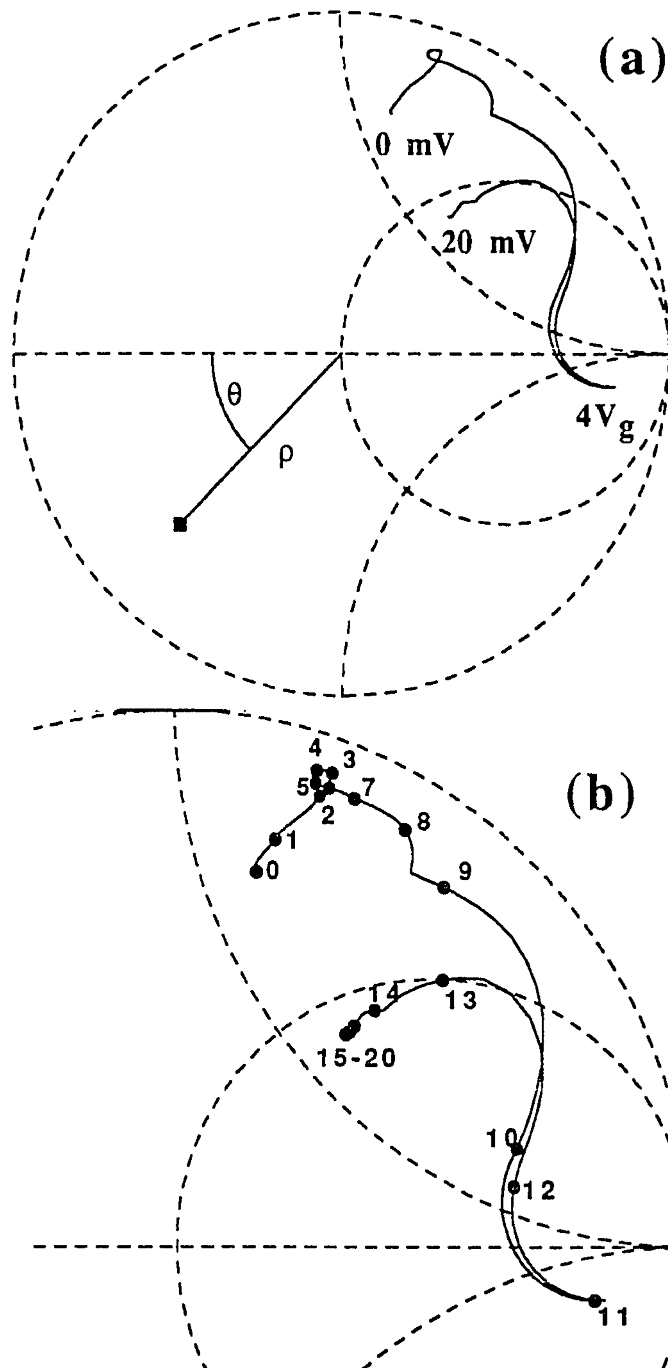

Fig. 6-16 a) The reflection coefficient and phase are defined as shown. The outer circle is described by ρ = 1. The theoretically expected load admittance of device J for the low-power input is shown by the solid line. b) An expanded view of the expected load admittance showing the location of the admittance at various bias voltages. The bias voltages are in mV.

Once γ and θ_R are determined, the theoretical predictions can be plotted against the experimental results as already shown in Figs. 6-12, 6-13, and 6-14. The data and the theoretical prediction showed similar structure, with the theoretical predictions being sharper than the experimentally measured data. A discussion of the discrepancies between the theory and the experiment is given in the section 6.7.

6.6.4 The Measured Quantum Admittance vs. DC Voltage

In order to find the experimentally measured quantum conductance and susceptance, the experimental data were corrected for γ and θ_R and then eqs. 6-14 and 6-15 were solved for G_Q and B_Q. The results for the low-power run are shown in Fig. 6-17. We see that the agreement was fairly good across the entire dc bias range. With the exception of the peak seen at the array-gap voltage, G_Q matches with theory very well. The conductance was large within one photon step of the gap, as expected by theory (shown by the solid line). The susceptance showed *all three* peaks predicted by theory. These peaks were spaced one photon width apart and correspond to the logarithmic singularity in I_{qp1}. This is the first reported observation of the singularity.

The results for the medium and high input power are shown in Figs. 6-18 and 6-19. They are plotted on the same scale to show that the magnitudes of G_Q and B_Q within one photon width of the array-gap voltage, both experimental and theoretical, were decreasing with increasing input power. As more photon processes became active, the single photon process currents decreased. All three power runs showed the singularity in B_Q. At high input power (Fig. 6-19), there was no longer a capacitive peak at dc bias voltages separated from the array-gap voltage by a photon width. The experimental data shows the first order peaks where they were theoretically expected, at bias voltages closer to the array-gap voltage. One also sees in the three traces an increase in the structure of the admittance as higher order photon processes become stronger. The high power conductance trace (Fig. 6-19) showed clear evidence for *fourth* order photon processes.

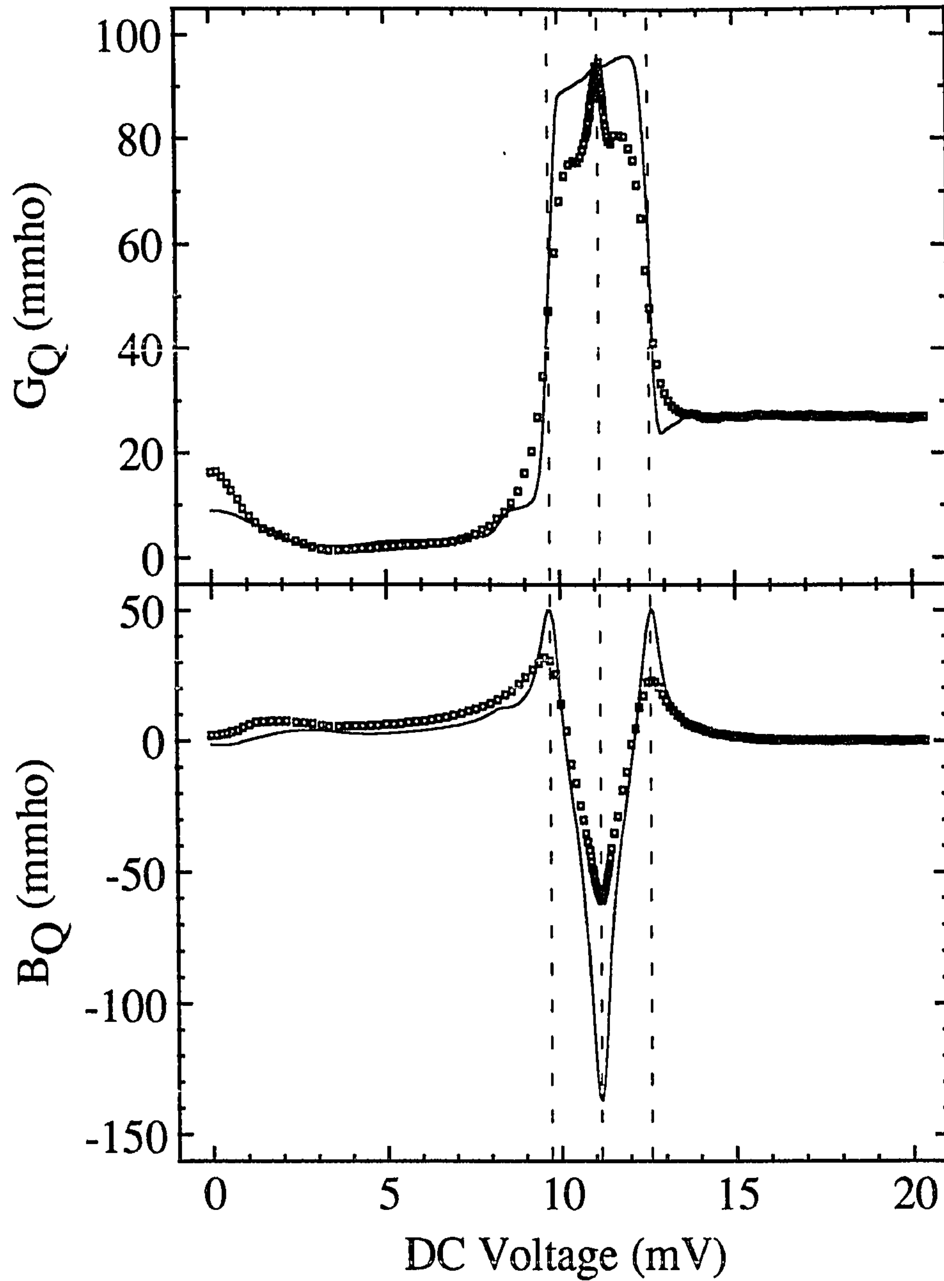

Fig. 6-17 The experimentally determined (open squares) and theoretically calculated (solid lines) G_Q and B_Q of device J for the low input power case. The dashed vertical lines correspond to (from left to right), one photon width below the array-gap, the array-gap, and one photon width above the array-gap voltage.

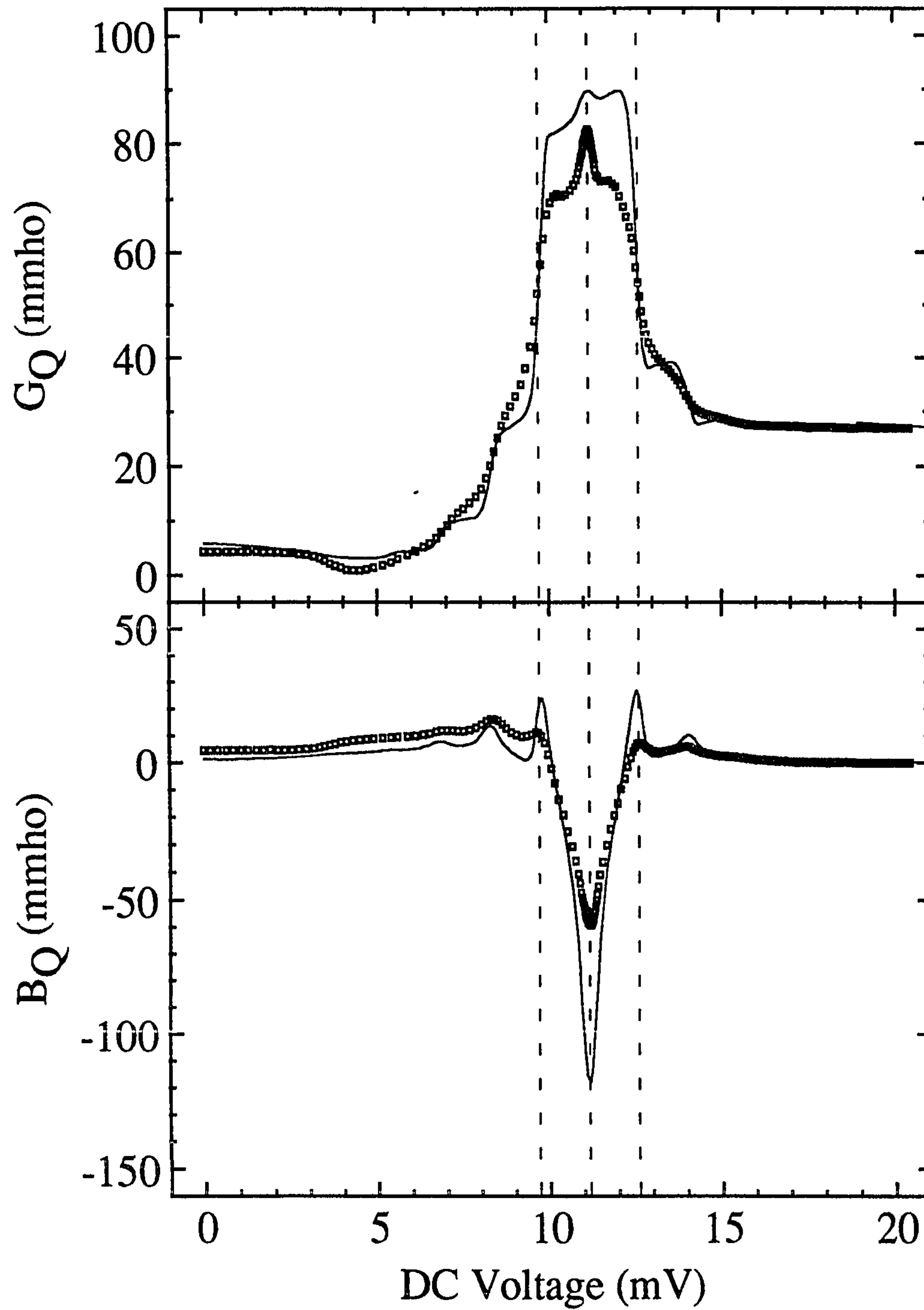

Fig. 6-18 The experimentally determined (open squares) and theoretically calculated (solid lines) G_Q and B_Q of device J for the medium input power case. The dashed vertical lines correspond to (from left to right), one photon width below the array-gap, the array-gap, and one photon width above the array-gap voltage.

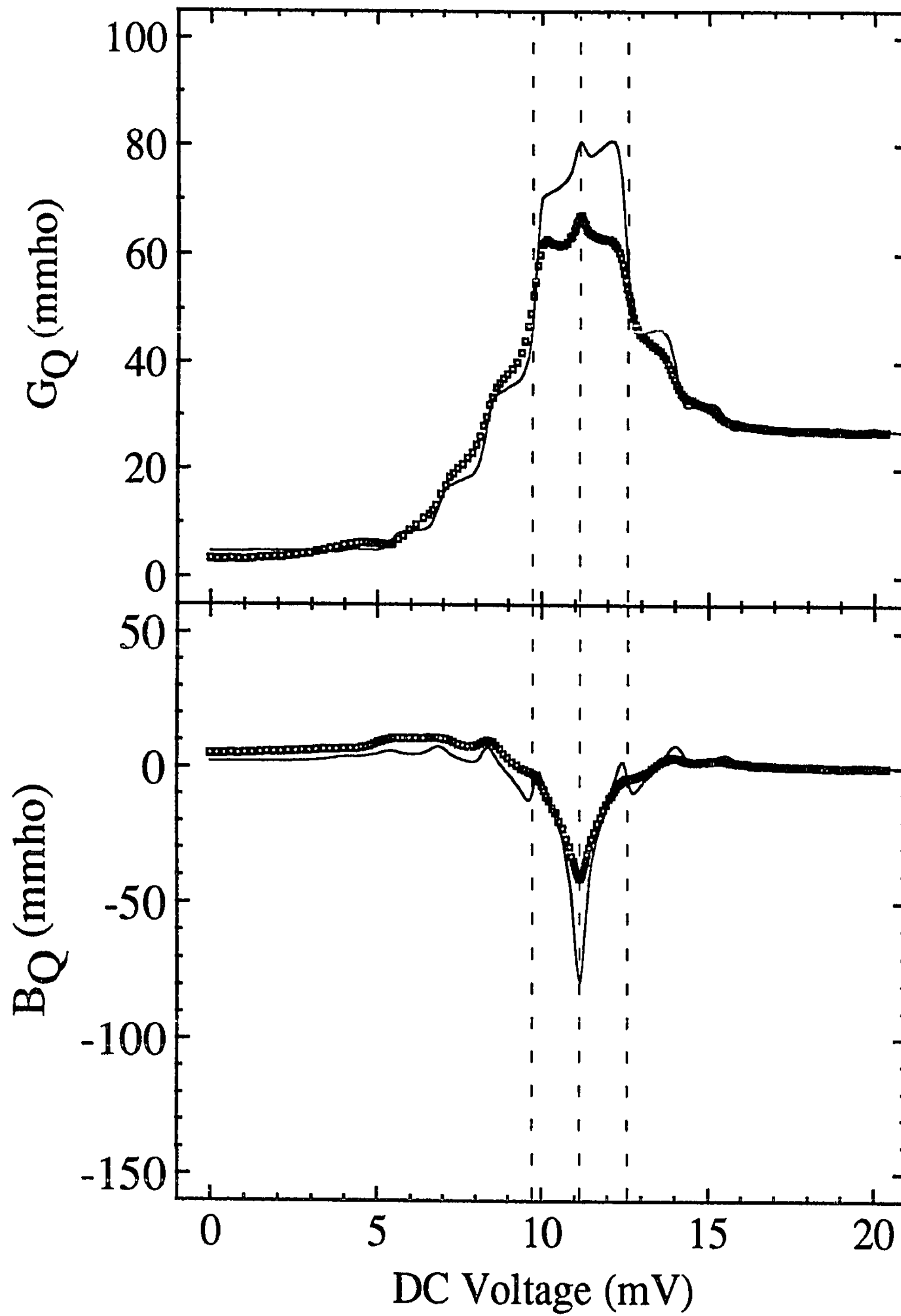

Fig. 6-19 The experimentally determined (open squares) and theoretically calculated (solid lines) G_Q and B_Q of device J for the high input power case. The dashed vertical lines correspond to (from left to right), one photon width below the array-gap, the array-gap, and one photon width above the array-gap voltage.

6.7 Discussion of Discrepancies

The reason for the disagreement between our experimental measurement of the quantum admittance and theoretical predictions was probably due to the uncertainty in the equivalent circuit parameters, noise rounding, and the non-ideal junction. I will treat each of these possibilities separately.

6.7.1 Passive Terms and Noise Rounding

By passive terms, I mean anything in the experiment which was not dc bias dependent. This included the output impedance of the ridge and microstripline, the geometric capacitance, stray capacitances and inductances, the on-chip structures, the vacuum window, and all elements in the waveguide path. It also refers to any thermal noise rounding which might affect the data.

The vacuum window and all waveguide connections had been carefully made such that they caused less than 3.5% of the incoming signal to be reflected. This was important since reflections along the waveguide were very difficult to model since the electrical location of the reflection point and the magnitude of the attenuation at that point must be known.

The on-chip circuitry was more difficult to determine. By looking at the pumped I-V curves, as we did in section 5.4.3, we could determine the embedding admittance and from this determine the passive on-chip elements. Unfortunately, this also involved knowing the exact electrical length of the ~ $\lambda/4$ microstripline section. Since this length depended upon the sample mounting, it was difficult to determine. In any case, the embedding admittances determined from the fitting were close to those expected from the equivalent circuit of Fig. 6-10b, but the fits were not perfect. Since we did not have a good fit to the pumped I-V curve of an array across the whole dc bias voltage range, we could not make any prediction based on the determined embedding admittance.

What we could look at was the effect of changing values of the circuit elements in the equivalent circuit of Fig. 6-10b. The specific capacitance of $Nb/AlO_x/Nb$ junctions is 45 ± 5 fF/(μm)^2 [Lichtenberger, et al., 1989; Han et al., 1989]. Given a current density of 5000 A/cm^2 and $R_n = 39\ \Omega$, ωC of the array device J was 24.7 ± 2.7 mmhos. Using this uncertainty in the capacitance, G_Q and B_Q are plotted in Fig. 6-20. We see that for the smaller capacitance, 22 mmhos, both the deduced G_Q and B_Q were reduced within one photon width of the array-gap voltage. Since the capacitance was smaller, it made up less of the load impedance of Fig. 6-10b. Thus the measured reflection coefficient change was attributed more to G_Q and B_Q. Since $i\omega C$ and iB_Q are both imaginary, they were indistinguishable in the circuit. A smaller capacitance (positive admittance) meant a smaller B_Q near the gap (negative admittance) to resonate it.

Surprisingly, the calculated values of G_Q were also strongly dependent upon the value of the capacitance in the equivalent circuit. The data were normalized well above the gap. At these bias voltages, most of the reflection was due to $i\omega C$ and $G_Q = 1/R_n$. A smaller capacitance gave a better expected match. When compared to the experimental data to determine the attenuation, the *smaller* capacitance in the circuit led to a *smaller* calculated attenuation. In other words, the smaller capacitance gave a load which was better matched. This is seen then at all dc voltages as a better match (G_Q closer to 20 mmhos) for the smaller capacitance of 22 mmhos compared to 24.7 mmhos.

The calculated experimental values of G_Q and B_Q were also be dependent upon the output impedance of the waveguiding system (waveguide, ridge, microstripline). This was perhaps more important than the uncertainty in the capacitance because we did not expect the output impedance to be 50 Ω. In fact, it would have been surprising if the machining of the ridge made it exactly 50 Ω. To complicate things, the $\sim\lambda/4$ 50 Ω microstripline will transforms the ridge output impedance from R_r into $\sim (2500\Omega)/R_r$. Ideally, one would have a 100 GHz network analyzer to measure the ridge and microstripline impedance. Unfortunately, we did not, so we were limited to educated guesses. In Fig. 6-21, we see

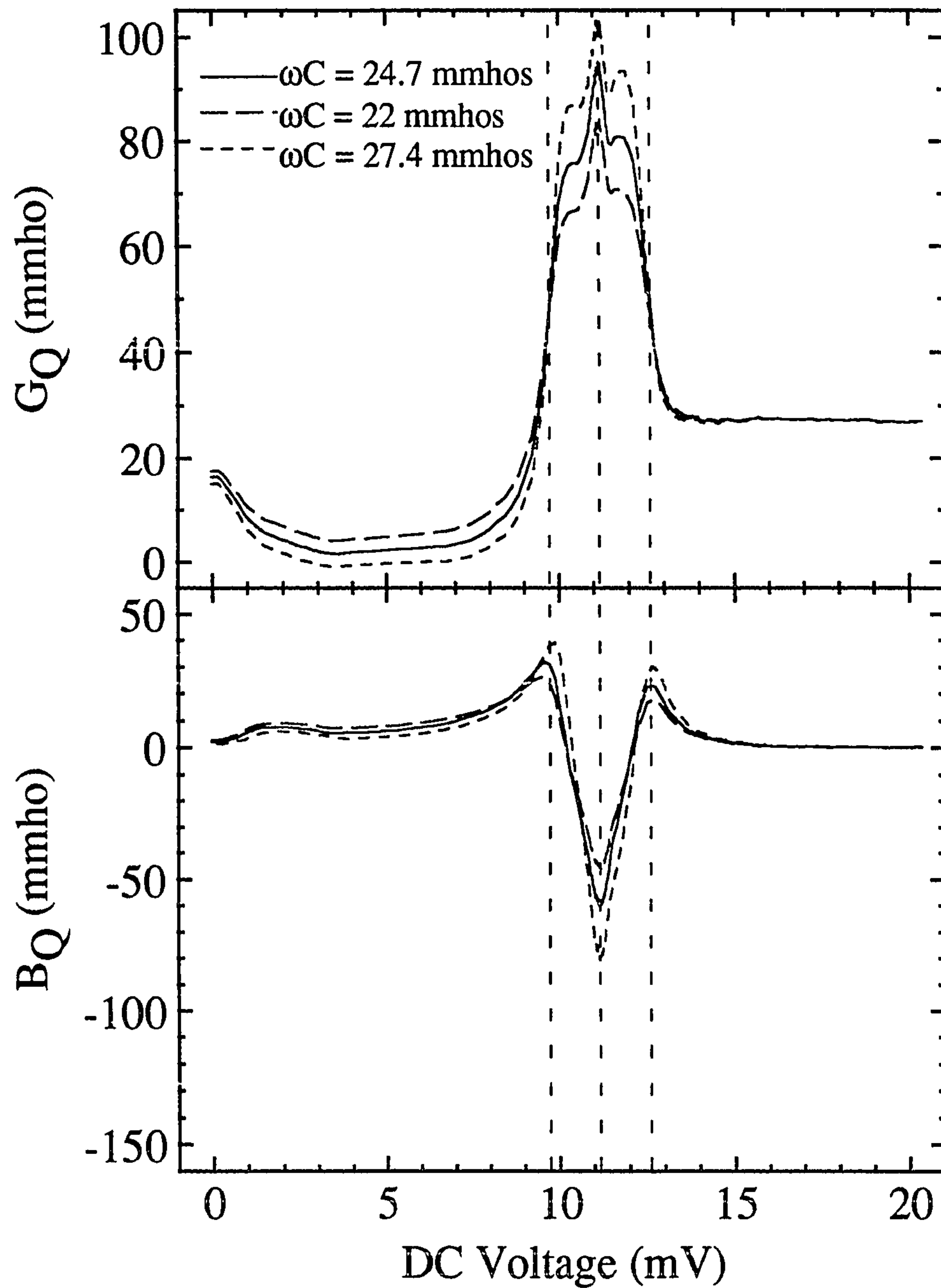

Fig. 6-20 The effect of the uncertainty in the capacitance on the experimentally deduced G_Q and B_Q. The dashed vertical lines correspond to (from left to right), one photon width below the array-gap, the array-gap, and one photon width above the array-gap voltage.

that the value of R_0 had a large influence on the calculated G_Q and B_Q. With $R_0 = 55\ \Omega$, the peak in the conductance at the array-gap voltage all but went away. This was because the 55 Ω value of R_0 made for a worse match at high bias and therefore a larger inferred attenuation. The mismatch near the array-gap voltage was even greater since here G_Q was on the order of 80 mmhos compared to Y_0 of 18 mmhos. Since the calculated attenuation factor was large, it compensated for this mismatch near the gap. For small attenuations, as with $R_0 = 40\ \Omega$, the mismatch at the array-gap voltage caused G_Q to peak sharply while decreasing the amplitude of B_Q.

All of these plots were generated using the measured $\gamma\rho$ and $\theta - \theta_R$. The variations with the circuit parameters were great. Unfortunately, we could not independently determine the value of the parameters. The data were therefore calculated using the design values, $R_0 = 50\ \Omega$, $iX_p = -i\ 5\ \Omega$, and $\omega C = 24.7$ mmhos. The very general trends in the data were still visible with changes in these parameters, such as the singularity in B_Q at the array-gap voltage.

Another possible source of the discrepancy between the theoretical and experimentally calculated G_Q and B_Q was noise rounding. Simulations have shown that a rounding on the order of 500 μV in dc voltage would be necessary in order to give the experimental results. Since the 23 dB cross coupler was removed in order to do this experiment, on the order of 200 K of noise is incident upon the junction through the waveguide. This noise should not effect the voltage uncertainty, although it will add power to the standing wave which is independent of probe position. This thermal noise, in addition to noise in the dc voltage bias source, could have caused rounding of the experimental data. The measured unpumped I-V curve may not represent the true tunneling density of states when there is significant noise rounding. Since this I-V curve is used in the theoretical predictions, it could lead to uncertainties in the deduced values of G_Q and B_Q.

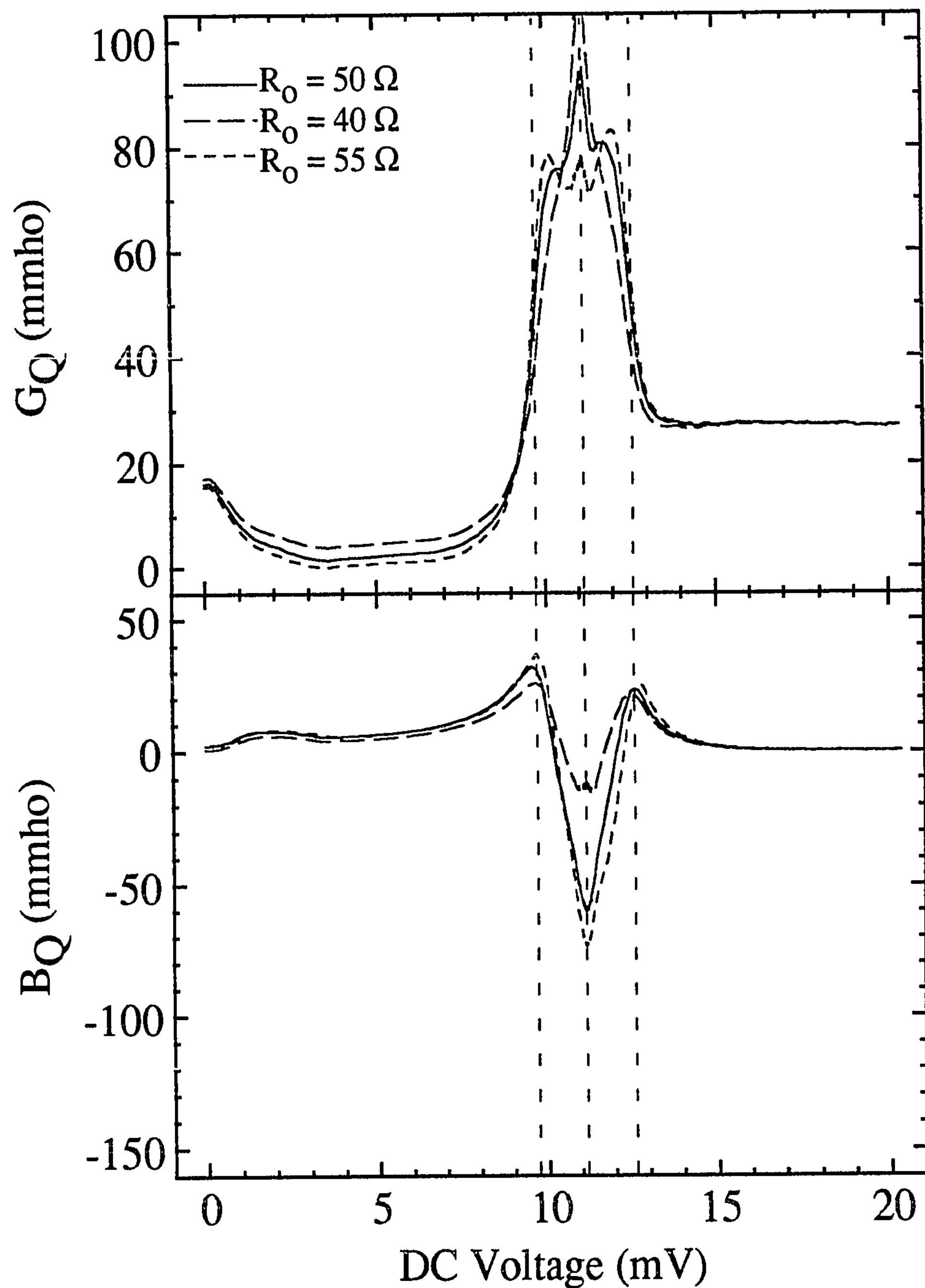

Fig. 6-21 The effect of changing the value of R_0 in the equivalent circuit. This parameter has a large effect on the deduced values of G_Q and B_Q. The dashed vertical lines correspond to (from left to right), one photon width below the array-gap, the array-gap, and one photon width above the array-gap voltage.

The uncertainty in the dc bias voltage is estimated to be $\pm 4\ \mu V$. This was determined by selecting the n'th data point in each power vs. probe position file and determining the stability of V_{on}. This voltage uncertainty does not account for the rounding of the data.

There may also have been noise incident with the signal. If this were the case, it should have been dependent upon the signal strength reaching the junction. We did not see a correlation between the lack of sharpness of the experimental data and the signal power.

An important source of data rounding is the frequency instability of the YIG oscillator. As discussed in section 6.3, a frequency instability of 10 MHz will lead to a phase uncertainty of $\sim 3^{o}$. The frequency instability also leads to an uncertainty in the measured $\gamma\rho$ since both $\gamma\rho$ and $(\theta - \theta_R)$ are detemined by least square fitting the measured standing wave. At this time, it is believed that the frequency instability of the YIG oscillator is the primary source of the experimental data rounding.

6.7.2 Quantum Discrepancies

The lack of perfect agreement between the measurements and the theory was certainly to some extent due to the non-ideal junctions. The pumped I-V traces could not be fit that well using the quantum theory, therefore we should not expect that the currents and admittance are also given exactly. Clearly, the dc I-V trace (Fig. 6-11a) was not perfect. It had a leakage current well in excess of a BCS junction and it had the proximity effect structure due to the unoxidized Al. Both of these non-idealities could cause a discrepancy with the theoretical prediction as has been seen by our group and others [Mears et al., 1991a] in the mixer results. Fortunately, as with mixers, ideal junctions are not necessary to demonstrate many aspects of the theory. The junctions studied here did show that G_Q was in fact large within one photon width of the gap for low input powers, and that multi-photon processes became larger with increasing input power. The results did show that the reactive singularity in the quasiparticle current was present and that it caused singularities in

the measured B_Q. This system and these junctions were not the perfect apparatus with which to study deviations from ideality; they were, however, a good apparatus with which to demonstrate the existence of G_Q and B_Q at small and large input powers and bias voltages.

6.8 Two Junction Array Results

In addition to the measurements of the four junction array, we have measured a two junction array whose dc and pumped I-V traces are shown in Fig. 6-22. Notice that the unpumped I-V trace was sharp. This gave rise to a sharp peak in the Kramers-Kronig current since the KK current is only dependent upon the curvature of the dc I-V curve. The experiment was done at two different pump powers. The low-input power gave the pumped I-V curve (b). This was the minimum power attainable given the sensitivity of the measurement system. The experimentally measured $\gamma\rho$ and θ - θ_R are shown in Fig. 6-23. The dashed curve assumed an equivalent circuit as for the four junction array results, with $Y_0 = 20$ mmhos and $\omega C = 9.7$ mmhos. One sees immediately that the very low reflection coefficient measured in the experiment was not reproduced well using these values in the equivalent circuit. In order to achieve this low reflection coefficient, the load and input impedances must be almost perfectly matched near the array-gap voltage. This implies that at the two bias voltages where the measured $\gamma\rho \approx 0$, $G_0 \approx G_Q$ and $\omega C \approx -B_Q$. The best value in the analysis circuit which fits these criterion was $G_0 = 34$ mmhos. This value of the waveguiding admittance leads to the solid curves in Fig. 6-23. Even with this improvement near the array-gap, the theoretical predictions are still seen to be stronger than those measured experimentally. At this time, we believe that the wafer mounting, including the location of the ridge relative to the junction, gave this input admittance different from the design value of 20 mmhos.

The G_Q and B_Q derived from the experimentally measured data and the analysis circuit are shown in Fig. 6-24. The results for $Y_0 = 34$ mmhos were reminiscent of those

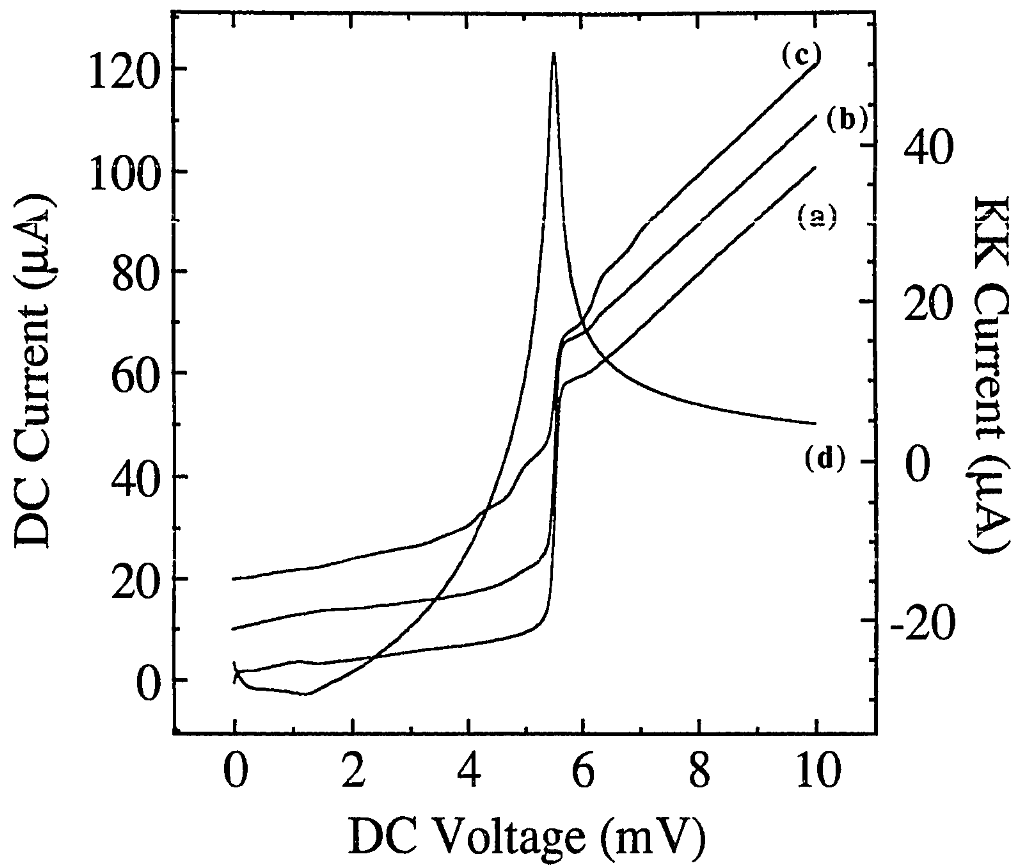

Fig. 6-22 a) The dc I-V trace of the two junction array, device K. b,c) The pumped I-V traces for two different input powers. d) The Kramers-Kronig transform of a). The pumped I-V curves are offset by 10 µA for clarity.

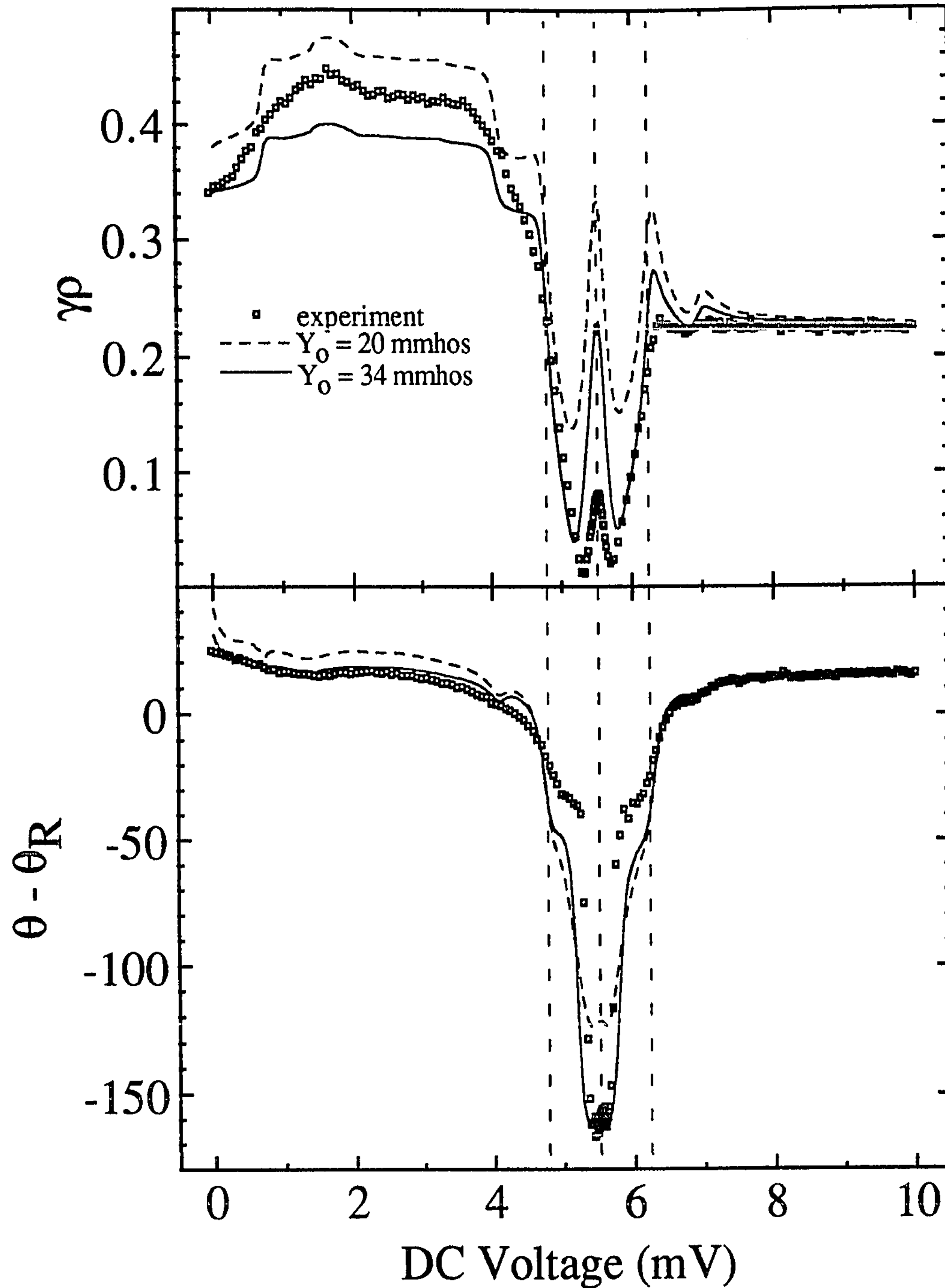

Fig. 6-23 The measured reflection coefficient and phase of device K at the low input power corresponding to curve b) in Fig. 6-22. The experimental data is shown as the open squares. Two different theoretical curves are shown, each generated with Y_0 as shown. The dashed vertical lines correspond to (from left to right), one photon width below the array-gap, the array-gap, and one photon width above the array-gap voltage.

seen in the four junction array at low power. Unfortunately, this did not fit the experimental data over the whole bias range. In particular, it predicted a G_Q which is *negative* at low bias voltages. The negative value of G_Q came from the fact that, given the correction for the attenuation, the calculated value of ρ at these bias voltages was greater than 1. Of course, this is unphysical. The failure of any combination of ωC and Y_0 to fit the theory across the whole bias voltage range indicated that the analysis circuit was not a comprehensive model. At this time, no effort has been made to add the effects of *resistive* losses (between the ridge and microstripline for instance) among the passive terms. These would add another term to the analysis circuit. In addition, it is possible that reflections at the ridge, although not bias voltage dependent, are influencing the measured data.

The results for the two junction array at input powers described by the pumped I-V labeled (c) in Fig. 6-22 are shown in Figs. 6-25 and 6-26. Once again, the measured $\gamma\rho$ was almost 0 at two bias voltages near the array-gap voltage (Fig. 6-23). The near perfect match again indicates that the output admittance of the waveguiding system was $\approx G_Q$ at these bias voltages. The theoretical curves generated using $Y_0 = 20$ and 34 mmhos again show that the assumption of a higher waveguiding output admittance gives a better fit near the array-gap voltage. Once again, this led to negative values of G_Q at low bias voltages. The singularity in B_Q at the array-gap voltage was clearly seen in all of the results.

This chapter reported the first direct observation of the full bias voltage and power dependence of the quantum conductance and quantum susceptance. In particular, the results here are the first observation of the singularity at the gap voltage associated with the singularity in the reactive quasiparticle current. The standing wave technique used in these experiments might also be used to determine the voltage dependence of the Josephson sine and cosine currents. Finally, the standing wave technique could be used in other waveguide systems to measure the admittance of any arbitrary device, provided that a proper equivalent circuit can be developed.

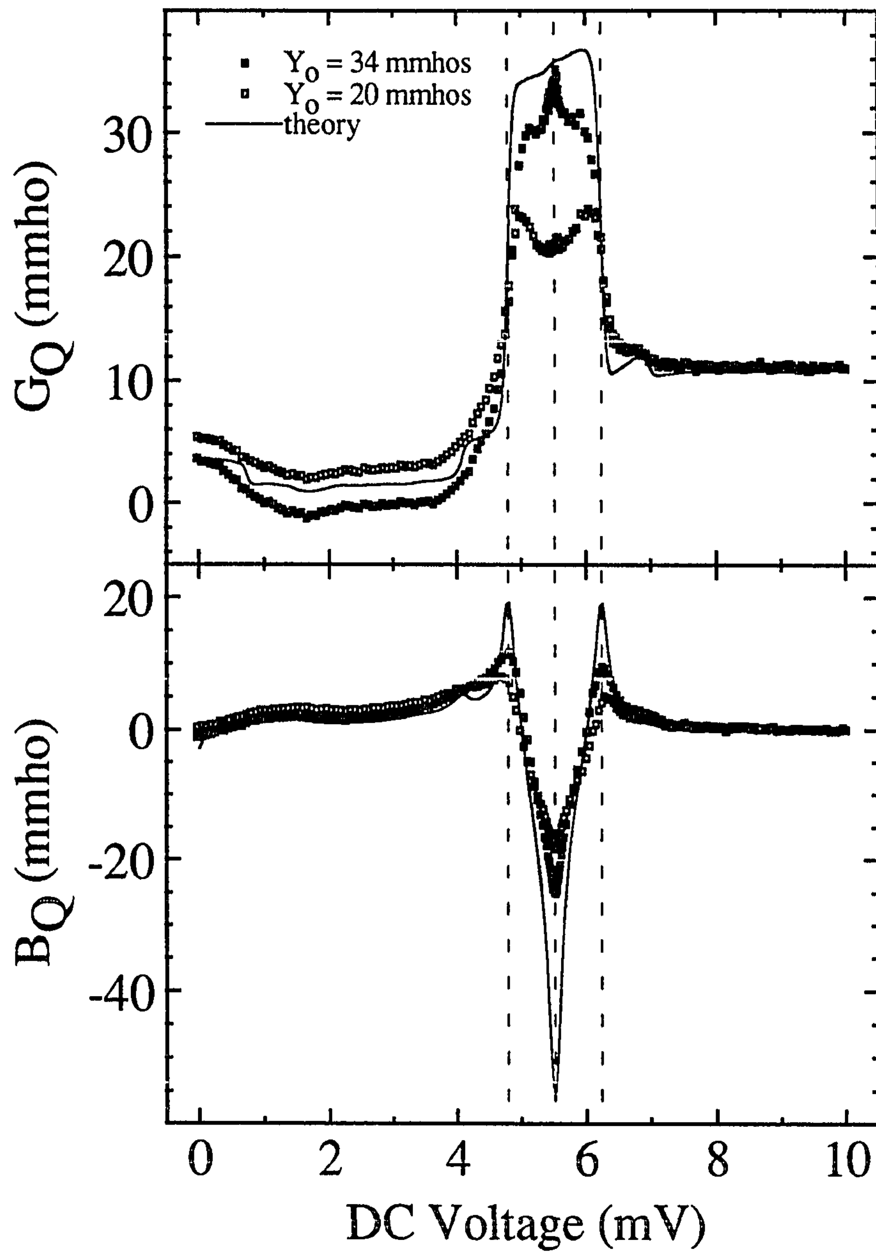

Fig. 6-24 G_Q and B_Q for the device K with low input power. The theory is shown by the solid line (using eqs. 6-2, 6-3 and equivalent circuit) the deduce G_Q and B_Q are dependent upon the value of Y_0 as shown. The dashed vertical lines correspond to (from left to right), one photon width below the array-gap, the array-gap, and one photon width above the array-gap voltage.

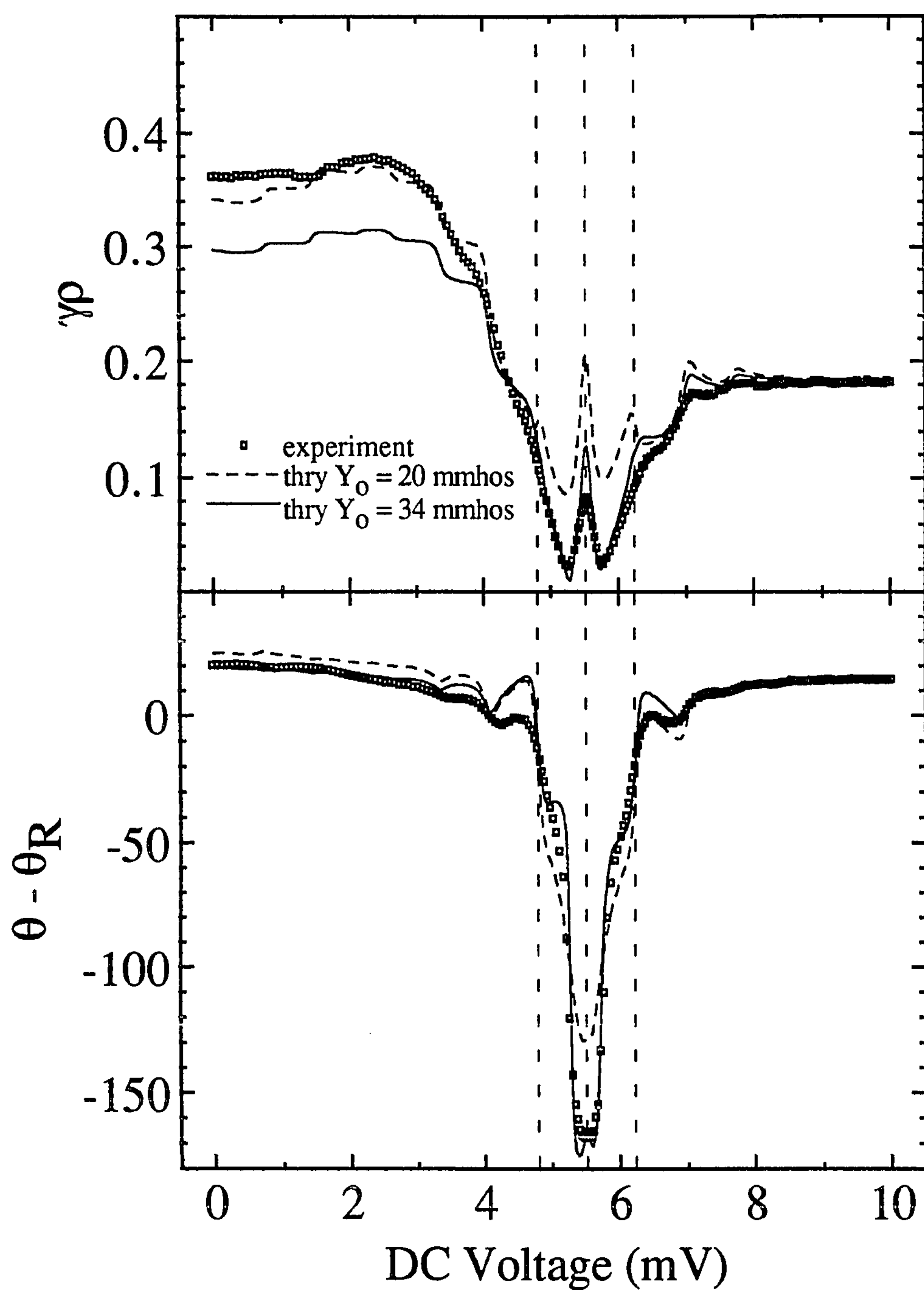

Fig. 6-25 The measured reflection coefficient and phase of device K at the high input power corresponding to curve c) in Fig. 6-22. The experimental data is shown as the open squares. Two different theoretical curves are shown, each generated with Y_0 as shown. The dashed vertical lines correspond to (from left to right), one photon width below the array-gap, the array-gap, and one photon width above the array-gap voltage.

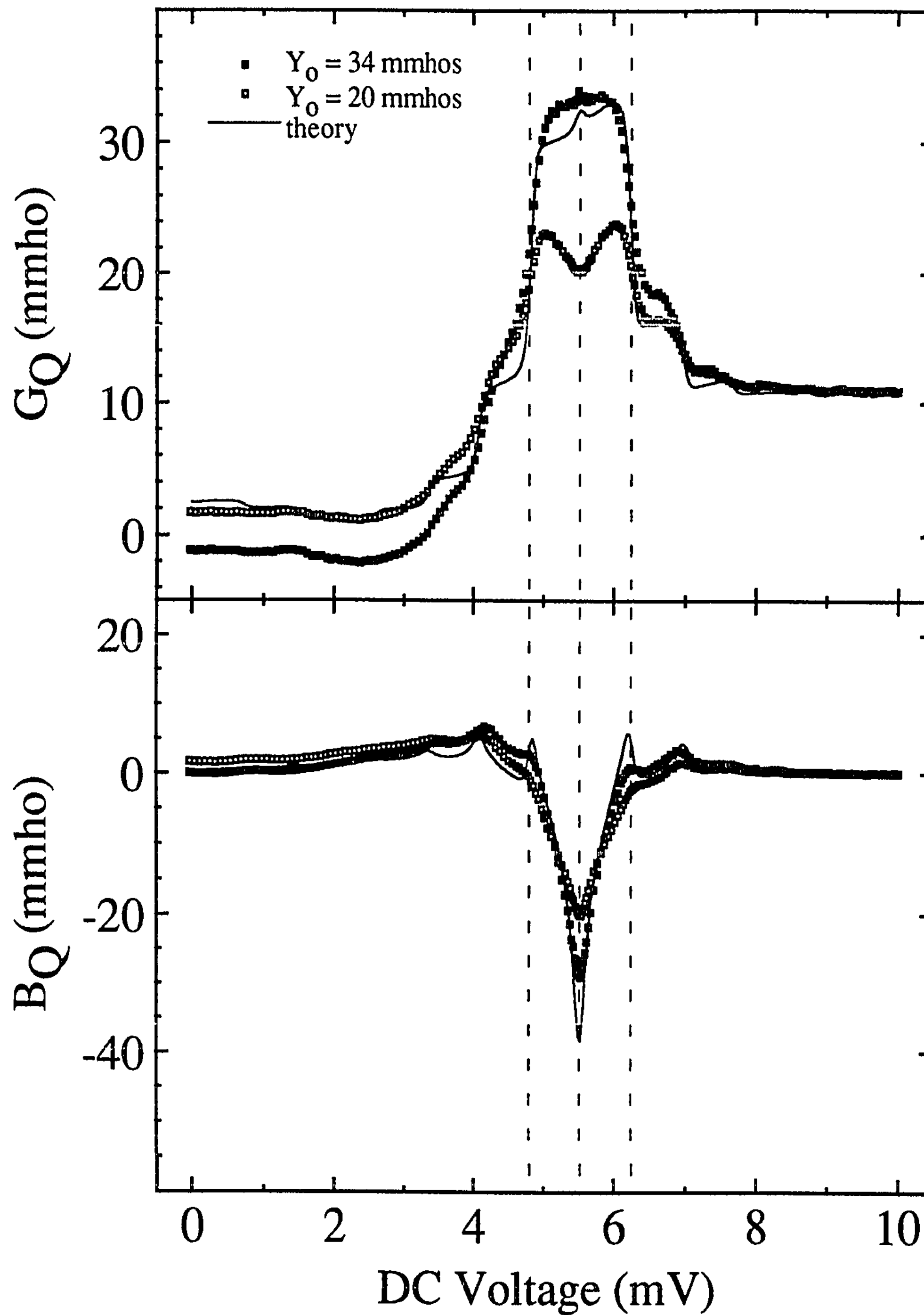

Fig. 6-26 G_Q and B_Q for the device K with high input power. The theory is shown by the solid line, the deduce G_Q and B_Q are dependent upon the value of Y_0 as shown. The dashed vertical lines correspond to (from left to right), one photon width below the array-gap, the array-gap, and one photon width above the array-gap voltage.

VII TUNING IN SIS MIXERS

This chapter is located at the end since the it combines ideas discussed in the single frequency chapters (II and VI) and multiple frequency chapters (III and V). The sections which discuss Josephson tuning and quantum tuning use devices like those described in chapter IV.

7.1 Mechanical and Passive Tuning

Most SIS mixer receivers in the 100 GHz range use some passive tuning elements in order to resonate the geometric capacitance. Tuning, in this chapter, refers to resonating the geometric capacitance. I will not discuss the coupling mechanisms of the *rf* into the device. The design of the tuning elements in SIS receivers has become a subfield in itself and is therefore included as a separate chapter here.

The most common tuning elements in use in SIS mixer receivers are the adjustable backshort and e-plane tuner. The standard for such tuning structures in the 100 GHz range is the NASA/GISS type-D mixer mount [Pan et al. 1983; Pan and Kerr, 1986]. In this design, the device is mounted across two quarter-height waveguides. Both waveguides are terminated by sliding short circuits. The electrical location of the shorts relative to the junction determines the overall embedding admittance of the device. With this tuning, a large area of the Smith plot is accessible as an embedding admittance [Pan et al., 1989]. Other configurations are possible, involving only one adjustable tuning element. This is usually a non-contacting sliding backshort [Räisänen et al. 1986; Blundell et al., 1982]. Another adjustable tuning structure is that of a sliding metallic bar over a coplanar strip transmission line [McGrath et al., 1990]. The problems with all of these approaches are that 1) it becomes increasingly more difficult to fabricate the adjustable tuning elements as the frequency becomes higher and 2) it is difficult to characterize their effect at higher frequencies. For these reasons, recent emphasis has been placed on receivers which contain

no adjustable tuning elements [Winkler et al. 1991a,b; Kerr et al. 1990; Büttgenbach et al., 1988; Hu et al., 1989].

Many devices contain lithographic fixed inductors which are designed to resonate the device capacitance. Our design (described in section 5.1) contained a microstripline inductor in *rf* parallel with the mixer chip. Another design which has been used is open circuited resonant stubs [Xizhi, Richards, and Lloyd, 1988; Kerr et al., 1988]. On-chip passive inductors usually become increasingly difficult to fabricate and characterize at higher frequencies. What is desired is an easily adjustable (and easily understandable) inductor which is not difficult to fabricate.

7.2 Josephson Tuning

The Josephson effect shows some promise for meeting the demands of an easily fabricated and characterized variable inductance [Irwin et al. 1981]. The basic idea is that the dc Josephson current acts as a variable inductance which is dependent upon the macroscopic phase across the junction. Using the two basic Josephson equations, $2eV_o = \hbar d\phi/dt$ and $I = I_J \sin\phi$, the Josephson current is related to the inductance defined by $V_o = L dI/dt$

$$L_J = \frac{\hbar}{2eI_J\cos\phi} = \frac{L_o}{\cos\phi} \qquad 7\text{-}1$$

Using a suitable design, this inductance could be used to resonate the capacitance of junctions used as mixing elements. The phase is given by

$$\phi = \phi_o + \frac{2eV_\omega}{p\hbar\omega}\sin\omega t = \phi_o + \alpha_1 \sin\omega t \qquad 7\text{-}2$$

where p is the number of junctions in the array of tuning junctions. For tuning, the dc bias current is $I_0 = I_J \sin\phi_0$, therefore

$$L_J = \frac{L_0}{\cos\phi} \approx \frac{L_0}{\sqrt{1 - \left(\frac{I_0}{I_J}\right)^2}} \qquad \text{for } \alpha_1 << 1 \qquad 7\text{-}3$$

The Josephson inductance is not linear with the dc current since the current is a function of sin ϕ. The junction response places limits upon the number of junctions to be used. Feldman (1987b) has shown that in order to have a linear inductance, one needs at least 7 times as many Josephson tuning junctions as mixer junctions. In addition, he suggests that the use of Josephson tuning junctions at frequencies above 230 GHz will be impractical since the tuning junctions should operate below the plasma frequency, $f < 1/[2\pi\sqrt{L_0 C}]$. The mixer device must also operate below the plasma frequency, and this places limits on the amount of *rf* voltage which can be applied to the mixer junction.

7.2.1 Chip Design

Since the Josephson tuning junctions are fabricated on chip with the mixer junctions, in practice it is easiest for them to have the same current density as the mixer junctions. The chip lay-out for our design is shown in Figs. 5-4 and 7-1a; the equivalent circuit is shown in Fig. 7-1b. The Josephson inductance is shown as a variable inductor. The inductance is not linear and it approaches infinity for ϕ near $\pi/2$ which is a current close to I_J. An expanded view of the junction area is shown in Fig. 7-1c.

The design incorporated in the Yale receiver accounts for the lead inductance in the wiring connecting junctions, as well as the junction capacitances. The designed operational range is ϕ from 0 to 65°, corresponding to the frequency range 80-110 GHz. When $\phi = 0$, the resonant condition is

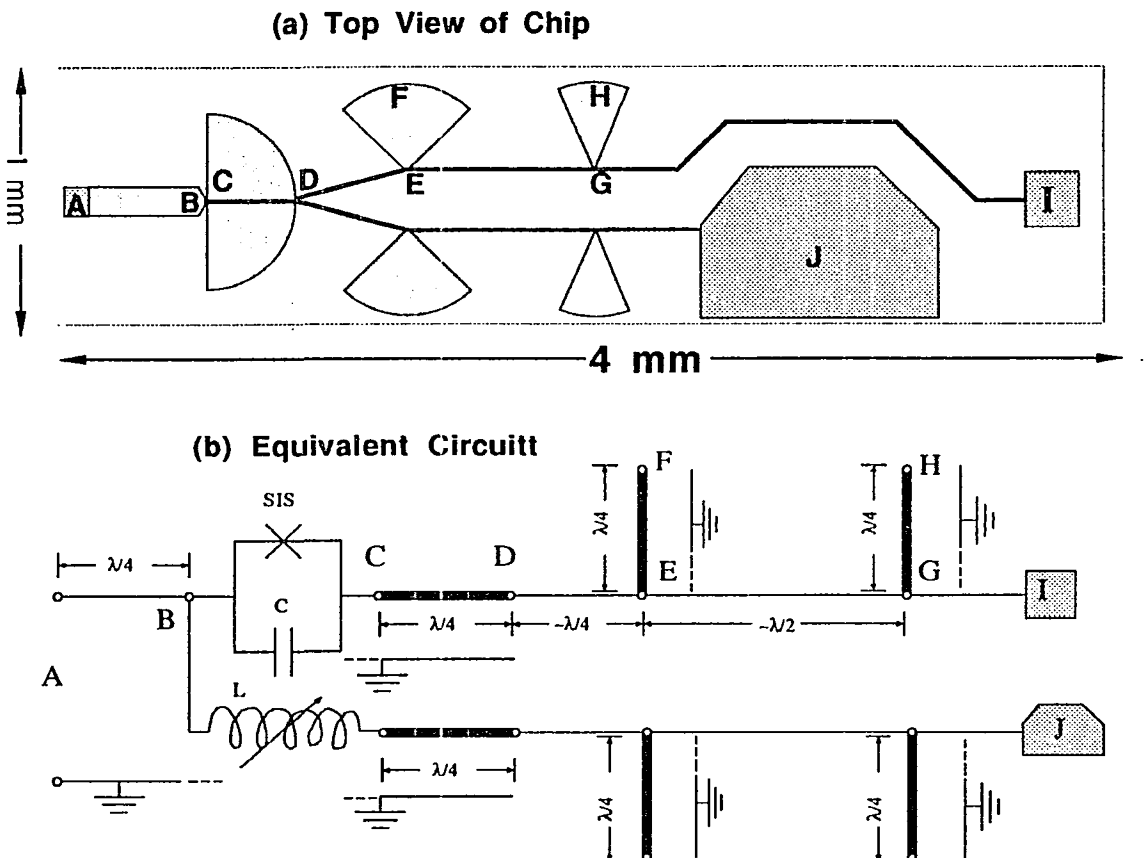

Fig. 7-1 a) The top view of the device. b) The equivalent circuit. c) An expanded view of the junction area (to scale).

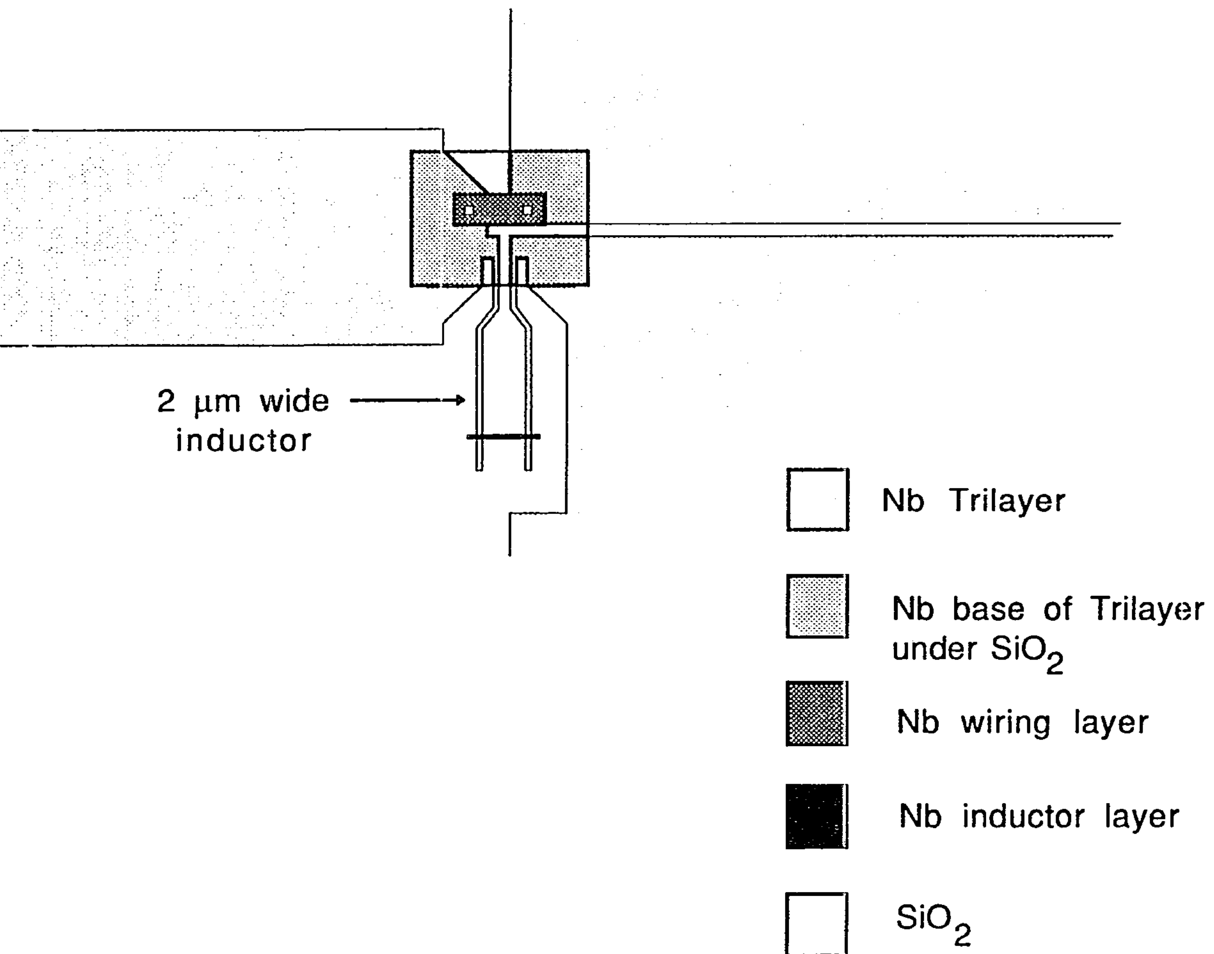

Fig. 7-1 cont.

$$\left[\left(\frac{\hbar}{2eI_J} + L_{series}\right)(C_J + C_M)\right]^{-1/2} = (2\pi)110 \text{ GHz} \qquad 7\text{-}4$$

where L_{series} is the lead inductance connecting junctions in an array (calculated using eq. 5-4), C_J and C_M are the capacitances of the Josephson tuning junctions and mixer junctions respectively. In practice, the design involved fixed area tuning junctions, such that L_J and C_J were available in increments depending upon the number of junctions employed. Using eq. 7-4, it was determined that three $1(\mu m)^2$ Josephson tuning junctions were necessary to tune one $1(\mu m)^2$ mixer junction. In the original design, the calculated inductances for this configuration were $L_0 \approx 16.5$ pH (for $J_c = 2000$ A/cm^2, $C = 60$ fF/(μm)^2) and $L_{series} \approx 9.7$ pH. The kinetic inductance due to the bunching of the current at the $1(\mu m)^2$ tunnel junctions was calculated to be < 50 fH, and thus negligible. An array of four $1(\mu m)^2$ mixer junctions required twelve $1(\mu m)^2$ tuning junctions. The ratio of 3:1 here, is less than the 7:1 suggested by Feldman (1987b), but these devices were intended to prove a concept, not be the final design for a real receiver.

7.2.2 Testing Results

The tests performed using the Josephson tuning junction were inconclusive. The dc Josephson current was suppressed in the absence of applied radiation, possibly due to noise in the dc current supply. This was not our intention. When radiation was applied, the dc Josephson current was even more suppressed, as was expected since the amplitude of the zero voltage current in the presence of applied radiation goes as the zero'th order Bessel function

$$I_J(V_\omega, V_0=0) = I_0 J_0(2eV_\omega/\hbar\omega) \approx I_0[1-\tfrac{1}{4}(2eV_\omega/\hbar\omega)^2] \qquad \text{for } 2eV_\omega/\hbar\omega \ll 1 \qquad 7\text{-}5$$

This effect has been used for radiation detection using weak link junctions [Grimes, et al., 1968]. Currently, work is being done to decrease our system noise.

7.3 Quantum Tuning

Quantum tuning is here defined as tuning which uses the quantum susceptance and conductance (Chapter VI) as a variable tuning element. The device realization of this idea is essentially the same as the device presented for the Josephson tuning inductance. If the mixer junction is in *rf* parallel with a set of tuning junctions, the dc bias voltage of the tuning junction will affect the *rf* coupling into the mixer junction through the quantum conductance and susceptance. In other words, by independently dc biasing an array of superconducting tunnel junctions in *rf* parallel with the mixer junctions, the embedding admittance presented to the mixer junctions can be changed. The value of the embedding admittance will be dependent upon the bias voltage of the quantum tuning junctions, as well as the frequency. Only preliminary experimental data have been taken to demonstrate this effect, and these will not be presented here. Instead, I will present some theoretical prediction of the magnitude of this effect. From these, I will attempt to assess its usefulness.

7.3.1 The Model

The modeling is done using the I-V of a real mixer device which has an embedding admittance (without including geometric capacitance) of $Y_{emb} = 0.5/R_n - 2i/R_n$. In addition, the modeling assumes an $\omega R_n C$ product of 2 at 100 GHz. The imaginary part of the embedding ($-2i/R_n$) is assumed to be due to a passive tuning inductor that is designed to resonate the device capacitance at 100 GHz. I chose these values as realistic for a mixer mount in the 100 GHz range. The I-V curves of the device studied are shown in Fig. 7-2. The tuning junctions are assumed to be in perfect *rf* parallel with the mixer device and dc

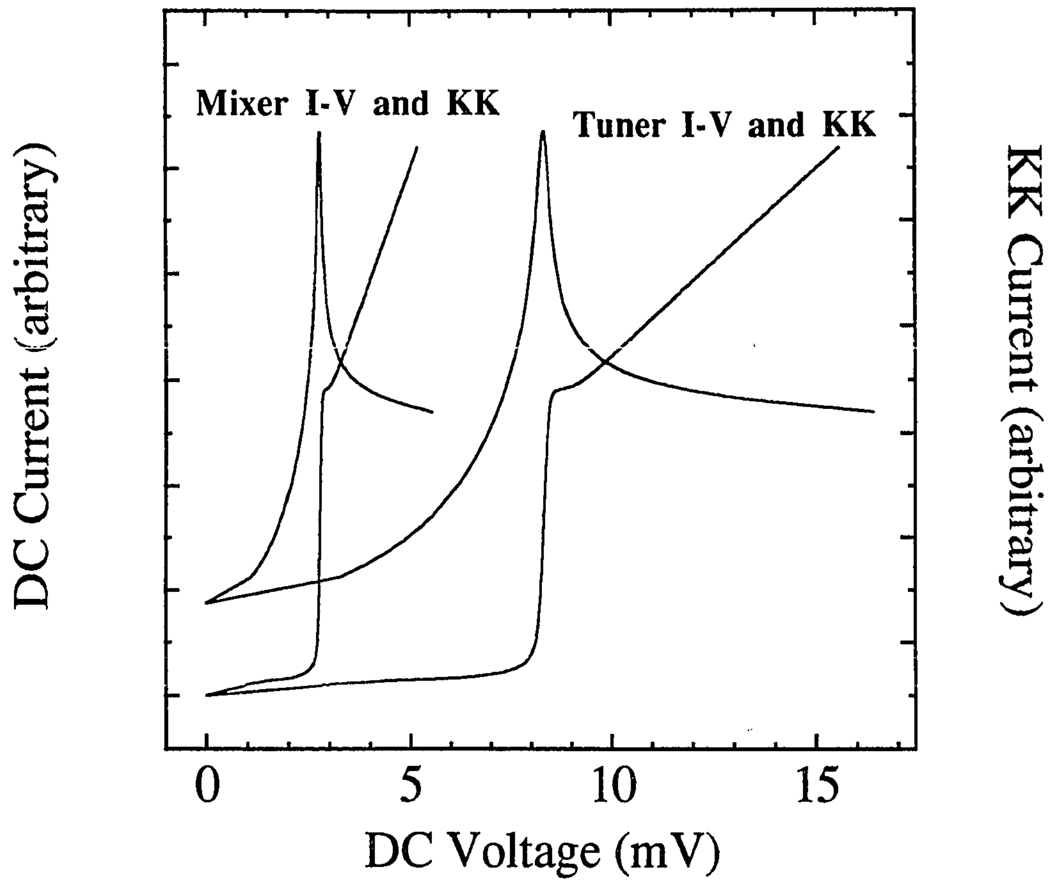

Fig. 7-2 The dc I-V and Kramers-Kronig currents of the modeled mixer junction and tuning junctions.

isolated. For the modeling, I used as the tuning junctions a three junction array of junctions identical to the mixer junction. The mixer junction gap voltage was 2.77 mV and the tuning junction array-gap voltage was 8.31 mV. In the model, the adjustable parameters are the input power, the dc bias voltage of the mixer junction, and the dc bias voltage of the tuning junctions.

7.3.2 The Variable Embedding Admittance

The quantum conductance and susceptance of the tuning junctions are assumed to be independent of the input power, i.e., I have used the low power limit of eqs. 6-4 and 6-5 to calculate their effect. This is justified since V_ω across the tuning junctions will be 3 times smaller than that across the mixer junctions because of the relative number of junctions. The embedding admittance is the sum of the base embedding, the geometric capacitance of the devices, and the quantum effects

$$Y_{emb}(V_{0t},\omega) = \left[\frac{1}{2R_n} + G_Q(V_{0t},\omega) \right] + i \left[\frac{-2i}{R_n} + \frac{4\omega C}{3} + B_Q(V_{0t},\omega) \right] \quad \text{7-6}$$

where V_{0t} is the dc bias voltage of the tuning junctions. The embedding admittance of this model at 100 GHz is shown as a function of V_{0t} in fig. 7-3. The Smith plots here are normalized to $1/R_n$. Since Y_{emb} now includes G_Q as well as the designed embedding conductance, Re(Y_{emb}) is large and the available Y_{emb} are all in the high conductance part of the Smith plot. This is not an ideal design for SIS mixers, where a typical best embedding admittance is found for $G_{emb} < 1/R_n$. This model and these calculations are intended to demonstrate that this structure can be used as a variable tuning element. A proper design for a real receiver could give the correct range of G_{emb}. The largest change in the embedding admittance due to G_Q and B_Q of the tuning junctions is within one photon width of the gap, 7.07 mV $< V_{0t} <$ 9.56 mV at 100 GHz.

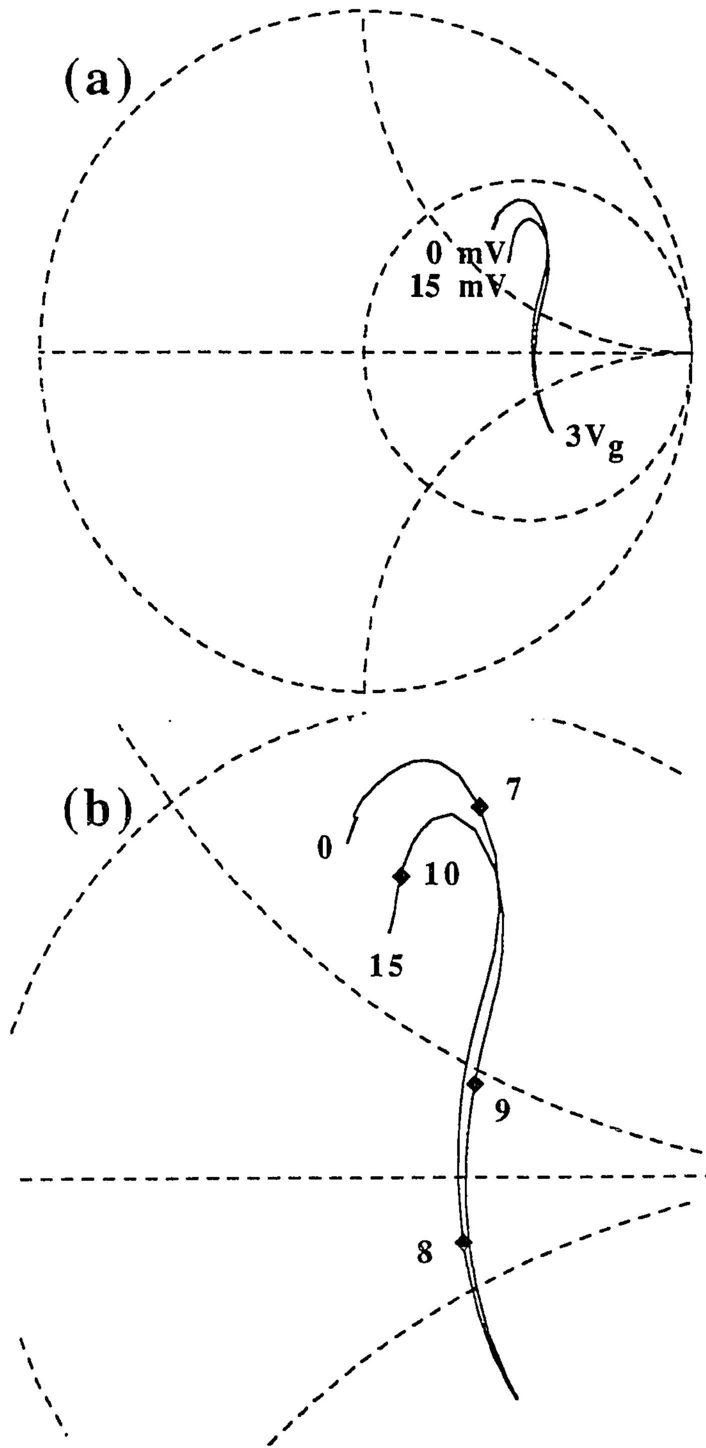

Fig. 7-3 a) The available embedding admittances in the model. The Smith plot is normalized to R_n. b) An expanded view of a). The numbers indicate the bias voltage of the tuning junctions in mV.

7.3.3 The Effects of the Quantum Admittance

The pumped I-V trace of the mixer junction at 100 GHz, at various dc bias voltages of the tuning junctions, is shown in Fig. 7-4. The changing embedding admittance, which resulted from the bias dependence of G_Q and B_Q of the *tuner* junctions, changed the shape of the pumped I-V curves of the *mixer* junction. This was seen especially near the array-gap voltage (~8.3 mV) of the tuning junctions where G_Q and B_Q had the largest effect on the embedding admittance. At this voltage, B_Q of the tuning junctions resonated the capacitance of the mixer junctions and caused the photon steps to be flat. All of the curves were normalized to $\alpha = 1$ at $V_{om} = V_g - \hbar\omega/2e = 2.56$ mV, where V_{om} was the dc bias voltage of the mixer junction. These results showed that evidence for the G_Q and B_Q can be found in a simple experiment which measures the pumped I-V trace of a junction in *rf* parallel with another junction or set of junctions using a device like that shown in Fig. 7-1.

Calculating the effect of G_Q and B_Q on the gain and noise of the mixer was more difficult. This was because the best pump power and bias voltages were difficult to find computationally. In order to make the solutions tractable, I held one variable constant, namely the input power was adjusted such that the condition $\alpha = 1$ at all bias voltages was met. This corresponded to the voltage bias case. The voltage bias case is an approximation, but renders the important effects. The mixer and tuning junction biases which gave the lowest noise and highest gain were then found, using an IF frequency of 1.5 GHz, IF load impedance of R_n, and T = 4.4 K.

Fig. 7-5a shows the main results of the simulations on this device. The results showed clearly that the mixer gain of one junction can be influenced by G_Q and B_Q of another junction(s). Since B_Q of the tuning junctions was large and negative near its array-gap voltage (shown by the middle dashed line in Fig. 7-5), it presented the mixer junction with an embedding admittance which was inductive. This inductance was dc voltage dependent. Fig. 7-5a shows the gain of the mixer junction within one photon width of the array-gap of the tuner junctions where B_Q was changing rapidly. Near the array-gap

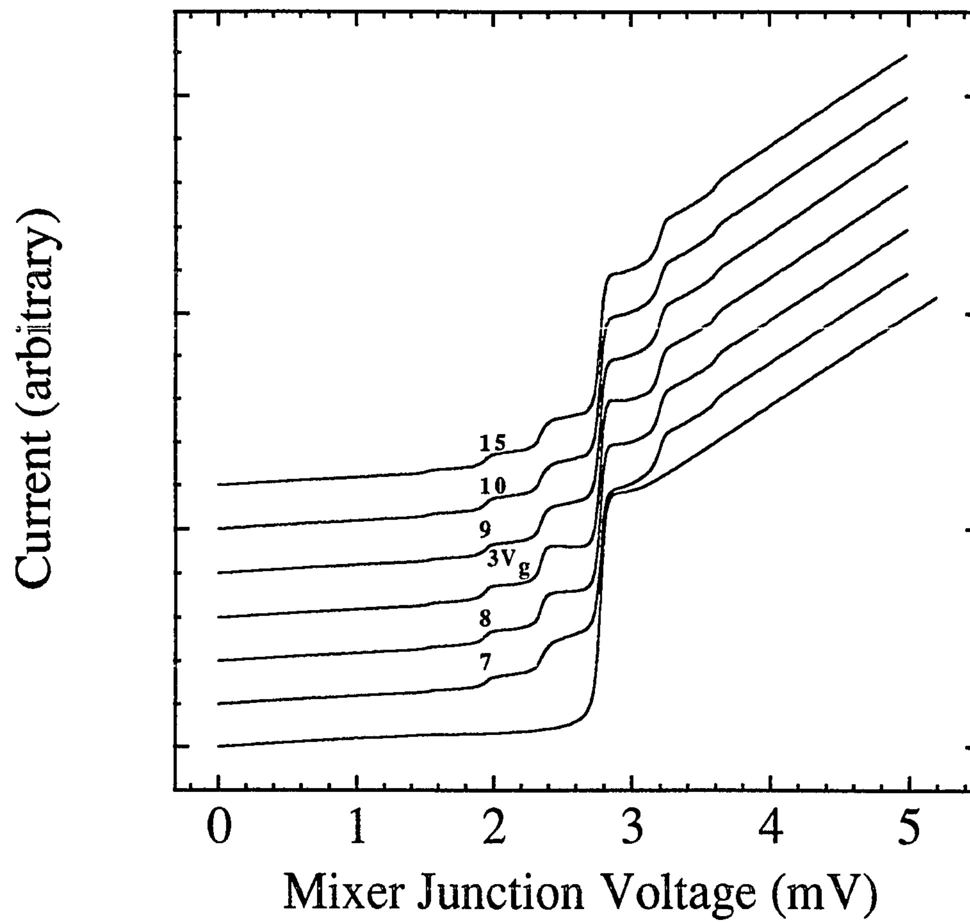

Fig. 7-4 The effect of the changing embedding admittance on the pumped I-V curves of the mixer junction. The numbers indicate the bias voltage of the tuner junctions. The curves are offset vertically for clarity. $3V_g = 8.31$ mV.

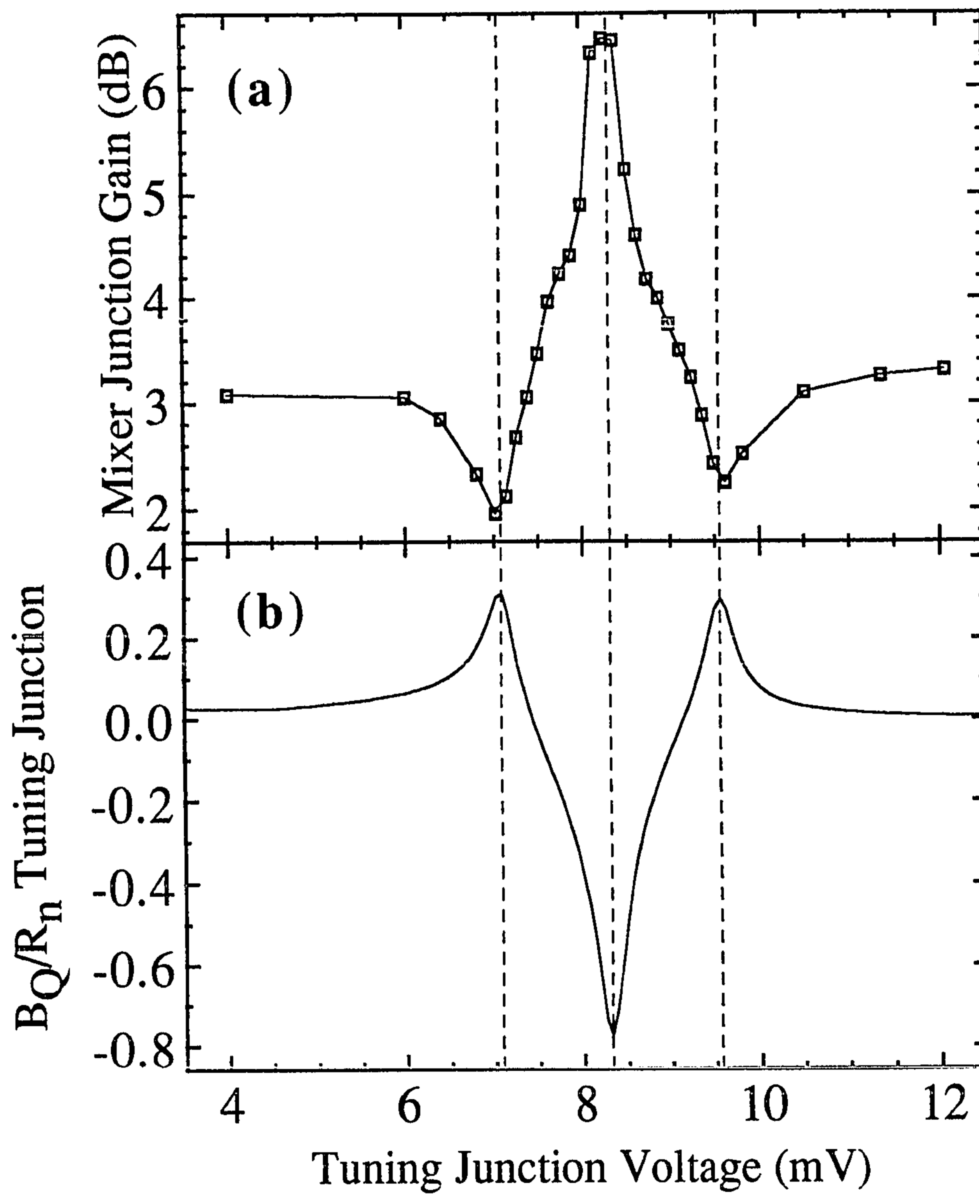

Fig. 7-5 a) The coupled gain of the mixer as a function of the quantum tuning voltage. b) The quantum susceptance of the quantum tuning junctions. The dashed lines indicate, from left to right, one photon width below the array-gap voltage, the array gap-voltage, and one photon width above the array-gap voltage of the quantum tuning junctions.

voltage, B_Q of the tuning junctions resonated ωC of the mixer junctions and provided for a large coupled gain. The calculated noise, T_R, of the mixer did not change much (4-5 K at all times) for each best V_{om} which gave the mixer gains shown in Fig. 7-6a. This noise is dependent upon the absolute current; for these results a value of $R_n = 50\ \Omega$ was used.

The change in mixer gain is due to the change in the embedding admittance and is *not seen for a fixed embedding admittance.* For a fixed $Y_{emb} = (1.25 - i\ 0.12)/R_n$, which is the admittance at $V_{ot} = 8$ mV, the gain and noise across the first photon step are plotted in Fig. 7-6. The horizontal axis of Fig. 7-6 covers the first photon width below the gap of the mixer junctions. Notice that the gain did not approach the value of +6.4 dB found by tuning with the quantum tuning element. In addition, the noise was seen to become significantly greater at the edges of the step than the 4-5 K found by using the quantum tuning element. Once again, $R_n = 50\ \Omega$ was used in order to give absolute values for the noise temperature. The gain was also found to be strongly dependent upon V_{om}, becoming large at the edges of the photon step.

Finally, the modeling showed that the optimal V_{om} changed as V_{ot} was changed in the quantum tuned junction. Mears et al. (1991b) have shown in simulations that the optimal mixer bias voltage shifts away from the middle of the first photon step toward lower bias voltages for devices with large inductive embedding admittances. They argue that this is due to the large change in the imaginary part of the signal to signal admittance matrix element, $Im(Y_{11})$. For inductive embedding, the coupling at the signal is better matched at lower bias voltages. In our simulations, this largest inductive embedding is seen at the array gap voltage of the tuning junctions where there is a singularity in B_Q. At this value of $V_{ot} =$ 8.31 mV, $V_{om} = 2.48$ mV for best performance. At the largest capacitive embedding, $V_{ot} = 3(V_g - \hbar\omega/e) = 7.07$ mV, $V_{om} = 2.58$ mV. The middle of the first photon step is at $V_{om} =$ 2.56 mV, so our results are consistent with those of Mears et al. (1991b).

It should be noted that recent ideas by Belitsky and Tarasov (1991) show promise for another variation on quantum tuning. In their design, two sets of identical junctions are

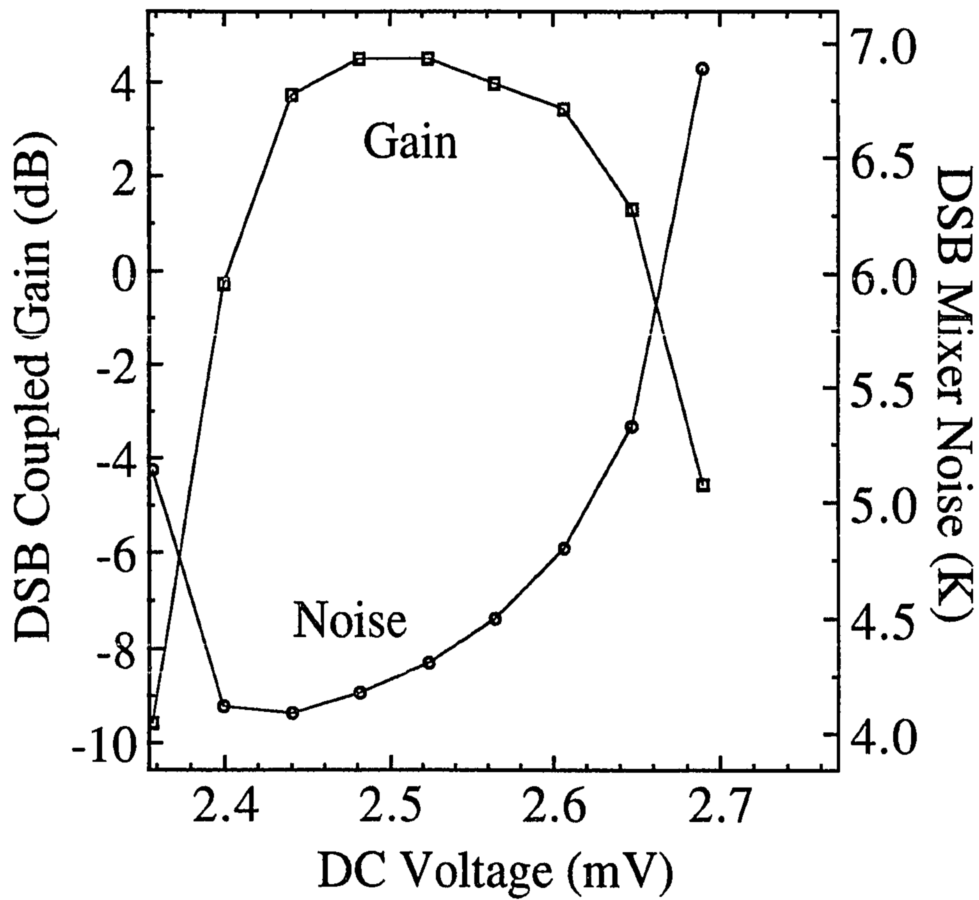

Fig. 7-6 The coupled gain and mixer noise of the mixer for a fixed embedding admittance, $Y_{emb} = (1.25 - i\,0.12)/R_n$. The upper bound on the horizontal axis corresponds to V_g of the mixer junction. The lower bound corresponds to $V_g - \hbar\omega/e$ at 100 GHz.

in *rf* parallel with each other. Connecting these devices is a line of length $n\lambda/2 + \lambda/4$ such that the imaginary admittance of one set of junction undergoes a quarter-wave transformation and resonates the imaginary admittance of the other set of junctions. This effectively resonates B_Q and ωC at *all* bias voltages, and there is no need for a passive tuning element. This design would probably benefit from a *variable* tuning element, since the ideal $Im(Y_{emb})$ is usually slightly inductive.

The ideas presented in this chapter for Josephson tuning and quantum admittance tuning may be applicable in future receivers where mechanical tuning may be difficult. The modeling shows that the quantum admittance has a large effect on the predicted gain, even in a device which is not of optimal design to take advantage of the variable inductance.

VIII CONCLUSIONS

The work described in this thesis addressed a number of important issues related to the interaction of radiation with an SIS tunnel junction, as well as the fabrication of the devices. The $Ta/Ta_2O_5/PbBi$ devices, which were of area 1 $(\mu m)^2$, proved to be the near ideal junctions for studying the quantum limited noise in SIS heterodyne mixing. The measured mixer noise of 0.61 ± 0.31 quanta at 93 GHz is the closest reported noise to the quantum limit of 0.5 quanta. The $Nb/AlO_x/Nb$ devices were fabricated using a relatively simple technique which allowed for high quality sub-micron devices to be fabricated on 2 mil thick quartz substrates. This technique could be extended to ~ 1 mil substrates, as might be needed in the higher frequency SIS mixer receivers of the future. These devices were used in a broadband mixer receiver with no mechanical tuning, and the noise results, T_R as low as 41 K at 80 GHz, are among the best reported, especially for receivers with no mechanical tuning elements. In addition, these devices were used to study the fundamental high frequency quasiparticle currents in the tunnel junction. This thesis reports the first observation of these currents over the entire dc bias voltage and input power range. In particular, this thesis reports the first direct observation of the singularity in the quantum susceptance, which is related to the singularity in the reactive quasiparticle currents. Finally, a novel device configuration was modeled. This configuration could have applications in future SIS mixer receivers.

APPENDIX A

Nb/AlO$_x$/Nb Tunnel Junction Fabrication Process

I Wafer cleaning and mounting

1) Ultrasonic clean 1" x 1" x 2 mil quartz wafer and 2" diameter Si wafer in

a) Trichloroethane (TCA), 2 min.

b) Acetone (ACE), 2 min.

c) DI water, 2 min.

d) Methanol (Meth), 2 min.

e) DI water, 2 min.

2) Spin dry both wafers, 4000 rpm, 30 sec.

3) Spread vacuum grease with wooden utensil in center 1" x 1" of Si wafer

4) Place quartz substrate on grease, bake 5 min. at 110 ^oC

5) Press wafers together using a clean mask in a maskaligner. Wafers are adequately stuck when no bubbles are visible between them. If bubbles are apparent and do not go away, repeat cleaning starting with 1) after TCA soak of 8 hours

6) Slowly release pressure between mask and wafers to remove wafers from aligner

7) Spin clean composite wafer (3000 rpm, 30 sec) using solvents listed in 1)

II Al underlayer deposition

1) Mount composite wafer in Lesker system, pump load lock to 5 x 10^{-6} Torr

2) Transfer composite wafer to cold stage (this is water cooled)

3) Presputter Al target, 200 W, 3 min

4) Sputter Al onto composite wafer, 5 mTorr Ar, 200 W, 4 min. giving 100 Å Al

5) Cool 5 minutes, unload

III Trilayer patterning

1) Spin AZ5218 at 3000 rpm, 30 sec on composite wafer

2) Bake in oven 25 min., 90 ^oC

3) Expose trilayer pattern in Quintel aligner, 4 sec., intensity = 7.0 mW/cm^2 at 365 nm

4) Bake in oven 10 min., 115 ^oC

5) Flood expose in Quintel, 60 sec.

6) Develop pattern in 1:1 AZ developer ~ 30 sec.

7) Rinse in DI, 3 min.

IV Trilayer deposition and liftoff

1) Mount composite wafer in Lesker system, pump load lock to 5 x 10^{-6} Torr

2) Transfer composite wafer to cold stage (base pressure < 5 x 10^{-8} Torr)

3) Presputter Nb target, 5 kW, 30 sec, with Nb shutter closed.

4) Sputter Nb to composite wafer, 7.1 mTorr Ar, 5 kW, 90 sec to give 2500 Å Nb

5) Presputter Al target, 200 W, 3 min, with Al shutter closed

6) Sputter Al to composite wafer, 5 mTorr Ar, 200 W, 4 min. giving 100 Å Al

7) Remove composite wafer to load lock chamber

8) Bleed oxygen to load lock to 20-50 mTorr (depending on desired current density)

9) Oxidize 30 min.

10) Pump oxygen from load lock to 5 x 10^{-6} Torr

11) Transfer composite wafer to cold stage

12) Presputter Nb target, 5000 W, 30 sec, with Nb shutter closed

13) Sputter Nb to composite wafer, 7.1 mTorr Ar, 5 kW, 30 sec to give 800 Å Nb

14) Cool 5 min. unload

15) Liftoff trilayer in ACE, ~ 5 min (ultrasonic should not be used, to avoid peeling)

16) Rinse in DI, 3 min.

V Junction area definition lithography (SNIP)

1) Spin AZ5209, 3000 rpm, 30 sec

2) Bake in oven 25 min, 90 ^oC

3) Place composite wafer on spinner chuck, cover surface with chlorobenzene

4) Wait 4 min

5) Spin dry wafer, 3000 rpm, 30 sec

6) Expose in Quintel, 4 sec.

7) Develop 3:1 DI water/AZ developer, ~ 60 sec.

8) Rinse in DI, 3 min.

VI Reactive ion etching (SNIP)

1) Load composite wafer to Semigroup 1000 Reactive Ion Etcher

2) Pump to 25 mTorr

3) RIE top Nb of trilayer in CCl_2F_2 with 8% Ar and 8% O_2, 100 mTorr, 50 W, 2 min.

4) RIE to shrink and passivate in O_2, 300 mTorr, 25 W, 30 sec.

VII Removal of Al underlayer

1) Wet etch Al in Phosphoric Aluminum Etch (PAE) 16:1:1:2 H_3PO_4, HNO_3, acetic acid, DI, at 65 °C, ~ 10 sec.

2) Rinse in DI, 3 min. (Note: in the future, the steps should be VI-3, VII-1, VII-2, VI-4)

VIII Deposition of SiO_2 and liftoff (SNIP)

1) Load composite wafer to MRC sputtering system, heat sinking with vacuum grease

2) Pump system to 1 x 10^{-6} Torr

3) Bleed system to 1.5 mTorr Ar to presputter SiO_2 target, 20 min.

4) Sputter 2000 Å of SiO_2 to composite wafer in 22 mTorr Ar, 2 mTorr O_2, 30 min.

5) Cool 30 min., unload

6) Liftoff SiO_2 in ACE, ~10 min.

7) Rinse in DI, 3 min.

IX Patterning and deposition of Wiring layer and Inductor cross bar layer

1) Spin, bake, soak, expose, develop, rinse using wiring layer mask and inductor cross bar layer mask as in section as in section III.

2) Load composite wafer to Lesker system.

3) Pump load lock to 1 x 10^{-6} Torr

4) Transfer composite wafer to cold stage.

5) Ion beam clean composite wafer at 14 mTorr Ar, 500 mA beam current, 3 min

6) Presputter Nb target, 5000 W, 30 sec

7) Sputter Nb to composite wafer, 7.1 mTorr Ar, 5 kW, 75 sec to give 2000 Å Nb

8) Cool 5 minutes, unload

9) Liftoff pattern in ACE, 5 min.

10) Rinse in DI, 3 min.

X Patterning and deposition of Contact layer

1) Spin, bake, expose, soak, develop, rinse as in section III.

2) Load composite wafer to MRC sputtering system, heat sinking with vacuum grease

3) Pump system to 1 x 10^{-6} Torr

4) Bleed system to 1.5 mTorr Ar to presputter Ti and Au target. 5 min. each sequentially

5) Backsputter sample, 500 W, 22 mTorr Ar, 1 min. (to etch Nb_2O_5 growth)

6) Sputter 100 Å of Ti to composite wafer in 22 mTorr Ar 10 min.

7) Sputter 500 Å of Au to composite wafer in 22 mTorr Ar 10 min.

8) Cool 30 min., unload

6) Liftoff in ACE, ~10 min.

7) Rinse in DI, 3 min.

XI Removal of quartz wafer from Si wafer and remounting

1) Soak composite wafer ~ 8 hours in TCA

2) Clean quartz wafer using processing steps I-1a-e

3) Remount quartz wafer to Si host following I 3-7, device side down

XII Deposition of backside metal

1) Load composite wafer to MRC sputtering system, heat sinking with vacuum grease

2) Pump system to 1 x 10^{-6} Torr

3) Bleed system to 1.5 mTorr Ar to presputter Nb, Ti, Au targets, 5 min. each

4) Sputter 3000 Å of Nb to composite wafer in 22 mTorr Ar 10 min.

5) Sputter 100 Å of Ti to composite wafer in 22 mTorr Ar 10 min.

6) Sputter 500 Å of Au to composite wafer in 22 mTorr Ar 10 min.

7) Cool 30 min., unload

APPENDIX B

$Ta/Ta_2O_5/PbBi$ Tunnel Junction Fabrication Process

I Wafer Cleaning

1) Ultrasonic clean 2" diameter x 5.8 mil quartz wafer in

a) Trichloroethane (TCA), 2 min.

b) Acetone (ACE), 2 min.

c) DI water, 2 min.

d) Methonol (Meth), 2 min.

e) DI water, 2 min.

II Ge underlayer deposition

1) Load wafer to Varian evaporator

2) Pump system to 3 x 10^{-6} Torr

3) Evaporate 3000 Å Ge at 10 Å/sec.

4) Cool 15 min., unload

III Base electrode patterning

1) Spin photoresist Shipley 1470 at 4000 rpm, 1 min.

2) Bake 90 ^oC, 10 min.

3) Soak in Chlorobenzene, 5 min.

4) Rinse with water, blow dry with N_2, spin 20 sec./4000 rpm.

5) Expose in HTG aligner, using base electrode mask, 5 sec. at 15 mJ/cm^2

6) Develop in 1:1 Microposit developer/water, ~ 1 min.

7) Rinse in DI and blow dry.

IV Base electrode deposition and liftoff

1) Load substrate to Varian ion beam sputtering system (shutter closed, no LN_2 in sheild)

2) Pump system to 5 x 10^{-7} Torr

3) Bleed chamber to 1.2 x 10^{-4} Torr Xe

4) Presputter Nb and Ta targets, > 30 min. each, ion gun at 1500 V, 34 mA beam

5) Sputter 100 Å Nb to sample, beam parameters above (shutter open), 1 min.

6) Sputter 3000 Å Ta to sample, beam parameters above, 30 min.

7) Cool > 30 min., unload

8) Liftoff in ACE, ~ 5 min., ultrasonic can be used for < 30 sec. during entire liftoff

9) Rinse DI, 3 min.

V Junction area definition lithography

1) Spin photoresist Shipley 1470 at 4000 rpm, 1 min.

2) Bake 90 °C, 10 min.

3) Cool 2 min.

4) Soak in Chlorobenzene, 5 min.

5) Rinse with water, blow dry with N_2, spin 20 sec./4000 rpm.

6) Bake 90 °C, 5 min.

7) Cool 2 min.

8) Expose 10 sec. each "dot" to define junction area, with Zeiss microscope projection "dot" mask with 404 nm filter in beam path, focus 4 full turns clockwise from focus on device with 40 X lens

9) Expose some large test features using any mask and the same parameters above.

10) Bake 5 min., 90 °C

11) Cool 2 min.

12) Develop in 1:1 Microposit developer/water, ~ 2 min. Development is apparent in large feature exposures.

VI Deposition of Insulator and liftoff

1) Load sample to Varian evaporator

2) Pump system to < 3 x 10^{-6} Torr

3) Evaporate 2000 Å SiO from sublimation boat at 30 Å/sec.

4) Cool 15 min., unload

5) Liftoff in ACE, ~ 10 min. This step is critical since the junction area is defined by this liftoff. The sample was checked in the Zeiss microscope for liftoff. Ultrasonic agitation may be used to enhance the liftoff, but no longer than 1 min. to avoid peeling of the SiO

6) Rinse in DI, blow dry.

VII Counter electrode patterning

1) Spin photoresist Shipley 1350J at 4000 rpm, 1 min.

2) Bake 90 ^{o}C, 10 min.

3) Soak in Chlorobenzene, 5 min.

4) Rinse with water, blow dry with N_2, spin 20 sec./4000 rpm.

5) Expose in HTG aligner, using counter-electrode mask, 5 sec. at 15 mJ/cm^2

6) Develop in 1:1 Microposit developer/water, ~ 1 min.

7) Rinse in DI and blow dry.

VIII Ion beam cleaning, barrier growth, deposition of counter-electrode, and liftoff

1) Load sample to Varian evaporator rotating stage, shutter closed, heat sink Ta away from junction area with Ag paint (resistance between substrate holder and Ta should be < 5 MΩ)

2) Pump system to < 3 x 10^{-6} Torr

3) Bleed chamber to partial pressures 9 x 10^{-5} Torr O_2, 8 x 10^{-5} Torr Xe

4) Ion gun should be "warmed up" > 20 min, 200 V and 2 mA beam (note: subsequent to the development of this process and fabrication of the Ta devices, a neutralizer was added to the ion gun)

5) Ion beam clean sample (shutter open), beam parameters above, 10 min.

6) Turn off O_2 flow, bring Xe pressure to 2 x 10^{-4} Torr

7) Ion beam clean sample, beam parameters above, 15 min.

8) Turn of ion beam, Xe flow. Bring O_2 in chamber to 120 mTorr

9) Rotate sample to face discharge plate

10) Glow discharge oxidize sample (~ 200 V, 2 mA, 15 sec.)

11) Rotate sample to face evaporation boats.

12) Evaporate 3000 Å PbBi at 30 Å/sec.

13) Evaporate 150 Å In at 4 Å/sec.

14) Cool 20 min., unload

15) Liftoff in ACE, ~5 min., ultrasonic not necessary

16) Rinse DI, 3 min.

APPENDIX C

The Programming Sequence to Analyze Standing Wave Data

Experiment

1) The data is in the form {probe position 1, V_{o1} , $P(V_{o1})$}.........{probe position n, V_{on}, $P(V_{on})$}

2) If the data was taken both by ramping the voltage up and down, all of the data must be sequenced the same from V_{omin} to V_{omax}. Prog: xordiv

3) A standing wave can now be generated from the data. The program takes the n'th data point from each probe position file. The generic program is d3k1wave

4) This standing wave must be least square fit to determine the best fit $\gamma\rho$ and $(\theta - \theta_R)$. It must be put in the correct format before doing this; the noise floor power and match power must be input for the normalization. Prog: simpform1

5) The output of simpform1 can be fit. The fitting parameters are λ_g, $\gamma\rho$, and $(\theta - \theta_R)$. Prog: fitall

6) Using these fitting parameters, a standing wave is generated and compared to the standing wave given by the output of step 3) above. Prog: genwave

7) This fit is critically examined for possible problems in the normalization. λ_g can be determined from the frequency; it should match the output of step 5).

8) Once satisfied with the normalization, all of the standing waves (at each bias voltage V_o) can be least square fit. The data is put in a large array. The generic program is d3kwaves

9) This output of 8) is normalized given the match power and noise power. Prog: simpform

10) The output of 9) is least square fit. The fitting parameters are $\gamma\rho$ and $(\theta - \theta_R)$. The output is in the format {n, $\gamma\rho_n$, $(\theta - \theta_R)_n$}. Prog: fitt

11) The output of 10) is merged with any V_{on} vs. P_{on} file to give two files, one is V_o vs. $\gamma\rho$, the other is V_o vs. $(\theta - \theta_R)$. Prog: merge

12) The values of γ and θ_R can now be solved. The input parameters are the values of the elements in the equivalent circuit, and the experimentally determined $\gamma\rho$ and $(\theta - \theta_R)$ at high bias voltages. Prog: hb

13) G_Q and B_Q from the experiment can now be determined. The input parameters are values of the equivalent circuit, the experimentally determined $\gamma\rho$ and $(\theta - \theta_R)$ at all bias voltages (outputs of step 11), γ, and θ_R. Prog: hbf

Theory

1) The theoretical predictions for G_Q and B_Q are found from the dc I-V trace and the equivalent circuit. First, one must generate the KK transform of I_{dc}. Prog: kk (from C.A. Mears).

2) G_Q and B_Q can now be calculated. The input parameters are I_{dc}, I_{KK}, ω, Y_{emb}, and the pumped current at a given bias voltage (usually on the first photon step below the gap) Prog: pmpdiv (from C.A. Mears).

3) One can compare the experimental $\gamma\rho$ and $(\theta - \theta_R)$ with the theoretical predictions. The theoretical $\gamma\rho$ and $(\theta - \theta_R)$ are determined using the equivalent circuit parameters, the output of theory step 2), γ, and θ_R. Prog. hbff

REFERENCES

Atwater, H.A., IEEE Trans. Microwave Theory Tech. MTT-31, 488 (1983).

Ambegaokar, V. and A. Baratoff, Phys. Rev. Lett. 10, 486 (1963).

Bardeen, J., L. Cooper, and J.R. Schrieffer, Phys. Rev. 108, 1175 (1957).

Bardeen, J., Phys. Rev. Lett. 6, 57 (1961).

Barone, A. and G. Paterno, Physics and Applications of the Josephson Effect, Wiley, New York, (1982).

Belitsky, V.Yu. and M.A. Tarasov, IEEE Trans. Magn. MAG-27, 2638 (1991).

Bhushan, M. and E.M. Macedo, Appl. Phys. Lett. 58, 1323 (1991).

Blamire, M.G., R.E. Sometkh, G.W. Morris, and J.E. Evetts, IEEE Trans. Magn. MAG-25, 1135 (1989).

Blaney, T.G., in Infrared and Millimeter Waves, K.J. Button Ed., pg. 62 (Academic, New York, 1980).

Blondel, J., R. Blundell, M.C. Carter, and J.Y. Chenu, unpublished results, (1988).

Blundell, R., H. Hein, K.H. Gundlach, and E.J. Blum, Int. J. of Infrared and Millimeter Waves 3, 793 (1982).

Blundell, R., K.H. Gundlach, and E.J. Blum, Electron. Lett. 19, 498 (1983).

Blundell, R., M.C. Carter, and K.H. Gundlach, Int. J. Infrared and Millimeter Waves 9, 361 (1988).

Blundell, R. and D. Winkler, to be published in NATO Applied Research Workshop on Superconducting Electronics and 2nd Workshop on Josephson Devices, eds. A. Davidson, N.F. Pedersen, S. Pagano, M. Russo, and G. Costabile (Plenum, London, 1991).

Brown, E.R., T.C.L.G. Sollner, C.D. Parker, W.D. Goodhue, and C.L. Chen, Appl. Phys. Lett. 54, 934 (1989).

Büttengenbach, T.H., R.E. Miller, M.J. Wengler, D.M. Watson, and T.G. Phillips, IEEE Trans. Microwave Theory and Tech. MTT-36, 1720 (1988).

Capasso, F., S. Sen, A.C. Gossard, A.L. Hutchinson, and J.H. English, IEEE Electron Dev. Lett. EDL-7, 573 (1986).

Caves, C.M., Phys. Rev. D 26, 1817 (1982).

Chang, C.C., M. Gurvitch, D.M. Hwang, and C.W. Blonder, J. Appl. Phys. 61, 5089 (1987).

Cohen, M.H., L.M. Falicov, and J.C. Phillips, Phys. Rev. Lett. 8, 316 (1962).

Collin, R.E., Proc. IRE 43, 179 (1955).

Cui, G.-J., D.W. Face, E.K. Track, D.E. Prober, A.V. Räisänen, and P.L. Richards, IEEE Trans. Magn. MAG-23, 688 (1987).

D'Addario, L.R., Int. J. Infrared Millimeter Waves 5, 1419 (1984).

Danchi, W.C., E.C. Sutton, P.A. Jaminet, and R.H. Ono, IEEE Trans. Magn. MAG-25, 1064 (1989).

Dayem, A.H. and R.J. Martin, Phys. Rev. Lett. 8, 246 (1962).

Devyatov, I.A., L.S. Kuzmin, K.K. Likharev, V.V. Migulin, and A.B. Zorin, J. Appl. Phys. 60, 1808 (1986).

Dicke, R.H., Rev. Sci. Instr. 17, 268 (1946).

Dolan, G.J., T.G. Phillips, and D.P. Woody, Appl. Phys. Lett. 34, 347 (1979).

Duke, C.B., Tunneling in Solids, Solid State Physics Series, Vol. 10, F. Seitz, D. Turnbull, and H. Ehrenreich, Eds., Academic Press, New York, (1969).

Ellison, B.N. and R.E. Miller, Int. J. Infrared and Millimeter Waves, 8, 609 (1987).

Ermakov, An. B, V.P. Koshelets, S.A. Kovtonyuk, and S.V. Shitov, IEEE Trans. Magn. MAG-27, 2642 (1991).

Face, D.W., S.T. Ruggiero, and D.E. Prober, J. Vac. Sci. Tech. A1, 329 (1983).

Face, D.W., D.E. Prober, W.R. McGrath, and P.L. Richards, Appl. Phys. Lett. 48, 1098 (1986).

Face, D.W. and D.E. Prober, J. Appl. Phys. 62, 3257 (1987).

Falco, C.M., W.H. Parker, and S.E. Trullinger, Phys. Rev. Lett. 31, 933 (1973).

Feldman, M.J., private communication.

Feldman, M.J., J. Appl. Phys. 53, 584 (1982).

Feldman, M.J. and S. Rudner, Rev. of Infrared and Millimeter Waves 1, ed. K.J. Button (Plenum, New York 1983), p. 47.

Feldman, M.J., S.-K. Pan, and A.R. Kerr, IEEE Trans. Magn. MAG-19, 494 (1983).

Feldman, M.J., IEEE Trans. Magn. MAG-23, 1054 (1987a).

Feldman, M.J., unpublished (1987b).

Feldman, M.J. and D.W. Face, Jap. Jour. of Appl. Phys. 26, 1633 (1987).

Feuer, M.D. and D.E. Prober, IEEE Trans. Electron Devices ED-28, 1375 (1981).

Fisher, J.C. and I. Giaever, J. Appl. Phys. 32, 172 (1961).

Flamm, D.L., Chap. 2 in Plasma Etching, an Introduction, D.M. Manos and D.L. Flamm, Eds., Academic Press, New York, 1989.

Giaever, I., Phys. Rev. Lett. 5 147 (1960), and Phys. Rev. Lett. 5, 464 (1960).

Goldsmith, P.F., in Infrared and Millimeter Waves, 6, Ed. K.J. Button: Academic Press, 335, 1982.

Gradshteyn, I.S. and I.M. Ryzhik, Table of Integrals, Series, and Products, Academic Press, New York (1965).

Grimes, C.C., P.L. Richards, and S. Shapiro, J. Appl. Phys. 39, 3905 (1968).

Gundlach, K.H., R. Blundell, J. Ibruegger, and E.J. Blum, in SQUID'85, H.D. Hahlbohn and H. Lübig, eds., Walter de Gruyter & Co., Berlin (1985)

Gundlach, K.H., Working Report 203, IRAM, Domaine Universitaire, 38406 St-Martin-D'Heres, France (1990).

Gurvich, M., M.A. Washington, and H.A. Huggins, Appl. Phys. Lett. 42, 472 (1983).

Halse, M.R. and J.C. Taunton, IC-SQUID 76, 171 (1976).

Hamilton, C.A., R.L. Kautz, F.L. Lloyd, R.L. Steiner, and B.F. Field, IEEE Trans. on Inst. and Meas. IM-36, 258 (1987).

Han, S., J. LaPointe, and J.E. Lukens, Phys. Rev. Lett. 63, 1712 (1989).

Harris, R.E., Phys. Rev. B10, 84 (1974).

Harris, R.E., Phys. Rev. B11, 3329 (1975).

Hasuo, S. and T. Imamura, Proc. IEEE 77, 1177 (1989).

Hatzakis, H., B.J. Canavello, and M.J. Shaw, IBM J. Res. Dev. 24, 452 (1980).

Hicks, R.G., M.J. Feldman, and A.R. Kerr, IEEE Trans. Magn. MAG-21, 208 (1985).

Hoefer, W.J.R. and M.N. Burton, IEEE Trans. Microwave Theory Tech. MTT-30, 2190 (1982).

Hopfer, S., IRE Trans. Microwave Theory Tech. MTT-3, 20 (1955).

Hu, Q., C.A. Mears, P.L. Richards, and F.L. Lloyd, IEEE Trans. Magn. MAG-25, 1380 (1989).

Hu, Q., C.A. Mears, P.L. Richards, and F.L. Lloyd, Phys. Rev. Lett. 64, 2945 (1990a).

Hu, Q., C.A. Mears, P.L. Richards, and F.L. Lloyd, Phys. Rev. B42, 10250 (1990b).

Huang, H.C.W., S. Basavaiah, C.J. Kircher, E.P. Harris, M. Murakami, M.S. Klepner, and J.H. Greiner, IEEE Trans. Electron Dev. ED-27, 1979 (1980).

Huggins, H.A. and M. Gurvitch, J. Appl. Phys. 57, 2103 (1985).

Huq, S.E., M.G. Blamire, J.E. Evetts, D.G. Hasko, and H. Ahmed, IEEE Trans. Magn. MAG-27, 3161 (1991).

Imamura, T. and S. Hasuo, J. Appl. Phys., 64, 1586 (1988).

Imamura, T. and S. Hasuo, IEEE Trans. Magn. MAG-25, 1119 (1989).

Irwin, K.E., S.E. Schwartz, and T. Van Duzer, in Digest of the Sixth International Conference on Infrared and Millimeter Waves, K.E. Button, ed., M-4-2 (1981).

Jain, A.K., K.K. Likharev, J.E. Lukens, and J.E. Sauvageau, Phys. Rep. 109, 309 (1984).

Josephson, B.D., Phys. Letters 1, 251 (1962).

Kang, J.H., D.L. Miller, J.X. Przybysz, and M.A. Janocko, IEEE Trans. Magn. MAG-27, 3117, (1991).

Kaufman, H.R., J.J. Cuomo, and J.M.E. Harper, J. Vac. Sci. Tech. 21, 725 (1982).

Kerr, A.R., S.-K. Pan, and M.J. Feldman, and A. Davidson, Physica 108B, 1369 (1981).

Kerr, A.R., S.-K. Pan, and M.J. Feldman, Int. J. Infrared and Millimeter Waves 9, 203 (1988).

Kerr, A.R. and S.-K. Pan, in Proc. First Int. Symp on Space Terahertz Tech., (1990).

Kerr, A.R., S.-K. Pan, S. Whiteley, M. Radparvar, and S. Faris, IEEE Microwave Theory Tech. MTT-S Digest, 851 (1990).

Kirk, E.C.G., D.G. Hasko, M.G. Blamire, J.E. Evetts, and H. Ahmed, Presented at Microcircuit Engineering 89, Cambridge (1989).

Kirk, E.C.G., M.G. Blamire, R.E. Somekh, J.E. Evetts, D. VanVechten, and M.N. Lovellette, IEEE Trans. Magn. MAG-27, 3137 (1991).

Kroger, H., L.N. Smith, and D.W. Jillie, Appl. Phys. Lett. 39, 280 (1981).

Larkin, A.I. and Yu. N. Ovchinnikov, Zh. Eksp. Teor. Fiz. 51, 1535 (1966); Sov. Phys. JETP 24, 1035 (1967).

Liboff, R.L. and G.C. Dalman, Transmission Lines, Waveguides, and Smith Charts, (Macmillan, New York, 1985), Chap. 4.

Lichtenberger, A.W., C.P. McClay, R.J. Mattauch, M.J. Feldman, S.-K. Pan, and A.R. Kerr, IEEE Trans. Magn. MAG-25, 1247 (1989).

Lichtenberger, A.W., D.M. Lea, C. Li, F.L. Lloyd, M.J. Feldman, M.J. Mattauch, S.-K. Pan, and A.R. Kerr, IEEE Trans. Magn. MAG-27, 3168 (1991).

Likharev, K.K., Rev. Mod. Phys. 51, 101 (1979).

Liu, H.C., Phys. Rev. B43, 12538 (1991).

Lumley, J.M., R.E. Somekh, J.E. Evetts, and J.H. James, IEEE Trans. Magn. MAG-21, 539 (1985).

Marriot, V., C.M. Garza, and M. Spak, Proc. SPIE 771, 221 (1987).

Martinez, J.M. and R.H. Ono, Appl. Phys. Lett. 57 629 (1990).

Matthews, P.A. and I.M. Stephenson, Microwave Components, (Chapman and Hall, London, 1968), Chap. 11.

Mears, C.A., private communication.

Mears, C.A., Qing Hu, and P.L. Richards, IEEE Trans. Magn. MAG-25, 1050 (1989).

Mears, C.A., Qing Hu, P.L. Richards, A.H. Worsham, D.E. Prober, A.V. Räisänen, Appl. Phys. Lett. 57, 2487 (1990).

Mears, C.A., Qing Hu, P.L. Richards, A.H. Worsham, D.E. Prober, A.V. Räisänen, IEEE Trans. Magn. MAG-27, 3363 (1991a).

Mears, C.A., Qing Hu, and P.L. Richards, IEEE Trans. Magn. MAG-27, 3384 (1991b).

Meier, D.L., J.X. Przybysz, and J.H. Kang, IEEE Trans. Magn. MAG-27, 3121 (1991).

McGrath, W.R., P.L. Richards, A.D. Smith, H. Van Kempen, R.A. Batchelor, D.E. Prober, and P. Santhanam, Appl. Phys. Lett. 39, 655 (1981).

McGrath, W.R., A.V. Räisänen, and P.L. Richards, IEEE Trans. Magn. MAG-21, 212 (1985).

McGrath, W.R., Ph.D. Thesis, UC Berkeley (1985).

McGrath, W.R., P.L. Richards, D.W. Face, D.E. Prober, and F.L. Lloyd, J. Appl. Phys. 63, 2479 (1988).

McGrath, W.R., V. Lubecke, and D.B. Rutledge, Digest of the 15'th International Conference on Infrared and Millimeter Waves, Orlando, 1990.

Moreno, T., Microwave Transmission Design Data, (Dover, New York, 1948), Chap. 7.

Moritz, H., IEEE Trans. Electron Devices ED-32, 672 (1985).

Morohashi, S., F. Shinoki, A. Shoji, M. Aoyagi, and H. Hayakawa, Appl. Phys. Lett. 46, 1179 (1985).

Morohashi, S., S. Hasuo, and T. Yamaoka, Appl. Phys. Lett. 48, 254 (1986).

Morohashi, S. and S. Hasuo, J. Appl. Phys. 61, (1987).

Movshovich, R., B. Yurke, P.G. Kaminsky, A.D. Smith, A.H. Silver, and R.W. Simon, IEEE Trans. Magn. MAG-27, 2658 (1991).

Nagatsuma, T., K. Enpuku, F. Irie, and K. Yoshida, J. Appl. Phys. 54, 3302 (1983).

Ogawa, H., A. Mizuno, H. Hoko, H. Ishikawa, and Y. Fukui, Int. J. Infrared and Millimeter Waves 11, 717 (1990).

Olsson, L., S. Rudner, E. Kollberg, and C.O. Lindström, Int. J. Infrared and Millimeter Waves 4, 847 (1983).

Pagano, S., R. Monaco, and G. Constabile, IEEE Trans. Magn. MAG-25, 1080 (1989).

Pan, S.-K., M.J. Feldman, A.R. Kerr, and P. Timbie, Appl. Phys. Lett. 43, 786 (1983).

Pan, S.-K. and A.R. Kerr, NASA Technical Memorandum 87792, July, 1986.

Pan, S.-K., A.R. Kerr, M.J. Feldman, A.W. Kleinsasser, J.W. Stasiak, R.L. Sandstrom, and W.J. Gallagher, IEEE Trans. Microwave Theory Tech. MTT-37, 580 (1989).

Phillips, T.G., D.P. Woody, G.J. Dolan, R.E. Miller, and R.A. Linke, IEEE Trans. Magn. MAG-17, 684 (1981).

Phillips, T.G. and G.J. Dolan, Physica 109 and 110B, 2010, (1982).

Przybysz, J.X., R.D. Blauer, and J. Buttyan, IEEE Trans. Magn. MAG-25, 1127 (1989).

Raider, S.I., private communication.

Räisänen, A.V., D.G. Crété, P.L. Richards, and F.L. Lloyd, Int. J. Infrared and Millimeter Waves 7, 1835 (1986).

Räisänen, A.V., D.G. Crété, P.L. Richards, and F.L. Lloyd, IEEE Trans. Microwave Theory and Tech. MTT-S Digest, 929 (1987).

Reed, M.A., W.R. Frensley, R.J. Matyi, J.N. Randall, and A.C. Seabaugh, Appl. Phys. Lett. 54, 1034 (1989).

Richards, P.L., T.-M. Shen, R.E. Harris, and F.L. Lloyd, Appl. Phys. Lett. 34, 345 (1979).

Richards, P.L., T.-M. Shen, R.E. Harris, and F.L. Lloyd, Appl. Phys. Lett. 36, 480 (1980).

Richards, P.L. and Qing Hu, Proc. of the IEEE 77, 1233 (1989).

Rickayzen, G., in Superconductivity Vol. 1, R.D. Parks, Ed., Marcel Dekker, New York, (1969).

Riedel, E., Z. Naturforsch. 19A, 1634 (1964).

Rogovin, D. and D.J. Scalapino, Ann. Phys. 86, 1 (1974).

Rose-Innes, A.C. and E.H. Rhoderick, Introduction to Superconductivity, Pergamon Press, Oxford, (1978).

Rudner, S. and T. Claeson, Appl. Phys. Lett. 34, 711 (1979).

Rudner, S., M.J. Feldman, E. Kollberg, and T. Claeson, IEEE Trans. Magn. MAG-17, 690 (1981).

Ruggiero, S.T., E.K. Track, D.E. Prober, G.B. Arnold, and M.J. DeWeert, Phys. Rev. B34, 217 (1986).

Schneider, M.V., B. Glance, and W.F. Bodtmann, Bell System Tech. J., 1703 (1968).

Shapiro, S., A.R. Janus, and S.H. Holly, Rev. Mod. Phys. 36, 223 (1964).

Shoji, A., S. Kosaka, F. Shinoki, M. Aoyagi, and H. Hayakawa, IEEE Trans. Magn. MAG-19, 827 (1983).

Skalare, A., Int. J. Infrared and Millimeter Waves 10, 1339 (1989); see also Internal Report, S.R.O.N. Space Res. Lab., Groningen, Netherlands, (1989).

Smith, A.D., W.R. McGrath, P.L. Richards, H. Van Kempen, D. Prober, and P. Santhanam, Physica B+C 108, 1367 (1981).

Smith, A.D., J.A. Carpenter, D.J. Durand, and L. Lee, IEEE Trans. Magn. MAG-27, 3370 (1991).

Sollner, T.C.L.G., W.D. Goodhue, P.E. Tannenwald, C.D. Parker, and D.D. Peck, Appl. Phys. Lett. 43, 588 (1983).

Spencer, E.G. and J.M. Rowell, IEEE Trans. Magn., MAG-17, 322 (1981).

Sutton, E.C., IEEE Trans. Microwave Theory Tech., MTT-31, 589 (1983).

Syrett, B.A., IEEE Trans. Microwave Theory Tech. MTT-28, 925 (1980).

Terman, F.E., in Radio Engineers Handbook, New York: McGraw Hill, p.51 (1943).

Tien, P.K. and J.P. Gordon, Phys. Rev. 129, 647 (1963).

Tinkham, M., Introduction to Superconductivity, McGraw Hill, New York, (1975).

Tong, C.E. and R. Blundell, IEEE Trans. Microwave Theory and Tech. MTT-38, 1391 (1990).

Torrey, H.C. and C.A. Whitmer, Crystal Rectifiers, New York: McGraw Hill, MIT Radiation Laboratory Series Vol. 15, 1948.

Tucker, J.R., IEEE J. Quantum Electron. QE-15, 1234 (1979).

Tucker, J.R., Appl. Phys. Lett. 36, 477 (1980).

Tucker, J.R. and M.J. Feldman, Rev. Mod. Phys. 57, 1055 (1985).

Ugras, N.G., unpublished (1991).

Van Duzer, T. and C.W. Turner, Principles of Superconducting Devices and Circuits, Elsevier North Holland, New York (1981).

Vincent, D.A. and B.S. Deaver, Jr., Phys. Rev. Lett. 32, 212 (1974).

Vinding, V.P., NEREM RECORD, 108 (1967).

Vowinkel, K. Eigler, W. Hilberath, K. Jacobs, and P. Muller, Int. J. Infrared and Millimeter Waves 10, 579 (1989).

Wan, K.L., A.K. Jain, and J.E. Lukens, IEEE Trans. Magn. MAG-25, 1076 (1989).

Wengler, M.J. and D.P. Woody, IEEE J. Quantum Electron. QE-23, 613 (1987).

Werthamer, N.R., Phys. Rev. 147, 255 (1966).

Wilkens, J.W., in Tunneling Phenomena in Solids, E. Burnstein and S. Lundquist, eds., Plenum, New York, 1969.

Winkler, D., Ph.D. dissertation, ISBN 91-7032-307-0 Department of Physics, Chalmers University of Technology, S-412 96 Gothenburg, Sweden, May 1987.

Winkler, D., D.E. Prober, N.R. Erickson, and P.F. Goldsmith, unpublished (1989).

Winkler, D., Z.G. Ivanov, and T. Claeson, to be published in Superconducting Technology: 10 Case Studies, ed. K. Fossheim (World Scientific, Singapore, June, 1991).

Winkler, D., A.H. Worsham, N.G. Ugras, D.E. Prober, N.R. Erickson, and P.F. Goldsmith, to be published in NATO Applied Research Workshop on Superconducting Electronics and 2nd Workshop on Josephson Devices, eds. A. Davidson, N.F. Pedersen, S. Pagano, M. Russo, and G. Costabile (Plenum, London, 1991a).

Winkler, D., N.G. Ugras, A.H. Worsham, D.E. Prober, N.R. Erickson, and P.F. Goldsmith, IEEE Trans. Magn. MAG-27, 2634 (1991b).

Winkler, D., N.R. Erickson, N.G. Ugras, A.H. Worsham, D.E. Prober, and P.F. Goldsmith, unpublished (1991c).

Withington, S. and E.L. Kollberg, IEEE Trans. Microwave Theory and Tech. MTT-37, 231 (1989).

Wolf, E.L., Principles of Electron Tunneling Spectroscopy, Oxford Press, New York, (1985).

Woody, D.P., R.E. Miller, and M.J. Wengler, IEEE Trans. Microwave Theory Tech. MTT-33, 90 (1985).

Worsham, A.H., D.E. Prober, J.H. Kang, J.X. Przybysz, and M.J. Rooks, IEEE Trans. Magn., MAG-27, 3165 (1991).

Xizhi, Li, P.L. Richards, and F.L. Lloyd, Int. J. Infrared and Millimeter Waves 6, 697 (1985).

Zorin, A.B., IEEE Trans. Magn. MAG-21, 939 (1985).